The Top and Beyond

Missing Energy and Little Higgs in ATLAS

ACADEMISCH PROEFSCHRIFT

ter verkrijging van de graad van doctor

aan de Universiteit van Amsterdam

op gezag van de Rector Magnificus

prof. dr. D.C. van den Boom

ten overstaan van een door het college van promoties ingestelde

commissie, in het openbaar te verdedigen in de Agnietenkapel

op donderdag 17 maart 2011, te 12:00 uur

door

Manouk Rijpstra

geboren te Delft

Promotor: Prof. dr. S.C.M. Bentvelsen
Co-promotor: Dr. M. Vreeswijk

Overige Leden: Prof. dr. ir. E.N. Koffeman
Prof. dr. E.L.M.P. Laenen
Prof. dr. P.M. Kooijman
Prof. dr. ir. P.J. de Jong
Prof. dr. N. de Groot
Dr. G.J. Bobbink
Dr. P. Ferrari

Faculteit der Natuurwetenschappen, Wiskunde en Informatica

This work is part of the research programme of the Foundation for Fundamental Research on Matter (FOM), which is part of the Netherlands Organisation for Scientific Research (NWO). It was carried out at the National Institute for Subatomic Physics (Nikhef) in Amsterdam, the Netherlands.

Contents

Preface

It has been a great privilege to be a part of the ATLAS experiment at CERN—a place I dreamed of in high school. In September 2008, when the very first protons were accelerated simultaneously in both directions along the LHC ring, I was there. Unfortunately, 9 days later, I also witnessed the fire department turn out because of an enormous helium leak in the accelerator. The damage turned out so severe that the recovery took over a year. This obviously interfered with the plans set out for my PhD research. Nevertheless, it allowed me to perform detailed and interesting studies on simulated collisions and ultimately, I even had the opportunity to "play" with the data that was recorded during the final months of my PhD.

Manouk Rijpstra, November 2010, Amsterdam

Introduction

The field of particle physics has recently entered a very exciting and long anticipated era: the Large Hadron Collider has started colliding beams of protons at higher energies than ever reached by particle accelerators. Its predecessor, the Tevatron, was the first to produce the top quark and completed the three generations of quarks in the Standard Model. In fact, all processes observed in particle accelerator experiments thus far are perfectly described by the Standard Model. Nevertheless, there are strong indications that this theoretical prescription may fail to describe elementary particles and the interactions between them at ever higher energies. More complete models are expected to take over at the TeV scale, which is currently being probed at the LHC. Numerous models have been proposed by theoretical physicists over the last decades, all of which are now to be tested by analyzing the proton collisions being recorded by the ATLAS detector.

Many of the proposed models predict a neutrino or another type of non-interacting particle in the expected signal at the proton collisions. These particles leave no trace in detectors and cause missing energy. In the plane transverse to the colliding proton beams, the projection of the missing energy can be deduced from the energy imbalance between the particles produced in the collision that *are* detected. As it plays a key role in the discovery of physics beyond the Standard Model, the reconstruction of the missing energy is to be well understood. The first major topic of this thesis is a study of its performance in top quark pair events, which provide a window to searches for new physics.

One particular class of proposed models to describe physics beyond the Standard Model are Little Higgs models. In these models, some of the Standard Model particles obtain heavier partners, amongst which the W' boson. Its mass is expected to be at the TeV scale, which allows it to decay into the heavy third generation of quarks: a top and a bottom quark. The discovery potential of this signal is the second major topic.

Outline

This thesis is organized as follows: The first four chapters describe the concepts and tools that are common to experimental particle physics as well as those particularly relevant for this thesis. The last four chapters deal with the actual analysis of events: selection, Monte Carlo studies on the missing energy, a method to assess the performance of its reconstruction, the discovery potential of the $W' \to tb$ signal as well as a first glimpse of the data recorded in 2010.

1

Theoretical Background and Motivation

The Standard Model of Particles is at present the best description of elementary particles and fundamental interactions. This chapter describes the remarkable successes as well as the shortcomings of the Standard Model. The first section summarizes the knowledge that is available in particle physics at this point. Section 1.2 goes into the limitations of the theory and the reasons why new physics models can be expected to come into play at LHC energy scales. The last section describes a class of proposed extensions of the Standard Model, the so-called Little Higgs Theories.

1.1 The Standard Model

The subject of particle physics has seen enormous progress in the second half of the twentieth century with the development of the Standard Model [1,2,3]. Simultaneously, new particles and phenomena were frequently observed in experiments, either providing input or in fact confirming the ongoing construction of the theory. The Standard Model is a relativistic quantum field theory that unifies electrodynamics and the two nuclear forces—the strong and the weak force. It is based on the symmetry group $SU(3)_C \times SU(2)_I \times U(1)_Y$, where the strong interactions are described by the $SU(3)_C$ group and the electroweak interactions by $SU(2)_I \times U(1)_Y$. The subscripts C, I and Y indicate the conserved quantum numbers that correspond to each symmetry, i.e. colour charge, weak isospin and hypercharge respectively.

Elementary particles are categorized into two classes of particles: *bosons* and *fermions*. Bosons have integer spin and obey the Bose-Einstein statistics, whereas fermions have half-integer spin and follow the Fermi-Dirac statistics. Each elementary particle has a corresponding anti-particle, whose quantum numbers are opposite in sign. Hereafter, all statements regarding particles hold just as well for the corresponding anti-particles, unless specified otherwise.

The three fundamental forces that are incorporated in the Standard Model are mediated by the twelve gauge bosons that are associated with the generators of the symmetry group: eight colour charged gluons, three weak bosons and the photon.

The fermion sector of the Standard Model contains leptons and quarks, which are generally arranged in three generations, as indicated in Table 1.1. All (known) stable matter of which the universe is composed consists of fermions from the first generation. The charged leptons are subject to electromagnetic and weak interactions, whereas the colour charged quarks are in addition subject to the strong force. Neutrinos are merely subject to the weak interaction and consequently very difficult to study in experiment. The electric charge[1] Q of quarks adopts fractional values, i.e. +2/3 for *up-type* quarks and -1/3 for *down-type* quarks, yet they are only observed as the integer charge combinations of three quarks (baryons) or a quark and an antiquark (mesons).

		Generation					
	Q	**I**		**II**		**III**	
Quarks	$+\frac{2}{3}$	up	(u)	charm	(c)	top	(t)
	$-\frac{1}{3}$	down	(d)	strange	(s)	bottom	(b)
Leptons	-1	electron	(e)	muon	(μ)	tau	(τ)
	0	electron neutrino	(ν_e)	muon neutrino	(ν_μ)	tau neutrino	(ν_τ)

Table 1.1: The fermion sector of the Standard Model. The three mass generations (I,II and III) are displayed in separate columns.

1.1.1 The Standard Model Lagrangian

The Standard Model Lagrangian is the result of the unification of electrodynamic, weak and strong interactions. The description of the interactions follows from the $SU(3)_C \times SU(2)_I \times U(1)_Y$ gauge symmetry, which is introduced in steps in the following.

QED

Quantum Electrodynamics (QED) is the relativistic quantum field theory based on the symmetry group $U(1)$ that describes electromagnetic interactions. The coupling of charged fermion fields ψ to the photon field A^μ is described by the QED Lagrangian density, which is given by

$$\mathcal{L}_{\text{QED}} = \bar{\psi}(i\gamma^\mu D_\mu - m)\psi - \frac{1}{4}F_{\mu\nu}F^{\mu\nu}. \tag{1.1}$$

The covariant derivative D_μ and the field strength tensor $F_{\mu\nu}$ are given by

$$D_\mu = \partial_\mu - ieA_\mu \tag{1.2}$$
$$F^{\mu\nu} = \partial^\mu A^\nu - \partial^\nu A^\mu \tag{1.3}$$

[1] The electric charge is given in units of the elementary charge, e, which is the charge carried by a positron.

such that the Lagrangian is invariant under local $U(1)$ gauge transformations. The γ^μ are the Dirac matrices, which satisfy $\{\gamma^\mu, \gamma^\nu\} = 2g^{\mu\nu}$. The strength of the interaction is characterized by the coupling $\alpha = e^2/(4\pi)$.

Electroweak Theory

In addition to electromagnetic interactions, fermions are subject to weak interactions. Both are manifestations of the unified electroweak theory, which is described by the gauge symmetry $SU(2)_I \times U(1)_Y$. The fermion fields are expressed by Dirac spinors which can be decomposed into a left- and a right-handed component. The matrix operator $\gamma^5 = i\gamma^0\gamma^1\gamma^2\gamma^3$ has eigenvalues -1 for left-handed fermions and $+1$ for right-handed fermions. Consequently, the left- and right handed projections are obtained by applying the chirality operators

$$P_L = \frac{1-\gamma^5}{2} \qquad P_R = \frac{1+\gamma^5}{2} \tag{1.4}$$

respectively. The left-handed fermion fields $\psi_i = \begin{pmatrix} \nu_i \\ l_i^- \end{pmatrix}$ and $\begin{pmatrix} u_i \\ d_i' \end{pmatrix}$ of the i^{th} generation transform as doublets under the $SU(2)_I$ symmetry group. The conserved quantum number under $SU(2)_I$ transformations is the third component of the weak isospin, I_3, which is equal to $+\frac{1}{2}$ for the upper component in each doublet and $-\frac{1}{2}$ for its isospin partner. The right-handed fermion fields are invariant under $SU(2)_I$. The violation of parity in weak interactions is thus incorporated in the Standard Model.

The weak eigenstates of the quark fields are not identical to their mass eigenstates. Instead, they are linear combinations parameterized by the CKM (Cabibbo-Kobayashi-Maskawa) matrix V_{ij} [4], such that $d_i' = \sum_j V_{ij} dj$. The coupling between fermions from different generations is thus proportional to the (very small) off-diagonal elements of the CKM matrix.

The gauge fields corresponding to the generators of the gauge symmetry are W_μ^i for $SU(2)_I$ and B_μ for $U(1)_Y$. The respective coupling strengths are denoted g and g' and the field strength tensors are given by

$$W_{\mu\nu}^i = \partial_\mu W_\nu^i - \partial_\nu W_\mu^i + g\epsilon_{ijk} W_\mu^j W_\nu^k \tag{1.5}$$

$$B_{\mu\nu} = \partial_\mu B_\nu - \partial_\nu B_\mu. \tag{1.6}$$

Analogous to $\mathcal{L}_{\text{QED}}$, the interactions between the gauge fields and fermions are described by the Lagrangian density

$$\mathcal{L}_{\text{EW}} = i \sum_f \bar{\psi}_f \gamma^\mu D_\mu \psi_f - \frac{1}{4} W_{\mu\nu}^i W^{i\ \mu\nu} - \frac{1}{4} B_{\mu\nu} B^{\mu\nu}, \tag{1.7}$$

which is invariant under local $SU(2)_I \times U(1)_Y$ gauge transformations when the covariant derivative is given by

$$D_\mu = \partial_\mu + \frac{1}{2} i g \tau^i W_\mu^i - \frac{1}{2} i g' Y B_\mu. \tag{1.8}$$

The generators associated with the $SU(2)$ symmetry group are the Pauli matrices τ_i and the generator of the $U(1)_Y$ symmetry is the hypercharge Y, which is defined via

$$Q = Y + I_3. \tag{1.9}$$

Glashow, Weinberg and Salam proposed the unified description of the electromagnetic and weak interactions by introducing the $SU(2)_I \times U(1)_Y$ electroweak theory. Initially, the proposal failed because it predicts massless gauge fields associated to the generators of the $SU(2)_I$ symmetry group, analogous to the photon in QED, which were not observed. Instead there was evidence for the massive charged W and neutral Z bosons and a mechanism was required for the weak bosons to acquire mass. The proposed solution involves *spontaneous symmetry breaking* and is termed the Higgs mechanism, after one of the main contributors.

The Higgs Mechanism

The Higgs mechanism [5,6,7] provides the possibility to introduce mass terms for the gauge bosons that are consistent with the symmetry of the Standard Model Lagrangian. To this end, a complex scalar field doublet $\Phi = \begin{pmatrix} \varphi_1 \\ \varphi_2 \end{pmatrix}$ is introduced as follows,

$$\begin{aligned} \mathcal{L}_{\text{Higgs}} &= (D_\mu \Phi)^\dagger (D^\mu \Phi) - V(\Phi) \\ V(\Phi) &= \mu^2 |\Phi|^2 + \lambda |\Phi|^4, \end{aligned} \tag{1.10}$$

where the covariant derivative is given by (1.8) such that local $SU(2)_I \times U(1)_Y$ invariance is obeyed. The spontaneous symmetry breaking is accomplished by the unconventional choice $\mu^2 < 0$ for the mass parameter. With the self-coupling $\lambda > 0$, the minimum of the scalar potential $V(\Phi)$ is nonzero and degenerate:

$$|\Phi_0|^2 = -\frac{\mu^2}{2\lambda} \equiv \frac{1}{2} v^2. \tag{1.11}$$

The Higgs doublet Φ is reparameterized in order to describe variations around the minimum. Without loss of generality, it is written in the unitary gauge as

$$\begin{aligned} \text{Re}(\varphi_1) &= \text{Im}(\varphi_1) = \text{Im}(\varphi_2) = 0 \\ \text{Re}(\varphi_2) &= \frac{1}{\sqrt{2}} (v + H(x)) \end{aligned} \tag{1.12}$$

and the Lagrangian becomes

$$\begin{aligned} \mathcal{L}_{\text{Higgs}} &= \frac{1}{8} \left[g^2 (W_1^2 + W_2^2) + (-g W_3 + g' Y B_\mu)^2 \right] (v + H(x))^2 \\ &+ \frac{1}{2} (\partial^\mu H)(\partial_\mu H) - \mu^2 H^2 - v \lambda H^3 - \frac{1}{4} \lambda H^4, \end{aligned} \tag{1.13}$$

i.e. mass terms appear for the vector fields and they couple to the massive real scalar field $H(x)$. The familiar bosons are identified as the mass eigenstates:

$$W_\mu^\pm = \frac{1}{\sqrt{2}} \left(W_\mu^1 \mp W_\mu^2 \right) \tag{1.14}$$

$$\begin{pmatrix} A_\mu \\ Z_\mu \end{pmatrix} = \begin{pmatrix} \cos\theta_W & \sin\theta_W \\ -\sin\theta_W & \cos\theta_W \end{pmatrix} \begin{pmatrix} B_\mu \\ W_\mu^3 \end{pmatrix} \tag{1.15}$$

where

$$\cos\theta_W = \frac{g}{\sqrt{g^2 + g'^2}} \qquad \sin\theta_W = \frac{g'}{\sqrt{g^2 + g'^2}}. \tag{1.16}$$

The observation that the photon field couples with the electromagnetic coupling strength e leads to the relation

$$e = g\sin\theta_W = g'\cos\theta_W. \tag{1.17}$$

The mass terms corresponding to the eigenstates that follow from the Lagrangian are

$$m_W = \frac{1}{2}gv \tag{1.18}$$

$$m_A = 0 \tag{1.19}$$

$$m_Z = \frac{1}{2}v\sqrt{g^2 + g'^2} \tag{1.20}$$

The value of v, the vacuum expectation value (vev), is determined to be $v = 246$ GeV and the values for the W and Z boson masses that follow are consistent with experimental data. The Higgs boson H itself, however, is yet to be observed. Therefore, the theory remains to be verified, which is a major goal of the ATLAS experiment. The mass of the Higgs boson, which is given by $m_H = \sqrt{2\lambda}v$, is not predicted by the Standard Model as the quartic self-coupling of the Higgs λ remains a free parameter. There are experimental bounds as well as theoretical constraints on the value of the Higgs mass though, which are discussed in Section 1.2.1.

The Higgs mechanism provides the gauge bosons with their masses by breaking the electroweak symmetry. The initial four degrees of freedom that are introduced as the Higgs doublet result in three mass parameters and the Higgs field H. The Standard Model remains invariant under $SU(2)_I \times U(1)_Y$ transformations, yet the ground state obeys the $U(1)_Q$ symmetry only.

The Higgs Mechanism builds upon the *Goldstone theorem*, which states that for every generator of a spontaneously broken symmetry, a massless boson emerges. In the Standard Model, the three would-be *Goldstone bosons* are absorbed by the W and Z bosons to acquire their masses, while leaving the photon massless.

The Higgs field so introduced also allows for fermionic mass terms to be incorporated by means of the Yukawa interaction, $\mathcal{L}_{\text{Yukawa}}$, which couples fermions to the Higgs field.

QCD

Quantum Chromodynamics (QCD) is the quantum field theory that describes strong interactions, i.e. the interactions between quarks and gluons. The QCD Lagrangian density is given by

$$\mathcal{L}_{\text{QCD}} = \sum_q \bar{\psi}_{q,a}\left(i\gamma^\mu(D_\mu)_{ab} - m_q\delta_{ab}\right)\psi_{q,b} - \frac{1}{4}G^A_{\mu\nu}G^{A\ \mu\nu}. \tag{1.21}$$

The $\psi_{q,a}$ are the quark fields for flavor q and carry a color index a, which runs from 1 to $N_c = 3$. The covariant derivative D_μ and the gluon field strength tensor $G^A_{\mu\nu}$ are given by

$$D_\mu = \partial_\mu + i g_s t^A \mathcal{A}^A_\mu, \tag{1.22}$$
$$G^A_{\mu\nu} = \partial_\mu \mathcal{A}^A_\nu - \partial_\nu \mathcal{A}^A_\mu - g_s f^{ABC} \mathcal{A}^B_\mu \mathcal{A}^C_\nu, \tag{1.23}$$

where $\mathcal{A}^A_\mu$ are the gluon fields with index A running from 1 to $N_c^2 - 1 = 8$. The 3×3 matrices t^A are the generators of the $SU(3)$ group and satisfy $[t^A, t^B] = i f^{ABC} t^C$. The strong coupling strength g_s is usually replaced by $\alpha_s = g_s^2/(4\pi)$. The QCD Feynman rules that follow from the Lagrangian are the quark and gluon propagators and the vertices $q\bar{q}g$, ggg and $gggg$.

The Standard Model

Altogether, the Standard Model interactions are completely described by the Lagrangian

$$\mathcal{L}_{\mathrm{SM}} = \mathcal{L}_{\mathrm{fermion}} + \mathcal{L}_{\mathrm{gauge}} + \mathcal{L}_{\mathrm{Higgs}} + \mathcal{L}_{\mathrm{Yukawa}} \tag{1.24}$$

where $\mathcal{L}_{\mathrm{Higgs}}$ is given by (1.10) and

$$\mathcal{L}_{\mathrm{fermion}} = i \sum_f \bar{\psi}_f \gamma^\mu D_\mu \psi_f \tag{1.25}$$
$$\mathcal{L}_{\mathrm{gauge}} = -\frac{1}{4} W^i_{\mu\nu} W^{i\ \mu\nu} - \frac{1}{4} B_{\mu\nu} B^{\mu\nu} - \frac{1}{4} G^A_{\mu\nu} G^{A\ \mu\nu} \tag{1.26}$$
$$\mathcal{L}_{\mathrm{Yukawa}} = -i \sum_f \lambda_f \bar{\psi}_f \Phi \psi_f \tag{1.27}$$

The field strength tensors are given by (1.5), (1.6) and(1.23), while the covariant derivative D_μ is given by

$$D_\mu = \partial_\mu + i g_s T^A \mathcal{A}^A_\mu + i g t_a W^a_\mu + i g' Y B_\mu.$$

The fermionic mass terms appear in $\mathcal{L}_{\mathrm{Yukawa}}$ when expanding the Higgs field around the vacuum expectation value. The Yukawa couplings λ_f determine the actual mass via $m_f = \frac{1}{\sqrt{2}} \lambda_f v$ and are free parameters of the theory.

1.1.2 The Top Quark

As the top quark plays a special role in the LHC era in many respects, some of its particular properties are reviewed here.

The top quark was first observed in $p\bar{p}$ collisions by the DØ and CDF detectors in 1995 [8,9]. The Tevatron data that have been accumulated since then result in the current best combined result from direct measurements for its mass [10]:

$$m_t = 171.3 \pm 1.1\ (\text{stat.}) \pm 1.2\ (\text{syst.})\ \text{GeV} \tag{1.28}$$

This makes the top quark by far the heaviest fermion in the Standard Model and is also the reason why it had not been produced in previous accelerator experiments. In fact, the top quark mass is five orders of magnitude larger than the masses of quarks in the first generation, as illustrated in Figure 1.1.

Since its mass passes the threshold $m_t > m_W + m_b$, and other decay channels are strongly suppressed by the corresponding entries of the CKM matrix[2], the top quark decays predominantly into a W boson and a b quark. Due to its large decay width and correspondingly short lifetime of $\mathcal{O}(10^{-25}\text{ s})$ [10], this decay actually occurs before the top quark is subject to hadronization. Consequently, unlike other quark flavours, no resonant states with top quarks are observed and the top quark is only detected through its decay products.

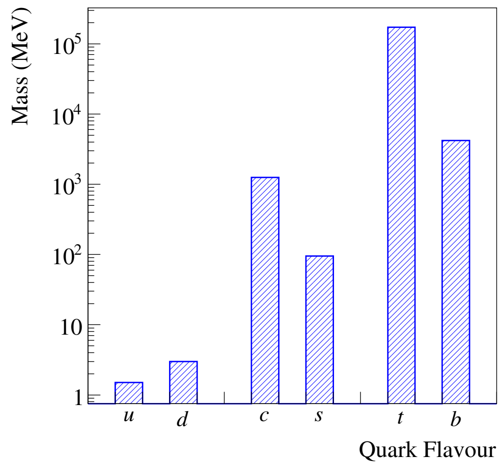

Figure 1.1: Quark masses according to the PDG [11] on a logarithmic scale.

The existence and the mass of the top quark were actually already predicted before it was observed. With the discovery of the b-quark in 1977, the third generation of fermions required its weak isospin partner to exist in order to be complete[3]. The configuration of quantum numbers of leptons and quarks in each generation ensures the cancellation of so-called *triangle anomalies*[4] and the suppression of flavour changing neutral currents, which are severely limited by experiment.

The prediction of the mass of the top quark is one of the remarkable manifestations of the internal consistency of the Standard Model. The mass of the W boson, m_W, can be expressed in terms of the three best measured electroweak parameters: the electromagnetic coupling constant α, the Fermi constant G_F and the Z boson mass m_Z. Quantum corrections to m_W are dominated by the loop diagram depicted in Figure 1.2, where the large mass of the top quark makes it contribute more than other fermion loops. Neglecting the mass of the b quark, the size of this correction is proportional to the top mass squared and combined measurements from the LEP experiments provided an indirect limit on the top mass of $m_t = 180^{+14}_{-11}$ GeV [13].

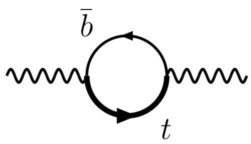

Figure 1.2: The virtual top quark loop diagram that contributes to the mass of the W boson.

At the LHC, the top quark is important for two main reasons. Firstly, top quark physics can be regarded as the final stepping stone within the Standard Model before entering the realm of discoveries. As such and thanks to the large production rate at LHC energies,

[2] More precisely, assuming three generations and unitarity, measurements of V_{ts} and V_{td} provide a 90% confidence level interval of $0.9990 < |V_{tb}| < 0.9992$ [12].

[3] Similarly, Glashow, Iliopoulos and Maiani predicted the existence of the charm quark in 1970 as the partner of the strange quark.

[4] In addition, the existence of exactly three colour charges is required for the cancellation to hold.

it provides an environment to test and understand the performance of the detector and reconstruction algorithms in a challenging (i.e. busy), yet familiar event topology. An important example is the performance of the reconstruction of missing transverse energy, which is the subject of Chapter 6. Secondly, the top quark plays a key role in the searches for physics beyond the Standard Model. Since top quarks will be produced copiously at the LHC compared to the Tevatron rate, more precise measurements of its properties can be achieved. Any deviations of these properties from Standard Model predictions reveal the interference of new physics. The cross section for single top production, for example, is directly proportional to V_{tb} and a precise measurement will reveal information about the unitarity of the CKM matrix. In addition, a precise measurement of m_t enhances the strength of the constraint on the Higgs boson mass. Moreover, the top quark is a possible decay product of heavy new particles as introduced in many models to describe physics beyond the Standard Model. Such channels are severely suppressed within the Standard Model and therefore very suitable to reveal the physics beyond. The discovery potential of such a decay channel, $W' \to tb$, is investigated in Chapter 7. Finally, Standard Model top quark events are the main background to signals expected by many proposed models and need to be understood in detail.

1.2 Beyond the Standard Model

The Standard Model successfully describes all aspects of fundamental particles from atomic scales down to the shortest length scales probed in experiment so far. In fact, its predictions have been verified by experiments with extraordinary precision in the last decades. So why look for physics beyond the Standard Model? The following are some of the most important indications that the Standard Model is unable to describe physics at ever smaller length scales:

- In the Standard Model, the neutrino is described as a massless particle, yet experimental evidence exists for a finite -albeit small- mass [14].
- The Standard Model successfully describes all matter as we know it on earth, but it does not account for the remaining 96 % of matter and energy in the universe (cf. Figure 1.3). The nature of this *dark matter* and *dark energy* is postulated to explain the energy density of the universe [15].
- It does not include a description for the gravitational force, which becomes significant at small length scales quantified by the *Planck scale* $M_{\text{Planck}} \sim 10^{19}$ GeV. Thus far, no satisfactory description in terms of a quantum field theory has been constructed.
- Evolution of the dependence of the three Standard Model couplings on the renormalization scale indicates that at some energy scale $\Lambda_{\text{GUT}} \sim 10^{15}$ GeV their strengths become of comparable size. In the Standard Model the running couplings nearly cross in one point, but not exactly, which supports the idea that the Standard Model may be the low-energy manifestation of some *Grand Unification Theory* in which the three forces are unified and described by one coupling strength. This would be accomplished

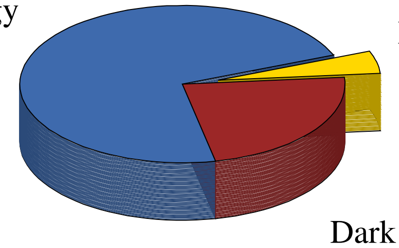

Figure 1.3: Estimated composition of baryonic matter, dark matter and dark energy in the universe.

by a symmetry group which contains $SU(3)_C \times SU(2)_I \times U(1)_Y$ as a subgroup and is spontaneously broken to that subgroup below Λ_{GUT}.

- Due to divergent loop contributions to the Higgs mass, the tree level mass parameter needs to be finely tuned in order to generate a value of the Higgs mass consistent with its upper bound. This *hierarchy problem* or *fine-tuning problem* is of a more aesthetic nature and is further discussed below.

1.2.1 The Hierarchy Problem

Being a free parameter of the Standard Model, the mass of the Higgs boson is not predicted by the theory. However, direct searches by the LEP experiments have resulted in a lower bound of 114.4 GeV at 95% confidence level [16]. More recently, CDF and DØ excluded the mass range between 158 GeV and 175 GeV with 95% confidence level [17]. Assuming that the Standard Model is the complete description, precision measurements of electroweak parameters set an indirect upper bound of 285 GeV at 95% confidence level [10].

Although its exact value is yet to be determined, the relative size of quantum corrections to the mass of the Higgs boson can be calculated from the Standard Model Lagrangian. The coupling of each fermion to the Higgs boson is proportional to its mass and thus the one-loop top quark contribution is by far the largest fermionic contribution. The Feynman diagrams of the main contributions are depicted in Figure 1.4: the one-loop contributions from the top quark, the gauge bosons and the Higgs boson itself. The size of the loop corrections depends on the cut-off of the loop momentum, Λ, the scale up to which the Standard Model is assumed to be valid, as follows [18]

$$\begin{aligned} m_H^2 &= (m_H^2)_0 + \delta m_H^2 \\ &= (m_H^2)_0 + \frac{3\Lambda^2}{64\pi^2}\left[-8\lambda_t^2 + 3g^2 + g'^2 + 8\lambda + \ldots\right] \end{aligned}$$

where λ_t is the top quark Yukawa coupling and $(m_H^2)_0$ is the bare Higgs mass squared. Using

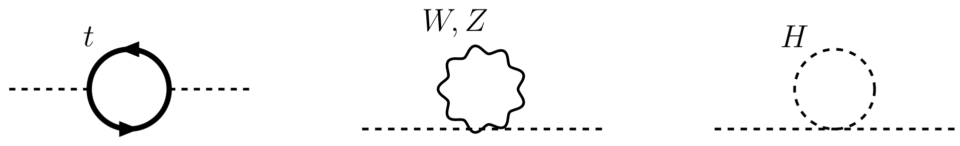

Figure 1.4: The three most significant quadratically divergent contributions to the Higgs mass in the Standard Model.

(1.18), (1.20), $m_H^2 = 2\lambda v^2$ and $m_t^2 = \lambda_t^2 v^2/2$, this is expressed in terms of mass parameters as

$$\delta m_H^2 = \frac{3\Lambda^2}{16\pi^2 v^2}\left[-4m_t^2 + 2m_W^2 + m_Z^2 + m_H^2 + \ldots\right]. \tag{1.29}$$

If the Standard Model is valid all the way up to the Planck scale, $\Lambda \approx M_{\text{Planck}} \sim \mathcal{O}(10^{19})$ GeV, each of the terms in δm_H^2 is extremely large with respect to $(m_H^2)_0$. In order for m_H to be in the expected range, i.e. of the order of a few hundred GeV, the quantum correction terms need to be balanced with enormous precision with respect to the bare Higgs mass. In principle, if the cut-off scale were drastically lowered, the correction terms would be of the same order of magnitude as the Higgs mass. However, precision electroweak data agree extremely well with the Standard Model and suggest $\Lambda \gtrsim 10$ TeV. Even if physics beyond the Standard Model starts taking effect at say $\Lambda \approx 10$ TeV, a fine-tuning of one part in a hundred is required:

$$m_H^2 \quad \approx \quad (m_H^2)_0 - [100 - 10 - 5 - 30]\,(200 \text{ GeV})^2$$

This is the *little hierarchy problem* and Figure 1.5 graphically displays the degree of fine-tuning that is required for the Higgs boson mass to be in the expected range.

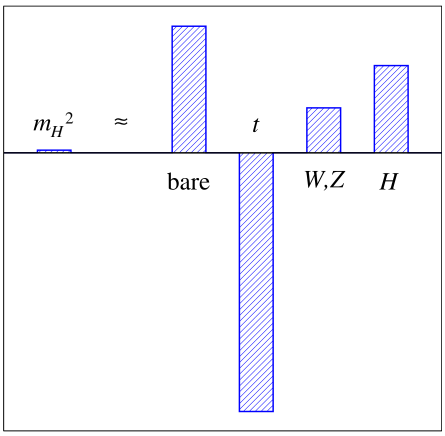

Figure 1.5: The required fine-tuning for a $\mathcal{O}$(200 GeV) Higgs mass in the Standard Model when the cut-off scale is about 10 TeV.

The concept *naturalness* refers to the property of physics at macroscopic scales to follow from a microscopic theory instead of the other way around. It is generally believed undesirable for a microscopic theory to contain free parameters that need careful adjustment for macroscopic properties to follow. As such, the required fine-tuning of the Higgs mass is considered unnatural and even a ‘problem’.

Although the hierarchy problem is no rigorous evidence or proof for the necessity of an extension of the Standard Model, it has served as an inspiration for several proposed models and in particular the properties of new particles that are introduced in those models. The idea is that a cancellation takes place naturally as a consequence of some symmetry, which is broken down at low energy scales making the cancellation appear coincidental in the Standard Model.

The fine-tuning argument can be turned around to provide a cut-off scale that corresponds to an acceptable amount of fine-tuning, say 10 %, which would be the case when $\Lambda \approx 1$ TeV. The new physics models that take over at energies above Λ would have to be realized in a delicate way in order not to affect the electroweak observables significantly. The most popular examples are super-symmetric (SUSY) models, in which each particle in the Standard Model obtains a super-symmetric partner that follows the opposite spin-statistics. Each loop diagram in Figure 1.4 is therefore accompanied by a similar diagram with a relative minus-sign and cancellations ensure a naturally small Higgs mass. In their minimal version, SUSY models require an additional 105 parameters with respect to the Standard Model, which is generally considered a high price to pay. More recently, an alternative class of models has been developed in which the desired cancellation of corrections to the Higgs mass is accomplished by new particles with the same spin-statistics: *Little Higgs Theories*. The next section covers the general idea and the resulting particle phenomenology relevant for the LHC experiments. Whether the argument of naturalness is stringent enough to be interpreted as a guideline for the development of physics models beyond the Standard Model will only become clear once the LHC data are fully investigated.

1.3 Little Higgs Theories

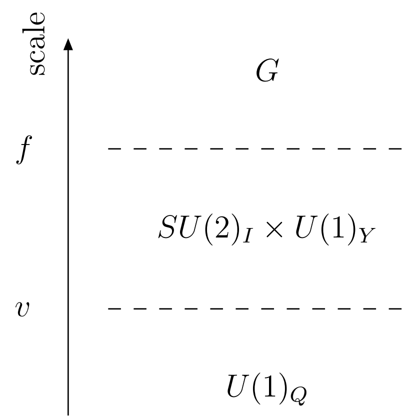

Figure 1.6: Schematic representation of the two stages of symmetry breaking in Little Higgs theories.

In Little Higgs theories, the electroweak gauge group is embedded in a larger group structure. Two stages of symmetry breaking are present, one being the familiar electroweak symmetry breaking described by the Higgs Mechanism (cf. Section 1.1.1) and another taking place at a higher energy scale f and introducing the Higgs boson as a *pseudo-Goldstone* boson. A pseudo-Goldstone boson is the equivalent of the Goldstone boson in case the broken symmetry is broken both explicitly and spontaneously. The bosons that result from such symmetry breaking are not exactly massless, although they typically remain relatively light since they acquire their mass through radiative corrections. The idea to account for the lightness of the Higgs boson by interpreting it as a pseudo-Goldstone boson first arose some thirty years ago. However, despite numerous attempts, no satisfactory realization of this idea was constructed until 2001 [19]. The breakthrough was the incorporation of a *collective* symmetry breaking mechanism, which will be explained shortly. The idea revived and many such models, named Little Higgs Theories, have been developed since.

The general idea[5] is to assume some global symmetry G, which is broken via a vacuum expectation value $f \approx 1$ TeV. A number of Goldstone bosons are generated in the process, amongst which the Higgs boson. The global symmetry G contains a gauged subgroup $G_1 \times G_2 \times \ldots$ and the corresponding gauge bosons absorb some of the available Goldstone bosons to acquire masses of order f. The global symmetry is merely approximate due to the presence of small gauge terms that break the global symmetry explicitly. The subgroups $G_1 \times G_2 \times \ldots$ are embedded in the global symmetry in such a way that the corresponding gauge couplings only break the global symmetry collectively, i.e. only when the combination is nonzero, the Higgs ceases to be an exact Goldstone boson. Consequently, any non-vanishing contribution to the Higgs mass must necessarily be proportional to a product of two coupling constants. In practice, this means that one-loop diagrams, which contain only one of the gauge couplings, are automatically absent. The cancellation is accomplished by the new gauge bosons that acquired masses when the global symmetry was spontaneously broken. Their couplings are related to the Standard Model couplings as a consequence of the global symmetry structure. Diagrams containing more than one coupling do contribute to the Higgs mass, yet at two-loop level only and their contribution is suppressed.

In a similar manner, the collective symmetry breaking approach makes it possible to introduce Yukawa terms in the Lagrangian that prevent the existence of the one-loop contribution from the top quark. The cancellation is realized by a new coloured fermion t' that emerges in the process. The self-contribution from the Higgs boson is evaded in a similar way.

In summary, in Little Higgs theories the Higgs boson is a pseudo-Goldstone boson and thus protected from quadratically divergent contributions by an approximate global symmetry. Or, in other words, Little Higgs theories accomplish the cancellation of quadratically divergent contributions to the Higgs mass by introducing new heavy particles that are related to the Standard Model particles thanks to a collective symmetry breaking mechanism. The number of additional particles depends on the specific model, although it generally includes a heavy top quark t', heavy charged and neutral gauge bosons W' and Z' and some additional Higgs fields. In contrast to SUSY models, there is no need for each and every particle in the Standard Model to obtain a partner. In fact, Little Higgs model are the smallest proposed extension of the Standard Model in which the the Higgs mass is stabilized, which is an attractive property.

Although the quadratically divergent contributions to the Higgs boson mass are naturally cancelled in Little Higgs models, a less severe logarithmic divergence remains. The little hierarchy problem is solved, yet the regular hierarchy problem remains. At the scale $\Lambda_S \sim 4\pi f \approx 10$ TeV additional contributions from a more complete theory need to become apparent. There are many candidates for such an *ultraviolet completion*, which are not studied here.

[5] A more elaborate introduction is found in the reviews [20, 21].

1.3.1 Littlest Higgs Model

A good many Little Higgs models have been proposed in the last decade, of which the Littlest Higgs Model [22] is the minimal version. The global symmetry G in this model is $SU(5)$, which contains two copies of the electroweak symmetry group, i.e. $G \supset G_1 \times G_2 = [SU(2)\times U(1)]_1 \times [SU(2)\times U(1)]_2$. Consequently, the covariant derivative in the Lagrangian contains two copies of the $U(1)$ generators, $B_{1\mu}$ and $B_{2\mu}$, with gauge couplings g_1' and g_2' as well as two copies of the $SU(2)$ generators, $W^a_{1\mu}$ and $W^a_{2\mu}$, with gauge couplings g_1 and g_2. At the scale f the global symmetry $SU(5)$ is spontaneously broken down to its subgroup $SO(5)$. Simultaneously, the gauge symmetry $[SU(2) \times U(1)]^2$ is broken into its subgroup $SU(2)_I \times U(1)_Y$, which is identified as the Standard Model gauge group. The global symmetry breaking results in $(5^2-1)-5(5-1)/2 = 14$ Goldstone bosons as prescribed by Goldstone's Theorem, which are parameterized by a 5×5 field Σ. Four of the Goldstone bosons are absorbed by the new gauge bosons, providing them with masses of order f. This occurs in perfect analogy with the Higgs mechanism in Standard Model as described in Section 1.1.1. The remaining ten Goldstone fields form a complex doublet h and a complex triplet φ. The mass eigenstates of the gauge bosons are found by expanding the Lagrangian around the vacuum expectation value Σ_0 in the usual way. The result is given by [23]

$$\begin{aligned} W^a_\mu &= sW^a_{1\mu} + cW^a_{2\mu} & \qquad W'^a_\mu &= -cW^a_{1\mu} + sW^a_{2\mu} \\ B_\mu &= s'B_{1\mu} + c'B_{2\mu} & \qquad B'_\mu &= -c'B_{1\mu} + s'B_{2\mu} \end{aligned} \tag{1.30}$$

where the mixing angles ψ and ψ' are introduced via

$$s = \sin\psi = \frac{g_2}{\sqrt{g_1^2+g_2^2}} \qquad\qquad s' = \sin\psi' = \frac{g_2'^2}{\sqrt{g_1'^2+g_2'^2}}. \tag{1.31}$$

The W_μ and B_μ eigenstates remain massless at this point and will acquire their masses from electroweak symmetry breaking in the usual way. In identifying them as the Standard Model gauge bosons, their gauge couplings constrain the gauge couplings of the new gauge bosons by the following relations:

$$g = g_1 s = g_2 c \qquad\qquad g' = g_1' s' = g_2' c'. \tag{1.32}$$

The mass terms for the orthogonal states are

$$m^2_{W'} = \frac{f^2}{4}(g_1^2+g_2^2) \qquad\qquad m^2_{Z'} = \frac{f^2}{4}\frac{1}{5}(g_1'^2+g_2'^2) \tag{1.33}$$

It can be shown [23] that the one-loop contributions of these new heavy gauge bosons to the Higgs mass are exactly equal to the contributions from the Standard Model gauge bosons, yet opposite in sign. This is a consequence of the relations in (1.32).

In the Littlest Higgs model, two Yukawa terms for the top quark are introduced with couplings λ_1 and λ_2. The mass eigenstates are found by expanding these terms around the vacuum expectation value Σ_0. One eigenstate is identified as the Standard Model top quark, which remains massless at this level, and the other is the quark t' with

$$m^2_{t'} = (\lambda_1^2+\lambda_2^2)f^2. \tag{1.34}$$

The couplings are constrained by the Standard Model Yukawa coupling for the top quark,

$$\lambda_t = \sqrt{2}\frac{\lambda_1\lambda_2}{\sqrt{\lambda_1^2+\lambda_2^2}}, \tag{1.35}$$

which ensures the cancellation of the one-loop contribution from the Standard Model top quark to the Higgs mass.

Being protected by the global symmetry, no potential is present for the Higgs field at tree level. Instead, a potential for the fields h and φ of the form (1.10) is automatically generated by the one-loop and higher order gauge and Yukawa interactions. For $\mu^2 < 0$, this potential triggers electroweak symmetry breaking. By minimizing the potential, expressions for the respective vacuum expectation values, $\langle h_0\rangle \equiv v/\sqrt{2}$ and $\langle \varphi_0\rangle \equiv v' \sim f$, are found. Fluctuations around the respective vacuum expectation values yield the mass eigenstates. Three of the Goldstone bosons are absorbed by the W_μ and B_μ fields to become massive, leaving the Higgs field H as a pseudo-Goldstone boson. In addition, the complex triplet picks up mass terms of order f for the fields Φ^0, Φ^+ and Φ^{++}:

$$m_\Phi^2 = \left(a(g_1^2+g_2'^2+g_2^2+g_2'^2) - a'\lambda_1^2\right) f^2, \tag{1.36}$$

where the parameters a and a' depend on the matching conditions to physics above the scale Λ_S.

In the Littlest Higgs model a number of new parameters are introduced, of which each pair of gauge couplings is fixed as a combination by the requirement to reproduce the Standard Model. A possible representation of the remaining five free parameters is listed in Table 1.2.

Parameter	**Description**
f	$SU(5)/SO(5)$ symmetry breaking vev
ψ	$SU(2)_1 \times SU(2)_2$ mixing angle
ψ'	$U(1)_1 \times U(1)_2$ mixing angle
λ_1 (or λ_2)	top sector Yukawa coupling
v'	vev for triplet Φ

Table 1.2: The free parameters of the Littlest Higgs model.

As a consequence of mixing with the newly introduced states, the mass terms for the Standard Model particles that emerge in the electroweak symmetry breaking process are affected by correction terms of order v^2/f^2. The Littlest Higgs Model is therefore disfavoured by precision electroweak data, which imply $f > 4$ TeV at 95% c.l. [24]. Such a high value of f would reintroduce fine-tuning at the percent level, which was the original motivation for the model to be constructed!

Various modifications or extensions of the Littlest Higgs model have been proposed in which the constraints from precision electroweak data can be avoided. The resulting particle spectrum for the LHC is usually similar to that in the Littlest Higgs model, which nevertheless serves as a benchmark description.

1.3.2 Twin Higgs Model

Even more recently, the Twin Higgs mechanism was proposed as a solution to the little hierarchy problem. Again, the Higgs boson is introduced as a pseudo-Goldstone boson of a spontaneously broken global symmetry. In this mechanism, the Higgs mass is protected from quadratically divergent contributions by an additional discrete symmetry. The discrete symmetry plays the role of the collective symmetry breaking mechanism that did the trick in Section 1.3.1. The Twin Higgs mechanism can be realized by two different types of discrete symmetry: mirror symmetry and left-right symmetry. In the first scenario, a complete copy of the Standard Model is introduced. The mirror particles only couple to the Standard Model particle via Higgs particles. At the LHC, these mirror particles would thus lead to invisible decays, which would be an interesting challenge - to put it mildly. Here, however, we focus on the more minimal scenario of left-right symmetric models.

In the left-right Twin Higgs (LRTH) model [25], the global symmetry is $U(4) \times U(4)$, which contains the gauged subgroup $SU(2)_L \times SU(2)_R \times U(1)_{B-L}$ [6]. The discrete symmetry is realized as the left-right symmetry, which implies an extension of the electroweak sector in which right-handed fermions couple to new gauge bosons. The gauge couplings corresponding to $SU(2)_L$ and $SU(2)_R$ are equal:

$$g_L = g_R. \tag{1.37}$$

Two Higgs fields are introduced,

$$H = \begin{pmatrix} H_L \\ H_R \end{pmatrix} \qquad \hat{H} = \begin{pmatrix} \hat{H}_L \\ \hat{H}_R \end{pmatrix}, \tag{1.38}$$

where the subscripts of the doublet components indicate that they transform under either $SU(2)_L$ or $SU(2)_R$. Each of the Higgs fields acquires a non-zero vacuum expectation value,

$$\langle H \rangle = \begin{pmatrix} 0 \\ 0 \\ 0 \\ f_1 \end{pmatrix} \qquad \langle \hat{H} \rangle = \begin{pmatrix} 0 \\ 0 \\ 0 \\ f_2 \end{pmatrix}, \tag{1.39}$$

such that the global symmetry $U(4) \times U(4)$ breaks down to $U(3) \times U(3)$ and fourteen $(= 2(4^2 - 3^2))$ Goldstone bosons appear. Simultaneously, the subgroup $SU(2)_R \times U(1)_{B-L}$ breaks down to the Standard Model subgroup $U(1)_Y$. Three of the fourteen Goldstone

[6] Here B and L are the baryon number and lepton number.

bosons are absorbed by the new gauge bosons to become massive, which gives rise to the usual Z' and $W'^{\pm}$ bosons. The mass term for the latter is given by [26]:

$$m_{W'}^2 = \frac{1}{2} g^2 \left[f_2^2 + f_1^2 \left(1 - \frac{v^2}{2 f_1^2} \right) \right]. \tag{1.40}$$

By setting $f_2 \gg f_1$, the Z' and W' masses are large enough to be consistent with lower bounds from direct searches. Amongst the remaining Goldstone bosons are the Standard Model Higgs doublet H_L and some additional Higgs fields.

The top quark sector is accounted for by introducing a pair of quarks with Yukawa couplings $\lambda_L = \lambda_R$ to the Higgs components H_L and H_R. A mass mixing term with coefficient M is included as well since it is allowed by gauge invariance. After the Higgs components take their vacuum expectation values, the mass eigenstates are identified as the Standard Model top quark and the t', which will cancel the one-loop contribution of the top quark to the Higgs mass as usual. In principle, similar Yukawa terms could be added for the other Higgs field $\hat{H}$. This would generate a large top quark mass though because of the choice $f_2 \gg f_1$. This is avoided by introducing a parity under which $\hat{H}$ is odd and all other fields are even. Yukawa terms in which $\hat{H}$ is involved are odd under this parity and therefore forbidden, whereas the gauge coupling terms are quadratic in $\hat{H}$ and therefore allowed. The lightest particle that is odd under this parity is automatically a dark matter candidate.

The gauge and Yukawa terms explicitly break the global symmetry and generate a potential for the Higgs fields. The cancellation of leading quadratically divergent contributions to the Higgs mass from gauge loops is ensured by the relation in (1.37). The contribution from the top quark is under control because it couples to the field H, which acquires the smaller vev f_1, and not to the field $\hat{H}$ because of the newly introduced parity conservation.

The potential for the remaining Goldstone fields triggers the breaking of electroweak symmetry $SU(2)_L \times U(1)_Y \to U(1)_Q$ when the doublet H_L acquires the vev $(0, v/\sqrt{2})$. Three more Goldstone bosons are absorbed by the Standard Model bosons W and Z to become massive, such that eight remain. They are parameterized by: a neutral field φ^0 and a pair of charged fields $\varphi^{\pm}$ for $SU(2)_R$, the Standard Model Higgs and the $SU(2)_L$ doublet $\hat{H}_L$. The latter contains the neutral field $\hat{h}_2^0$ which is stable and qualifies as a dark matter candidate.

1.3.3 The W' Boson

Being motivated by the required cancellation of the three diagrams in Figure 1.4, all Little Higgs theories introduce

- A new heavy fermion t' with $Q = 2/3$;
- New heavy gauge bosons W' and Z' that couple to fermions and Higgs doublets;
- New Higgs fields

at the very least. The masses of the new particles are expected to be $\mathcal{O}$(TeV) and they generally provide promising signatures at the LHC.

Studies presented here focus on the discovery potential of the W' boson through its decay into third generation quarks, i.e. $W'^{+} \to t\bar{b}$ and $W'^{-} \to \bar{t}b$. The coupling of the W' boson to fermions is assumed to be equivalent to that of the Standard Model W boson. The mass of the W' boson and its production cross section at the LHC are strongly model-dependent. Apart from the many possible realizations of the gauge group G, the phenomenology depends on the parameters within each model. Moreover, apart from Little Higgs theories, other proposed extensions of the Standard Model introduce a heavy charged vector boson as well. Therefore, the analysis in Chapter 7 is based on a model-independent search for a mass peak. The Littlest Higgs Model and the LRTH Model serve as benchmark models to illustrate the procedure. Constraints on the mass of the W' boson do exist, both from experimental and theoretical considerations. The lower bound follows from direct searches at Tevatron experiments [27][7]:

$$m_{W'} > 731 \text{ GeV} \qquad \text{at 95\% confidence level.} \tag{1.41}$$

An upper bound on $m_{W'}$ follows from the naturalness constraint that none of the one-loop corrections exceed the Higgs mass by more than a factor of 10 [22]:

$$m_{W'} \leq 6 \text{ TeV} \left(\frac{m_H}{200 \text{ GeV}}\right)^2. \tag{1.42}$$

One of the distinguishing features between the Littlest Higgs Model and the LRTH Model is the mass hierarchy. As a consequence of the introduced parity in the LRTH Model, the mass of the t' quark is smaller than the masses of the new gauge bosons W' and Z', which is not the case in the Littlest Higgs Model. Therefore, the decay channel $W' \to t'b$, which is suppressed in the Littlest Higgs Model, has a large branching ratio in the LRTH Model. The branching ratio of the decay channel of interest, $W' \to tb$, is thus reduced in the LRTH Model with respect to the Littlest Higgs Model and the experimental challenge is bigger.

Another difference in the particle phenomenology of the models arises under the likely assumption that the mass of the right-handed neutrino in the LRTH Model is larger than $m_{W'}$. The leptonic decay channel $W' \to l\nu$ is absent, whereas its branching ratio is large in the Littlest Higgs Model. In a realization of the LRTH model in which $m_{W'} > 1250$ GeV, an additional distinctive feature that opens up is the cascade decay $W' \to t'b \to \varphi^{\pm}bb \to tbbb \to l\nu bbbb$ [26].

Chapter 7 introduces a method to isolate the $W' \to tb$ signal at the LHC with the ATLAS detector and quantifies the discovery potential for the two benchmark models discussed here.

[7] Under particular assumptions on the underlying model, more severe limits are obtained, which vary up to $m_{W'} > 1000$ GeV.

2

The ATLAS Detector

This chapter describes the experimental setup that provides the data of interest: the ATLAS detector. It is one of the four particle detectors that are designed to measure physics processes that occur at collisions of hadrons produced by the Large Hadron Collider. In the first section, the Large Hadron Collider is described. The subsequent sections cover the ATLAS detector and each of its components.

2.1 The Large Hadron Collider

The Large Hadron Collider (LHC) is a circular particle accelerator situated at CERN in the tunnel where the Large Electron Positron accelerator (LEP) operated between the years 1989 and 2000. The LHC is designed to collide beams of protons with 14 TeV center of mass energy[1], whereas LEP collided electrons on positrons with center of mass energies from 91 GeV up to 209 GeV. The larger energy and the fact that the two beams of particles are not mutual antiparticles require a more advanced accelerator machine.

The counter-rotating beams cross each other in four points along the tunnel, where the particle detectors ALICE [28], ATLAS, CMS [29] and LHCb [30] are located. Figure 2.1 locates the detectors along the LHC ring as well as the pre-accelerators: the linear accelerator (LINAC), the Proton Synchotron Booster (PSB), the Proton Synchotron (PS) and the Super Proton Synchotron (SPS). Protons are produced by stripping electrons from hydrogen atoms and are subsequently accelerated to 50 MeV in the LINAC. The protons are then accelerated in three steps by the circular pre-accelerators to 1 GeV, 26 GeV and 450 GeV respectively. An arrangement of the protons into bunches of 10^{11} protons each and a 25 ns bunch separation are established. The SPS finally injects the bunches both in clockwise and counter-clockwise direction into the LHC, which accelerates them to energies up to 7 TeV.

The LHC [31] consists of eight arcs and eight straight sections, adding up to a circumference of 27 km. The two vacuum beam pipes are surrounded by several thousands of superconducting magnets, which accomplish the bending and focusing of the beams. As the radius of the accelerator is fixed by the existing tunnel, the energy of the proton beams

[1] Occasionally beams of lead ions are accelerated and collided at $\sqrt{s}$ =1148 TeV instead.

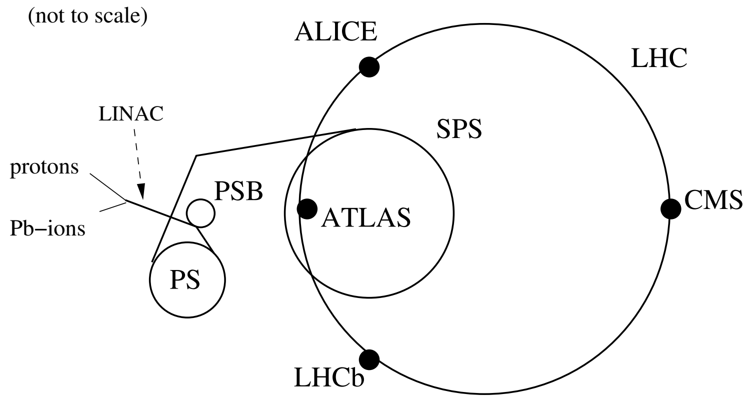

Figure 2.1: Schematic view of the particle accelerators and detectors at CERN.

is constrained by the strength of the bending magnets. The bending is achieved by 1232 dipole magnets, which are cooled to 1.9 K by liquid helium and provide a field strength of 8.33 T. A special twin aperture design of the magnets allows the two beams to be subject to opposite magnetic fields while sharing the iron structure and helium vessel.

The actual acceleration of the proton beams is established in radio frequency cavities, where an oscillating electric field of 2 MV is generated. The oscillation frequency of 400 MHz is tuned to the bunch spacing of the beams.

In addition to the center of mass energy of the provided collisions, an important characteristic of an accelerator machine is the beam intensity or *luminosity* L. It determines the rate of proton-proton interactions and thereby the rate of interesting events that occur in the center of the ATLAS detector:

$$\frac{\mathrm{d}N_{\mathrm{events}}}{\mathrm{d}t} = L\sigma_{\mathrm{events}}, \tag{2.1}$$

where σ_{events} is the cross section of those events at a given $\sqrt{s}$. The achieved luminosity of an accelerator is described as

$$L = \frac{fNn^2}{A}, \tag{2.2}$$

where f is the revolution frequency, N is the number of bunches per beam, n is the number of particles per bunch and A is the cross section of the beam. The target luminosity of the LHC, $L = 10^{34}$ cm^{-2}s^{-1}, is reached by operating at the values given in Table 2.1.

The luminosity is subject to degradation due to beam losses from collisions and imperfections, resulting in an expected beam lifetime of approximately 15 hours [31]. Refilling the LHC requires roughly 4 minutes per beam and ramping up the energy from 450 GeV to 7 TeV in the LHC machine takes an additional 20 minutes, thus defining the minimum turnaround time. In a realistic scenario, the acquired integrated luminosity is estimated at 100 fb^{-1} per year when running at design luminosity.

Operating the LHC machine at design beam energies and design luminosity is a delicate procedure for which no test setup exists. Initially, in 2008, a faulty electrical connection

Circumference	26659 m
Injection energy	450 GeV
Bunch spacing	25 ns
Particles per bunch n	10^{11}
Bunches per beam N	2808
Revolution frequency f	11 kHz
Beam radius	16 μm

Table 2.1: Properties of the LHC at $\sqrt{s} = 14$ TeV proton-proton operation and design luminosity $L = 10^{34}$ cm^{-2}s^{-1}.

between two magnets caused severe damage to the accelerator and a full year was needed for recovery. At the next attempt, in November 2009, the beams were maintained at injection energy to get acquainted with the steering and stabilizing. Thousands of events were recorded with the ATLAS detector at $\sqrt{s} = 900$ GeV and provided the first opportunity to test reconstruction algorithms and detector performance with proton collisions[2]. The energy was gradually ramped up to reach the world record center of mass energy of 2.36 TeV on December 8th, 2009. The collision energies were expected not to exceed 10 TeV until 2012, after a scheduled maintenance shutdown, which is therefore the focus of the studies in this thesis.

Ultimately, during summer 2010, a center of mass energy of 7 TeV was maintained and a total integrated luminosity of 3.46 pb^{-1} was recorded by ATLAS up until the sixth of September. The instantaneous luminosity reached a maximum of 10^{31} cm^{-2}s^{-1}, which is a thousandth of the design luminosity. Figure 2.2 displays the course of integrated luminosity delivered by the LHC as well as the part recorded by the ATLAS detector. The recorded collisions are investigated in Chapter 8.

2.2 The ATLAS Detector

The ATLAS detector was designed to observe the wide range of particles that are expected to be created in proton-proton collisions at the unprecedented energies and luminosity. To this end, it is built up of several subdetectors, configured in concentric layers around the interaction point, each optimized for the detection of a specific type of particles. Charged particles leave traces in the tracking detectors and all particles except for muons and neutrinos deposit their energy in the calorimeters. Muons are detected by the muon detectors in the outermost layer, whereas neutrinos escape the detector without leaving a trace[3].

From the interaction point outwards, the first subdetector of ATLAS is the *inner detector*, one of the two tracking detectors. The subsequent subdetector is the calorimeter system, divided into an electromagnetic and a hadronic component, which measures

[2] During 2008 several runs of cosmic muon data were taken with ATLAS.

[3] Their transverse momenta can nevertheless be reconstructed by means of momentum conservation in the transverse plane. This procedure is addressed in detail in Section 4.6 and Chapter 6.

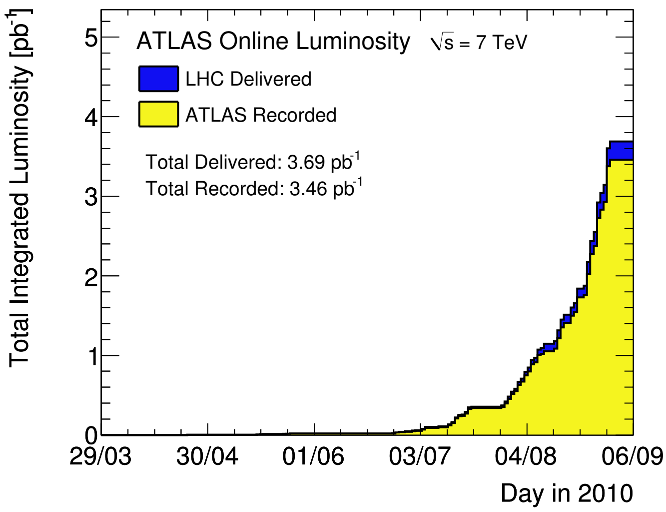

Figure 2.2: Integrated luminosity delivered by the LHC (blue) and recorded by ATLAS (yellow) up to September 6, 2010 during stable beams with $\sqrt{s} = 7$ TeV. Figure taken from [32].

the energy of particles by total absorption. The outer tracking detector is the *muon spectrometer*, designed to measure tracks of muons in particular. Both tracking detectors operate in a magnetic field, provided by a solenoidal and a toroidal magnet system respectively. Figure 2.3 illustrates the arrangement of the subdetectors and magnets that compose the ATLAS detector. In addition, the dimensions are shown, which indicate that it is the largest particle detector ever built for an accelerator experiment. The detector was installed in the underground cavern between 2003 and 2008 after many years of research, preparation and construction.

The Coordinate System

The origin of the ATLAS coordinate system is defined as the nominal interaction point in the center of the detector. The z-axis runs parallel to the beam line in counterclockwise direction. The half of the detector that corresponds to positive values of z is referred to as *side A* and the other half as *side C*. The x-axis points to the center of the LHC ring and the y-axis points upwards to the surface, resulting in a righthanded orientation. The xy-plane is referred to as the *transverse plane*.

The ATLAS detector has a global cylindrical structure, where each subdetector consists of concentric layers around the beam axis, the *barrel* component, and two *endcaps* formed by disks perpendicular to the z-axis on each side of the interaction point. A coordinate system closely related to cylindrical coordinates is convenient. The radial distance is given by $R = \sqrt{x^2 + y^2}$. The azimuthal angle $\varphi \in [-\pi, \pi]$ is the angle with the positive x-axis and increases in clockwise direction when looking down the positive z-axis. The polar angle $\theta \in [0, \pi]$ is defined as the angle with the positive z-axis, albeit generally replaced by the

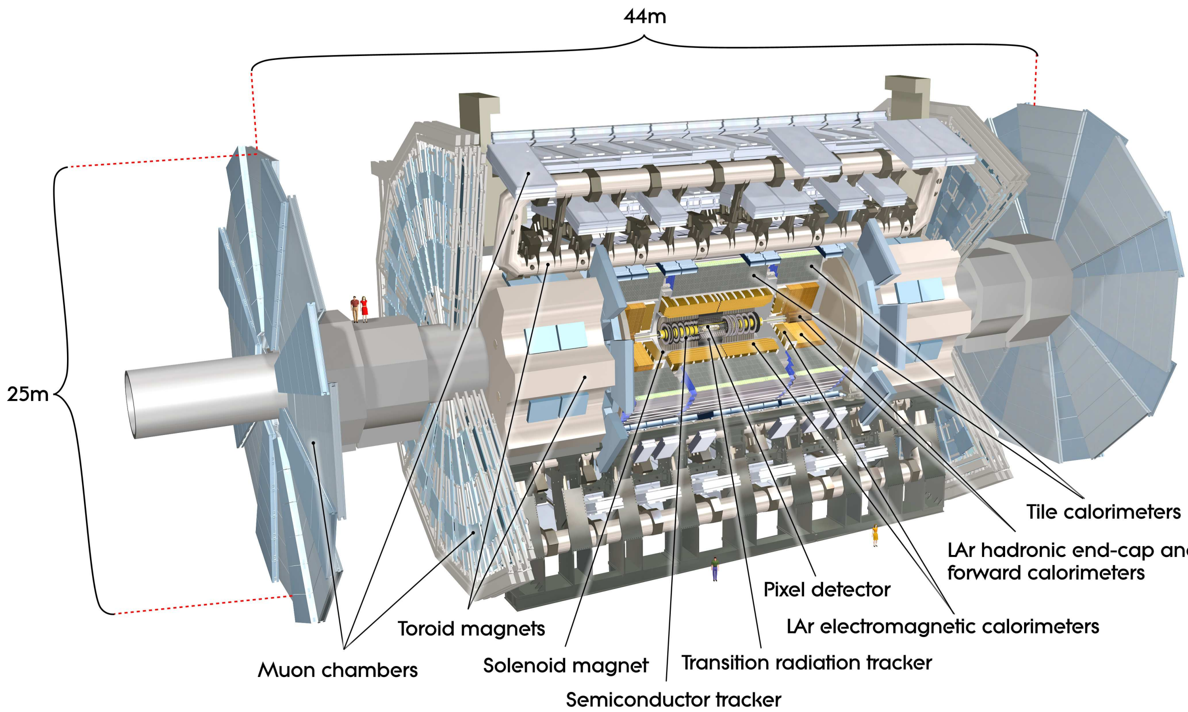

Figure 2.3: Computer generated image of the ATLAS detector. A part is cut away in order to reveal the structure of concentric subdetectors that constitute the detector.

pseudorapidity η, which is given by

$$\eta = -\ln\left[\tan\left(\frac{\theta}{2}\right)\right]. \tag{2.3}$$

The preference for this quantity is motivated by the particle flux being roughly constant as a function of η. A direction (η, φ) is assigned to reconstructed final state objects and the opening angle between two of them is denoted ΔR, i.e.

$$\Delta R = \sqrt{(\Delta\eta)^2 + (\Delta\varphi)^2}. \tag{2.4}$$

Requirements

The performance requirements for the design of the ATLAS detector are based on the processes that may be observed at this new energy scale, such as the production of the Higgs boson, SUSY particles or heavy gauge bosons W' and Z'. The extensive variety of objects to be detected, the broad energy range of particles to be measured, the high radiation conditions and the high collision rate impose strict requirements on the detector's precision, speed, performance, radiation hardness, efficiency and acceptance. The performance requirements in terms of resolution as well as the acceptance of each subdetector are summarized in Table 2.2. An additional challenge is the instantaneous selection of collisions to be stored, which is taken care of by the trigger system. This is addressed in Section 2.2.5, after the three subdetectors and the magnet system are described in more detail in Sections 2.2.1 through 2.2.4.

Subdetector	Required Resolution	η coverage
Inner Detector	$\sigma(p_T)/p_T = 0.05\%\ p_T \oplus 1\%$	$\lvert\eta\rvert < 2.5$
Electromagnetic Calorimeter	$\sigma(E)/E = 10\%/\sqrt{E(\text{GeV})} \oplus 0.7\%$	$\lvert\eta\rvert < 3.2$
Hadronic Calorimeter	$\sigma(E)/E = 50\%/\sqrt{E(\text{GeV})} \oplus 3\%$	$\lvert\eta\rvert < 3.2$
	$\sigma(E)/E = 100\%/\sqrt{E(\text{GeV})} \oplus 10\%$	$3.1 < \lvert\eta\rvert < 4.9$
Muon Spectrometer	$\sigma(p_T)/p_T = 10\%$ at $p_T = 1$ TeV	$\lvert\eta\rvert < 2.7$

Table 2.2: Performance requirements for the subdetectors of the ATLAS detector [33].

2.2.1 The Inner Detector

The inner detector is the subdetector closest to the interaction point, where the density of particles is largest. High granularity and good radiation tolerance are required. With an inner radius of 45 mm it is as close as 10 mm to the beam pipe and it extends to a radius of 1150 mm. It is contained inside a solenoidal magnetic field of 2 T (cf. Section 2.2.4) and designated to the reconstruction of tracks of charged particles. In order to achieve high momentum resolution over the entire range of momenta as well as precise vertex measurements, the inner detector consists of three complementary tracking devices: the *pixel detector*, the *semi-conductor tracker* (SCT) and the *transition radiation tracker* (TRT). Their configuration is illustrated in Figure 2.4.

The Pixel Detector

The innermost part of the inner detector is the pixel detector, consisting of three concentric layers around the beam axis and three discs perpendicular to the beam axis on each side of the interaction point. The 1744 modules that constitute the pixel detector each consist of a 250 μm layer of silicon implanted with readout pixels that measure $50 \times 400\ \mu\text{m}^2$, adding up to a total of 80 million pixels. Electron-hole pairs are created in the silicon when charged particles pass through and a current is induced due to the p-n junction in the doped silicon, which is read out by the pixels. The pixel detector primarily contributes to the precise identification of the primary vertex and secondary vertices.

The Semi-Conductor Tracker

The middle component of the inner detector is the SCT, which is composed of four concentric barrels around the beam axis and nine endcap disks along the beam line on each side. It thus extends radially from 255 mm to 549 mm and longitudinally from 810 mm to 2797 mm from the interaction point. Its detection principle is similar to that of the pixel

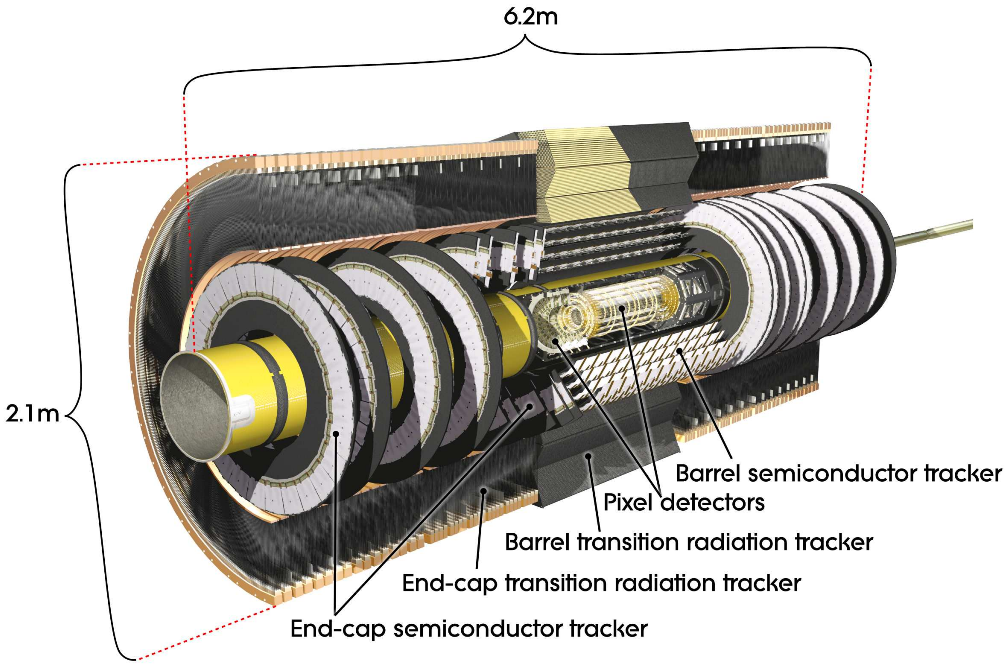

Figure 2.4: The inner detector and the configuration of its three components: the pixel detector, the SCT and the TRT.

detector, although the lower particle density allows for long, narrow silicon strips rather than small rectangular pixels. The strips are configured in two layers under a small angle with respect to each other, such that a position measurement along the strip length can be obtained from hits in overlapping strips.

The Transistion Radiation Tracker

The technology employed in the outer component of the inner detector, the TRT, is twofold: gaseous straw tubes are interleaved with transition radiation material. The barrel contains 73 such layers and the 20 wheels on each endcap are covered with 160 such planes, adding up to approximately 350k readout channels.

When charged particles pass through, the gas inside the tubes is ionized and a voltage difference between the tube and the anode wire in its center causes the free electrons to drift towards the wire. The drift time is converted into the distance of the track to the wire.

Transition radiation is emitted when highly relativistic charged particles pass the transition between two materials with different dielectric constants. The intensity of the transition radiation photons is proportional to the Lorentz factor of the traversing particle, which is much higher for electrons than for pions, at equivalent energies, due to their mass difference. The gas mixture inside the straw tubes contains xenon, which absorbs the radiation photons and thus produces a signal with a high amplitude when an electron passes through.

The readout electronics of the tubes apply two distinct thresholds: a lower one that detects the ionization clusters and a higher one that is optimized for transition radiation from electrons and allows for rejection of tracks from $\pi^{\pm}$ background.

A particle originating from the interaction point, given that it satisfies $|\eta| < 2.0$ and $p_{\mathrm{T}} > 5.0$ GeV, typically gives rise to three pixel hits, four SCT measurements and around 30 TRT hits. The semiconductor trackers provide three-dimensional space points with high precision, yet the high number of TRT hits over the larger part of the track length contributes significantly to the momentum measurement. In addition, efficient electron identification is provided by the TRT. The expected inverse transverse momentum resolution on a reconstructed track with $0.25 < |\eta| < 0.50$ is [33]

$$\sigma(1/p_{\mathrm{T}}) = 0.34\ \mathrm{TeV}^{-1}(1 \oplus 44\ \mathrm{GeV}/p_{\mathrm{T}}), \tag{2.5}$$

where the first term indicates the expected asymptotic resolution at infinite transverse momentum and the second term represents the impact of multiple scattering at low momenta. The expected resolution on the transverse impact parameter is

$$\sigma(d_0) = 10\ \mu\mathrm{m}(1 \oplus 14\ \mathrm{GeV}/p_{\mathrm{T}}). \tag{2.6}$$

2.2.2 The Calorimeters

After having traversed the inner detector, particles enter the calorimeter system, which is situated outside the solenoidal magnet that surrounds the inner detector. It extends from approximately 1.4 m to 4.2 m from the interaction point in the transverse plane. Firstly encountered is the electromagnetic calorimeter, which is optimized for the identification and energy determination of photons and electrons. The hadronic calorimeter is dedicated to the reconstruction of hadronic showers from quarks, gluons and hadronically decaying taus. Altogether, the calorimeter system covers the full azimuth and the pseudorapidity range $|\eta| < 4.9$. The configuration of the calorimeters is depicted in Figure 2.5.

Muons generally deposit a mere fraction of their energy in the calorimeters and continue to be detected by the muon spectrometer (cf. Section 2.2.3). Neutrinos remain undetected entirely. The transverse component of the undetected energy can be nevertheless estimated by means of the expected energy balance in the transverse plane. The performance of the calorimeters is of direct influence on this quantity, the missing transverse energy, which will be discussed in more detail in Chapter 6.

Both the electromagnetic and the hadronic calorimeter consist of *sampling detectors*, i.e. layers of passive, dense material alternated with layers of active material. The passive material causes incident particles to initiate a shower or cascade of secondary particles, which are detected in the active material. In sufficient successive layers, the primary particle will have transferred all its initial energy.

Electromagnetic showers are the result of Bremsstrahlung and e^+e^- pair production and the characteristic interaction distance is the radiation length X_0 of the material[4]. Hadronic showers are the result of nuclear interactions and develop over larger distances. The required

[4] X_0 is the mean distance over which an electron loses all but $1/e$ of its energy.

depth of the material for complete containment of the shower is larger and is expressed in terms of the nuclear interaction length λ of the passive material.

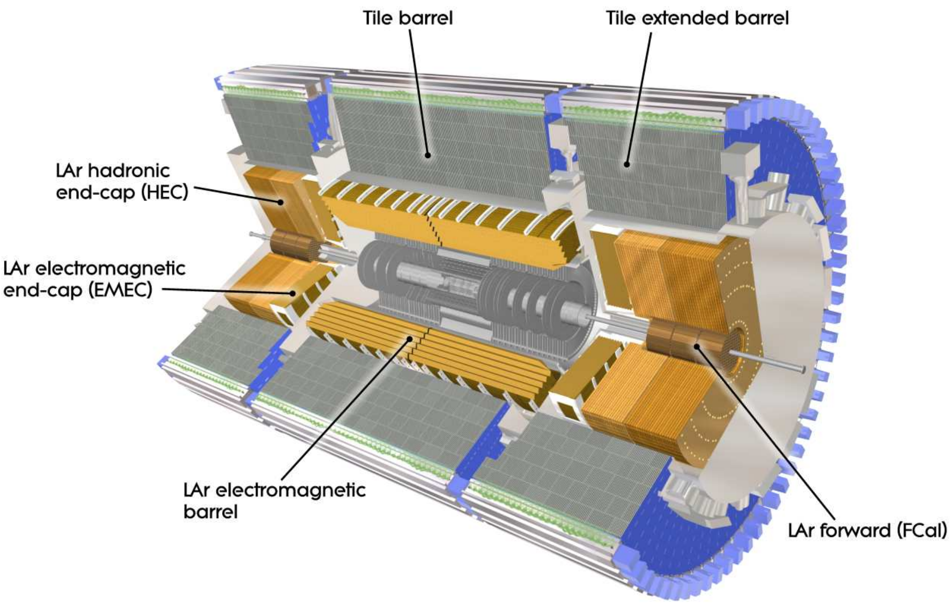

Figure 2.5: Configuration of the ATLAS calorimeters, indicating the electromagnetic components as well as the tile calorimeters.

The Electromagnetic Calorimeter

The electromagnetic calorimeter consists of a barrel that covers $|\eta| < 1.475$ and two endcap wheels at $1.375 < |\eta| < 3.200$ The passive material employed in the electromagnetic calorimeter are lead plates folded into an accordion shape. The space between the plates contains a honeycomb structure that is filled with liquid argon. Charged particles produced in showers induce free charge by ionizing the liquid argon, which is collected on the readout electrodes. The barrel component shares its cryostat vessel with the solenoid magnet (cf. Section 2.2.4) in order to minimize the amount of inactive material. Between the barrel and each endcap wheel, around $|\eta| = 1.4$, some space is available for cables and services for the inner detector. The thickness of the electromagnetic calorimeter varies from $22X_0$ to $33X_0$.

The modules of which the electromagnetic calorimeter is composed are divided into three longitudinal layers, as illustrated in Figure 2.6. The front layer is finely segmented in η, which facilitates γ/π^0 separation. The middle layer is thickest and receives the larger part of the energy deposited by electromagnetic showers. The third layer has a coarse granularity and is mainly used to recover the tails of highly energetic electromagnetic showers and to discriminate between hadronic and electromagnetic showers based on the larger energy deposit by the former.

The achieved resolution on the energy E as measured in a test beam of electrons [34] is

$$\frac{\sigma(E)}{E} = \frac{10\%}{\sqrt{E(\text{GeV})}} \oplus 0.17\%. \tag{2.7}$$

The first term represents the stochastic response of the calorimeter, whereas the constant term is due to systematic effects, such as non-uniformity and stability.

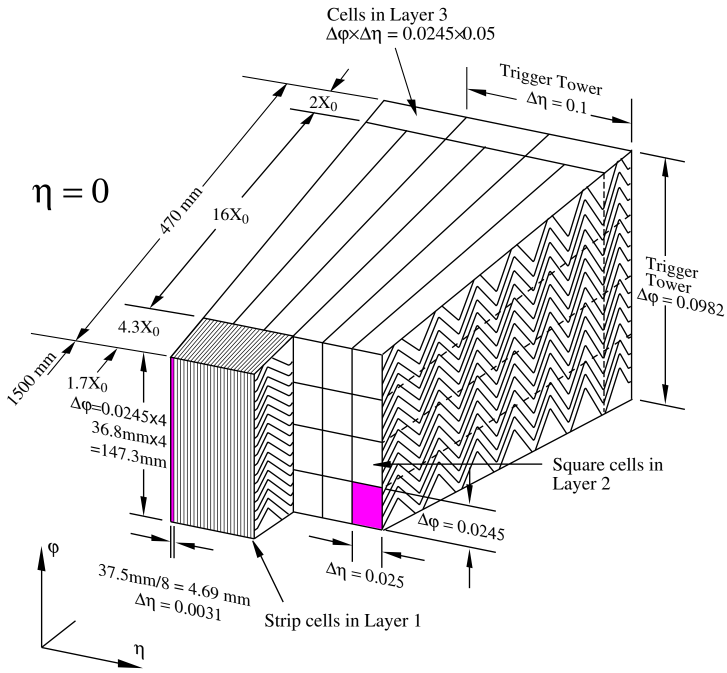

Figure 2.6: Schematic view of a module in the electromagnetic calorimeter, showing the typical accordian shape and the granularity of the different layers.

The Hadronic Calorimeter

The hadronic calorimeter surrounds the electromagnetic calorimeter and constitutes a scintillator tile calorimeter at $|\eta| < 1.7$ and two endcap wheels at $1.5 < |\eta| < 3.2$. The tile calorimeter in turn is divided into a central barrel at $|\eta| < 1$ and two extended barrels at $0.8 < |\eta| < 1.7$. The gap in between contains cables, services and power supplies for the inner detector as well as for the electromagnetic calorimeter. The passive material is steel, which functions simultaneously as return yoke for the solenoid magnet. The active medium is formed by scintillating plastic tiles that emit the absorbed energy in the form of light. The scintillation light is picked up by wavelength shifting fibers and propagated to photomultiplier tubes, where the signal is amplified and detected. The thickness of the hadronic calorimeter is approximately 10 λ. It follows from pion test beam results [34] that the achieved energy resolution meets the requirement

$$\frac{\sigma(E)}{E} = \frac{50\%}{\sqrt{E}(\text{GeV})} \oplus 3\%. \tag{2.8}$$

Hadronic showers are more complex than electromagnetic showers and the resolution is limited by binding energy losses and *non-compensation*, i.e. the electromagnetic component of the shower is detected more efficiently than the hadronic component. The electromagnetic fraction is energy dependent and its fluctations contribute to the resolution. The ratio of the electron response and pion response is determined as a function of energy in test beams and used in the calibration (cf. Section 4.2).

In the hadronic endcap wheels the passive layers are made of copper and the active medium in between is liquid argon. The readout cells measure $\Delta\eta \times \Delta\varphi = 0.1 \times 0.1$ in the region $1.5 < |\eta| < 2.5$ and 0.2×0.2 in the more forward region.

The Forward Calorimeter

In order to estimate the missing transverse energy, as large hermetic calorimeter coverage as possible is pursued. The coverage in the very forward region, $3.1 < |\eta| < 4.9$, is provided by three wheels on either side: one electromagnetic component and two hadronic components. With inner radii of approximately 8 cm, they are situated close to the beam and the expected radiation level is high. Closest to the interaction point is the electromagnetic component in which copper acts as the passive material. The two hadronic components employ tungsten and the active material in all three of them is liquid argon. On each side, the forward calorimeter wheels share the liquid argon cryostat with the electromagnetic and hadronic endcaps.

2.2.3 The Muon Spectrometer

The muon spectrometer is the largest and outermost subdetector of ATLAS. With inner and outer radii of approximately 4.5 m and 11 m respectively and stretching out from about 7 m to 23 m from the interaction point on each side in the longitudinal direction, it occupies a volume of around 16000 m^3. It was designed to trigger on muons with high momenta, which play a role as a distinguishing feature in several interesting physics channels, as well as to reconstruct the tracks of muons that pass through with high precision. The components providing the first functionality are the Resistive Plate Chambers (RPC) and the Thin Gap Chambers (TGC), while the latter is achieved by the Monitored Drift Tube (MDT) chambers and the Cathode Strip Chambers (CSC). A three-dimensional representation of the muon spectrometer is shown in Figure 2.7(a), indicating the four different types of components. The arrangement is such that a particle originating from the interaction point will traverse three layers of muon stations as it is bended by the magnetic field (cf. Section 2.2.4).

The Barrel

The barrel of the muon spectrometer consists of three concentric cylindrical layers of muon stations that cover space up to a pseudorapidity of $|\eta|$=1 and in nearly full azimuth. The stations are organized in sixteen sectors, alternating small (S) and large (L), thus following the structure of the eight barrel toroid magnet coils (cf. section 2.2.4). Muon stations in the innermost layer are single MDT chambers located just outside the hadronic calorimeter and named Barrel Inner (BI) chambers. Stations in the middle layer consist of a Barrel Middle

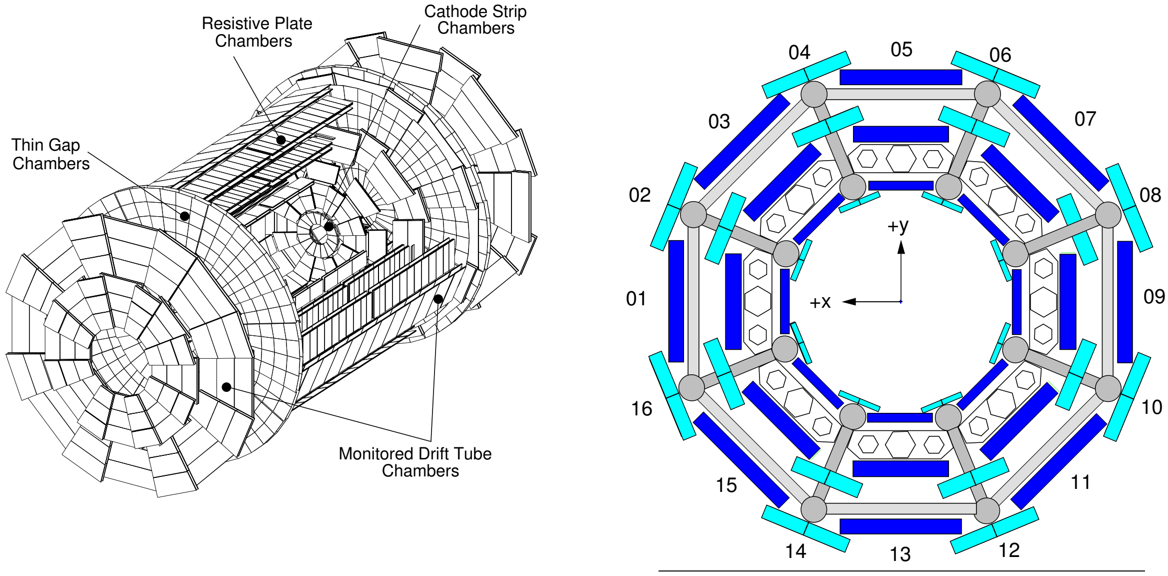

(a) A three-dimensional schematic view of the muon spectrometer.

(b) A schematic view of the transverse cross section of the muon spectrometer, indicating the numbering convention of the sectors as well as the arrangement of the muon stations around the barrel toroid magnet.

Figure 2.7: The muon spectrometer.

(BM) MDT chamber with a RPC on either side and are situated inside the barrel toroid magnet. The outer layer consists of stations that each comprise a Barrel Outer (BO) MDT chamber and a RPC and are positioned just outside the barrel toroid magnet. A transverse cross section of the barrel of the muon spectrometer is shown in Figure 2.7(b), indicating the numbering scheme of the sixteen sectors.

The chamber coverage is limited in the region $|\eta| < 0.1$ to accommodate inner detector and calorimeter services as well as in the barrel/endcap transition region where most of the middle stations are not installed yet for first operation. In sectors 12 and 14, around $\varphi \sim -\frac{9}{24}\pi$ and $\varphi \sim -\frac{15}{24}\pi$, the support feet of the toroidal magnet system prevent full azimuthal coverage.

The Endcaps

The two endcaps of the muon spectrometer consist of four disks each and cover a pseudorapidity range of $1.0 < |\eta| < 2.7$. The greater part of the disks consists of trapezoidally shaped MDT chambers, yet the innermost disk of the innermost layer of each endcap is equipped with CSCs. Thus, in the pseudorapidity range $2.0 < |\eta| < 2.7$ in which the largest particle flux is expected, a better spatial resolution and faster measurements are accomplished. The trigger information in the forward regions is provided by three planes of TGCs in each endcap, which cover $1.05 < |\eta| < 2.4$.

Precision Chambers

The precision measurement of muon trajectories is accomplished by MDTs and CSCs, designed to reach a transverse momentum resolution of approximately 10% for muon momenta of 1 TeV.

MDTs consist of two multilayers of aluminium tubes and a support structure, as shown in Figure 2.8. The cathode tubes of 30 mm diameter are filled with a gas mixture and

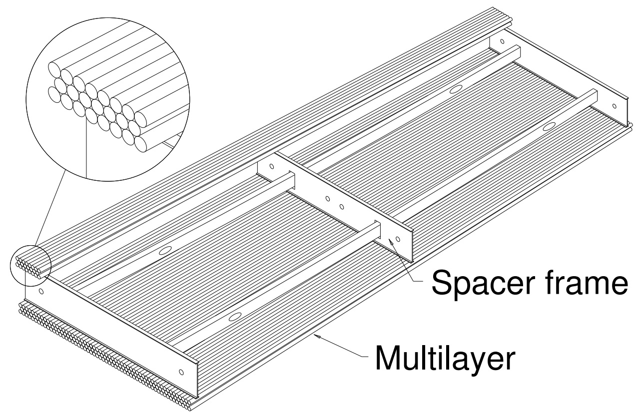

Figure 2.8: Schematic layout of a monitored drift tube chamber.

contain an anode wire to which a voltage is applied during operation. When a charged particle passes through, ionization clusters are created in the gas, which will drift to the anode wire where the signal is propagated to the readout electronics. The position of the incident particle is derived from the timestamp corresponding to the signal pulse passing a threshold of five times the noise level by making use of the relation between the drift time and the distance of the particle to the wire.

CSCs consist of four planes of anode wires and two cathode planes equipped with strips. The coordinates of a traversing charged particle are obtained from the relative measurement of induced charge on adjacent cathode strips. The strips on each of the two cathode planes are positioned orthogonally, thus allowing for determination of two coordinates.

The actual reconstruction of muon tracks is further described in Section 4.5.

Trigger Chambers

Trigger chambers serve the purpose of providing rapid information about charged particles traversing the muon system.

RPCs are gaseous detectors with a time resolution of 1.5 ns and a typical spatial resolution of 1 cm. They consist of two rectangular detectors, contiguous to each other, each composed of two gas volumes and two readout strip panels. A gas volume is enclosed by two resistive plates separated by 2 mm to which a voltage is applied, such that avalanches induced by ionizing tracks are accelerated towards the anode plane, where the signal is read out.

TGCs are based on the same technology as CSCs, although the spacing between the wires and the cathodes is relatively small in order to guarantee a drift time that does not exceed the 25 ns LHC bunch separation.

2.2.4 The Magnet System

The ATLAS magnet system generates a magnetic field configuration such that the trajectories of charged particles are bended when traversing the tracking devices, the inner detector and the muon spectrometer. It consists of two superconducting magnet systems, a toroidal system and a central solenoid, that add up to a diameter of 22 m and a length of 26 m. The toroidal magnet system provides a magnetic field inside the volume of the muon spectrometer, while the solenoidal magnet generates a homogeneous field parallel to the beam axis inside the inner detector. The curvature of the trajectory followed by a charged particle when passing through the field is used to determine its momentum. A schematic view of the configuration of the toroidal and solenoidal magnets in ATLAS is depicted in Figure 2.9.

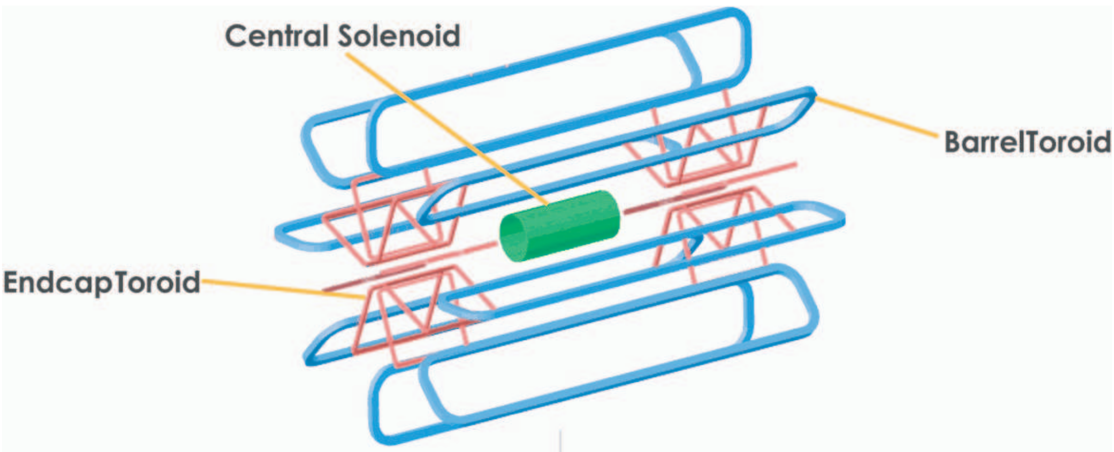

Figure 2.9: Three dimensional schematic view of the magnet system, showing the eight rectangular barrel coils, eight endcap coils on either side and the solenoid in the center.

The Toroidal Magnet System

The toroidal magnet system is built up of a barrel toroid and two endcap toroids.

The barrel toroid consists of eight superconducting rectangular coils, each encased in a cryostat. The total assembly weighs 830 tons and adds up to 25.3 m axial length and inner and outer diameters of 9.4 m and 20.1 m respectively. Cooling down to the nominal operational temperature of 4.6 K takes 5 weeks. The field strength provided by the barrel toroid at the nominal operational current of 20.5 kA varies from 0.15 T to 2.5 T.

The endcap toroid systems consist of eight coils each, which are located interleaved with the barrel toroid coils on either side, thus generating a magnetic field in the endcap regions of the muon spectrometer. With an inner and outer diameter of 1.65 m and 10.7 m and an axial length of 5.0 m each endcap toroid weighs 239 tons. Powered in series with the barrel toroid, the endcap toroids generate a field strength that varies from 0.2 T to 0.35 T at nominal operational current.

The Central Solenoid

The solenoidal magnet system is aligned with the beam axis and produces an axial field throughout the volume of the inner detector. At the 7.730 kA nominal operational current, the strength of the field varies from 2 T at the interaction point to 0.9 T. With an axial length of 5.8 m and a diameter of about 2.5 m, it is embedded inside the electromagnetic calorimeter. In contemplation of a minimal amount of material in front of the calorimeters, the solenoid shares its cryostat with the electromagnetic calorimeter.

In order to monitor the magnetic field inside the inner detector, four NMR (Nuclear Magnetic Resonance) probes are mounted on the wall of the vessel at z=0, equally spaced in φ, that measure the magnitude of the magnetic field, $|\boldsymbol{B}|$, with an accuracy of 10 μT.

Magnetic Field Sensors in the Muon Spectrometer

A precise knowledge of the strength of the magnetic field, $\boldsymbol{B}$, at each given point inside the volume of the muon spectrometer is required to reconstruct a muon's momentum. To this end a magnetic field map is computed from contributions to the Biot-Savart integral from the toroidal and solenoidal magnet systems as well as other ferromagnetic material present in the various detector systems. During operation however, the exact position of these components is continuously influenced by temperature fluctuations and material-induced magnetic forces. Therefore approximately 1800 magnetic field sensors are installed throughout the MDT system to support the calculation of the magnetic field. Their position in ATLAS is displayed in Figure 2.12(c). Each sensor is equipped with Hall probes on three of its orthogonal faces that determine the components of the magnetic field from the induced voltage due to the Hall effect. The number of sensors mounted on a MDT chamber varies from zero to four, each including its own readout electronics and a temperature sensor to allow for local calibration. By measuring the response of each Hall probe as a function of field strength, field orientation and temperature T in test stands at CERN [35], the Hall voltage of each sensor was calibrated. The achieved accuracies on the magnitude $|\boldsymbol{B}|$ of the magnetic field are 0.2 mT up to $|\boldsymbol{B}|$=1.4 T and 1 mT up to 2.5 T. In addition, two NMR probes are mounted on the barrel toroid system in order to monitor potential long-term drifts in the response of the Hall probes.

A number of criteria are defined in order to assess the quality of the value read out by each magnetic field sensor. The criteria include, amongst other,

- $|T - 20°\mathrm{C}| < 10°\mathrm{C}$;
- $|\boldsymbol{B}| < 2.0$ T in the endcaps and $|\boldsymbol{B}| < 3.0$ T in the barrel;

- RMS($|\boldsymbol{B}|/I$) < 1.0 T/A;
- RMS(T) < 2°C;
- $|B_i - \langle B_i \rangle| < 3\ \sigma(B_i)$ for each component $i \in \{x, y, z\}$, where the average is taken over all sensors;
- $|T - \langle T \rangle| < 3\ \sigma(T)$ where the average is taken over all sensors.

In case any of the criteria is not satisfied, the sensor is flagged and disregarded in the field map calculation.

Magnet Operation

After installation in ATLAS, the barrel toroid, each of the endcap toroids and the solenoid were cooled down to 4.6 K and ramped to their nominal current during separate standalone tests. In 2008, the barrel toroid and endcap toroids were powered in series and commissioned as an assembly. During the first duration test of the combined configuration, the current was initially ramped up to 20400 A in about three hours time, subsequently ramped up to slightly over the 20500 A nominal operational current and finally the magnets were slowly discharged. The behaviour of the toroid current and the magnetic field sensors mounted on MDT chambers of type BOL (Barrel Outer Large) is shown in Figures 2.10(a) and 2.10(b) respectively.

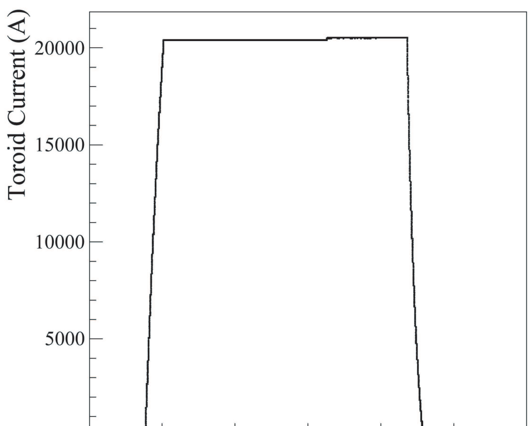

(a) The toroid current versus time during the first duration test of the toroidal magnet system.

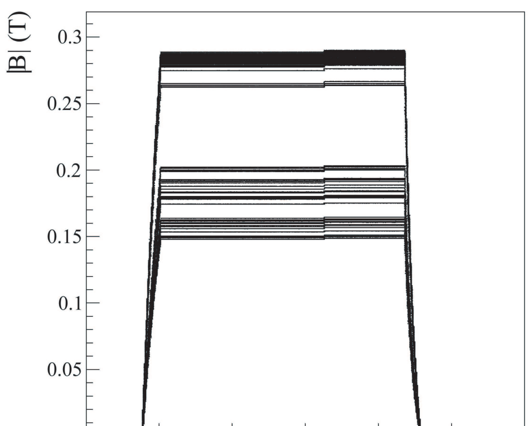

(b) The magnitude of the magnetic field as measured by the magnetic field sensors on MDT chambers of the type BOL versus time during the first duration test of the toroidal magnet system.

Figure 2.10: The first duration test of the toroidal magnet system.

Figure 2.11 displays the RMS of the magnitude of the magnetic field as read out by the magnetic field sensors during the current plateau of 20504.8 A that was part of the duration test. The figure contains the measurements of all 95% of the magnetic field sensors that passed the quality criteria at that moment. In addition, the distribution is displayed for measurements taken in 2010 during full operation. The number of sensors passing all criteria has increased to 100% and the RMS values of the measurements have not degraded in two years time. The relative RMS values with respect to the mean value of $|\boldsymbol{B}|$ are of the order $\mathcal{O}(10^{-5})$, which meets the requirement $5 \cdot 10^{-4}$ from muon reconstruction performance [33].

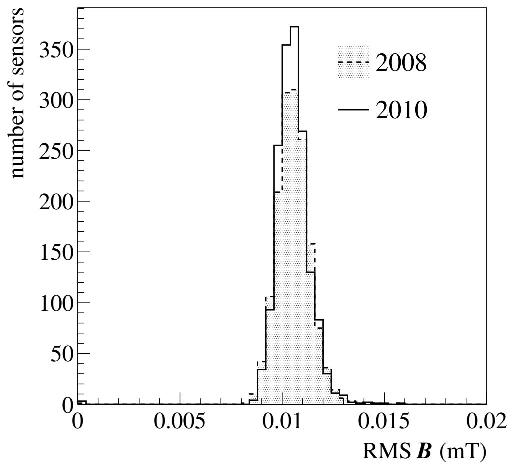

Figure 2.11: The RMS of the magnitude of the magnetic field during constant current as read out by the magnetic field sensors throughout the MDT system.

Figure 2.12(c) shows the magnitude $|\boldsymbol{B}|$ of the magnetic field measured by each sensor during operation, i.e. at 7.730 kA solenoid current and 20.5 kA toroid current.

The temperature fluctuations of the four sensors on a MDT chamber in the top sector, BIL2C05, are displayed in Figure 2.13. The temperature decreases slightly during the night and starts incrementing again around 7:00. It turns out that the temperature difference between the sensor locations on a chamber is considerable. The fluctuations of the temperature are accounted for in the calibration of the magnetic field components being read out by the Hall probes. The RMS on the temperature measurement is well within the allowed range not to be flagged for each of the sensors in the figure.

2.2.5 The Trigger System

Operating at a bunch crossing frequency of 40 MHz, with approximately 23 interactions occurring per bunch crossing, the LHC will produce as many as one billion events per second. Merely a fraction of these events are of interesting nature as most of the interactions are so called *minimum bias* events, i.e. partonic interactions with transverse momenta too small for perturbation theory to be valid. Moreover, it is not feasible to store the corresponding amount of data, approximately 1 PB s^{-1}, on technical grounds. Therefore, a highly efficient selection of interesting events within a minimal time span is required. To this end, a complex trigger system is developed that reduces the rate of events to be stored by a factor of $\mathcal{O}(10^7)$. The event rejection procedure takes place in three subsequent stages: the *Level-1 Trigger*, the *Level-2 Trigger* and the *Event Filter*.

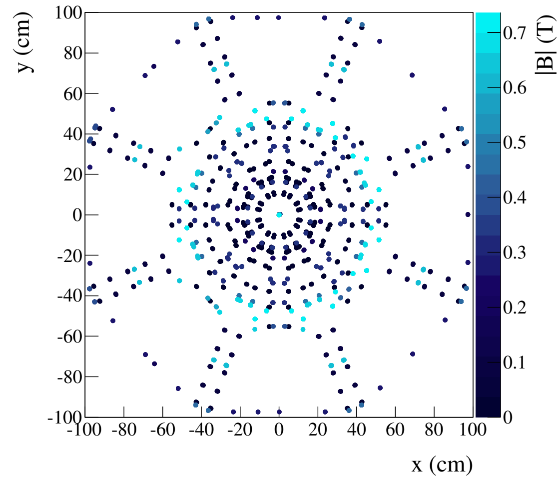

(a) The projection onto the transverse plane.

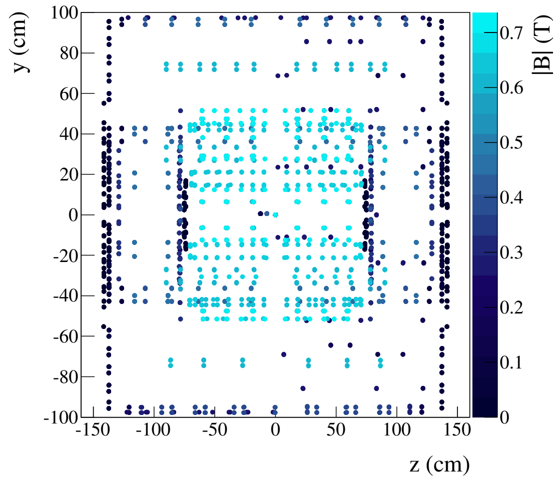

(b) The longitudinal projection onto the yz-plane

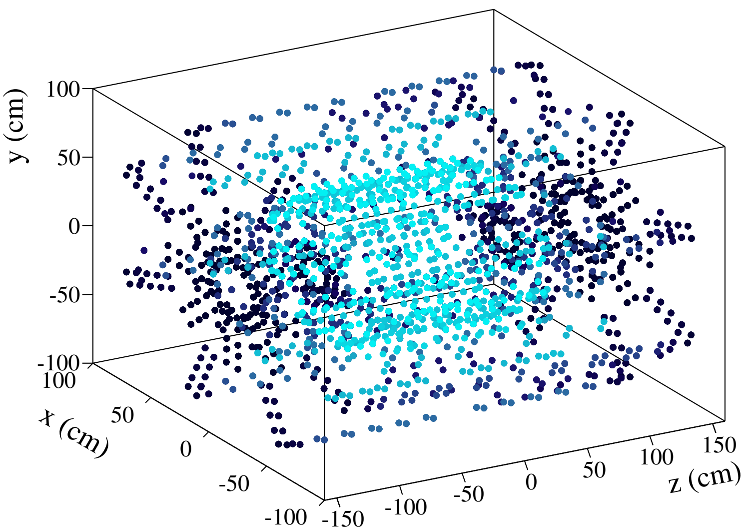

(c) Three dimensional view.

Figure 2.12: The magnitude of the magnetic field during operation as read out by sensors throughout the MDT system.

The Level-1 Trigger

The first level of the trigger system bases its decision on coarse granularity information from the calorimeters and information from the muon trigger chambers only. The decision time is constrained to 2 μs by the *pipeline memory* in which all detector channel data of a bunch crossing are stored until a decision is reached. In order to minimize the propagation time through cables, the dedicated electronics are located as close as possible to the ATLAS detector. The Level-1 Trigger defines *Regions of Interest* (RoIs) in (η, φ) space where object

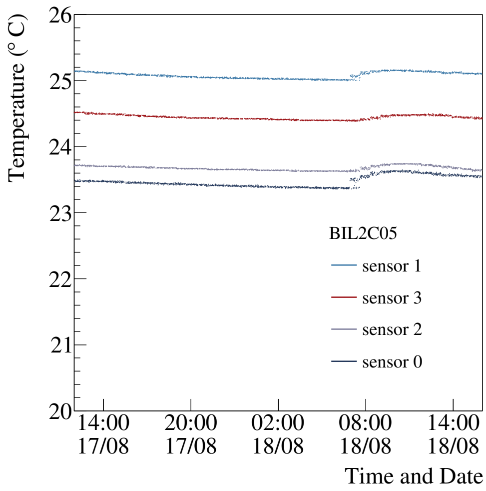

Figure 2.13: The temperate measured by the four sensors on the MDT chamber BIL2C05 during part of the duration test.

candidates satisfy certain energy thresholds. Based on the multiplicity of RoIs, an event is passed on to the Level-2 Trigger or rejected, which results in a reduction of the event rate to 75 kHz.

The Level-2 Trigger

The second level of the trigger system refines the Level-1 Trigger decision by using full granularity information from all detectors, including the inner detector. Dedicated software examines the previously defined RoIs in more detail and attempts to reconstruct physics objects, i.e. electrons, photons, muons and jets, and it calculates the missing transverse energy from the information from the calorimeters. Subsequently, a set of selection criteria is applied and the resulting event rate is 2 kHz.

The Event Filter

The Event Filter is designed to reduce the event rate from 2 kHz to the 200 Hz permanent storage acceptance. In addition, it organizes the data into *streams* based on physics object candidates, as further described in Section 4.1. It accesses the full precision data from the complete detector and generally makes use of the same sophisticated algorithms as the reconstruction of the events that are eventually stored (cf. Chapter 4), yet looser criteria are applied. The available processing time per event is approximately 4 s.

The sequence of algorithms that define a certain object candidate at each stage will be referred to as a *trigger chain*. The final energy threshold and quality requirements are naturally determined by the last stage, the Event Filter. The naming convention for a trigger chain is [N][TYPE][THRESHOLD](i)_[QUALITY], where TYPE specifies the object candidate (as indicated in Table 2.3), N indicates its multiplicity, THRESHOLD is a number corresponding to a (transverse) momentum threshold, i indicates isolation and QUALITY refers to the severity of requirements in the algorithm (e.g. loose, medium or tight in case of electrons, cf. Section 4.4).

Object	**TYPE**
muon	mu
electron	e
photon	g
electron/photon	em
jet	j
forward jet	fj
tau	tau
total energy	te
total jet energy	tj
missing energy	xe
minimum bias	mb

Table 2.3: The naming convention for TYPE in trigger chains.

The trigger chain `e20_loose` for instance, which is used in the following chapters, is designed to trigger on electrons. The algorithms in this chain aim to be as efficient as possible for electrons with a transverse momentum larger than 20 GeV and which satisfy the loose requirements defined in the reconstruction algorithm.

The available trigger chains are defined in terms of a *trigger menu*, which varies in time with increasing instantaneous luminosity. The events that pass any trigger chain in the given menu are arranged in luminosity blocks, each containing typically a couple of minutes of data taking, and stored. The beam conditions and detector performance are stored per luminosity block. Subsequently, the collected data is passed on to the reconstruction software, which is described in Chapter 4.

3

Phenomenology and Simulation of Proton Collisions

In preparation of collision data from the LHC, the expected interactions in proton-proton collisions and their expected signature in the ATLAS detector are studied in simulated events. Apart from providing an environment to develop analysis strategies and estimate the discovery potential of new physics scenarios, the simulation is vital for the development of reconstruction algorithms (cf. Chapter 4). The simulation and reconstruction of events in ATLAS is performed in the `Athena` framework [36]. This software suite handles the following steps:

- **Event generation**: simulation of the proton collisions. It takes care of the production and decay of particles in a given process;
- **Detector Simulation**: describes the interaction and energy losses of the generated particles when traversing the active and inactive parts of the detector;
- **Digitization**: simulates the detector readout, i.e. the conversion of energy deposits in the detector to times, currents and voltages;
- **Reconstruction**: consists of algorithms that employ pattern recognition, track fitting, calibration, et cetera on the detector readout to construct primary physics objects. These algorithms are applied to simulated data and collision data in exactly the same manner. This step is fully described in Chapter 4.

Section 3.1 describes the properties of hadronic collisions that are relevant for Monte Carlo event generators, some of which are subsequently presented in Section 3.2. Section 3.3 presents all Monte Carlo samples that are used in the analyses in the following chapters. The simulation of the ATLAS detector response is briefly discussed in Section 3.4.

3.1 Phenomenology of Proton Collisions

Protons are baryons composed of two up quarks and a down quark, which are the valence quarks, plus additional virtual quark-antiquark pairs and gluons which constitute the *sea*.

For the generation of processes that occur in proton-proton collisions, the basic ingredients are related to the manifestations and limitations of (perturbative) QCD. The main aspects are reviewed here.

3.1.1 The Running Coupling

When calculating physical observables from the Standard Model Lagrangian, all Feynman diagrams with the initial and final state of interest need to be summed over. Often this involves divergent contributions from loop diagrams. The final result, however, is a measurable and thus finite quantity due to the cancellation between divergencies from different diagrams. In practice, calculations can be performed up to a limited amount of loop corrections only and some divergent diagrams are left uncancelled. The antidote is to absorb the infinities into physical parameters such as mass or coupling strength. In this *renormalization* procedure, the infinities are separated from the finite contributions first by means of a regularization scheme. When performing calculations up to a fixed order, the result depends on the regulator, which is traded for the renormalization scale μ_R. It parameterizes the extend to which loop corrections that are not taken into account affect the physics.

Since the renormalization scale μ_R is entirely arbitrary, no physical observable O should depend on it, i.e.

$$\begin{aligned} \mu_R^2 \frac{\partial}{\partial \mu_R^2}\, O(Q^2/\mu_R^2, \alpha) &= \left[\mu_R^2 \frac{\partial}{\partial \mu_R^2} + \mu_R^2\, \frac{\partial \alpha}{\partial \mu_R^2}\, \frac{\partial}{\partial \alpha} \right] O(Q^2/\mu_R^2, \alpha) \\ &= 0. \end{aligned} \tag{3.1}$$

The dependence of the coupling α on the scale μ_R is described by the β-function, which can be calculated order by order in perturbation theory:

$$\begin{aligned} \mu_R^2 \frac{\partial \alpha}{\partial \mu_R^2} &\equiv \beta(\alpha) \\ &= -\alpha \sum_i \beta_i \left(\frac{\alpha}{4\pi} \right)^{i+1}, \end{aligned} \tag{3.2}$$

As it is no longer a constant, $\alpha(\mu_R)$ is referred to as the *running coupling.*

Neglecting all but the leading order contribution, the following differential equation follows from (3.2)

$$\mu_R^2 \frac{\partial \alpha}{\partial \mu_R^2} = -\beta_0 \frac{\alpha^2}{4\pi}. \tag{3.3}$$

The solution is readily found by integration to be

$$\alpha(\mu^2) = \frac{\alpha(\mu_0)}{1 - \frac{\beta_0}{2\pi}\, \alpha(\mu_0) \ln \frac{\mu}{\mu_0}}, \tag{3.4}$$

which means that the coupling strength at any scale μ is related to the coupling strength at a reference scale μ_0. For the QCD coupling α_s, the first four coefficients of the β function are presently known, yet we focus on the first coefficient, β_0, which is given by

$$\beta_0(\alpha) = -\frac{4}{3} \tag{3.5}$$

$$\beta_0(\alpha_s) = 11 - \frac{2}{3}n_f \tag{3.6}$$

for the QED and QCD coupling strengths respectively. The latter depends on the number of quark flavours n_f that are relevant in the calculation at hand. Its value is maximally six though and the coefficient is positive. Consequently, the strong coupling strength decreases with increasing energy scales whereas the electromagnetic coupling strength exhibits the opposite behaviour.

The reference scale μ_0 is often set equal to the mass of the Z boson, at which the values of the coupling strengths are determined to be [10]

$$\alpha(m_Z^2) \approx 1/127 \tag{3.7}$$

$$\alpha_s(m_Z^2) = 0.1184 \pm 0.0007 \tag{3.8}$$

Both values are the world average of a large number of independent consistent measurements.

Two important properties of QCD are direct consequences of the behaviour of the strong coupling α_s:

- **Asymptotic freedom** is the property of quarks and gluons to behave as free particles at very short distances. As opposed to the electromagnetic coupling, the strength of the strong coupling decreases with increasing energy scale μ_R and within a hadron, the partons interact weakly. As a consequence, the parton model [37], which treats the partons as free and non-interacting, turns out to describe hadrons sufficiently well. An important consequence of asymptotic freedom is the fact that perturbation theory can be applied at high energy scales.

- **Colour Confinement** is the phenomenon that partons are tightly bound together in colour neutral combinations, hadrons, and rapidly recombine into such combinations when forced apart by highly energetic collisions. Consequently, no quarks or gluons are observed directly in experiment. The corresponding energy scale is denoted Λ_{QCD}:

$$\lim_{\mu_R \to \Lambda_{\mathrm{QCD}}} \alpha_s(\mu_R^2) = \infty. \tag{3.9}$$

3.1.2 Factorization

According to the *factorization theorem* [38], the cross section for hadronic collisions is well described by the convolution over functions describing the long distance dynamics and functions describing the hard process. The separation is specified by the factorization scale μ_{F}.

The cross section of proton-proton scattering is therefore expressed in terms of the interaction between two incoming partons, $q_a q_b \to X$:

$$\sigma_{pp\to X} = \sum_{a,b} \int \mathrm{d}x_1\ \mathrm{d}x_2\ f_a(x_1, \mu_{\mathrm{F}}^2) f_b(x_2, \mu_{\mathrm{F}}^2)\, \hat{\sigma}_{q_a q_b \to X}(x_1, x_2, \alpha_s(\mu_{\mathrm{R}}^2), \mu_F^2)\ + \mathcal{O}\left(\frac{\Lambda_{\mathrm{QCD}}^2}{Q^2}\right), \tag{3.10}$$

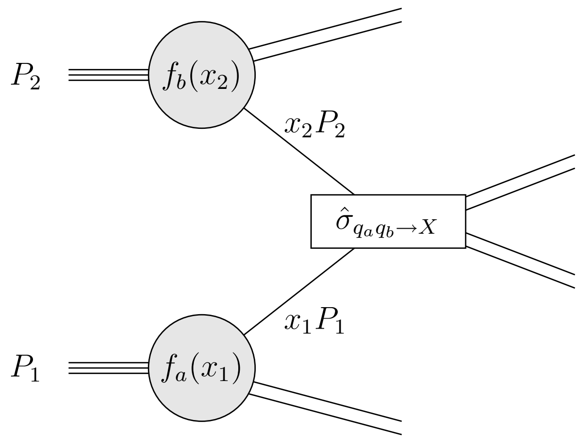

Figure 3.1: Schematic representation of a proton-proton collision: the partons q_a and q_b with momentum fractions x_1 and x_2 of the incoming protons take part in the hard process $\hat{\sigma}_{q_a q_b \to X}$.

where $Q^2 = -q^2$ is the process dependent momentum transfer in the hard interaction, $x_{1,2}$ are the fractions of proton momenta carried by the two initial state partons, and $f_a(x, \mu_{\mathrm{F}}^2)$ are the *parton distribution functions* (PDFs). They describe the probability density for a parton with flavour a to carry a fraction x of the longitudinal momentum of the proton, when probed ad a scale μ_{F}^2. In practice, the PDF is often transformed into the *parton momentum density* by means of a multiplication with the momentum fraction x. By definition, the contributions of all partons sum up to unity, i.e.

$$\sum_a \int_0^1 \mathrm{d}x \; x f_a(x, \mu_{\mathrm{F}}^2) = 1. \tag{3.11}$$

Both the factorization scale μ_{F}^2 and the renormalization scale μ_{R}^2 are commonly set to the characteristic scale of the process, Q^2. Because of the non-perturbative nature of QCD bound states, PDFs cannot be derived from calculations and they are extracted from data obtained at previous generations of collider experiments instead. Several realizations of such parameterizations exist, all containing a major input contribution from electron-proton collision data recorded by the detectors at HERA [39]. Figure 3.2 shows the behaviour of $x f_a(x, Q^2)$ for each parton flavor according to the CTEQ parametrization [40], which is used as the default. The density increases at lower values of x as the scale Q^2 increases, which is illustrated by the comparison between the parton momentum densities at $Q^2 = 4$ GeV^2 (left) and at $Q^2 = 10^4$ GeV^2 (right).

The momenta involved in the partonic process, $q_a q_b \to X$, are high and at this scale the strong coupling $\alpha_s(Q^2)$ is small enough for perturbation theory to be valid. The partonic cross section is expressed as a power series in the expansion parameter $\alpha_s(Q^2)$:

$$\hat{\sigma}(x_i, x_j, Q^2) = \sum_{n=0}^{\infty} \hat{a}_n \alpha_s^n(Q^2). \tag{3.12}$$

This expression is well defined and the coefficients are in principle calculable to all orders by means of Feynman rules. In practice, however, the order to which the calculations are

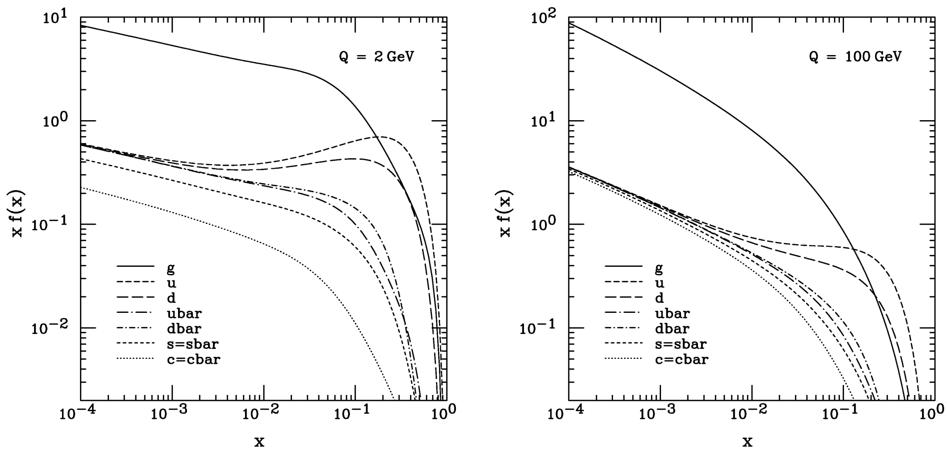

Figure 3.2: Parton momentum density parametrizations according to CTEQ [40] for two different energy scales as a function of the momentum fraction x of the proton carried by each parton flavour.

performed is severely limited as the number of additional diagrams to be calculated increases rapidly with each order. The main contribution to the amplitude of a given process are the diagrams with the lowest power in the expansion parameter, which are generally tree level diagrams. They contribute at leading order (LO) to the partonic cross section. In case of $t\bar{t}$ production, these diagrams contain two QCD three-vertices and contribute at order $\mathcal{O}(\alpha_s^2)$ (cf. Figure 3.3). At next-to-leading order (NLO), diagrams with an additional power of the expansion parameter come into play, for instance due to real or virtual gluon emission. The size of the contributions are suppressed by the additional power of the expansion parameter, yet the number of diagrams increases. Most importantly, the dependence on the renormalization scale and the corresponding uncertainty on the cross section decrease when including the additional diagrams.

Additional Phenomena

The partons that take part in the hard process are colour charged and therefore subject to gluon emission. Usually, a distinction is made between radiation from the incoming partons, which is called *initial state radiation*, and radiation from the outgoing partons, which is called *final state radiation*. The emitted gluons split into quark/anti-quark pairs or gluon pairs et cetera, which may result in cascades of additional partons. These cascades are described by parton showering models.

When partons created in these processes move away from each other, the colour field between them increases and quark/antiquark pairs are created from the vacuum. *Hadronization* is the process where the partons combine into colour neutral states, hadrons, which are energetically favourable. Hadronization occurs at a much later time scale than the hard process and the corresponding energy scale is too low for perturbation theory to be valid. The non-perturbative description is modelled by fragmentation functions, which are the final state equivalent of PDFs.

The resulting hadrons, in turn, are often unstable and decay further into stable particles, which eventually interact with the ATLAS detector.

3.2 Monte Carlo Generators

Monte Carlo (MC) generators are computational algorithms that make use of random numbers to simulate systems in nature that behave stochastically. In collider physics, they are applied in the simulation of events as produced in collisions. On an event by event basis, the properties of each particle involved are determined by expected probability densities using random number generators. These techniques are indispensable when describing the expected interactions between particles because the complexity of the corresponding phase space integrals is such that analytic calculations are not feasible.

MC generators make use of the factorization principle and the various elements in the description of the collisions are considered independently. First, the matrix elements corresponding to the hard process are calculated perturbatively. The decays of short-lived resonances produced in parton collisions, e.g. top quarks or W' bosons, are regarded as part of the hard process. Presently, matrix element event generators up to NLO are available. Monte Carlo techniques are utilized to generate the momenta of the incoming partons according to their PDFs.

Subsequently, initial and final state radiation are simulated according to a parton showering model, in which *splitting functions* are used to describe the probability for a parton to split into two partons. The splitting functions are derived from QCD, albeit in a tree level approximation.

No descriptions from first principles exist for hadronization nor for hadron decays. These processes are implemented in MC generators via phenomenological models.

There are several possibilities to model parton showering and hadronization. In addition, various methods exist to combine the matrix elements from the hard process with the modelled behaviour of the soft phenomena. As a consequence, a long list of MC generators is available, a subset of which is listed here:

Pythia [41] is an event generator capable of performing the full simulation chain and a large range of hard processes is available at LO. The hadronization process is described by the *string fragmentation* model [42], in which the colour field between partons is represented by a string potential.

Herwig [43] is the second major event generator that takes care of the full simulation chain, but uses a slightly different approach for parton showering and for hadronization than `Pythia`. The *cluster fragmentation* model is employed in the hadronization step, in which gluons are split into quark pairs and combined with neighbouring quarks into colour neutral clusters.

MCatNLO [44] is a specialized matrix element generator, which calculates the matrix elements of the hard process up to NLO. It is interfaced with `Herwig` for the parton showering and an advanced matching scheme is applied to prevent double counting of gluon emissions.

Alpgen [45] is a specialized matrix element generator that generates tree level matrix elements for processes with up to six additional final state partons. Interfaces to both `Pythia` and `Herwig` are available to perform the parton showering.

AcerMC [46] is another matrix element generator optimized for the simulation of background processes. The matrix element calculation can be interfaced to `Pythia` as well as `Herwig` for parton shower development.

The kinematic distributions for a given process may differ between the MC generators. Extensive studies on the comparison have been performed for instance in [47, 48]. When available,the NLO matrix elements are preferred over LO, yet the different phenomenological descriptions of the soft phenomena are used in parallel. Eventually, each of the MC generators will be tuned to the LHC data by means of free parameters, as will the PDFs. The final level of agreement may provide insight in the best choice of hadronization model.

Parton Multiplicities

The event generator `Alpgen` [45] is specialized in the generation of multi-parton hard processes with up to six final state partons. The distance between the generated partons is required to satisfy $\Delta R > 0.7$ and their transverse momenta satisfy $p_{\mathrm{T}} > 15$ GeV. The multi-parton hard process is complemented with parton showering to describe the additional radiation. This procedure has to be considered with care in order to prevent double counting. An event with N final state partons can be obtained by several configurations of the number of hard partons and the number of showered partons. This is taken care of by the so called MLM matching scheme [49], in which final state *jets* (cf. Section 4.2) are matched to the hard partons with $\Delta R < 0.7$ and events are vetoed in case not all jets and partons are matched bijectively. Only in the sample with the highest hard parton multiplicity, additional jets from showering are allowed to be present.

3.3 Event Samples for $t\bar{t}$ and $W' \to tb$ Analyses

The simulated events that are studied in Chapters 4, 5 and 6 are $t\bar{t}$ events, i.e. proton collisions that result in a top/antitop quark pair. The MC generation of these events and relevant background events is discussed in Section 3.3.1. Chapter 7, on the other hand, focuses on the production of W' bosons in the context of Little Higgs models and in particular the decay channel $W' \to tb$. The generation of these events is the subject of Section 3.3.2.

The majority of the MC samples are produced and validated centrally by the ATLAS collaboration. For the analysis of $t\bar{t}$ events, all samples are available in full detector simulation, i.e. with `GEANT4`, which is described in Section 3.4. For the analysis described in Chapter 7, two samples with $W' \to tb$ events are generated privately with `Pythia` [41]. In this case, the software used for the simulation of the detector response is `ATLFAST II` (cf. Section 3.4).

3.3.1 Samples for $t\bar{t}$ Analysis

Production of $t\bar{t}$ Events

Figure 3.3 shows the four diagrams[1] that contribute to the production of top quark pairs at leading order (LO). At the high LHC beam energies, partons with small momentum fractions x contribute significantly to the production of $t\bar{t}$ events. Figure 3.2 shows that the PDF for gluons dominates in this region. As a consequence, the three diagrams with initial state gluons give the main contribution.

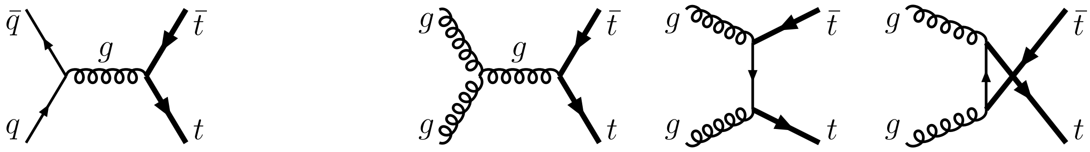

Figure 3.3: The Feynman diagrams that contribute at leading order to the production of $t\bar{t}$ events.

Semileptonic $t\bar{t}$ Events

Each top quark decays into a W boson and a b quark, as other decay channels are strongly suppressed by the corresponding entries of the CKM matrix. In Chapters 5 and 6, semileptonic $t\bar{t}$ events are selected, i.e. events in which one of the W bosons decays leptonically ($t \to Wb \to l\nu b$), while the other decays hadronically ($t \to Wb \to qq'b$).

Because of fermion universality in weak interactions, in approximately 1/3 of the cases the W boson decays leptonically, i.e. into a charged lepton and the corresponding neutrino, and the remaining 2/3 are hadronic decays, i.e. into a pair of quarks. This results in a classification of three types of decays, namely *hadronic*, *semileptonic* and *dileptonic $t\bar{t}$* decays. The corresponding branching ratios are 45.7 %, 43.8 % and 10.5 % respectively, as follows from the individual branching fractions of the W boson decay modes according to the `PDG` [11]. The share of each type of decay is schematically illustrated in Figure 3.4.

The reconstruction, the characteristics and the selection of semileptonic $t\bar{t}$ events are described in detail in the following chapters. In short, the final state contains a single charged lepton, four quarks (when ignoring initial and final state radiation) and a neutrino.

The sample of $t\bar{t}$ events is generated with `MCatNLO`. At the event generation stage, the decay of the top quarks is restricted such that at least one of them decays leptonically. As a consequence, the sample consists of both semileptonic and dileptonic $t\bar{t}$ events and the corresponding cross sections are determined from the branching fractions. Although the dileptonic events are contained in the same sample for production convenience, they are considered as background in the analysis.

Backgrounds to $t\bar{t}$ Events

Apart from dileptonic $t\bar{t}$ events, the following processes are expected to exhibit signatures in the ATLAS detector similar to semileptonic $t\bar{t}$ events and are considered as background:

[1] All Feynman diagrams are drawn with the use of `Axodraw` [50].

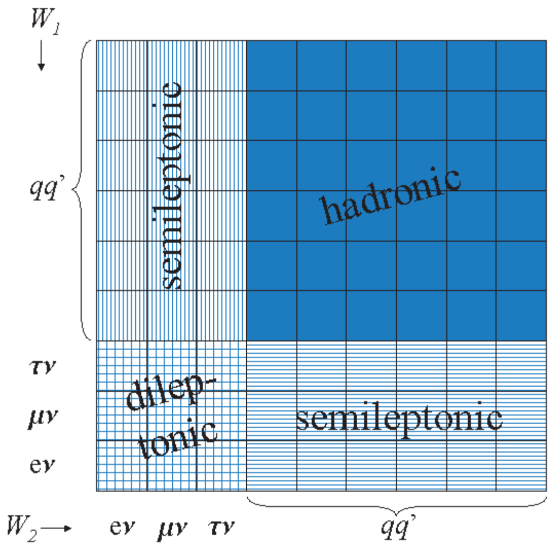

Figure 3.4: Schematic display of the classification of $t\bar{t}$ events in hadronic, semileptonic and dileptonic decays, based on the decay modes of the W bosons.

- **W + jets**: The largest contribution is expected from W boson production in association with jets, where the W boson decays leptonically. Additional jets originate from gluon radiation, which at times in fact results in the exact same composition of final state objects as $t\bar{t}$ events. The cross section does decrease with increasing numbers of additional jets.

- **multi-jet**: In proton-proton collisions, any two initial state partons may interact through a QCD 3-vertex and the intermediate parton in turn splits into another two outgoing partons. Each incoming and outgoing parton may radiate additional quarks and gluons, resulting in a final state with large hadronic activity. These type of events are hereafter referred to as *multi-jet* events, with the exception of events where the two outgoing partons are both top quarks. The latter are treated separately, namely as $t\bar{t}$ events.

  The predicted inclusive cross section for multi-jet events is enormous compared to $t\bar{t}$ production, since the relatively heavy top quarks require a minimum value of x_1x_2s to be produced. In fact, the uncertainty on the multi-jet cross section is large due to the fact that loop corrections are ignored in the calculation and because large powers of α_s are involved. Nevertheless, the only multi-jet events that contribute as a background are the small fraction in which a lepton is reconstructed in the final state. Therefore, in order to save computing time, the generated MC samples include a filter, which is described below. One sample is produced specifically for the electron channel and one for the muon channel analysis.

- **single top** : Figure 3.5 displays the LO diagrams for single top production. Since the weak interaction is involved in the production, the cross sections are small compared to $t\bar{t}$ production. The generated MC samples are restricted to contain leptonically decaying top quarks only.

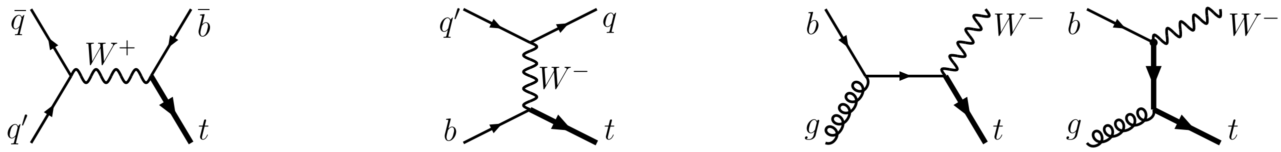

Figure 3.5: The Feynman diagrams corresponding to single top production at LO via the s-channel (left), the t-channel (middle) and the Wt channel (right).

Monte Carlo Samples and Cross Sections

Table 3.1 contains the cross sections and applied filters for all event samples relevant to the semileptonic $t\bar{t}$ event selection. The first column indicates the integrated luminosity that corresponds to the samples, given the number of generated events. The studies performed in this thesis are all based on Monte Carlo simulations of proton collisions at 10 TeV center of mass energy, with the exception of the very last chapter. For comparison, the cross sections corresponding to the design collision energy of 14 TeV are given in Table 3.1 as well. It is observed that the signal to background ratio will improve a great deal as soon as the design collision energy of 14 TeV is reached. The $t\bar{t}$ production cross section is most sensitive to $\sqrt{s}$ due to the threshold on $x_1 x_2 s$ required to produce the massive top quarks.

Sample	$\int L$	**Filter**	$\boldsymbol{\sigma}$**(10 TeV)**	$\boldsymbol{\sigma}$**(14 TeV)**
semileptonic $t\bar{t}$	1250 pb^{-1}	none	176 pb	387 pb
dileptonic $t\bar{t}$	1250 pb^{-1}	none	42.2 pb	92.7 pb
$W+$ jets (e)	~900 pb^{-1}	`3jet`	377 pb	505 pb
$W+$ jets (μ)	~900 pb^{-1}	`3jet`	120 pb	168 pb
$W+$ jets (τ)	~900 pb^{-1}	`3jet`	221 pb	181 pb
single top				
leptonic s-channel	~8000 pb^{-1}	none	2.27 pb	3.45 pb
leptonic t-channel	~800 pb^{-1}	none	43.4 pb	79.9 pb
semi- and dileptonic Wt	175 pb^{-1}	none	14.3 pb	35.8 pb
multi-jet (e)	9.6 pb^{-1}	`top_jet`	$2.10 \cdot 10^6$ pb	-
multi-jet (μ)	9.6 pb^{-1}	`top_mu`	$108 \cdot 10^3$ pb	-

Table 3.1: The cross sections for $\sqrt{s}$ =10 TeV and $\sqrt{s}$ =14 TeV respectively. The numbers include the efficiencies of the applied filters, which are described in the text.

Filters

Only a fraction of the W+jet and multi-jet events actually contributes to the background in a $t\bar{t}$ analysis. In order to save computing time, events are pre-selected already at event generation level. Despite the enormous cross section, the generation of multi-jet becomes feasible in terms of computing time when such a filter is included. The applied filters are designed specifically for studies involving $t\bar{t}$ events [47]:

- `3jet`: The presence of at least three jets reconstructed by `Cone4TruthJets` (cf. Section 4.2) that satisfy $p_{\mathrm{T}} > 30$ GeV is required.

- `top_mu`: At least one muon is present with $p_{\mathrm{T}} > 10$ GeV and $|\eta| < 2.8$.

- `top_jet`: At least four jets reconstructed with `Cone4TruthJets` are present, satisfying $p_{\mathrm{T}} > 17$ GeV and $|\eta| < 5.0$, while at least three jets are reconstructed with `Cone4TruthJets` that satisfy $p_{\mathrm{T}} > 35$ GeV and $|\eta| < 5.0$.

For all processes involving W bosons, the branching fractions of the leptonic decay is equal for each lepton flavour. This does not hold for the numbers in Table 3.1 for the $W+$ jets samples as a consequence of the varying efficiency of the `3jet` filter, which is why they are mentioned separately for each lepton flavour. The efficiency of the filter is largest on the muon channel as muons do not result in jets reconstructed with `Cone4TruthJets` as often as electrons and taus.

Both the W+jet and multi-jet samples are generated with the event generator `Alpgen`, as it specializes in the generation of multi-parton hard processes (cf. Section 3.2). In the hard process, only the first two generations of quarks are represented and the $b\bar{b}$ pairs that result from parton showering are generally restricted to low values of p_{T}. In order to cover the phase space properly, the separate processes $W+b\bar{b}$+jets and $b\bar{b}$+jets are generated with the restrictions $p_{\mathrm{T}}(b) > 20$ GeV and $\Delta R(b, \bar{b}) > 0.7$ to complement the default $W+$ jets and multi-jet samples.

3.3.2 Samples for $W' \to tb$ Analysis

In Chapter 7, the aim is to select events in which a W' boson decays into a top and a bottom quark, where the top quark decays leptonically. The notation $W' \to tb$ is used hereafter to indicate the sum of the decay modes $W'^{+} \to t\bar{b}$ and $W'^{-} \to \bar{t}b$. The W' boson is produced in proton-proton collisions through the interaction of two quarks, as depicted in Figure 3.6. The production cross section in proton collisions is small as the $q'\bar{q}$ initial state involves a sea parton and high values of the momentum fractions x_1 and x_2 are required for the massive W' boson to be produced.

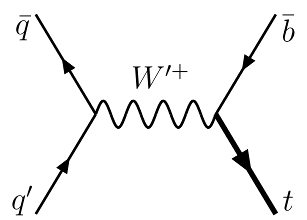

Figure 3.6: Feynman diagram of the production of W' at LO.

Two private samples are produced with `Pythia` [41] and `ATLFAST II` to describe the signal. The applied parameter settings are given in Appendix B. A large part of the samples described above in the context of the $t\bar{t}$ analysis are considered as background in the analysis in Chapter 7 as well. Furthermore, W+jet samples without a jet filter come into play. The cross sections are listed in Table 3.2.

For the two $W' \to tb$ samples, the mass of the W' boson is set to $m_{W'} = 750$ GeV and $m_{W'} = 1$ TeV respectively. Approximately 10^4 events are generated for each sample. The parameters describing the W' couplings to fermions are set equal to the Standard Model W boson couplings to fermions. Only events in which the top quark decays leptonically are generated. The predicted cross sections depend on the model in which the W' boson is introduced, two of which are listed here as benchmarks.

In case of the Littlest Higgs Model, the coupling of the W' boson to fermions is equivalent to that of the Standard model W boson when setting the mixing angle parameter $\cot\psi$ equal to unity (cf. Section1.3.1). The production cross section is proportional to $\cot^2\psi$ and decreases with increasing values of $m_{W'}$. The values for the production cross section times branching ratio, i.e. $\sigma(pp \to W') \times \mathrm{BR}(W' \to tb)$, follow from `Pythia`.

The $W' \to tb$ cross sections for the LRTH Model are evaluated with `Calchep` [51], setting the proton PDFs to the CTEQ parametrization. More details on the parameters can be found in Appendix B.

Sample	**σ(10 TeV)**	
	Littlest Higgs	**LRTH**
$W' \to tb$ ($m_{W'} = 750$ GeV)	4.34 pb	1.35 pb
$W' \to tb$ ($m_{W'} = 1$ TeV)	1.39 pb	0.26 pb
W + jets (unfiltered)	$48 \cdot 10^3$ pb	

Table 3.2: The cross sections for $W' \to tb$ at $\sqrt{s} = 10$ TeV. The branching fraction for the leptonic decay of the Standard Model W boson is included.

Here, the interference of the $W' \to tb$ diagram with the Standard Model single top s-channel diagram is neglected. This is motivated by the large mass difference between the Standard Model W boson and the W' boson, which results in an inevitable suppression of either of the propagators.

3.4 Detector Simulation

`GEANT4` [52] is an extensive particle simulation toolkit that governs all aspects of the propagation of particles through detectors, based on a description of the geometry of the detector components and the magnetic field. The physics processes include ionization, Bremsstrahlung, photon conversions, multiple scattering, scintillation, absorption and transition radiation.

The detector is described in terms of almost 30 million volumes with properties, which in case of the ATLAS detector are constructed based on two databases: the geometry database and the conditions database. The former contains all basic constants, e.g. dimensions, positions and material properties of each volume. The latter is updated according to the circumstances at a given time and contains for instance dead channels, temperatures and misalignments. As a result, several layouts of the detector are available. Test beam data taken with components of the ATLAS detector before completion have aided the validation and further improvement of the detector simulation [33].

Due to the detailed and complicated geometry of the ATLAS detector and the diversity and complexity of the physics processes involved, the consumed computing time per event is large ($\mathcal{O}$(1 hour)). This has been a motivation for the development of *fast simulation* alternatives, which make use of parameterizations of the detector response. The standard `GEANT4` simulation that exploits the full potential is referred to as *full simulation*. The majority of the events studied in this thesis are produced with full simulation, with the exception of the $W' \rightarrow tb$ samples in the analysis in Chapter 7, which have been produced with `ATLFAST II`.

ATLFAST II

`ATLFAST II` [53] is a compromise between full and fast simulation; both the inner detector and the muon spectrometer are fully simulated with `GEANT4`, whereas the propagation of particles through the calorimeters is described by a parameterization [54]. This configuration is motivated by the fact that `GEANT4` spends approximately 80 % of its computing time on particles producing showers in the calorimeters.

After propagation through the inner detector, all remaining particles except muons are disregarded. The muons are further propagated in the full detector simulation to produce the energy deposits in the calorimeters as well as the hits in the muon spectrometer. The absent electromagnetic and hadronic showers in the calorimeters from the disregarded particles are estimated by a parameterization which is obtained from a fully simulated sample of single photons and single charged pions. To assess the parameterization, the energies of the generated particles vary from 0.2 to 500 GeV and their directions are evenly distributed in $|\eta| < 5$ and $-\pi < \varphi < \pi$. The particle showers are described by two parameterizations: one corresponding to the total energy deposit in each calorimeter layer and another describing the energy distribution over the cells within a layer. The latter, the *shape* parametrization, is based on the assumption that the energy distribution perpendicular to the direction of flight is radially symmetric. In `ATLFAST II`, the calorimeter particle showers of electrons and photons is approximated by the photon parameterization and all hadrons are described by the pion parameterization. The consumed computing time per event proves to decrease with a factor of 20 compared to full simulation [55]. Concerning physics performance, the agreement is at the percent level.

4

Event Reconstruction

This chapter describes the reconstruction of physics objects with four-momenta as they are used in analyses; i.e. jets, electrons, muons and missing transverse energy. The reconstruction algorithms perform best in events with a low multiplicity of final state objects, yet the environment of the analyses in this thesis is more challenging. In the ATLAS general performance note [56], the expected reconstruction performance of all final state objects in *clean* events is discussed at length. The expected performance in the more dense type of events is illustrated here by means of simulated semileptonic $t\bar{t}$ events at collision energies $\sqrt{s} = 10$ TeV and in versions of the reconstruction algorithms that are improved with respect to the performance note.

For an event to be processed by the reconstruction algorithms, it first needs to have passed the trigger system. The available data streams are discussed in the first section. Sections 4.2 and 4.3 cover the reconstruction of jets and the identification of b-jets. The reconstruction and performance of electrons and muons is discussed in Sections 4.4 and 4.5. Finally, the reconstruction of missing transverse energy is explained in Section 4.6. Its performance in $t\bar{t}$ events is discussed in detail in Chapter 6.

4.1 Trigger Chains

As described in Section 2.2.5, the trigger system reduces the enormous amount of incoming data and aims to select all interesting events.

The incoming data is categorized into data streams, each of which contains the events that pass at least one of a set of trigger chains. These sets are defined such that the data streams contain a maximum amount of interesting events while minimizing the overlap between them. The available physics data streams are listed in Table 4.1. The trigger chains that are contained in each of these physics data streams in the trigger menu for initial luminosity, $L = 10^{31}$ cm^{-1}s^{-1}, are specified in Appendix A.1.

The minimum bias triggers are designed to select all types of inelastic interactions, across the full acceptance of the detector. During non-collision running, they monitor beam background, such that it can be excluded during collision running. Apart from the physics data streams, an *express stream* is defined. It contains a subset of the physics triggers with the purpose of monitoring and validating the quality of the data. It is processed within a few hours such that any problems may be fixed before the data in all physics streams are reconstructed.

egamma
muon
jet/EtMiss/tau
minimum bias

Table 4.1: The physics data streams.

The processes of interest in this thesis contain virtually all physics objects, namely (b)-jets, muons, electrons and missing transverse energy in their final state. Out of all the trigger possibilities, the single lepton triggers are expected to be most reliable and most discriminating—especially against multi-jet backgrounds. In fact, they are specifically designed to trigger high-p_{T} events involving leptons, like $t\bar{t}$ decays. Furthermore, the robustness and efficiency of these triggers are expected to be validated at an early stage in the data taking period. Therefore, the muon and egamma data streams are selected for the analyses and in particular the trigger chains `e20_loose` and `mu10` are part of the event selection criteria.

The purpose of the trigger chains `e20_loose` and `mu10` is to select events that contain an electron with $p_{\mathrm{T}} > 20$ GeV or a muon with $p_{\mathrm{T}} > 10$ GeV as efficiently as possible in the available time span. The achieved efficiencies are affected by detector limitations and depend on the η and p_{T} of the trigger object candidate. The p_{T} dependence of `e20_loose` and `mu10` in $t\bar{t}$ events is displayed in Figures 4.1(a) and 4.1(b). They show the ratio of the p_{T} distributions of the electron or muon from the leptonically decaying top quark before and after the trigger requirement. Similarly, Figures 4.1(c) and 4.1(d) show the ratio of the η distributions. The efficiency of `e20_loose` is decreased in the barrel/endcap transition region $|\eta| \approx 1.4$ as well as in the very forward region. Figure 4.1(d) shows that the efficiency of `mu10` is clearly affected by the limited detector coverage in the barrel/endcap transition region around $|\eta| \approx 1$ as well as by the gap around $|\eta| \approx 0$.

Due to a technical problem in the Level-2 algorithm, the efficiency of `e20_loose` is hereafter described by a parametrization, which is discussed in detail in Appendix A.2.

4.2 Jet Reconstruction

At high energy collisions between protons, such as those in the center of the ATLAS detector, the presence of partons is overwhelming. As a result of colour confinement, they hadronize before they enter the calorimeters. The resulting collimated sprays of particles, the jets, are detected and reconstructed using jet algorithms. Many different approaches and definitions are available, each of which is characterized mainly by its treatment of close-by hard particles and soft radiation. The first step in a jet algorithm is to combine calorimeter cells into objects with physically meaningful four-momenta, either *signal towers* or *TopoClusters*.

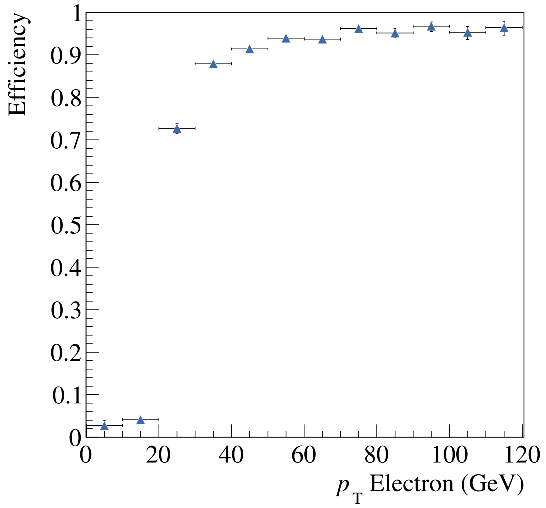

(a) The efficiency of `e20_loose` versus the p_{T} of the electron from the leptonically decaying top quark, which satisfies $|\eta| < 2.5$

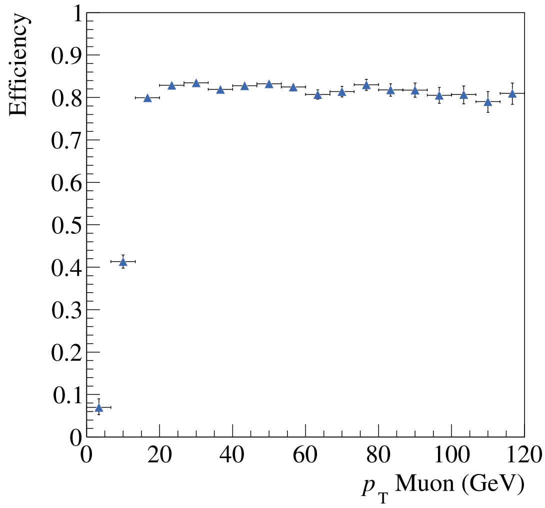

(b) The efficiency of `mu10` versus the p_{T} of the muon from the leptonically decaying top quark, which satisfies $|\eta|$ <2.4.

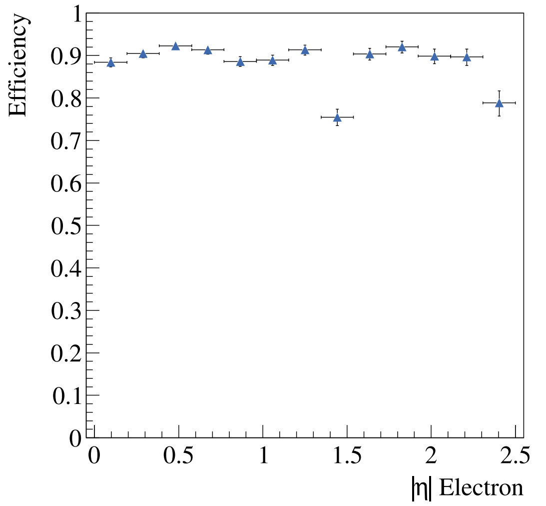

(c) The efficiency of `e20_loose` versus the η of the electron from the leptonically decaying top quark, which satisfies $p_{\mathrm{T}} > 20$ GeV.

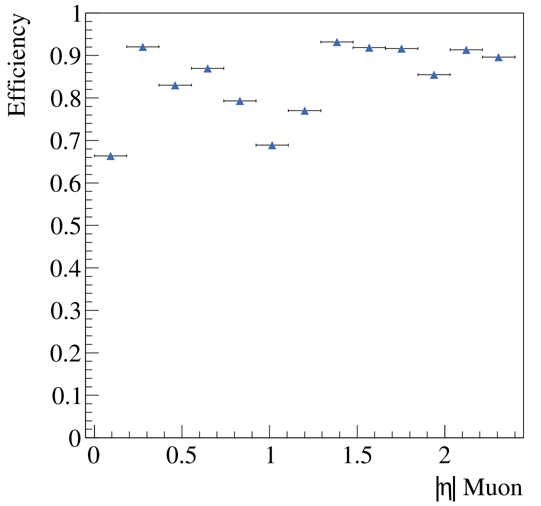

(d) The efficiency of `mu10` versus the η of the muon from the leptonically decaying top quark, which satisfies $p_{\mathrm{T}} > 20$ GeV.

Figure 4.1: The expected trigger efficiency dependence on the p_{T} and η of the lepton in simulated semileptonic $t\bar{t}$ events.

Signal towers are constructed by projecting calorimeter cells onto a grid with tower bin size $\Delta\eta \times \Delta\varphi = 0.1 \times 0.1$. Depending on the overlap between the area of the projected cell and the tower bin, each cell contributes the corresponding fraction of its signal to that tower. Some towers end up with a negative net signal due to noise fluctuations.

Instead of ignoring them completely, they are combined with nearby towers with positive signal in order to avoid biases and to achieve cancellations of noise.

Topological cell clusters or TopoClusters are combinations of cells around seed cells that exceed a signal-to-noise ratio threshold. For each cell with $|E^{\text{cell}}/\sigma_{\text{noise}}^{\text{cell}}| > 4$, its directly neighbouring cells in all three dimensions are assigned to the cluster. Subsequently, their neighbouring cells are included if the signal-to-noise ratio exceeds a second threshold $|E^{\text{cell}}/\sigma_{\text{noise}}^{\text{cell}}| > 2$. Finally, one additional shell of neighbouring cells is added to the cluster.

Cone Jet Finder

In ATLAS, a general cone jet finder algorithm is implemented[1], which takes a cone size R_{cone}, a seed threshold T and the previously defined combinations of cells as input. These signal towers or TopoClusters are first arranged in decreasing order in p_{T}. Then, if the highest p_{T} object exceeds the threshold, $p_{\text{T}} > T$, all objects that satisfy $\Delta R < R_{\text{cone}}$ are grouped into a new input object and the corresponding four-momentum is calculated. Again, a cone is constructed around its center and the objects within this cone are grouped into a new input object. This procedure is repeated until the direction of the cone is stable and the resulting cone is called a jet. The subsequent object is then tested against the seed threshold and the same iterative combination is performed for this seed. This continues until no more objects pass the seed threshold.

Finally, jets with common constituents are merged if their shared p_{T} is larger than 50% of the p_{T} of the softer jet. Otherwise, the overlapping part is assigned to the harder jet.

H1 Calibration

So far, the raw signal from the calorimeter cells is used for the jet constituents and the only corrections applied are related to the detector geometry and the electronics. In order to account for the non-compensating response for hadrons, the so called H1 calibration scheme for jets [57] applies a weight w to each cell. The weight factor is a function of the location $\boldsymbol{X}_i$, the signal energy E_i and the volume V_i of the cell. For cells with high signal densities E_i/V_i, which are more likely to be induced by electromagnetic showers, the assigned weighting factor is close to 1. The lowest signal densities are associated with hadronic showers and weighted with factors up to 1.5, corresponding to the electron/pion signal ratio.

In addition, the calibration scheme aims to correct for detector effects like energy loss in inactive material by making use of reference jets obtained in a full simulation di-jet sample [56]. The calibrated four-momentum for each jet becomes

$$(E_{\text{jet}}, \boldsymbol{p}_{\text{jet}}) = \sum_{i}^{N_{\text{cells}}} w(\boldsymbol{X}_i, E_i, V_i)\,(E_i, \boldsymbol{p}_i)\,, \tag{4.1}$$

where N_{cells} is the number of calorimeter cells contained in the cone. Only jets that satisfy $p_{\text{T}} > 7$ GeV after calibration pass the jet definition.

[1] At the time of this research, alternative algorithms that are infrared and collinear safe were still under development.

The jet algorithms used in the analyses of Chapters 6 and 7 are the `Cone4H1TopoJets` and `Cone4H1TowerJets`, based on TopoClusters and signal towers respectively. In both cases the cone jet finder uses cone size $R_{\text{cone}} = 0.4$ and seed threshold $T = 1$ GeV.

The flexibility of the algorithms allows the possibility for final state particles from Monte Carlo generators to be used as input for the cone jet finder, which results in `Cone4TruthJets`. The performance of `Cone4H1TopoJets` in simulated semileptonic $t\bar{t}$ events is illustrated here by matching reconstructed jets to the highest-p_{T} `Cone4TruthJet` with $\Delta R < 0.4$. Figure 4.2 shows the fractional transverse momentum resolution, $\sigma(p_{\text{T}})/p_{\text{T}}$, as a function of the p_{T} and η of the `Cone4TruthJet`. The jet resolution suffers from the limited calorimeter coverage around the barrel/endcap transition at $|\eta| \approx 1.4$. The line in Figure 4.2(a) corresponds to the best fit of the function

$$\frac{\sigma(p_{\text{T}})}{p_{\text{T}}} = \frac{a}{\sqrt{p_{\text{T}}}},$$

where $a = 0.77$ represents the stochastic calorimeter response.

Figure 4.3 shows the so called *jet response* of the `Cone4H1TopoJets`, i.e. the ratio of the reconstructed transverse momentum to the transverse momentum of the `Cone4TruthJet`. The jet response is quite stable and linear to within 1% for jets satisfying $p_{\text{T}} > 40$ GeV. Figure 4.3(b) shows how the non-uniformity is maximally 2%.

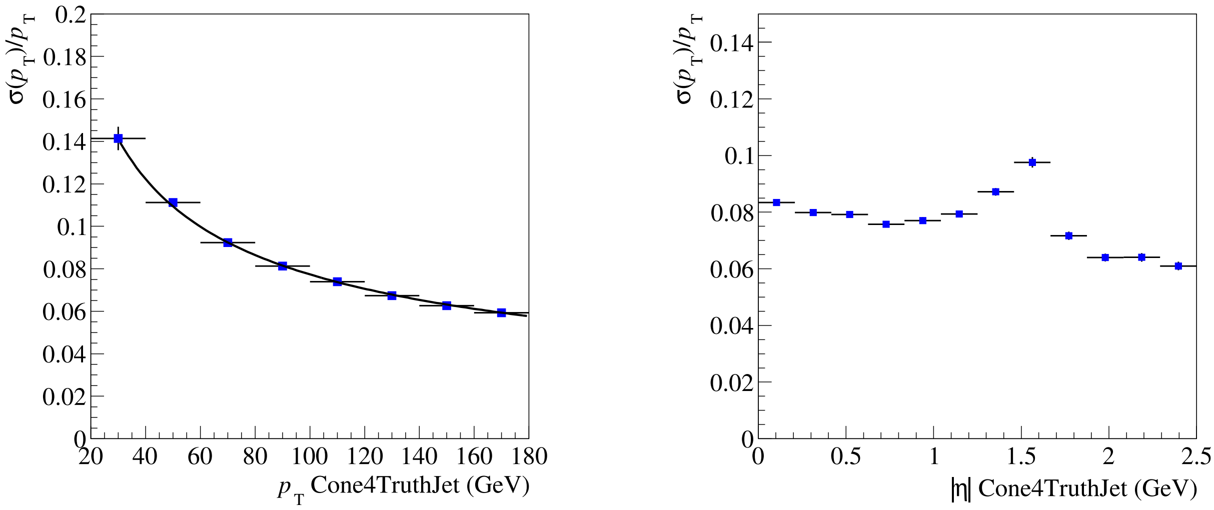

(a) p_{T} dependence.

(b) $|\eta|$ dependence

Figure 4.2: The fractional p_{T} resolution $\left(\frac{\sigma(p_{\text{T}})}{p_{\text{T}}}\right)$ of `Cone4H1TopoJets` in simulated semileptonic $t\bar{t}$ events.

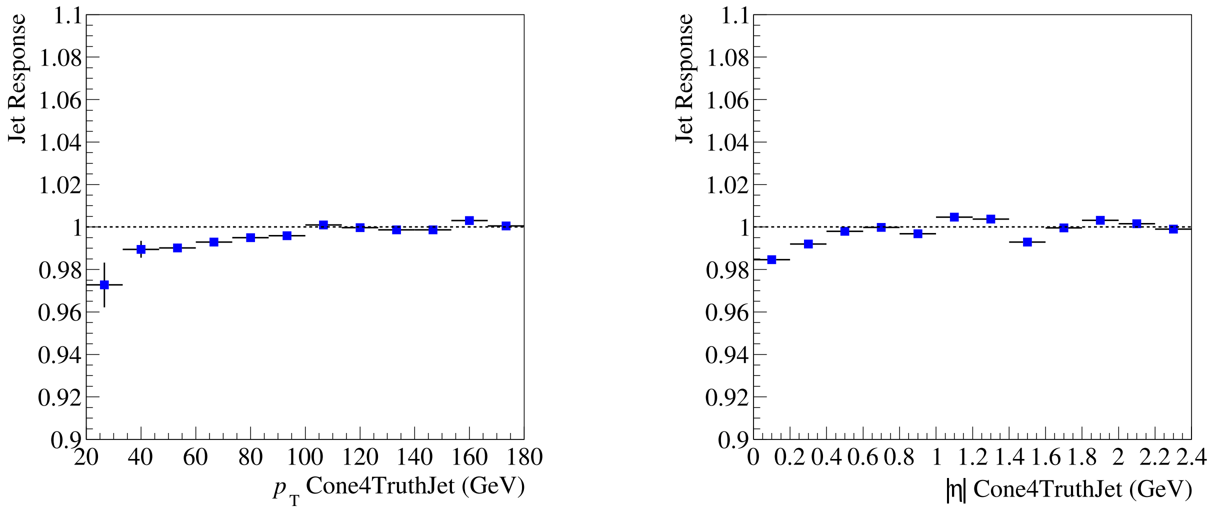

(a) p_{T} dependence.

(b) $|\eta|$ dependence

Figure 4.3: The ratio of the reconstructed p_{T} of `Cone4H1TopoJets` to the p_{T} of `Cone4TruthJets` which are matched with $\Delta R < 0.4$ in semileptonic $t\bar{t}$ events.

4.3 *b*-Tagging

Due to their relatively long lifetime, mesons or baryons containing b quarks typically travel several millimeters before they decay. This provides a very useful handle when identifying a final state. The procedure of assigning a probability to a jet that it originates from a b quark, is called *b-tagging*. The main distinguishing feature is the presence of a number of tracks pointing to a secondary vertex. Figure 4.4 shows a sketch of a jet that contains such a secondary vertex.

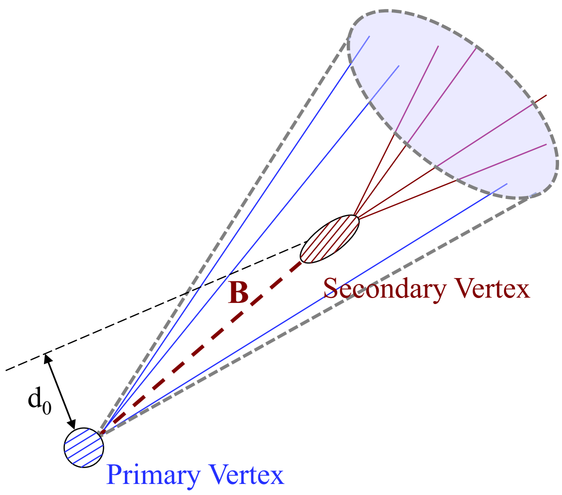

Figure 4.4: Sketch of a jet containing a secondary vertex. The distance of closest approach to the primary vertex, d_0, is indicated for one of the tracks.

Before their relevant properties are calculated, the tracks need to meet some basic quality requirements. A total of at least seven hits is required in the pixel detector and the SCT, two of which must be in the pixel detector (cf. Section 2.2.1). Only tracks within a distance

$\Delta R < 0.4$ from the jet axis and $p_{\mathrm{T}} > 1$ GeV are taken into account. The selected tracks are used for the impact parameter and secondary vertex algorithms described below.

Impact Parameters

The presence of a displaced or secondary vertex is inquired by determining the impact parameters of tracks. The transverse impact parameter d_0 is defined as the distance of closest approach in (r, φ) of the track to the primary vertex. The longitudinal impact parameter z_0 is the z coordinate of the track at this point of closest approach.

In fact, the impact parameter tagging algorithms employ the significance of the impact parameters in order to enhance the contribution of precisely measured tracks. I.e. the algorithms `IP1D`, `IP2D` and `IP3D` make use of z_0/σ_{z_0}, d_0/σ_{d_0} and a combination of them respectively. For each measured value of the significance S_i of a track, a weight W_i is defined as a likelihood ratio:

$$W_i = \frac{b(S_i)}{u(S_i)}, \tag{4.2}$$

where $b(S_i)$ and $u(S_i)$ are the distributions of the hypotheses for b- and light jets respectively. The weight of a jet is then simply defined as the combination of weights of the tracks that are associated to the jet:

$$W_{\mathrm{jet}} = \sum_{i=1}^{N_{\mathrm{tracks}}} \ln W_i. \tag{4.3}$$

Secondary Vertex Reconstruction

Apart from using the properties of individual tracks, the secondary vertex may also actually be reconstructed and provide a second handle to distinguish b-jets from light jets. As a first step in secondary vertex reconstruction, tracks are selected with sufficiently large impact parameter significances within $\Delta R < 0.4$ from the jet axis. Secondly, pairs of selected tracks that combine into a good two-track vertex inside the jet are formed. All pairs are then combined into one vertex and a vertex fit is done. In an iterative procedure, the track with the largest contribution to the χ^2 of the fit is removed until the vertex fit is accepted according to a χ^2 threshold.

The secondary vertex tagging algorithm makes use of three properties of the reconstructed vertex:

- The invariant mass of all the tracks associated to the secondary vertex, which is generally higher for b-jets than for light jets;
- The ratio of the sum of energies of the tracks associated to the vertex and the sum of energies of all tracks in the jet. Tracks associated to b-jets generally contain a larger fraction of the energy;
- The number of track pairs contained in the vertex, which is much larger in case the vertex actually corresponds to a b-jet.

Each of these properties is converted into a likelihood ratio and again the weight of a jet is the sum of the logarithms of the individual weights.

Combined Weight

A high b-tagging efficiency in association with a high light jet tagging rejection is achieved when combining the transverse and longitudinal impact parameter significances with all three secondary vertex properties. The combined weight for a jet is obtained by summing up the weights of the individual tagging algorithms described above. The resulting distributions in semileptonic $t\bar{t}$ events are shown in Figure 4.5 for b-, c- and light jets separately. All jets for which a $b(c)$ quark with is found within $\Delta R < 0.3$ with respect to the jet axis are labelled $b(c)$-jets. When no heavy flavoured quarks nor taus are found in its vicinity, a jet is labelled a light jet. Because the lifetime of hadrons which contain a c quark is relatively long as well, c-jets are less easily separated from b-jets than light jets, which is reflected by the distribution. The fraction of c-jets in $t\bar{t}$ events is however small.

Each of the hypothesis distributions that contribute to the combined weight need to be commissioned with data. Therefore initially more simple and robust tagging algorithms will be favoured. Monte Carlo studies show that a relative precision on the b-tagging efficiency of 6% is expected to be achieved with 100 pb^{-1} of data [56].

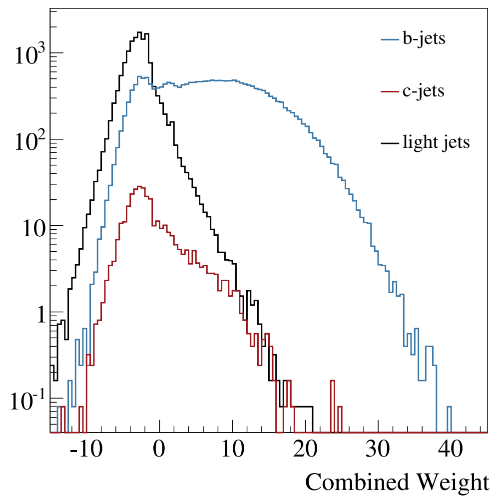

Figure 4.5: The combined weight for b-,c- and light jets with $p_T > 20$ GeV in semileptonic $t\bar{t}$ events. It contains both impact parameter and secondary vertex information.

A jet is labelled as a b-jet when it passed a certain combined weight threshold. The optimal value, i.e. the optimal balance between b-tagging efficiency and light jet tagging rejection, depends strongly on the event topology and the strategy of the analysis at hand.

4.4 Electron Identification and Reconstruction

The main purpose of the electromagnetic calorimeter is the identification and reconstruction of photons and electrons. As photons play no part in the selection criteria applied in the analyses in Chapters 6 and 7, merely the electron reconstruction is discussed here. The challenges lie in differentiating isolated electrons from those within jets and correcting for the energy losses in the material in front of the calorimeters.

The algorithm for electron reconstruction of interest here is the `egamma` algorithm [58], which is dedicated to the reconstruction of isolated electrons with high p_T. Firstly, a cluster of cells in the electromagnetic calorimeter is constructed by the *sliding window algorithm* [59]. It divides the electromagnetic calorimeter into a grid of elements of size $\Delta\eta \times \Delta\varphi = 0.025 \times 0.025$ up to $|\eta| = 2.5$. Subsequently, it slides a window of 5×5 of these elements over the grid and computes the sum of the transverse energy in the cells contained in this window. When this exceeds the threshold energy of 3 GeV, the cells qualify as a cluster, which is subsequently tested against photon and electron hypotheses.

If the resulting cluster matches a photon conversion in the inner detector, it is flagged as a photon. Otherwise, the algorithm attempts to match inner detector tracks to the cluster by extrapolating them to the calorimeter. An electron candidate is required to have an associated track within $(|\Delta\eta|, |\Delta\varphi|) < (0.05, 0.10)$ for which the momentum p is roughly compatible with the cluster energy E, i.e. $E/p < 10$.

The energy of the electron candidate is determined as a weighted average between the cluster, which is corrected for energy losses through η-dependent weight functions, and the track momentum. The charge is deduced from the curvature of the associated track. In addition, a number of variables describing the shape of the electromagnetic shower and the quality of the inner detector track are available. According to increasingly strict requirements on these properties, the reconstructed electrons are categorized into *loose*, *medium* and *tight* electrons as follows:

- **Loose electrons** are identified based on a part of the available calorimeter information only. An η dependent requirement is applied to the ratio of the E_T in the first layer of the hadronic calorimeter to the E_T of the entire cluster. The shower shape is estimated from the middle layer of the electromagnetic calorimeter only. The corresponding identification efficiency is very high at the expense of very low background rejection.

- For **medium electrons**, the quality of the inner detector track is held to higher standards; at least one hit is found in the pixel detector, the total number of hits in the pixel detector and the SCT is larger than nine and the transverse impact parameter satisfies $|d_0| < 5$ mm. In addition, double maxima in the first layer of the electromagnetic calorimeter are rejected in order to minimize contributions from $\pi^0 \to \gamma\gamma$ decays.

- **Tight electrons** are required to be isolated, i.e. the ratio of transverse energy in a cone $\Delta R < 0.2$ to the total cluster energy is limited. The track matching to the cluster is more strict, i.e. $(\Delta\eta, \Delta\varphi) < (0.005, 0.02)$ is required. In addition, a minimum is applied to the ratio of the number of transition radiation hits that exceed the high threshold to the total number of TRT hits. The requirement on the transverse impact parameter is tightened to $|d_0| < 1$ mm.

Table 4.2 shows the corresponding jet rejection rates based on a Monte Carlo sample containing di-jet events, prompt photon production and W/Z events [56]. An E_T threshold of 17 GeV is applied on the electron candidates.

Figure 4.6 shows the p_T and η dependence of the electron reconstruction efficiency in simulated semileptonic $t\bar{t}$ events for loose, medium and tight electrons. Only events in

Category	Jet Rejection
Loose	567 ± 1
Medium	2184 ± 13
Tight	$(9.8 \pm 0.4) \cdot 10^4$

Table 4.2: The expected jet rejection rates for loose, medium and tight electron definitions [56]. The jet rejection rate is defined as the ratio of the number of Cone4TruthJets to the number of electrons that are reconstructed within $\Delta R < 0.4$ from Cone4TruthJets. The numbers are taken from [56].

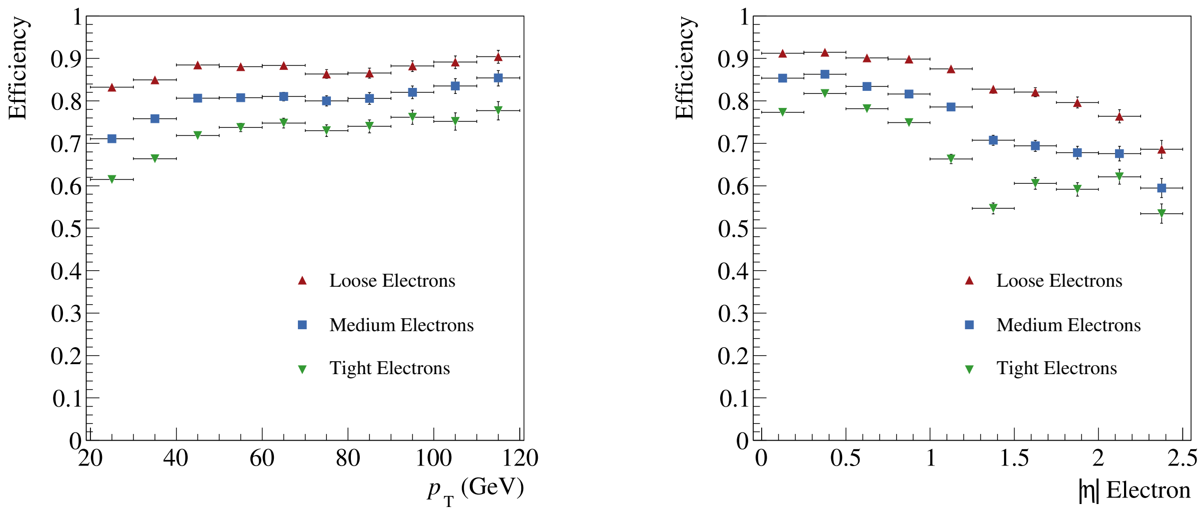

(a) p_{T} dependence (b) $|\eta|$ dependence

Figure 4.6: The expected reconstruction efficiency for loose, medium and tight electrons in simulated semileptonic $t\bar{t}$ events. No trigger chain requirement is applied.

which one of the W bosons decays into an electron and a neutrino are considered and the reconstructed electron is matched to that electron when $\Delta R < 0.05$. The reconstruction efficiency for electrons with $p_{\mathrm{T}} > 60$ GeV is better than 75 % for tight electrons and close to 90 % for loose electrons. Note that these numbers are limited by detector geometry inefficiencies. The impact of the barrel/endcap transition in the electromagnetic calorimeter is clearly reflected in Figure 4.6(b) by the drop in efficiency around $|\eta| = 1.4$. In addition, the increase of material in the inner detector with $|\eta|$ impacts the tracking efficiency as electrons suffer increasingly from Bremsstrahlung effects. The expected reconstruction efficiencies in semileptonic $t\bar{t}$ events are approximately 5% lower than in the clean environment of $Z \to ee$ events [60].

In the following, the medium reconstruction algorithm is used, considering the good jet rejection and electron reconstruction efficiency.

The fractional energy resolution for medium electrons in $t\bar{t}$ events is displayed in Figure

4.7. The resolution is better than 2% for electrons that satisfy $E > 20$ GeV and it improves with increasing energy. The curve corresponds to the best fit of the function

$$\frac{\sigma(E)}{E} = \frac{a}{\sqrt{E}} \oplus b, \tag{4.4}$$

where $a = 0.051$ and $b = 0.016$. Figure 4.7(b) shows how the electron reconstruction is affected by the barrel/endcap transition in the electromagnetic calorimeter.

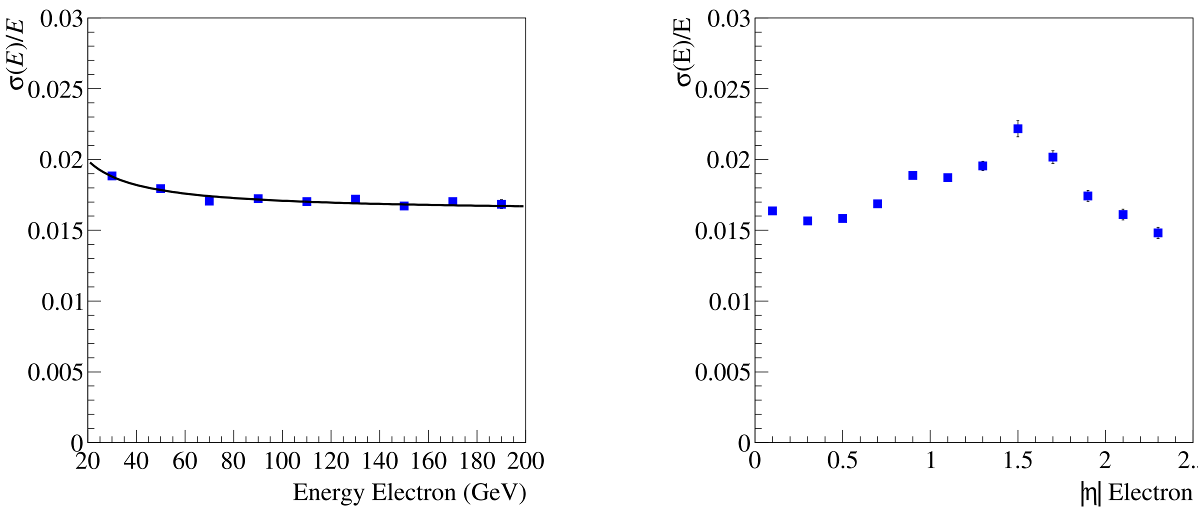

(a) Energy dependence.

(b) $|\eta|$ dependence

Figure 4.7: The fractional energy resolution ($\frac{\sigma(E)}{E}$) of medium electrons in simulated semileptonic $t\bar{t}$ events.

4.5 Muon Identification and Reconstruction

The muon spectrometer was designed exclusively for the detection and reconstruction of muons. Information from the inner detector and calorimeters can be used to complement measurements in the spectrometer for a higher precision. The basic approach where reconstructed tracks in the muon spectrometer are extrapolated to the beam line results in *standalone* muons. *Combined* muons are obtained by matching standalone muons to inner detector tracks and refitting the combination. By starting from inner detector tracks and matching the extrapolated track with raw information from the spectrometer, *tagged* muons are found.

Several algorithms are available in the ATLAS software, yet the focus will be on those relevant to the analyses in Chapters 6 and 7.

Standalone Muons

The algorithm used for track reconstruction in the muon spectrometer is `Muonboy` [61]. It starts by defining a region of activity of size $\Delta\eta \times \Delta\varphi = 0.4 \times 0.4$ around each RPC or TGC hit. A track *segment* is build by performing a straight line fit to the 4 to 8 hits in each individual muon station that intersects with the region of activity. Figure 4.8 shows an example of a reconstructed track segment in a muon station with seven MDT hits and five associated RPC hits. These track segments are used as seeds for a global track finding

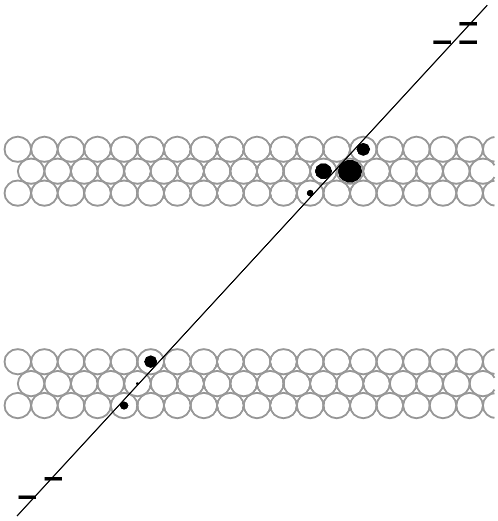

Figure 4.8: The two multilayers of a MDT chamber, indicating seven hits in the tubes, five RPC hits and the resulting track segment.

algorithm. Each resulting track candidate, containing a minimum of two segments, is then fitted using all the drift time measurements instead of the segments. Finally, the selection of reconstructed standalone muon tracks is based on the χ^2 of this last global fit and the tracks are extrapolated to the beam line, correcting the momentum for the energy loss in the material in front of the muon spectrometer. A parametrization of this material traversed by muons as well as the magnetic field strength at every given space point and alignment corrections to chamber positions are accounted for in the detector geometry description.

The momentum is determined from the bending radius of the muon trajectory due to the magnetic field. This is expressed in terms of the *sagitta*: the distance from the middle track segment to the straight line that connects the outer segment to the inner.

Combined Muons

`Staco` [61] is the algorithm that combines inner detector tracks with standalone `Muonboy` tracks. The track parameter vectors are combined for pairs of tracks with a reasonable matching in (η, φ). When several combinations are possible, the pair with the best χ^2 qualifies as combined muon.

Combining the information of the inner detector and the muon spectrometer naturally results in a better estimation of the track parameters and a higher rejection of background muons. It turns out that the momentum resolution improves compared to that of standalone muons and the improvement is largest in the low p_{T} regime. However, this procedure is more sensitive to the relative alignment of the inner detector and the muon spectrometer and to the parametrization of the material in between. The coverage is limited by the inner detector acceptance to the range $|\eta| < 2.5$.

Performance

Figure 4.9 shows the expected efficiency for combined reconstruction of muons in simulated semileptonic $t\bar{t}$ events and its dependence on η, φ and p_{T}. Muons are evidently lost in the gap for services at $\eta \approx 0$ (cf. Section 2.2.3). Likewise, the limited coverage of the muon spectrometer and the limited bending power of the magnetic field in the barrel/endcap transition region severely impact the efficiency of the reconstruction. Figure 4.9(c) shows that around $\varphi \approx -\frac{9}{24}\pi$ and $\varphi \approx -\frac{15}{24}\pi$ the efficiency is affected by the support feet of the toroidal magnet system. All such areas with limited coverage of the muon spectrometer are visualized in Figure 4.9(d), which shows all muons from the leptonically decaying top quark which are not reconstructed. In regions that suffer from limited coverage, muons can be recovered by including tagged muons, yet these are generally muons with low momenta ($p_{\mathrm{T}} < 6$ GeV) and fake muons are introduced this way. In the analyses in the following chapters, the muons of interest satisfy $p_{\mathrm{T}} > 20$ GeV and the rejection of fake muons is crucial. Figure 4.9(a) shows that the overall efficiency for combined reconstruction without tagged muons is still better than 92% for muons with $p_{\mathrm{T}} > 20$ GeV.

Figure 4.10 shows the expected transverse momentum resolution dependence on p_{T} and $|\eta|$ for combined muons. Reconstructed muons are matched to the muon from the leptonically decaying W boson when $\Delta R < 0.05$. Overall, the transverse momentum resolution for combined muon reconstruction is better than 3.5%. The resolution in the barrel/endcap transition region, $1.1 < |\eta| < 1.7$, is affected by two effects: the limited chamber coverage due to missing stations (cf. Section 2.2.3) and the limited bending power of the magnetic field (cf. Section 2.2.4).

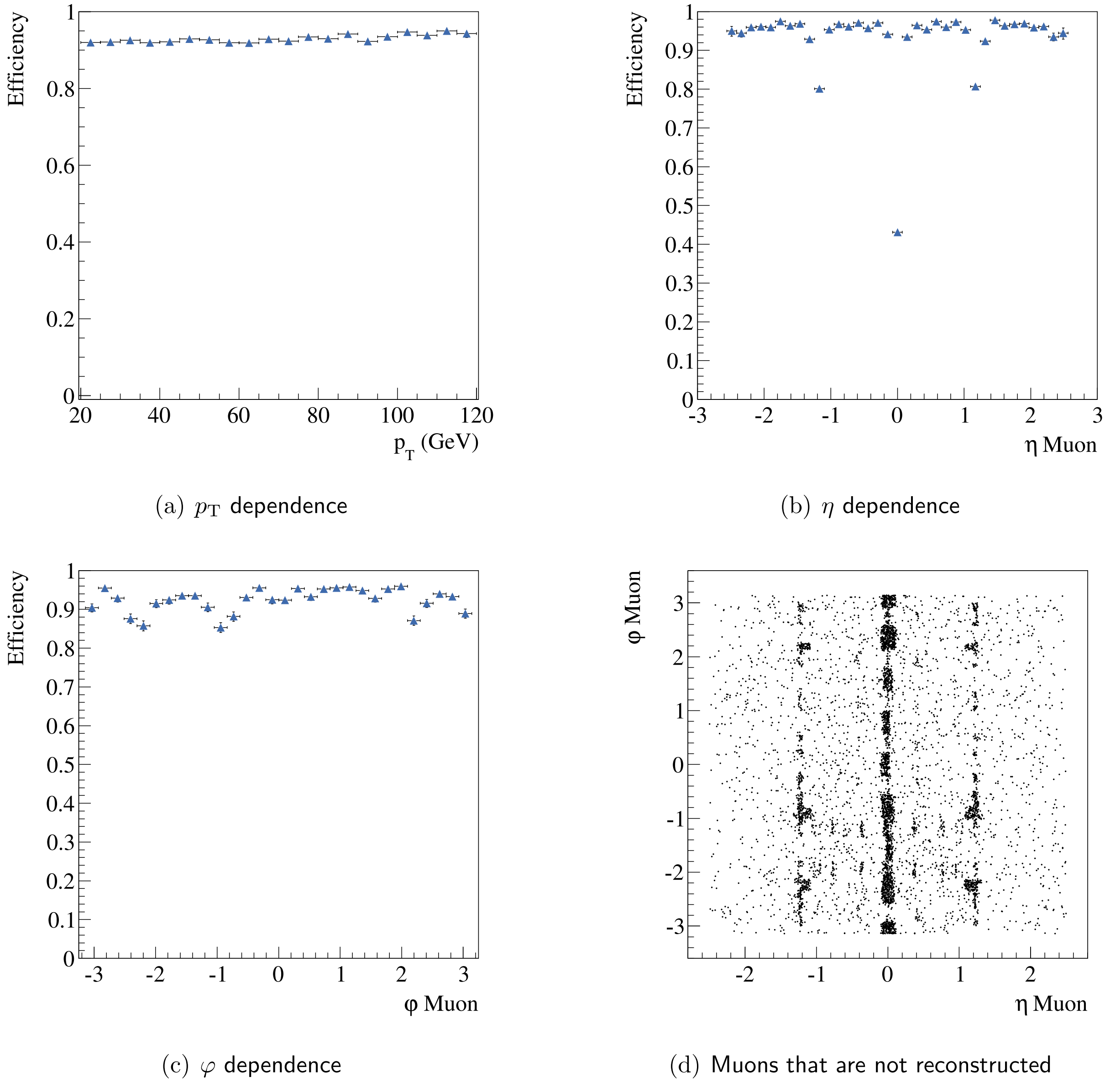

Figure 4.9: The expected reconstruction efficiency for combined muons in simulated semileptonic $t\bar{t}$ events. No trigger chain requirement is applied.

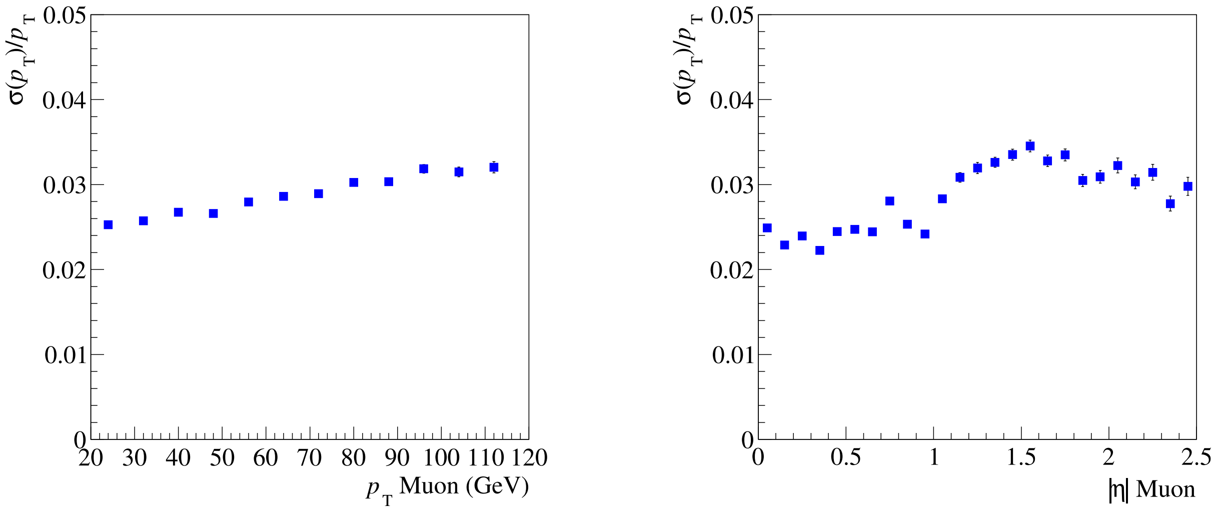

(a) p_{T} dependence. (b) $|\eta|$ dependence.

Figure 4.10: Expected fractional momentum resolution for combined muon reconstruction in simulated semileptonic $t\bar{t}$ events.

4.6 Reconstruction of Missing Transverse Energy

Finally, the missing transverse energy is the most challenging quantity to reconstruct. If all energy deposits in the detector are measured and calibrated correctly, their sum in the transverse plane should be balanced out by a vector that corresponds to the transverse momenta of all noninteracting particles that were produced. The algorithm that calculates the missing transverse energy sums up all the contributions to the x and y components of this vector, i.e. E_x^{Final} and E_y^{Final} respectively.

$$\not{E}_{x,y}^{\mathrm{Final}} = \not{E}_{x,y}^{\mathrm{Calo}} + \not{E}_{x,y}^{\mathrm{MuonBoy}} + \not{E}_{x,y}^{\mathrm{Cryo}}, \tag{4.5}$$

where

$$\not{E}_{x,y}^{\mathrm{Calo}} = -\sum_{\mathrm{TopoCells}} E_{x,y}, \tag{4.6}$$

$$\not{E}_{x,y}^{\mathrm{MuonBoy}} = -\sum_{\mathrm{muons}} E_{x,y} \tag{4.7}$$

$$\not{E}_{x,y}^{\mathrm{Cryo}} = -\sum_{\mathrm{jets}} w^{\mathrm{Cryo}} \sqrt{E_{x,y}^{\mathrm{EM3}} \cdot E_{x,y}^{\mathrm{HAD}}}. \tag{4.8}$$

In order to suppress noise, only calorimeter cells that are associated to a TopoCluster contribute to $\not{E}_{x,y}^{\mathrm{Calo}}$ (cf. Section 4.2).

Because the first term in (4.5) accounts for the energy deposits from muons in the calorimeter, the momenta of muons as measured by the muon spectrometer only are used in the second term. The sum over muons runs over combined muons in the region $|\eta| <$

2.5, i.e. muons in the muon spectrometer with a matched track in the inner detector, and over `Muonboy` standalone muons in the region $2.5 < |\eta| < 2.7$ (cf. Section 4.5). The last term in (4.5) recovers the energy loss in the inactive material of the cryostat (cf. Section 2.2.2) by making use of the relation between energy deposits in the last layer of the electromagnetic calorimeter, $E_{x,y}^{\mathrm{EM3}}$, and in the first layer of the hadronic calorimeter, $E_{x,y}^{\mathrm{HAD}}$. The corresponding calibration weight is denoted w^{Cryo} and adopts values of typically 0.5 [62].

Refined Missing Transverse Energy

The calculation can be refined by calibrating each contribution to $\not{E}_{x,y}^{\mathrm{Calo}}$ according to the reconstructed object to which it is assigned. The assignment is done in the following order: electrons, photons, muons, hadronically decaying taus, b-jets, light jets.
Thus the components of the refined missing transverse energy become

$$\not{E}_{x,y}^{\mathrm{RefFinal}} = \not{E}_{x,y}^{\mathrm{RefCalo}} + \not{E}_{x,y}^{\mathrm{MuonBoy}} + \not{E}_{x,y}^{\mathrm{Cryo}}, \tag{4.9}$$

where

$$\not{E}_{x,y}^{\mathrm{RefCalo}} = \not{E}_{x,y}^{\mathrm{RefEle}} + \not{E}_{x,y}^{\mathrm{RefGamma}} + \not{E}_{x,y}^{\mathrm{RefTau}} + \not{E}_{x,y}^{\mathrm{RefJet}} + \not{E}_{x,y}^{\mathrm{RefMuon}} + \not{E}_{x,y}^{\mathrm{CellOut}} \tag{4.10}$$

and each term in the latter expression is calculated as the negative sum of calibrated cells inside a specific object. All calorimeter cells from TopoClusters that were not assigned to any reconstructed object are accounted for in $\not{E}_{x,y}^{\mathrm{CellOut}}$ and are calibrated according to the H1 calibration scheme (cf. Section 4.2).

To prevent the energy from isolated muons being double counted, i.e. in the muon spectrometer as well as in the calorimeter, only non-isolated muons contribute to the term $\not{E}_{x,y}^{\mathrm{RefMuon}}$.

Subsequently, the scalar quantity $\not{E}_{\mathrm{T}}^{\mathrm{RefFinal}}$ is obtained by taking the length of the vector and from now on referred to as $\not{E}_{\mathrm{T}}$:

$$\begin{aligned} \not{E}_{\mathrm{T}}^{\mathrm{RefFinal}} &= \sqrt{(\not{E}_{x}^{\mathrm{RefFinal}})^2 + (\not{E}_{y}^{\mathrm{RefFinal}})^2} \\ &\equiv \not{E}_{\mathrm{T}}. \end{aligned} \tag{4.11}$$

Equivalently, the vector $\boldsymbol{\not{E}}_{\mathrm{T}}$ is given by

$$\boldsymbol{\not{E}}_{\mathrm{T}} = \left(\not{E}_x, \not{E}_y\right) = \left(\not{E}_x^{\mathrm{RefFinal}}, \not{E}_y^{\mathrm{RefFinal}}\right) \tag{4.12}$$

and the azimuthal angle in the transverse plane is

$$\varphi(\not{E}_{\mathrm{T}}) = \arctan\left(\frac{\not{E}_y}{\not{E}_x}\right). \tag{4.13}$$

The performance of the $\boldsymbol{\not{E}}_{\mathrm{T}}$ reconstruction in $t\bar{t}$ events is discussed in detail in Chapter 6.

The Total Transverse Energy

The final concept related to $\not{E}_{\mathrm{T}}$ that needs to be defined is the total transverse energy, $\sum E_{\mathrm{T}}$. It is a measure for the total energy deposit in the calorimeter and it is calculated as the scalar sum of the transverse energy of all TopoCells,

$$\sum E_{\mathrm{T}} = \sum_{\text{TopoCells}} E_{\mathrm{T}}, \tag{4.14}$$

where the object dependent calibration is applied to the TopoCells. A similar quantity can be defined for muons, i.e.

$$\sum E_{\mathrm{T}}^{\text{MuonBoy}} = \sum_{\text{muons}} E_{\mathrm{T}}, \tag{4.15}$$

where the sum runs over all `MuonBoy` standalone muons reconstructed in the muon spectrometer.

4.7 Discussion

The expected performance of the reconstruction of physics objects in semileptonic $t\bar{t}$ events was presented. The overall performance is very good, albeit slightly limited by inevitable gaps for services in some regions of the ATLAS detector. This is reflected both by the efficiencies and by the momentum or energy resolutions of the reconstructed objects. Moreover, the busy environment of $t\bar{t}$ events provides an additional challenge when identifying and reconstructing final state objects.

This is illustrated in Figure 4.11, which shows the reconstruction efficiency of medium electrons and combined muons as a function of the number of reconstructed jets with $p_{\mathrm{T}} > 20$ GeV. The electron (muon) is matched to the electron (muon) from the leptonically decaying top quark with $\Delta R < 0.05$. The reconstruction of electrons clearly suffers from large activity in the calorimeters. The reconstruction of muons is less affected by the presence of jets as a result of the absorption of hadronic showers in the calorimeters before reaching the muon spectrometer.

Due to its dependence on all reconstructed objects in an event, the $\not{E}_{\mathrm{T}}$ is most sensitive to the presence of a large number of final state objects. This is addressed in Chapter 6.

Altogether, the heavy demands on the detector performance described in Chapter 2 are fulfilled.

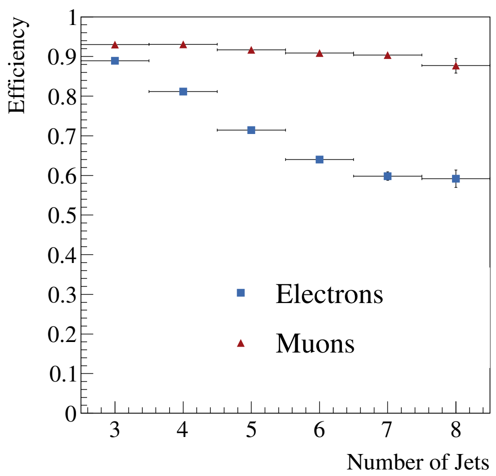

Figure 4.11: The reconstruction efficiency for medium electrons and combined muons versus the number of reconstructed jets in simulated semileptonic $t\bar{t}$ events.

5

Top Quark Pair Selection

At proton collisions of 10 TeV center of mass energy and initial luminosity of $L = 10^{31}\ \mathrm{cm}^{-2}\mathrm{s}^{-1}$, hundreds of top quark pairs will be created in the ATLAS detector per day. The abundance together with the complexity of the final state make top quark pair events an excellent benchmark on the road to searches for physics beyond the Standard Model. This chapter describes the strategy to select these events. The procedure is illustrated by means of the samples of simulated events as introduced in Section 3.3.1. The characteristics of top quark pair events are discussed in Section 5.1, Section 5.2 describes each step in the selection process, Section 5.3 shows the distributions of the relevant kinematic variables and Section 5.4 contains the resulting selection efficiencies for signal as well as background samples.

5.1 Semileptonic Decays

As described in Section 3.3.1, the branching ratio of semileptonic $t\bar{t}$ decays is 43.8 %. Due to the presence of the charged lepton and the neutrino, semileptonic decays render a distinct signature in the ATLAS detector which makes them suitable to fire triggers and to be distinguished from other events by requiring certain properties of the final state. They are favoured over dileptonic decays when studying missing transverse energy (cf. Chapter 6) as the presence of an additional neutrino in the latter type of events prevents the association between the missing transverse energy and the p_{T} of the neutrino.

Each of the three lepton flavours is equally represented, yet taus are difficult to identify and reconstruct. Moreover, they often render additional neutrinos in the final state, which complicate the kinematics. Therefore only the muon and the electron channel of the W boson decay are pursued here. In order to efficiently select these 29% of all $t\bar{t}$ decays and to reject background events, a set of selection criteria is applied. First, the characteristics of semileptonic $t\bar{t}$ events are outlined.

The final state of semileptonic $t\bar{t}$ decays contain a high multiplicity and variety of reconstructed objects. This specific signature contributes to the possibility to distinguish them from other processes that occur in proton-proton collisions. The main characteristics of semileptonic $t\bar{t}$ events are the presence of a single charged high-p_{T} isolated lepton, large

$\not\!\!E_{\mathrm{T}}$ due to the corresponding neutrino that escapes detection and at least four jets, two of which originate from b quarks. The kinematic variables on which the event selection criteria are based are shown here for semileptonic $t\bar{t}$ events. The distributions correspond to an integrated luminosity of 200 pb^{-1} and the W boson decays either through the electron or through the muon channel. None of the event selection criteria are applied yet.

Figure 5.1(a) shows the normalized η distribution of the electron or muon from the leptonically decaying top quark. The majority of the leptons is produced quite centrally due to the large transverse momentum of the top quark. The η distributions of the reconstructed electron and muon are shown here as well and reflect the limited inner detector coverage in the very forward region, the gap in the muon spectrometer at $\eta \approx 0$ and the barrel/endcap transition region in the calorimeters. For the reconstructed electron or muon with the highest p_{T}, the corresponding p_T distribution is displayed in Figure 5.1(b). The normalized distribution for $\not\!\!E_{\mathrm{T}}$ in semileptonic $t\bar{t}$ events is shown here as well.

Figure 5.1(c) displays the number of reconstructed jets satisfying $p_{\mathrm{T}} > 20$ GeV. Figure 5.1(d) shows the p_{T} distributions of the four highest p_{T} jets. These characteristics can now be used to select semileptonic $t\bar{t}$ events.

5.2 Event Selection

The aim is to obtain a sample of events that is rich in semileptonic $t\bar{t}$ events and simultaneously contains a limited number of background events. As described in Section 3.3, the predominant backgrounds are W production with associated jets, multi-jet events and single top production. The cross sections of the first two are much larger than that of the signal, yet fortunately the experimental signature is only similar in a fraction of the events and the following selection criteria reduce their contribution significantly.

- **The trigger requirement:** The event passed the trigger chain `e20_loose` in case of the electron selection channel and `mu10` in case of the muon selection channel (cf. Section 4.1);

- **The lepton requirement:** The presence of exactly one well reconstructed muon or electron satisfying $p_{\mathrm{T}} > 20$ GeV and $|\eta| < 2.5$ is required. To guarantee the quality of the reconstruction, additional requirements are introduced in Section 5.2.2;

- **The missing transverse energy requirement:** $\not\!\!E_{\mathrm{T}} > 20$ GeV;

- **The jets requirement:** At least four jets are reconstructed with $p_{\mathrm{T}} > 20$ GeV and $|\eta| < 2.5$, three of which satisfy $p_{\mathrm{T}} > 40$ GeV.

Sections 5.2.1 through 5.2.4 describe each of the selection criteria in detail and contain the expected distributions for signal and background events. The event samples and applied filters are described in Section 3.2 and the corresponding cross sections are listed in Table 3.1. The studies performed here are all based on Monte Carlo simulations corresponding to collisions of 10 TeV center of mass energy.

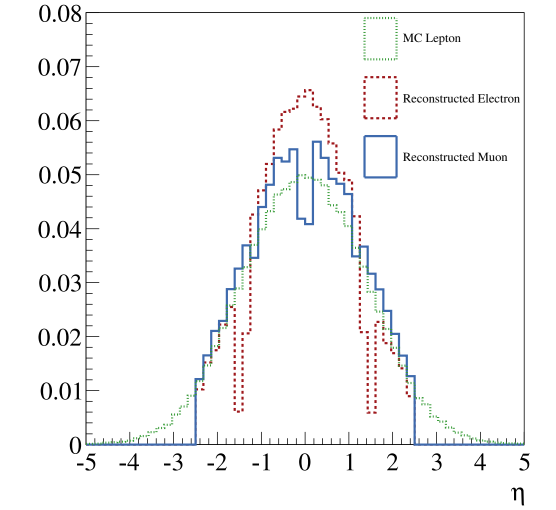

(a) The normalized η distribution of the electron or muon from the leptonically decaying top quark (MC) as well as the normalized η distributions of the reconstructed electron and the reconstructed muon that satisfy the requirements of Section 5.2.2.

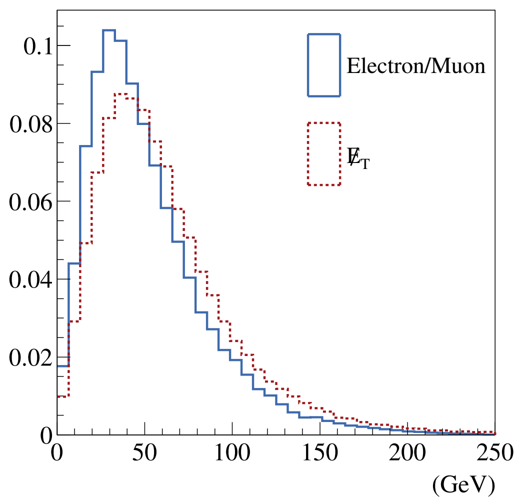

(b) The normalized distribution of the p_T of the reconstructed electron or muon and the normalized distribution of the missing transverse energy.

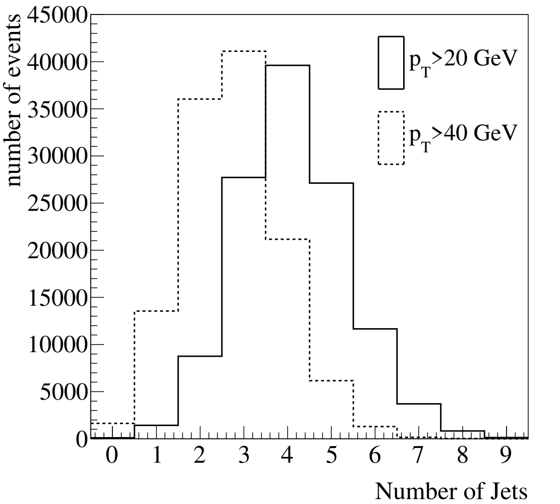

(c) The number of jets with $p_T > 20$ GeV (full) and with $p_T > 40$ GeV (dashed) per semileptonic $t\bar{t}$ decay.

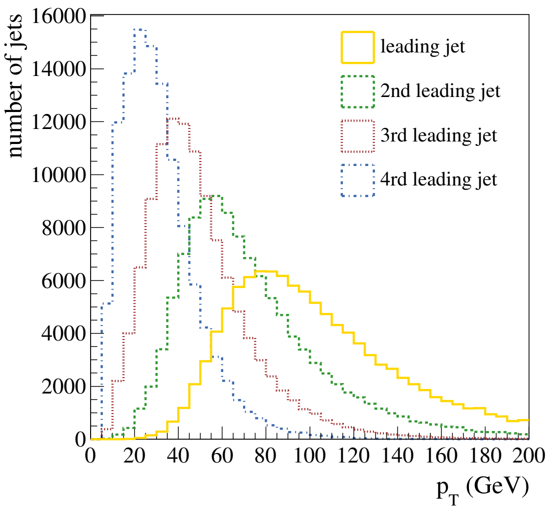

(d) The p_T distributions of the leading four jets in semileptonic $t\bar{t}$ events.

Figure 5.1: Characteristics of simulated semileptonic $t\bar{t}$ events. No selection criteria are applied yet.

5.2.1 The Trigger Requirement

The lepton trigger requirement is essential to reject the enormous number of multi-jet events that are produced in collisions and to allow for a pre-selection with high efficiency. The subsequent selection criteria are indispensable for the purity of the sample, yet without a suitable trigger, signal events would be lost either because of the trigger requirement or because of an inevitable prescale. Figure 5.2(a) shows the p_{T} distribution of the highest-p_{T} reconstructed electron in each event and illustrates that this provides a strong handle on the rejection of multi-jet events. The impact of the trigger requirement `e20_loose` on this distribution is shown in Figure 5.2(b) The structure in the distribution at low values of p_{T} in Figure 5.2(b) is explained as follows: An electron candidate may be accepted by the `e20_loose` trigger algorithm albeit not reconstructed by the more stringent medium electron algorithm afterwards. The latter algorithm may however find another medium electron at lower p_{T} in the event.

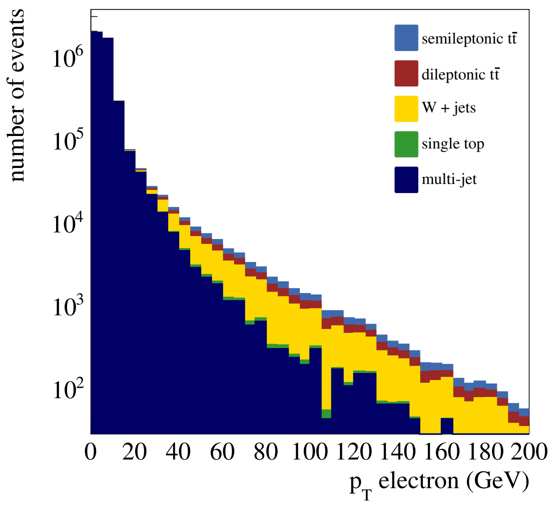

(a) The cumulative p_{T} distributions of the highest-p_{T} reconstructed electron in each event.

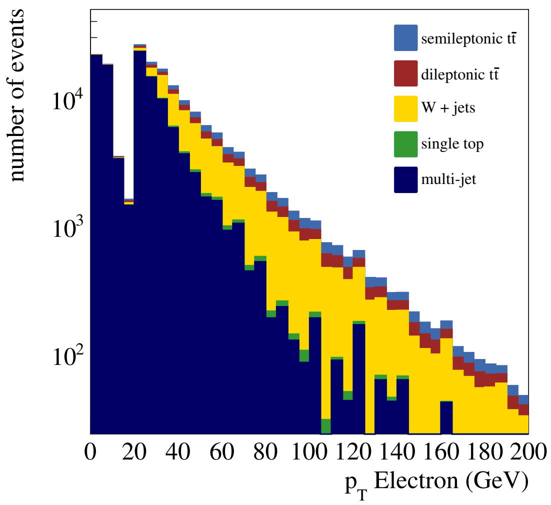

(b) The cumulative p_{T} distributions of the highest-p_{T} reconstructed electron in each event that passes the trigger chain `e20_loose`.

Figure 5.2: The impact of the electron trigger requirement on the number of events in 200 pb^{-1}.

5.2.2 The Lepton Requirement

Multi-jet events will generally not contain an isolated charged lepton in their final state and muons from jet fragmentation will usually not reach the muon spectrometer. In multi-jet events that do pass the lepton requirement, a jet is mis-identified as an electron or muon. Often, these mis-identifications are accompanied by hadronic activity, which is quantified by means of the $E_{\mathrm{T}}^{\mathrm{cone20}}$ variable, i.e. the E_{T} in a cone of radius $\Delta R = 0.2$ centered around the lepton, excluding the E_{T} of the reconstructed lepton itself. Figure 5.3(a) shows the distributions of $E_{\mathrm{T}}^{\mathrm{cone20}}$ for the reconstructed medium electrons that satisfy $p_{\mathrm{T}} > 20$ GeV and $|\eta| < 2.5$ in multi-jet events compared to those in $t\bar{t}$ events which are matched to the electron from the leptonically decaying top quark with $\Delta R < 0.05$. Figure 5.3(b) shows the distribution of $E_{\mathrm{T}}^{\mathrm{cone20}}$ for the reconstructed combined muons that satisfy $p_{\mathrm{T}} > 20$ GeV and $|\eta| < 2.5$ in multi-jet events compared to those in $t\bar{t}$ events, which are matched to the muon from the leptonically decaying top quark with $\Delta R < 0.05$. The falsely identified leptons are generally associated to jets and therefore less isolated.

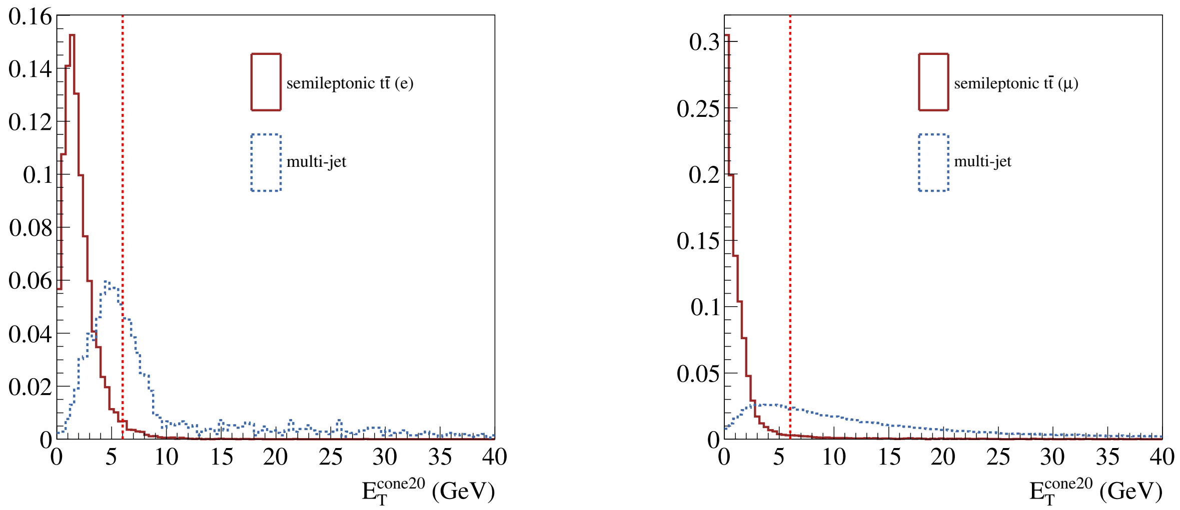

(a) Medium electrons with $p_{\mathrm{T}} > 20$ GeV and $|\eta|$ <2.5.

(b) Combined muons with $p_{\mathrm{T}} > 20$ GeV and $|\eta|$ <2.5.

Figure 5.3: The isolation of charged leptons, $E_{\mathrm{T}}^{\mathrm{cone20}}$, in multi-jet events (dashed) compared to semileptonic $t\bar{t}$ events (full). The vertical lines indicate the selection requirement $E_{\mathrm{T}}^{\mathrm{cone20}} < 6$ GeV and the distributions are normalized to unity.

The number of falsely identified electrons and muons is reduced by demanding the following additional qualities:

Electrons

- The electron is classified as medium according to the `egamma` algorithm (cf. Section 4.4);
- The medium electron satisfies $p_{\mathrm{T}} > 20$ GeV;
- The electron is required to be isolated, i.e. $E_{\mathrm{T}}^{\mathrm{cone20}} < 6$ GeV;
- $|\eta| \notin [1.35, 1.57]$ to avoid electrons in the transition regions between the barrel and endcaps of the electromagnetic calorimeter for which the energy measurement is less reliable (cf. Figure 4.7). Simultaneously, the enhanced contribution from fake electrons in this region is eliminated.

Muons

- The muons considered here are combined muons as reconstructed by the `Staco` algorithm (cf. Section 4.5);
- The combined muon satisfies $p_{\mathrm{T}} > 20$ GeV;
- The muon is required to be isolated, i.e. $E_{\mathrm{T}}^{\mathrm{cone20}} < 6$ GeV.

The rate at which these high quality electrons or muons are falsely reconstructed in multi-jet events is expected to be about $5 \cdot 10^{-4}$ per jet [63], yet the large uncertainty on the cross section of multi-jet events complicates the prediction on the number of events that enter the data sample.

The effect of the lepton requirement on the contribution of background events is illustrated by Figure 5.4(a), which shows the transverse momentum of the highest-p_{T} muon in events that passed the `mu10` trigger chain. Recall that the sample of multi-jet events is generated such that they already passed the `top_mu` filter (cf. Section 3.3). Nevertheless, before the lepton requirement is applied, their contribution is enormous and a multiplication by 10^{-3} is applied to the multi-jet distribution in Figure 5.4(a) for the other distributions to be visible. The requirement that a muon or electron be reconstructed, which satisfies the restrictions described here as well as $p_{\mathrm{T}} > 20$ GeV, contributes strongly to the reduction of multi-jet events in addition to the impact of the trigger requirement.

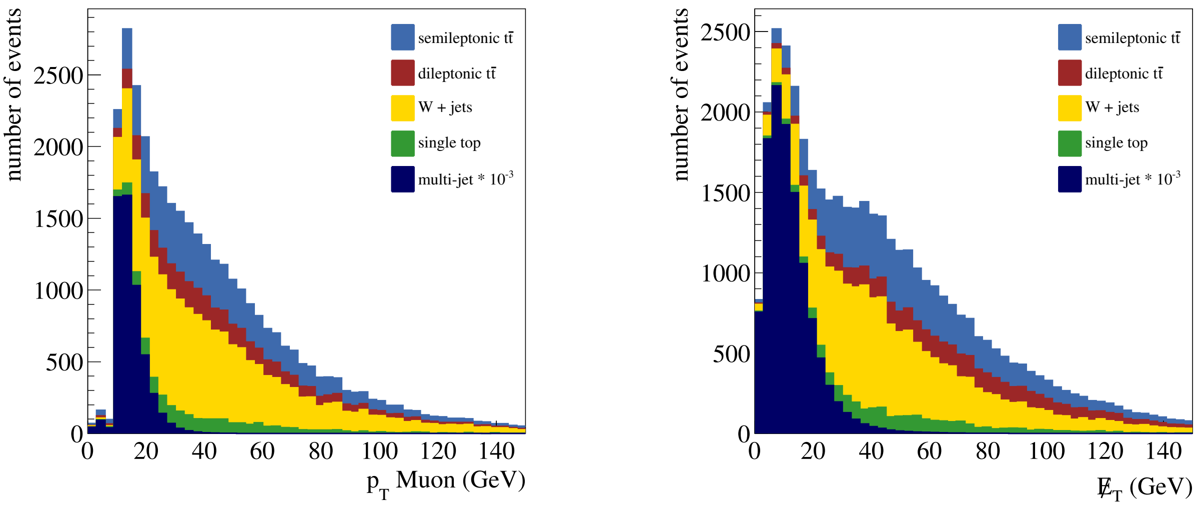

(a) Distribution of the p_{T} of the highest-p_{T} muon.

(b) Distribution of $\not{E}_{\mathrm{T}}$.

Figure 5.4: Cumulative distributions of the p_{T} of the muon and of the $\not{E}_{\mathrm{T}}$ for events that pass the trigger chain `mu10`. The number of events corresponds to 200 pb^{-1}, except for the contribution of multi-jet events, which has been multiplied by 10^{-3} for cosmetic reasons.

5.2.3 The Missing Transverse Energy Requirement

The $\not\!\!E_{\mathrm{T}}$ criterion is applied to the refined missing transverse energy as defined in (4.9). Multi-jet events hardly contain any real missing transverse energy as there are no high-p_{T} neutrinos present in their decays. Leptonic decays of B hadrons in jets actually are accompanied by neutrinos, yet their momenta are generally low. Unfortunately, the mis-identification of jets as leptons, which allows some events to pass the lepton requirement, often results in a mis-reconstruction of the missing transverse energy. Moreover, detector and reconstruction imperfections generally add to nonzero values of $\not\!\!E_{\mathrm{T}}$, which may exceed the 20 GeV requirement.

The distribution of $\not\!\!E_{\mathrm{T}}$ is shown in Figure 5.4(b). The selection requirement, $\not\!\!E_{\mathrm{T}} >$ 20 GeV, mainly impacts the contribution of multi-jet events, which is scaled by 10^{-3} in the figure. The $W+$ jets background events do contain actual missing transverse energy when the W boson decays leptonically, as do the leptonic single top events.

5.2.4 The Jets Requirement

Jets are reconstructed using the `Cone4H1TopoJets` algorithm (cf. Section 4.2), i.e. their constituents are H1 calibrated TopoClusters and their cone size is $R_{\mathrm{cone}} = 0.4$. Due to their energy deposit in the calorimeter, electrons generally classify as jet candidates as well. Therefore, jets within $\Delta R < 0.2$ from reconstructed electrons that satisfy the requirements of Section 5.2.2 are not taken into account.

In semileptonic $t\bar{t}$ events, four jets are naively expected to enter the detector, two resulting from the b quarks and another two from the quarks from the hadronically decaying W boson. However, initial state radiation (ISR) and final state radiation (FSR) often result in additional jets. At the same time, not all jets are identified as such and the number of expected reconstructed jets actually varies between zero and ten, as shown in Figure 5.1(c). Nevertheless, in order to reject background events, at least four reconstructed jets with $p_{\mathrm{T}} > 20$ GeV are required in the event selection. The distributions of the number of jets per event are shown in Figure 5.5(a). The requirement that this number exceeds three severely reduces the contribution of multi-jet events and $W+$ jets events. The p_{T} distribution of the hardest jet is shown in Figure 5.5(b). Again, the multi-jet contribution is scaled by a factor 10^{-3} in the figures.

5.3 Kinematic Distributions

In this section, the final impact of each of the event selection criteria on the signal to background ratio is illustrated. The Monte Carlo samples and the corresponding cross sections are listed in Table 3.1. The distributions correspond to 200 pb^{-1} integrated luminosity and contain the events that pass all event selection criteria except for the one of interest. The electron selection channel and muon selection channel selection are treated separately in Figures 5.6 and 5.7 respectively. The selection criterion that is applied to the displayed variable is indicated by a dashed line in each histogram.

Figures 5.6(a) and 5.7(a) show the p_{T} distributions of the highest-p_{T} electron and muon in events that pass the trigger, the $\not\!\!E_{\mathrm{T}}$ and the jets requirements. The reconstructed electron

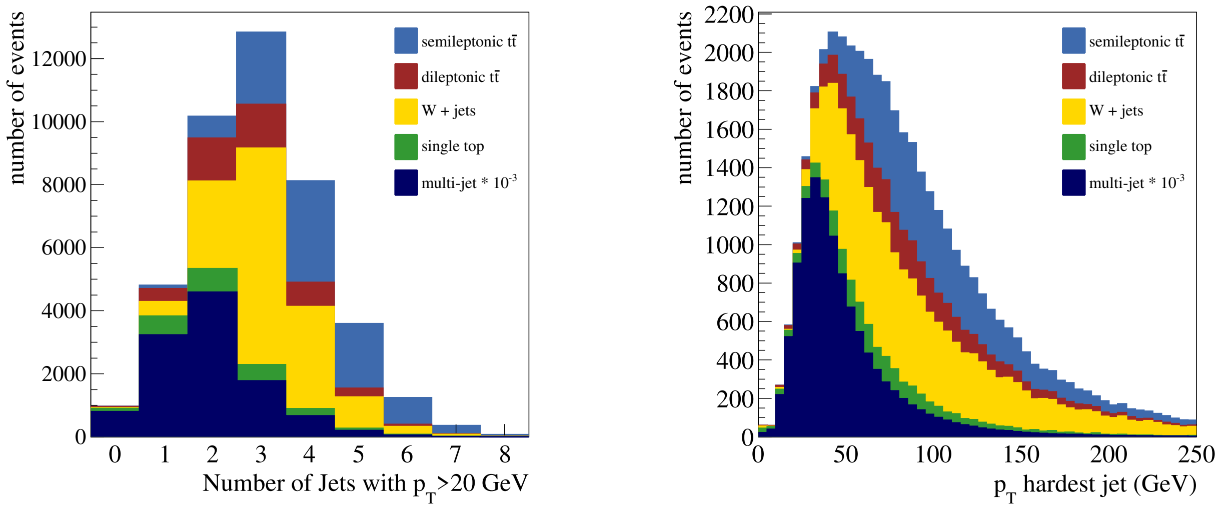

(a) Number of jets with $p_{\mathrm{T}} > 20$ GeV.

(b) Transverse momentum of the leading jet.

Figure 5.5: Reconstructed jets in all events that pass the trigger chain mu10. The number of events corresponds to 200 pb^{-1} except for the contribution of multi-jet events, which has been multiplied by 10^{-3}.

or muon satisfies the criteria of Section 5.2.2. The distributions clearly display the impact of the trigger requirement and in case of the muon channel, the effect of the top_mu filter on the multi-jet contribution is visible. The $\not{E}_{\mathrm{T}}$ distributions for events that pass the trigger, the lepton and the requirements are displayed in Figures 5.6(b) and 5.7(b). The selection of events that satisfy $\not{E}_{\mathrm{T}} > 20$ GeV severely reduces the contribution of multi-jet events.

Figures 5.6(c) and 5.7(c) contain the number of reconstructed jets satisfying $p_{\mathrm{T}} > 40$ GeV for events that pass the trigger, the lepton and the $\not{E}_{\mathrm{T}}$ criteria and in which at least four jets are reconstructed with $p_{\mathrm{T}} > 20$ GeV. This number is required to be at least three. Finally, Figures 5.6(d) and 5.7(d) show the p_{T} distribution of the fourth highest-p_{T} jet in events that pass the trigger, the lepton and the $\not{E}_{\mathrm{T}}$ requirement and in which at least three jets satisfy $p_{\mathrm{T}} > 40$ GeV. In case of the electron channel, the multi-jet contribution displays a structure which can be explained by the top_jet filter. According to the jet selection criterion, the p_{T} of the fourth jet needs to be larger than 20 GeV for an event to be selected.

As a result, all selected events contain at least four jets, which together with the electron or muon and the missing transverse energy allow for the reconstruction of the top quarks. The combination of all four selection criteria results in a good suppression of background events, which is quantified in the next section.

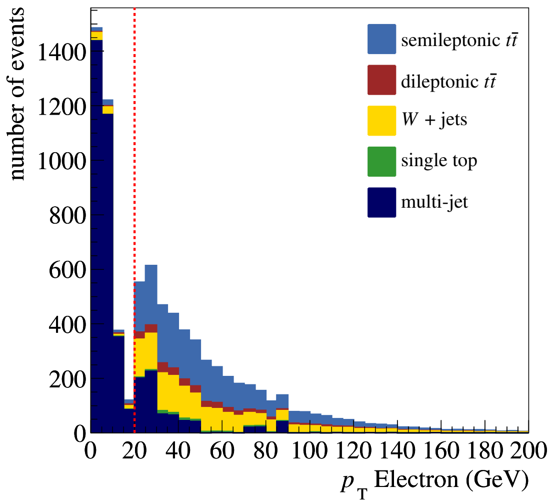

(a) The p_T distribution of the electron that satisfies the requirements of Section 5.2.2.

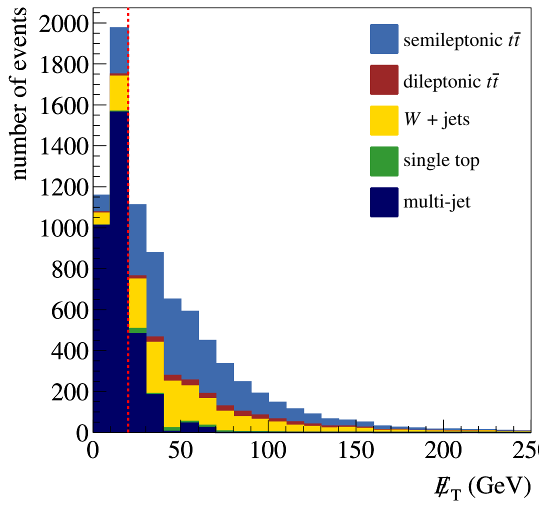

(b) The $\not{E}_T$ distribution.

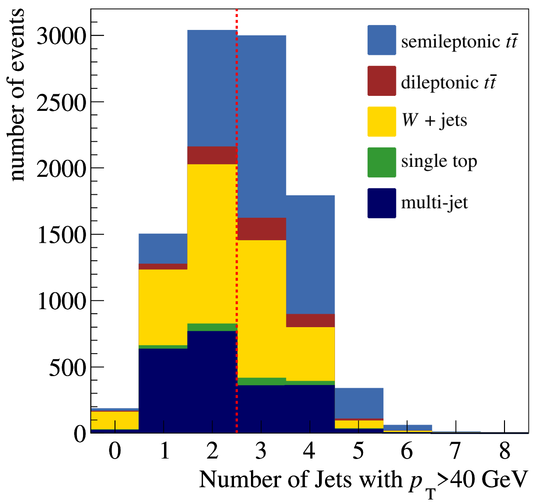

(c) The number of reconstructed jets with $p_T > 40$ GeV.

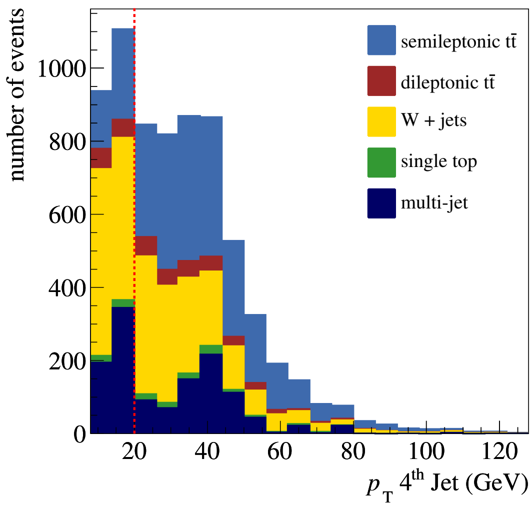

(d) The p_T distribution of the fourth highest-p_T jet.

Figure 5.6: Cumulative kinematic distributions for signal and background events that pass all electron channel selection critera except for the one of interest in 200 pb^{-1}. The vertical lines indicate the selection requirement corresponding to each variable.

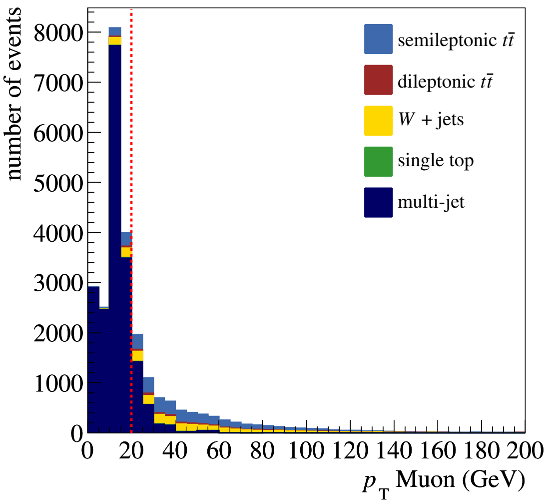

(a) The p_T distribution of the muon that satisfies the requirements of Section 5.2.2.

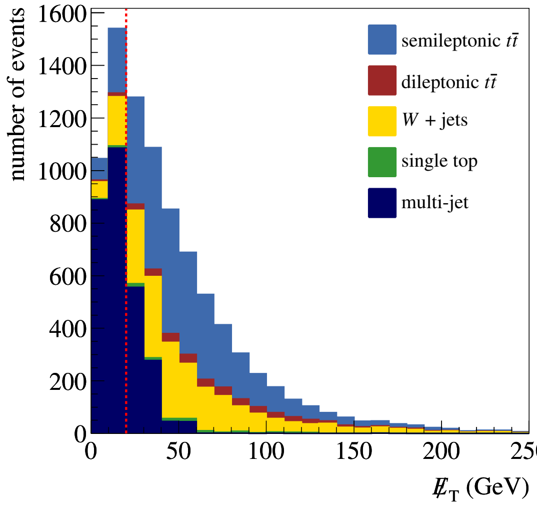

(b) The $\not{E}_T$ distribution.

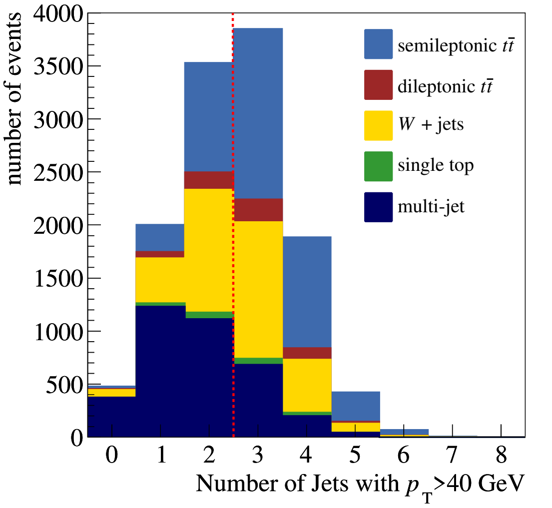

(c) The number of reconstructed jets with $p_T >$ 40 GeV.

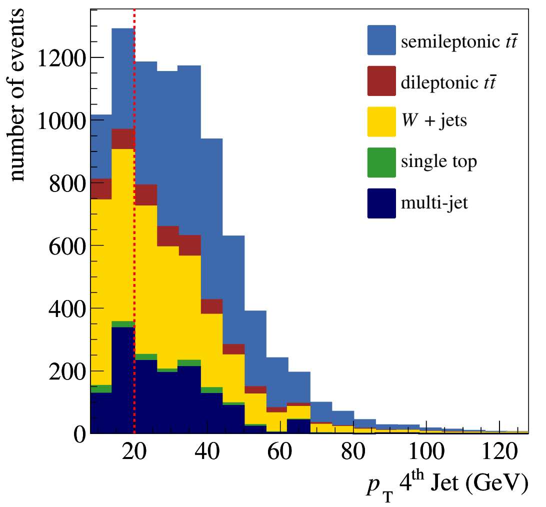

(d) The p_T distribution of the fourth highest-p_T jet.

Figure 5.7: Cumulative kinematic distributions for signal and background events that pass all muon channel selection critera except for the one of interest in 200 pb^{-1}. The vertical lines indicate the selection requirement corresponding to each variable.

5.4 Selection Efficiencies

Table 5.1 shows the fraction of events that pass each of the requirements in Section 5.2 for the samples of $t\bar{t}$, $W+$ jets, single top and multi-jet events. The impact of the combination of all four requirements on each sample is shown in the last column and the strategy proves effective in rejecting the background contributions. The large difference in efficiency between the electron and muon channel requirements in the multi-jet samples is not physical and simply due to the filters applied at event generation level (cf. Section 3.3). As a consequence of the `top_mu` filter, the trigger and lepton requirement efficiencies are severely biased in case of the muon channel.

The resulting composition of selected events in 200 pb^{-1} is given in table 5.2 for the electron and muon channel separately. The purity of the sample of selected events is thus expected to be 51 % for the electron channel and 50 % for the muon channel. Chapter 6 will make use of this sample of events to study the performance of the missing transverse energy reconstruction.

	Selection Criterion				
Sample	Trigger	Lepton	$\not{E}_{\mathrm{T}}$	Jets	**All**
$t\bar{t}(e)$	72 (7.8) %	56 (0.2) %	90 %	52 %	22.0 (0.05) %
$t\bar{t}(\mu)$	2.3 (74) %	0.2 (71) %	91 %	46 %	0.05 (25.6) %
$t\bar{t}(\tau)$	8.4 (15) %	4.0 (5.1) %	92 %	55 %	1.67 (1.86) %
dileptonic $t\bar{t}$	46 (50) %	22 (27) %	94 %	19 %	3.32 (4.07) %
$W+$ jets	39 (12) %	28 (10) %	85 %	12 %	1.05 (1.31) %
single top	33 (36) %	24 (31) %	91 %	10 %	1.23 (1.44) %
multi-jet	1.4 (49) %	$6.7{\cdot}10^{-2}$ (2.2) %	16 (16) %	17 (8.8) %	5.7 (40) $\cdot 10^{-4}$ %

Table 5.1: Selection efficiencies of each requirement for the electron (muon) channel.

Sample	**Electron**	**Muon**
semileptonic $t\bar{t}(e)$	2547±23	6±1
semileptonic $t\bar{t}(\mu)$	6±1	2977±26
semileptonic $t\bar{t}(\tau)$	193±6	214±7
dileptonic $t\bar{t}$	288±8	344±9
$W+$ jets	1509±20	1885±27
single top	98±10	90±10
multi-jet	743±133	929±148

Table 5.2: The expected composition of selected events in 200 pb^{-1}. The statistical uncertainties are determined by the size of the Monte Carlo samples.

6

Missing Transverse Energy in $t\bar{t}$ Events

When reconstructing the missing transverse energy of an event, $\not{E}_{\mathrm{T}}$, a good understanding of all reconstructed final state objects is required, as follows from its definition in (4.9). In many new physics channels, like SUSY decays or heavy resonances like W', the events are *busy*, i.e. a large number of final state objects is produced. This large number as well as the diversity of final state objects may complicate the $\not{E}_{\mathrm{T}}$ reconstruction. Semileptonic $t\bar{t}$ decays render a diverse and busy final state as well. Therefore, they provide an excellent environment to study and understand the reconstruction of $\not{E}_{\mathrm{T}}$ in topologies similar to those of several possible new physics scenarios.

In this chapter, the nomenclature is such that the phrase 'semileptonic $t\bar{t}$ events' refers to $t\bar{t}$ events that are identified as semileptonic based on Monte Carlo information and decay via either the electron channel or the muon channel. As discussed in Chapter 5, the tau decay channel is not considered. Events that pass the selection criteria described in Section 5.2 are referred to as *selected* events.

Section 6.1 discusses the $\not{E}_{\mathrm{T}}$ reconstruction in semileptonic $t\bar{t}$ events. In Section 6.2 a method is introduced to assess the performance of the $\not{E}_{\mathrm{T}}$ reconstruction in selected events by means of the transverse mass distribution of the W boson. The results are shown and discussed in Section 6.3.

6.1 Missing Transverse Energy

In semileptonic $t\bar{t}$ events, the assumption $p_{\mathrm{T}}^{\nu} \approx \not{E}_{\mathrm{T}}$ is usually made, for example when reconstructing the mass of the top quark. However, additional neutrinos are generally present in the event as a result of decaying b-quarks, B-, D-, K-mesons and pions. In fact, the average number of additional neutrinos is six per semileptonic $t\bar{t}$ event. Generally their transverse momenta are small compared to that of the neutrino from the W boson. Nevertheless, even with a hypothetically perfect detector, the association of $\not{E}_{\mathrm{T}}$ to p_{T}^{ν} is merely an approximation. The quantity that is to be compared to the reconstructed $\not{E}_{\mathrm{T}}$ is the actual expected missing transverse energy, ${\not{E}_{\mathrm{T}}}^{\mathrm{True}}$. It is obtained by summing up the energies of all stable particles that are expected not to leave any trace in the detector, i.e.

$$\begin{aligned} \not\!\!\boldsymbol{E}_{\mathrm{T}}{}^{\mathrm{True}} &= \left(\not\!\!E_x^{\mathrm{True}}, \not\!\!E_y^{\mathrm{True}}\right) \\ \not\!\!E_{x,y}^{\mathrm{True}} &= \sum_{\substack{\text{noninteracting}\\ \text{particles}}} E_{x,y}. \end{aligned} \tag{6.1}$$

The sum runs over all neutrinos that are generated by Monte Carlo in case of $t\bar{t}$ events, whereas in case of SUSY events, the lightest supersymmetric particle is regarded as noninteracting as well. The level of agreement between $\boldsymbol{p}_{\mathrm{T}}{}^{\nu}$ and $\not\!\!\boldsymbol{E}_{\mathrm{T}}{}^{\mathrm{True}}$ in simulated semileptonic $t\bar{t}$ events is shown in Figure 6.1. Figure 6.1(a) displays the scalar difference[1], $\not\!\!E_{\mathrm{T}}^{\mathrm{True}} - p_{\mathrm{T}}^{\nu}$, which reflects a good agreement between the quantities in the majority of the events, although long tails are present up to 20 GeV. The comparison of the azimuthal angles is shown in Figure 6.1(b). The difference is generally small and most events in the tails correspond to low values of p_{T}^{ν}, i.e. to events in which the azimuthal angle is not well defined. This is illustrated by the distribution for events with $p_{\mathrm{T}}^{\nu} > 40$ GeV in the same figure, for which the tails have largely disappeared.

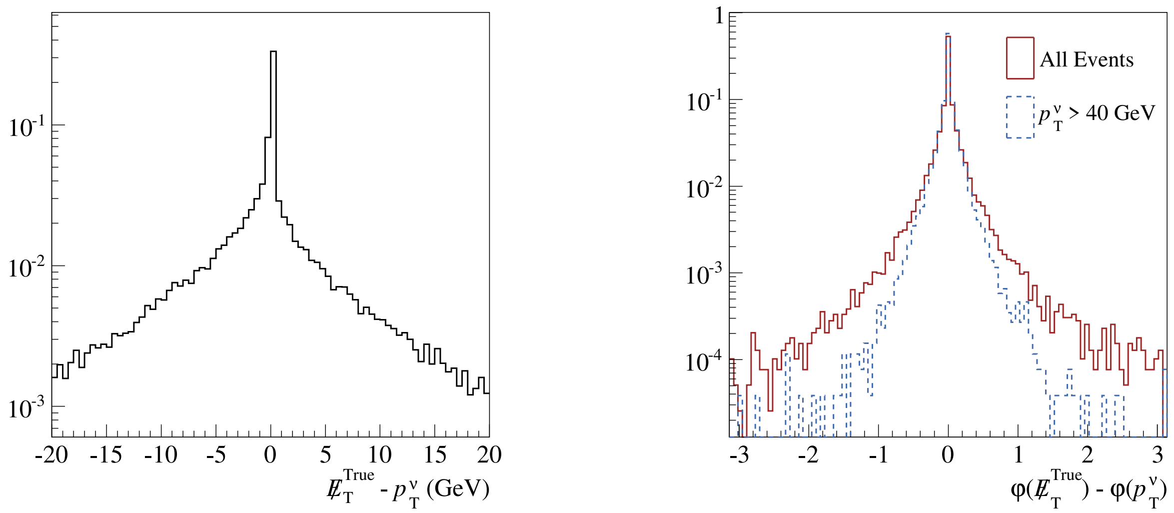

(a) The difference between the magnitudes $\not\!\!E_{\mathrm{T}}^{\mathrm{True}}$ and p_{T}^{ν}.

(b) The difference between the azimuthal angles $\varphi(\not\!\!\boldsymbol{E}_{\mathrm{T}}{}^{\mathrm{True}})$ and $\varphi(p_{\mathrm{T}}^{\nu})$.

Figure 6.1: Comparison between $\not\!\!\boldsymbol{E}_{\mathrm{T}}{}^{\mathrm{True}}$ and the $\boldsymbol{p}_{\mathrm{T}}$ of the neutrino in semileptonic $t\bar{t}$ events. The distributions are displayed on a logarithmic scale and normalized to unity.

[1] The notation is such that for instance the scalar quantity $|\not\!\!\boldsymbol{E}_{\mathrm{T}}{}^{\mathrm{True}}| = \sqrt{\left(\not\!\!E_x^{\mathrm{True}}\right)^2 + \left(\not\!\!E_y^{\mathrm{True}}\right)^2}$ is denoted $\not\!\!E_{\mathrm{T}}^{\mathrm{True}}$.

Reconstruction and Performance of $\not\!\!E_{\mathrm{T}}$

The sum of transverse momenta of noninteracting particles, ${\not\!\!E_{\mathrm{T}}}^{\mathrm{True}}$, is by definition balanced out by the sum of transverse momenta of all interacting particles. The latter are reconstructed and form the input to the missing transverse energy reconstruction. As described in Section 4.6, the $\not\!\!E_{\mathrm{T}}$ is composed of contributions of all reconstructed objects as well as energy deposits in calorimeter cells outside of reconstructed objects and a correction for inactive material. As a consequence, the quality of the reconstruction is sensitive not only to the detector resolution and coverage, but also to the parametrization of inactive material, the calibration of reconstructed objects and the presence of dead or noisy channels. The impact of noise in the calorimeters is suppressed by making use of cells associated to TopoClusters (cf. Section 4.2).

To illustrate the share of each type of contribution to $\not\!\!E_{\mathrm{T}}$ in semileptonic $t\bar{t}$ events, the total energy deposit in the calorimeter, $\sum E_{\mathrm{T}}$, is decomposed in Figure 6.2(a). It shows the composition of $\sum E_{\mathrm{T}}$, as defined in (4.14), for events in which the top quark decays through the electron channel. The main contribution of $\sim 70\%$ is coming from jets (RefJet) and as expected, the reconstructed electrons contribute as well (RefEle). It turns out that the contribution from calorimeter cells not assigned to any reconstructed object, $E_{\mathrm{T}}^{\mathrm{CellOut}}$, is more prominent than that of electrons. Figure 6.2(b) shows the distribution of the three largest components together with the total $\sum E_{\mathrm{T}}$. In conclusion, the calibration of calorimeter cells, in particular those that belong to jets, is highly important for a correct determination of the missing transverse energy in semileptonic $t\bar{t}$ events.

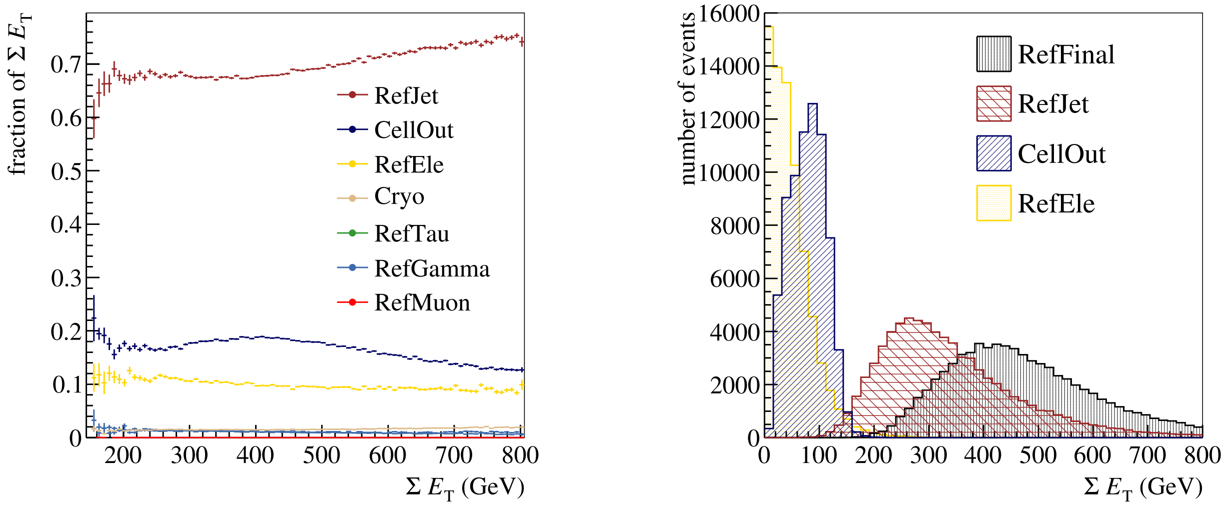

(a) Fraction of $\sum E_{\mathrm{T}}$ assigned to each type of reconstructed object.

(b) Contribution to $\sum E_{\mathrm{T}}$ of the three largest components and the total $\sum E_{\mathrm{T}}$.

Figure 6.2: Contributions to $\sum E_{\mathrm{T}}$ of TopoCells assigned to each type of object in simulated semileptonic $t\bar{t}$ events that decay through the electron channel.

Figure 6.3(a) shows the distribution of reconstructed $\not{E}_{\mathrm{T}}$ in simulated semileptonic $t\bar{t}$ events. Recall that the event selection described in Section 5.2 includes the requirement $\not{E}_{\mathrm{T}} > 20$ GeV, which rejects only a small fraction of signal events. In the following, the performance of the reconstruction of $\not{E}_{\mathrm{T}}$ is investigated in events that pass all selection criteria described in Section 5.2.

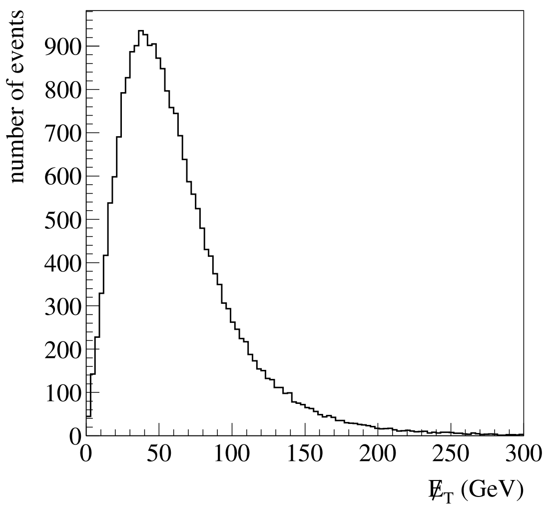

(a) The distribution of reconstructed $\not{E}_{\mathrm{T}}$.

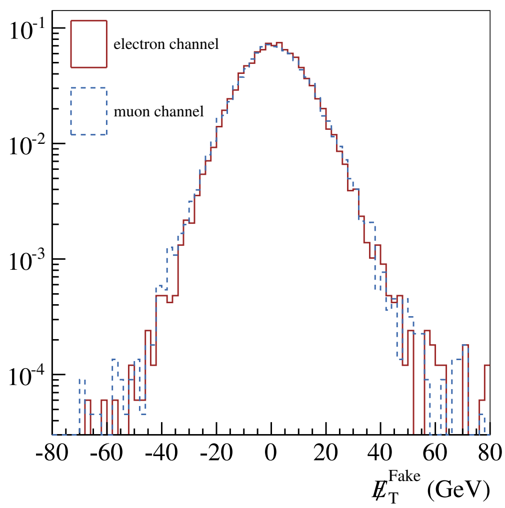

(b) The normalized distributions of $\not{E}_{\mathrm{T}}^{\mathrm{Fake}}$ for the electron and muon channel respectively.

Figure 6.3: Missing transverse energy in simulated semileptonic $t\bar{t}$ events.

The fake missing transverse energy, $\not{E}_{\mathrm{T}}^{\mathrm{Fake}}$, is defined as the scalar difference between the reconstructed and expected $\not{E}_{\mathrm{T}}$, i.e.

$$\not{E}_{\mathrm{T}}^{\mathrm{Fake}} = \not{E}_{\mathrm{T}} - \not{E}_{\mathrm{T}}^{\mathrm{True}}. \tag{6.2}$$

Figure 6.3(b) shows the distribution of $\not{E}_{\mathrm{T}}^{\mathrm{Fake}}$ for selected $t\bar{t}$ events in the electron and muon channel separately. The resolution corresponding to the width of a Gaussian fit is 11.37 GeV for the electron channel and 11.97 GeV for the muon channel, yet small non-Gaussian tails are present. Nonzero values of $\not{E}_{\mathrm{T}}^{\mathrm{Fake}}$ generally enhance background contributions in searches for new physics. In fact, such an enhancement came to light in Chapter 5, concerning the multi-jet contribution to the semileptonic $t\bar{t}$ event selection.

The $\not{E}_{\mathrm{T}}$ resolution, i.e. the Gaussian width of the $\not{E}_{\mathrm{T}}^{\mathrm{Fake}}$ distribution, depends on $\sum E_{\mathrm{T}}$ and practically behaves stochastically for selected $t\bar{t}$ events as can be seen in Figure 6.4(a). The curve is the result of the best fit of the function $a\sqrt{(}\sum E_{\mathrm{T}})$, which corresponds to $a = 0.48$. The angular resolution for selected events is depicted in Figure 6.4(b). It displays the width of a Gaussian fit to the distribution of $\varphi(\not{E}_{\mathrm{T}}) - \varphi(\not{E}_{\mathrm{T}}^{\mathrm{True}})$, which improves with increasing values of $\not{E}_{\mathrm{T}}$.

Another figure of merit for the performance of $\not{E}_{\mathrm{T}}$ reconstruction is the relative bias, which is given by $\not{E}_{\mathrm{T}}^{\mathrm{Fake}}/\not{E}_{\mathrm{T}}^{\mathrm{True}}$ The mean value of its distribution for selected $t\bar{t}$ events is

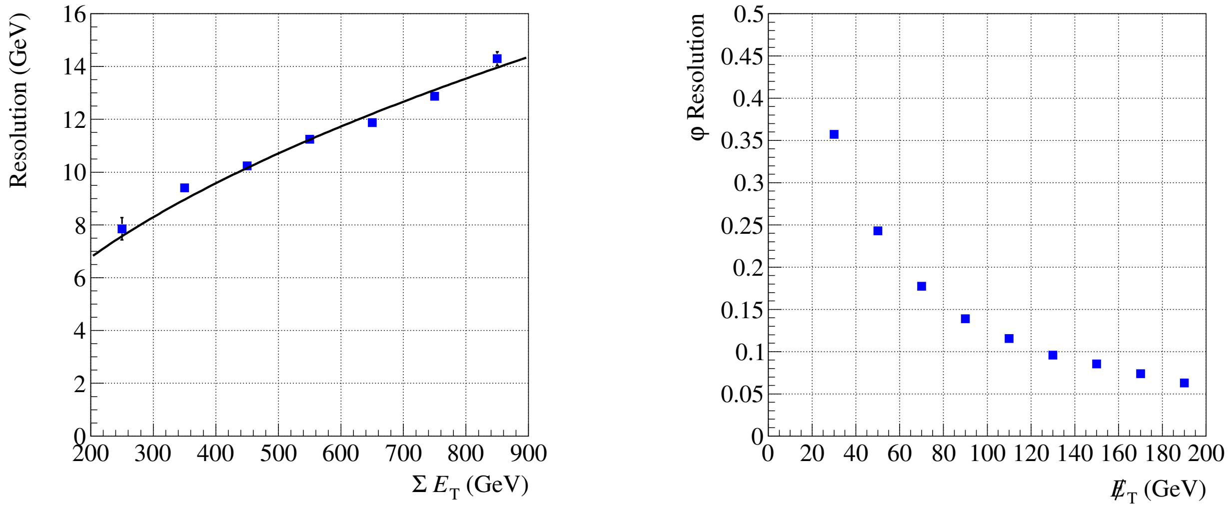

(a) $\not{E}_{\mathrm{T}}$ resolution versus $\sum E_{\mathrm{T}}$.

(b) Resolution of $\varphi(\not{E}_{\mathrm{T}})$ versus $\not{E}_{\mathrm{T}}$.

Figure 6.4: Resolution of $\not{E}_{\mathrm{T}}$ in selected $t\bar{t}$ events.

shown in Figure 6.5 as a function of $\not{E}_{\mathrm{T}}^{\mathrm{True}}$. For values $\not{E}_{\mathrm{T}}^{\mathrm{True}} > 50$ GeV, the bias is smaller than 2%.

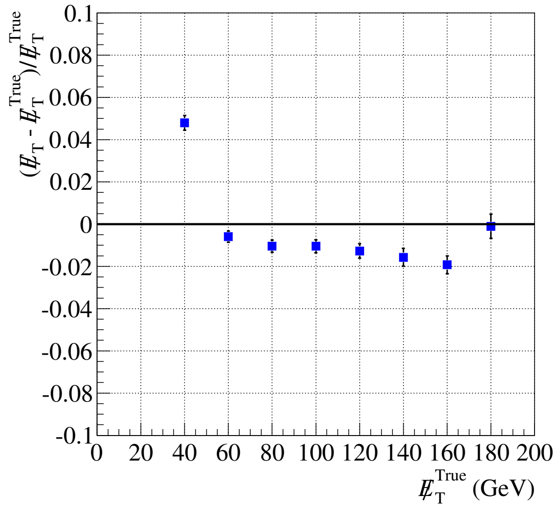

Figure 6.5: The relative bias in selected semileptonic $t\bar{t}$ events. The error bars indicate the statistical error on the mean of the distribution in each bin of $\not{E}_{\mathrm{T}}^{\mathrm{True}}$.

The azimuthal angle of $\varphi(\not{E}_{\mathrm{T}})$ is expected to be a flat distribution based on the symmetry of the detector. However, Figure 6.6 displays a small asymmetry in the $\varphi(\not{E}_{\mathrm{T}})$ distribution. This is mainly caused by the position of the primary vertex in the version of the detector simulation that was used. It is displaced by $(x_0, y_0, z_0) = (1.50, 2.50, -8.65)$ mm from the center of the ATLAS detector. A similar effect is observed in collision data in Chapter 8.

In general, the reconstructed $\varphi(\not{E}_{\mathrm{T}})$ is very sensitive to any unexpected irregularities the detector. The squares in Figure 6.6 show the distribution in a $t\bar{t}$ sample in which a quadrant of the HEC on side C was not powered in the detector simulation. As expected, the impact is substantial in the interval $[-\pi/2, 0]$. This illustrates that $\varphi(\not{E}_{\mathrm{T}})$ is a powerful

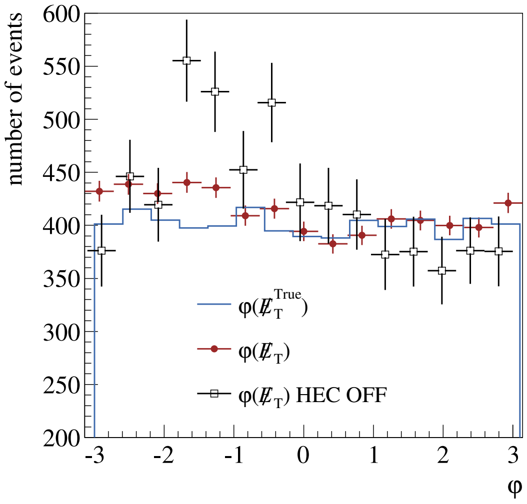

Figure 6.6: The distributions of the reconstructed $\varphi(\not\!\!E_T)$ and the $\varphi(\not\!\!E_T^{\mathrm{True}})$ in selected $t\bar{t}$ events.

observable to quickly spot detector problems.

6.2 Transverse W Boson Mass

In order to estimate the performance of $\not\!\!E_T$ reconstruction in data, the distribution of the transverse W boson mass is studied. The mass and width of the W boson are measured by previous accelerator experiments with great precision. The combination of the LEP and Tevatron results gives [10]

$$\begin{aligned} m_W &= 80.398 \pm 0.025 \text{ GeV} \\ \Gamma_W &= 2.141 \pm 0.041 \text{ GeV}. \end{aligned} \tag{6.3}$$

Under the assumption that the W boson mass and the kinematics of its decay products are well modelled by Monte Carlo, the accuracy of the simulated detector response can be investigated by means of a comparison with data. Obviously, the outcome of such a study is not to be used as input for a W boson mass measurement.

6.2.1 Sensitivity to $\not\!\!E_T$ Reconstruction Performance

The missing transverse energy in semileptonic $t\bar{t}$ events is mainly caused by the undetected neutrino from the leptonically decaying W boson. The combination of the transverse momentum of the neutrino and that of the corresponding charged lepton l, results in the transverse mass of the W boson:

$$\begin{aligned} (m_{\mathrm{T}}^{W,\mathrm{true}})^2 &= (P_{\mathrm{T}}^{l,\mathrm{true}} + P_{\mathrm{T}}^{\nu})^2 \\ &= 2p_{\mathrm{T}}^{l,\mathrm{true}} p_{\mathrm{T}}^{\nu} \left[1 - \cos\left(\Delta\varphi(l^{\mathrm{true}}, \nu)\right)\right], \end{aligned} \tag{6.4}$$

under the assumption that the mass of the charged lepton is negligible. The angle $\Delta\varphi(l^{\mathrm{true}}, \nu)$ is the opening angle in the transverse plane between the charged lepton and

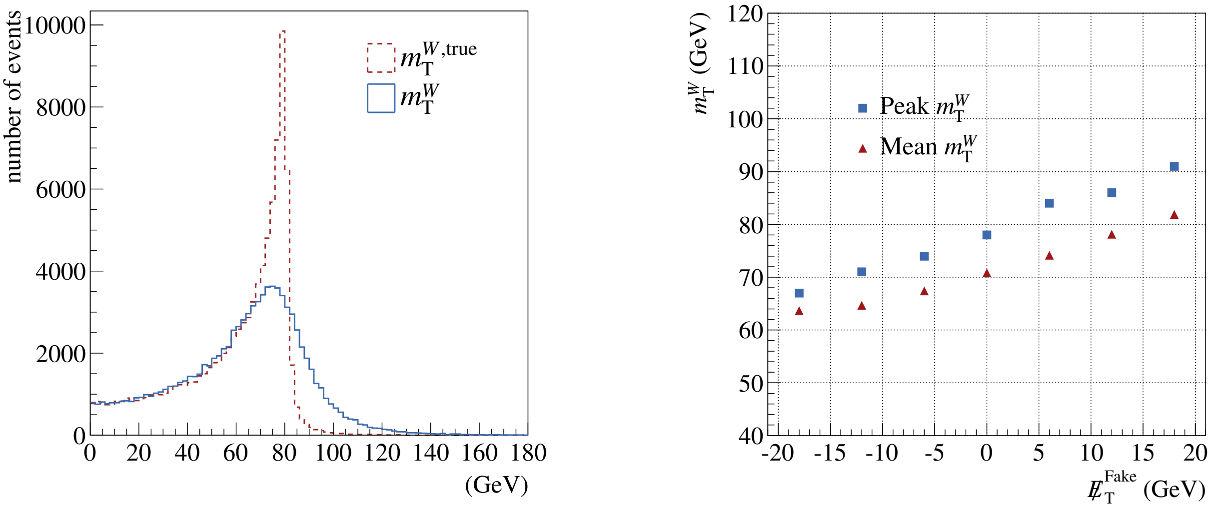

(a) The distributions of the reconstructed (full) and true (dashed) transverse W boson mass.

(b) The dependence of the mean and peak of the m_T^W distribution on the amount of $\not{E}_T^{\text{Fake}}$.

Figure 6.7: The transverse W boson mass in simulated semileptonic $t\bar{t}$ events.

the neutrino. The reconstructed $\not{E}_T$ approximates p_T^ν and the transverse W boson mass is reconstructed as

$$(m_T^W)^2 \quad = \quad 2p_T^l \not{E}_T \left[1 - \cos\left(\Delta\varphi(l, \not{E}_T)\right)\right]. \tag{6.5}$$

This expression is clearly sensitive to the quality of the reconstruction of missing transverse energy, both in magnitude and direction. Figure 6.7(a) shows the distributions of $m_T^{W,\text{true}}$ and m_T^W in simulated semileptonic events. The characteristic shape of the transverse projection is the Jacobian peak. The sharp edge around 80 GeV in the $m_T^{W,\text{true}}$ distribution is determined by the value of the W boson mass as given in (6.3). A small tail is observed above m_W which is caused by the corresponding nonzero intrinsic width of the W boson mass. The resolution on the reconstructed transverse momentum of the charged lepton is better than 2 % for electrons and better than 4 % for muons (cf. Chapter 4), which is why the width of the Jacobian peak in the reconstructed m_T^W distribution in Figure 6.7(a) is dominated by the resolution on the missing transverse energy.

The position of the Jacobian peak as well as the width of the distribution are sensitive to the amount of $\not{E}_T^{\text{Fake}}$ in the event. Figure 6.7(b) shows how the position of the maximum as well as the mean value of the entire distribution shift with varying amounts of $\not{E}_T^{\text{Fake}}$.

Several scenarios of badly reconstructed $\not{\boldsymbol{E}}_T$ are imaginable and their impact on the m_T^W distribution is illustrated here by means of some examples.

In the first example, we assume that the calibration of TopoClusters inside jets is affected by systematic effects and the contribution of $\not{\boldsymbol{E}}_T{}^{\text{RefJets}}$ is under- or overestimated by 20%. Such a large effect is expected to be unlikely, but serves the purpose of illustrating the impact on the reconstructed m_{T}^{W}. The contribution of $\not{\boldsymbol{E}}_{\mathrm{T}}{}^{\mathrm{CellOut}}$ is subject to the same calibration as $\not{\boldsymbol{E}}_{\mathrm{T}}{}^{\mathrm{RefJets}}$ and thus adjusted as well. The resulting m_{T}^{W} distributions are tilted with respect to the nominal distribution, which is illustrated for selected events in Figure 6.8(a). An overestimation of the contribution from jets and TopoCells outside of final state objects results in a worse $\not{E}_{\mathrm{T}}$ resolution, which in turn renders a broader m_{T}^{W} distribution. In addition, the magnitude $\not{E}_{\mathrm{T}}$ is scaled and an increased number of events passes the event selection.

The second example concerns the scenario in which the contribution from electrons is subject to a systematic effect. Apart from the impact on $\not{\boldsymbol{E}}_{\boldsymbol{x,y}}{}^{\mathrm{RefEle}}$, the transverse momentum of the electron in (6.5) is adjusted accordingly as well. The impact on the m_{T}^{W} distribution is a shift. This is illustrated in Figure 6.8(b), which shows the m_{T}^{W} distributions when $\not{\boldsymbol{E}}_{\mathrm{T}}{}^{\mathrm{RefEle}}$ is under- or overestimated by 5 %. In this scenario, the $\not{E}_{\mathrm{T}}$ is scaled with respect to the nominal distribution, yet the resolution is hardly affected.

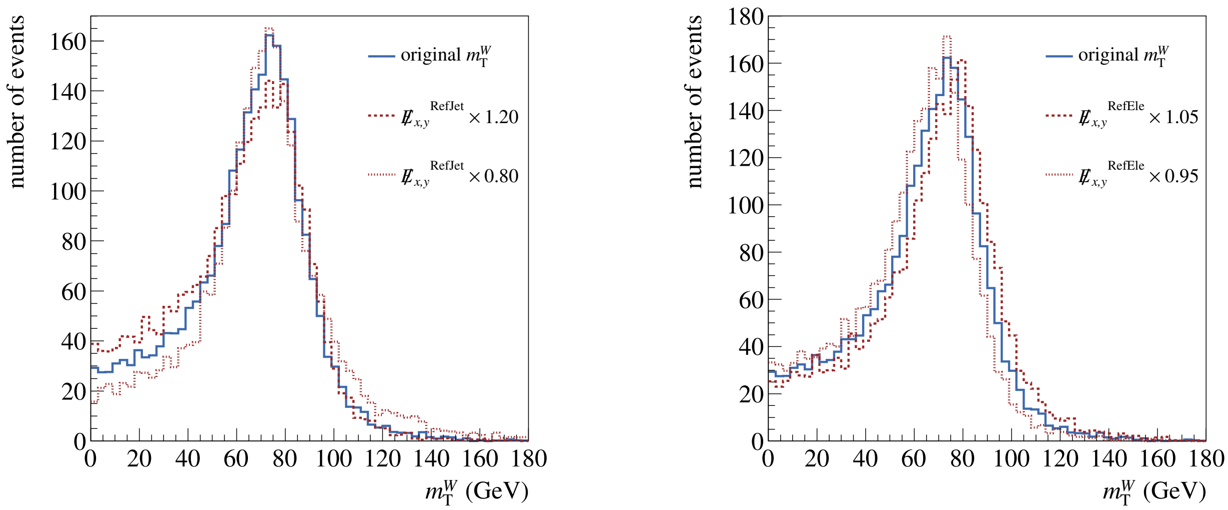

(a) H1 calibration of TopoCells off by 20%.

(b) $\not{\boldsymbol{E}}_{\boldsymbol{x,y}}{}^{\mathrm{RefEle}}$ and $p_{x,y}^{e}$ off by 5%.

Figure 6.8: The impact of badly reconstructed $\not{E}_{\mathrm{T}}$ on the m_{T}^{W} distribution in events that pass the electron channel selection in 200 pb^{-1}.

In conclusion, systematic variations of the $\not{E}_{\mathrm{T}}$ reconstruction result in deformations of the m_{T}^{W} distribution; either in a shift of the distribution or a broadening of the peak. This effect is utilized in order to asses the quality of the $\not{E}_{\mathrm{T}}$ reconstruction in data in the following section. The final aim is to recognize and quantify a total systematic deviation of the $\not{E}_{\mathrm{T}}$ reconstruction from the simulation. The difference in impact on the distribution between the examples mentioned above may in fact hint to the source of the deviation and inspire further investigations.

6.2.2 Fit Method

In order to exploit the sensitivity of the transverse W boson mass to the $\not{\boldsymbol{E}}_{\mathrm{T}}$ reconstruction performance, the distribution as reconstructed from data is compared to a number of Monte

Carlo generated templates in each of which a scenario of wrongly reconstructed $\not{E}_{\mathrm{T}}$ is assumed. Rather than investigating each of the many possible sources of a deviation of the $\not{E}_{\mathrm{T}}$ reconstruction in data from simulation, the possible deviation is more generally decomposed into a scale α and an additional resolution r. In each template, the x- and y- components of $\not{E}_{\mathrm{T}}$ are scaled with a parameter α and convoluted with a normalized two-dimensional Gaussian distribution of width r. A template with $r = 0$ and $\alpha = 1$ thus corresponds to the nominal $\not{E}_{\mathrm{T}}$ resolution according to the simulation as addressed in Figure 6.4(a). For every set of $\alpha \in [0.70, 1.30]$ and $r \in [0, 30]$, the transverse W mass distribution from Monte Carlo, $m_{\mathrm{T}}^{W,\mathrm{MC}}(\alpha, r)$, is compared to the distribution obtained from the data. In the interval $m_{\mathrm{T}}^{W} \in [50, 120]$ GeV, the χ^2 is calculated by comparing the two distributions in each bin i,

$$\chi^2 = \sum_i \left(\frac{m_{T,i}^{W} - m_{T,i}^{W,\mathrm{MC}}}{\sigma_i^2} \right)^2 , \tag{6.6}$$

where σ_i^2 is the sum of the squared statistical uncertainties on the two histograms in the ith bin. The normalization is determined by requiring the number of Monte Carlo events in the region $m_{\mathrm{T}}^{W,\mathrm{MC}} \in [50, 120]$ GeV to be equal to the number of data events, i.e. no assumption is made concerning the absolute production cross section. For each value of α and r for which a template exists, the χ^2 is calculated. The two-dimensional χ^2 distribution is subsequently fitted with a parabola in order to retrieve the position of its minimum, $(\alpha, r)^{\mathrm{fit}}$. The statistical uncertainty is determined from the contour line that describes where the χ^2 is increased with 2.30 with respect to its minimum[2]. The values $(\alpha, r)^{\mathrm{fit}}$ corresponding to the minimum χ^2 reveal if the reconstructed $\not{E}_{\mathrm{T}}$ is under- or overestimated by some scale α and/or displaying a higher resolution than expected from simulation.

In practice, the sample of events that is acquired by applying the event selection of Section 5.2 contains contributions from $W+$ jets, single top, multi-jet and dileptonic $t\bar{t}$ events in addition to the semileptonic $t\bar{t}$ events. Fortunately, the dominant background contribution from $W+$ jets events in fact contains an actual W boson and the m_{T}^{W} distribution is still a good reflection of the performance of the $\not{E}_{\mathrm{T}}$ reconstruction in events that resemble the semileptonic $t\bar{t}$ topology. Although from a physics point of view, these events are a background to $t\bar{t}$ events, in the reconstruction performance study at hand, they are regarded as signal. This statement is motivated in Section 6.2.3. Multi-jet events, however, are expected to distort the distribution as neither the reconstructed electron or muon nor the reconstructed $\not{E}_{\mathrm{T}}$ are caused by a leptonically decaying W boson. The distributions of the reconstructed transverse W boson mass in simulated events that pass the selection criteria are shown in Figure 6.9(a) for the electron channel and in Figure 6.9(b) for the muon channel. Table 6.1 shows the expected composition of selected events in the interval $m_{\mathrm{T}}^{W} \in [50, 120]$ GeV for 200 pb^{-1}.

[2] In case of one fit parameter, $\Delta\chi^2 = 1$ corresponds to a coverage probability of 68 %, i.e. the standard error. Here the number of fit parameters is two and $\Delta\chi^2 = 2.3$ gives the standard error.

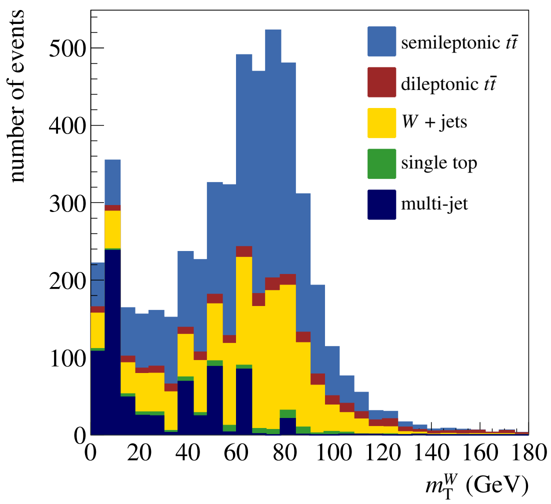

(a) The electron channel.

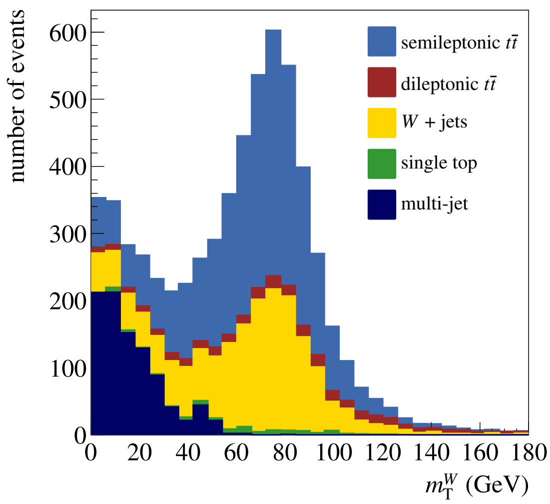

(b) The muon channel.

Figure 6.9: The cumulative reconstructed transverse W mass distribution in events that pass the selection criteria. The number of events corresponds to 200 pb^{-1} integrated luminosity.

Sample	Electron	Muon
semileptonic $t\bar{t}(e)$	1851±20	3±1
semileptonic $t\bar{t}(\mu)$	3±1	2199±22
semileptonic $t\bar{t}(\tau)$	43±3	52±3
dileptonic $t\bar{t}$	151±6	176±6
$W+$ jets	1050±16	1310±22
single top	62±8	60±8
multi-jet	159±55	6±2

Table 6.1: The expected composition of selected events in 200 pb^{-1} in the interval $m_T^W \in [50, 120]$ GeV for the electron channel and the muon channel.

6.2.3 $W+$ jets Contribution

The selected $W+$ jets events can be regarded as signal in the context of this performance study, which enhances the number of events that is available in 200 pb^{-1} of accumulated data and statistical fluctuations are reduced. Because an actual W boson is reconstructed, the shape of the m_T^W distribution for $W+$ jets events that pass the selection criteria is similar to that for $t\bar{t}$ events. The agreement is explicitly investigated by constructing a scenario in which the contribution from $W+$ jets events in the sample of simulated events is multiplied by a factor of two. The templates that are compared to this "diluted" distribution contain all samples except for the multi-jet events and they contain the nominal share of $W+$ jets events. Figure 6.10 shows the result of the fit for the muon channel in a scenario in

Figure 6.10: Template fit in the muon channel in a scenario with a double contribution from $W+$ jets events.

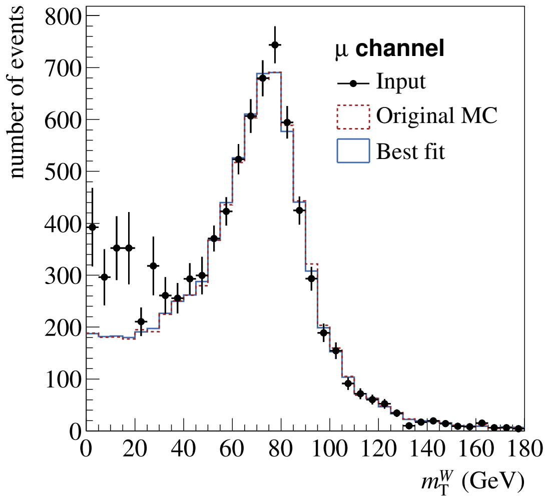

which the contribution from $W+$ jets events is multiplied by a factor of two. The outcome of the fit is $(\alpha, r)^{\text{fit}} = (0.99^{+0.016}_{-0.013}, 0.8^{+2.68}_{-0.78}$ GeV), i.e. the shape of the diluted distribution is in good agreement with the nominal template distribution. Hence, the fit method is independent of the ratio of the $W+$ jets cross section to the $t\bar{t}$ cross section.

6.2.4 Multi-jet Events

Estimation of the Contribution

As shown in Table 6.1, the restriction to perform the template fit only in the interval $m_T^W \in [50, 120]$ GeV strongly reduces the influence of multi-jet events. However, due to the uncertainty on the production cross section (cf. Section 3.3.1), the prediction on the multi-jet contribution from Monte Carlo is not reliable. The aim is to extract this contribution from the data instead. To this end, the m_T^W distribution of multi-jet events is disentangled from the other contributions by means of the template fit.

Figure 6.9 showed that multi-jet events are characterized by small values of the reconstructed m_T^W. This observation is further clarified below. As a consequence, the impact of multi-jet events on the template fit is expected to be minor given that the fit is performed in the interval $m_T^W \in [50, 120]$ GeV. However, the difference between the complete data distribution and the best template is expected to be due to multi-jet events, which are not contained in the template. Therefore, the multi-jet contribution is estimated by subtracting the template for $(\alpha, r)^{\text{fit}}$ from the data distribution.

The procedure is tested here by means of an input distribution which contains events from all Monte Carlo samples, but in which the actual number of events is limited to 200 pb^{-1}. First, the m_T^W distribution for events in the muon channel is regarded. The outcome of the template fit is $(\alpha, r)^{\text{fit}} = (0.99^{+0.014}_{-0.011}, 1.6^{+3.22}_{-1.58}$ GeV)., i.e. the scale of $\not{E}_T$ is compatible with the nominal value $\alpha = 1.0$ and the additional resolution r is small with respect to the nominal resolution of approximately 12 GeV. Figure 6.11(a) shows the template corresponding to these values and the resulting estimation of the multi-jet contribution. The estimation agrees very well with the multi-jet contribution according to

Monte Carlo. To illustrate the robustness of the method, the same procedure is applied to a scenario in which the multi-jet contribution is multiplied by a factor of two. The result is shown in Figure 6.11(b).

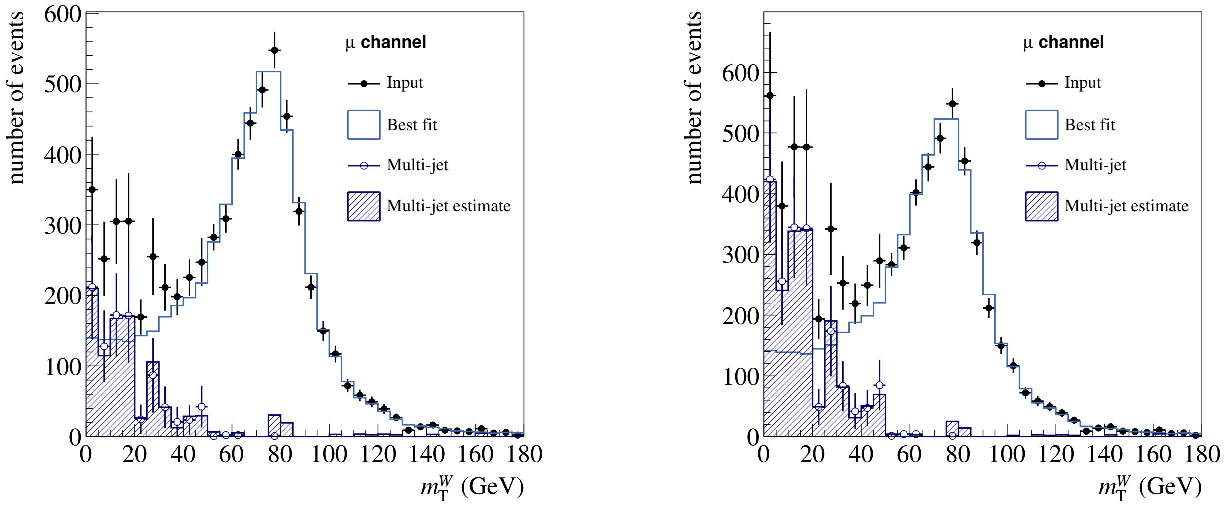

(a) Estimation of the multi-jet contribution to the m_T^W distribution by means of a template fit.

(b) Same procedure in a scenario that contains a double multi-jet contribution.

Figure 6.11: The outcome of the multi-jet estimation based on the template fit in the muon channel. The number of input events corresponds to 200 pb^{-1} integrated luminosity.

Secondly, the multi-jet contribution in the electron channel is investigated. Figure 6.12 shows the estimation of the multi-jet contribution in the electron channel as extracted from the template fit. The best template corresponds to $(\alpha, r)^{\text{fit}} = (0.99^{+0.020}_{-0.021}, 1.1^{+3.50}_{-1.10}\text{ GeV})$ and also in the electron channel, the obtained multi-jet estimation is in good agreement with the distribution according to Monte Carlo.

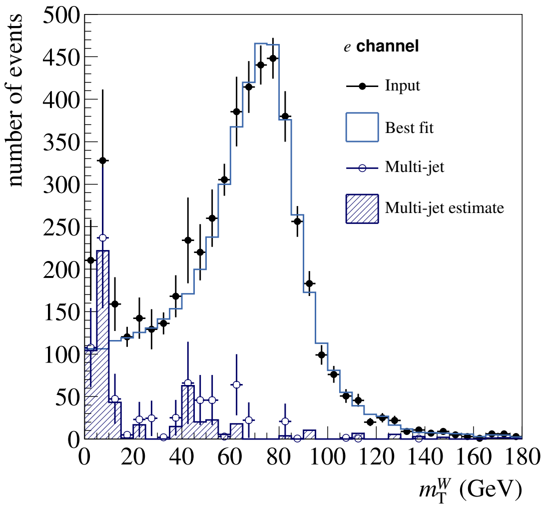

Figure 6.12: Estimation of the multi-jet contribution to the m_T^W distribution by means of a template fit in the electron channel.

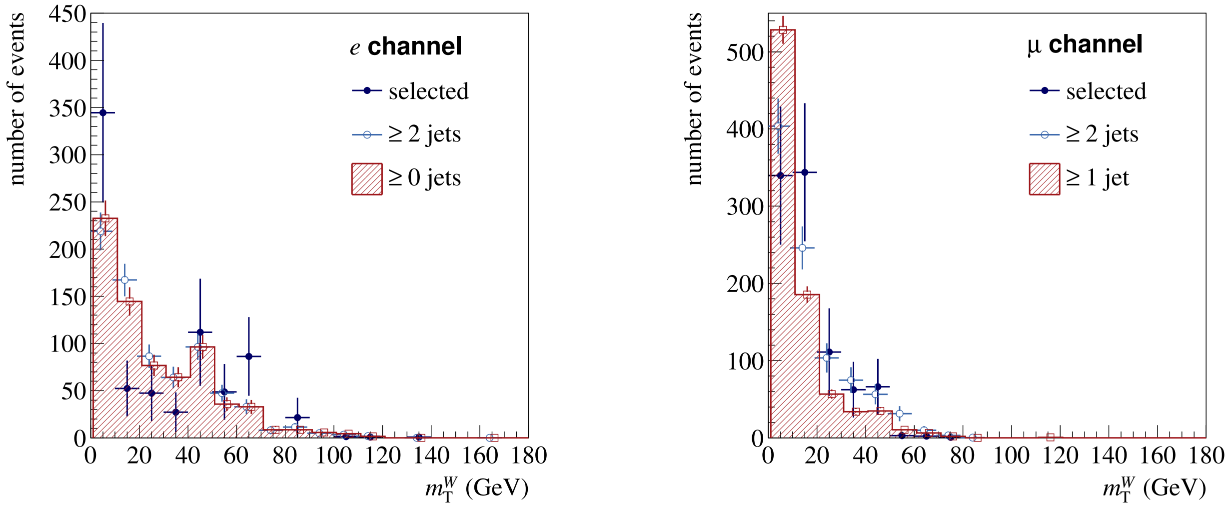

(a) The electron channel. (b) The muon channel.

Figure 6.13: Comparison between the m_T^W distributions for different jet selection criteria in simulated multi-jet events. The number of events corresponds to the number of selected events in 200 pb^{-1} integrated luminosity.

Multi-jet Characteristics

The shape of multi-jet contribution in Figure 6.9 clearly differs from the contributions from other types of events. Moreover, the contribution in the electron channel differs from that in the muon channel. Further investigation is limited by the number of events in the Monte Carlo samples, due to which the multi-jet events in Figure 6.9 obtained large weight factors to correspond to 200 pb^{-1}. Although the error bars are scaled accordingly, the size of the samples is not sufficient to mimic the expected statistical fluctuations in 200 pb^{-1}. In order to overcome this obstacle, an ad hoc procedure is introduced to obtain a larger sample of multi-jet events. For the purpose of this study, a larger sample is obtained by loosening the selection criteria.

The jets requirement described in Section 5.2.4 is modified as follows: merely one reconstructed jet with $p_T > 40$ GeV is required in the muon channel and the jets requirement is completely disregarded in the electron channel. The m_T^W distributions with the new criteria are then scaled to agree with the number of events that are expected pass the complete event selection in 200 pb^{-1} as given in Table 6.1. The kinematics of the additional events that are accepted in this scheme could differ from the original events, but recall that all multi-jet events in the electron channel pass the `top_jet` filter described in Section 3.3. In fact, Figure 6.13 shows that the obtained distributions are in reasonable agreement with the original description with the full event selection applied. The increased number of events allows for a more detailed investigation of the shape of the m_T^W distribution in multi-jet events. Note that this ad hoc scenario serves the purpose of this illustration only and would not be necessary when studying collision data.

It has been shown that in the majority of the multi-jet events, the reconstructed m_T^W

is considerably smaller than m_W and the events do not enter the range in which the fit is performed. The explanation follows from the definition of m_T^W in (6.5). Generally, in multi-jet events that pass the lepton requirement, a jet is falsely reconstructed as an isolated charged lepton. As a consequence of the incorrect assignment, nonzero $\not{E}_T$ is introduced, which is likely to point in the direction of the missed jet. This $\not{E}_T$ may also be caused by actual neutrinos that originate from semileptonically decaying b-jets. Figure 6.14 shows that indeed the opening angle in the transverse plane generally adopts smaller values in multi-jet events than in $t\bar{t}$ events. The peak around zero is particularly narrow for multi-jet events in the muon channel, where the reconstructed muon most often originates from a semileptonically decaying B hadron and is thus accompanied by a neutrino.

However, in part of the multi-jet events the opening angle $|\Delta\varphi(l, \not{E}_T)|$ adopts larger values. Either the reconstructed $\varphi(\not{E}_T)$ suffers from an inferior resolution or the presence of two semileptonically decaying b-jets complicates the interpretation of $\varphi(\not{E}_T)$. In such events, in which $\cos(\Delta\varphi(l, \not{E}_T)) \approx -1$, the expression in (6.5) becomes more sensitive to the reconstructed values of $\not{E}_T$ and p_T^l. Both are steeply falling distributions with a lower threshold at 20 GeV, which is determined by the selection criteria (cf. Figure 5.4). In these type of events, the reconstructed m_T^W is likely to adopt values around 40 GeV, which is indeed observed in Figure 6.13.

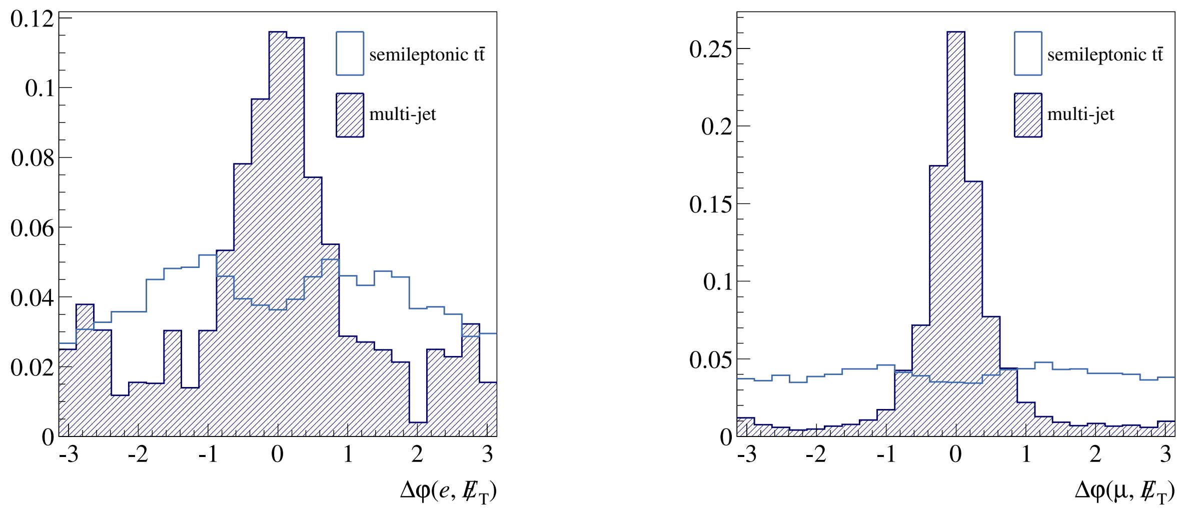

(a) The electron channel.

(b) The muon channel.

Figure 6.14: Comparison between the $\Delta\varphi(l, \not{E}_T)$ distribution in selected multi-jet events and in selected $t\bar{t}$ events. The distributions are normalized to unity.

Multi-jet events in which the opening angle $\Delta\varphi(l, \not{E}_T)$ is small are already suppressed by the restriction $m_T^W > 50$ GeV. In order to further suppress the multi-jet contribution, an additional requirement is imposed when performing the template fit method. Instead of the opening angle with respect to the lepton, the azimuthal angle of $\not{\boldsymbol{E}}_T$ is now compared to that of the closest reconstructed jet:

- The opening angle in the transverse plane between the reconstructed $\not{\boldsymbol{E}}_T$ and the closest reconstructed jet is to satisy $|\Delta\varphi(\not{E}_{\mathrm{T}}, \mathrm{jet})| > 0.3$.

The motivation for this requirement is illustrated by Figure 6.15, which displays the normalized distributions for multi-jet events and $t\bar{t}$ events that are selected in the muon channel and satisfy $m_{\mathrm{T}}^{W} > 50$ GeV. When the $\not{E}_{\mathrm{T}}$ in an event points in the same direction as a reconstructed jet, large $\not{E}_{\mathrm{T}}^{\mathrm{Fake}}$ is likely to be present due to a mis-reconstruction of the jet.

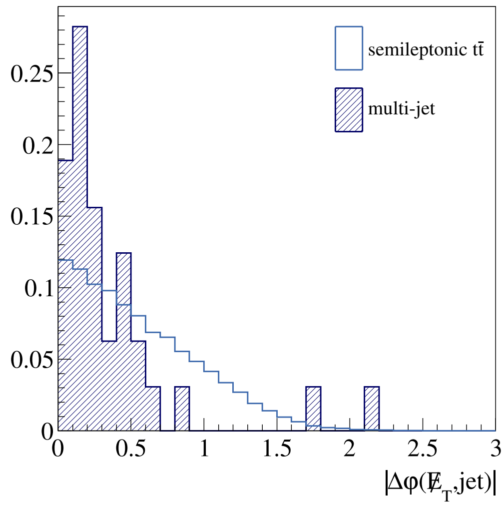

Figure 6.15: The angle $|\Delta\varphi(\not{E}_{\mathrm{T}}, \mathrm{jet})|$ between the reconstucted $\not{E}_{\mathrm{T}}$ and the closest reconstructed jet in the transverse plane. The distributions are shown for $t\bar{t}$ and multi-jet events that are selected in the muon channel and satisfy $m_{\mathrm{T}}^{W} > 50$ GeV.

6.2.5 b-Tagging

In the future, as soon as the efficiency of the b-tagging algorithm is reasonably well understood, the event selection can be extended to include the requirement that two b-tagged jets are reconstructed. Such an additional requirement will greatly improve the purity of the sample of selected events. However, the number of available events in 200 pb^{-1} decreases since all contributions are affected. In particular the contribution from $W+$ jets events will be severely diminished. The cumulative distributions for the muon channel are shown in Figure 6.16, where jets are b-tagged if their combined weight is larger than 5.0 (cf. Figure 4.5). Depending on the progress of b-tagging validation, the performance of the $\not{E}_{\mathrm{T}}$ reconstruction may be investigated in such a sample as well by means of the m_{T}^{W} template fit.

6.3 Results of the Template Fit

The proposed method to investigate the performance of the $\not{E}_{\mathrm{T}}$ reconstruction is now tested in a wide range of scenarios. The templates include all event samples except for multi-jet events. The input scenarios contain all Monte Carlo samples, yet the number of events in each of the input distributions is restricted as to correspond to 200 pb^{-1}. The input distributions are obtained by scaling the components of the reconstructed $\not{E}_{\mathrm{T}}$ in these events with α and convoluting them with a Gaussian of width r GeV. For events that pass

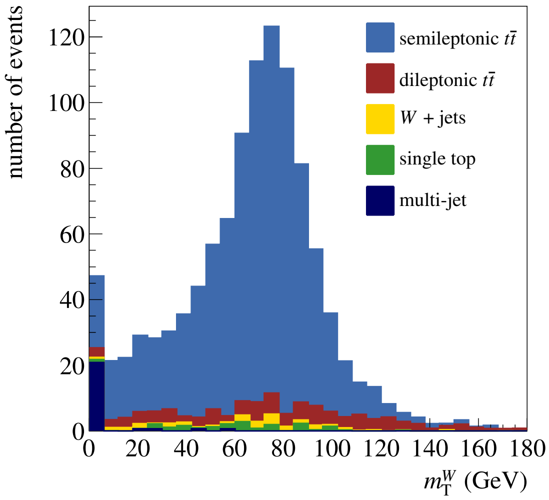

Figure 6.16: The cumulative distributions of m_{T}^{W} for selected events in the muon channel with the additional requirement that two b-tagged jets are reconstructed.

the selection criteria after this modification, the transverse W boson mass is reconstructed and fitted to the templates.

To illustrate the procedure, the m_{T}^{W} distributions corresponding to the input, the nominal template and the best fit are shown in Figure 6.17(a) for one specific scenario. The input distribution corresponds to events in which $\not{E}_{\mathrm{T}}$ is subject to $\alpha = 0.8$ and $r = 8$ GeV and the events pass the electron channel selection criteria. The template that renders the

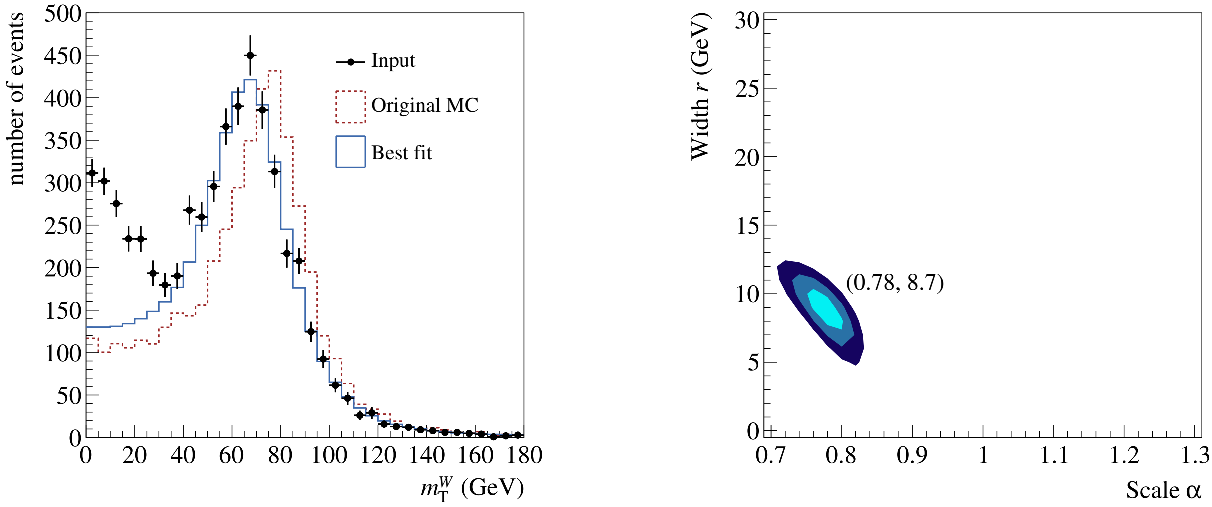

(a) The m_{T}^{W} distribution in selected events in which $\not{E}_{\mathrm{T}}$ is modified (markers), the distribution corresponding to the best template (line) and the original distribution (dashed line).

(b) The contours corresponding to deviations of 1σ, 2σ and 3σ around the point that provides the minimal χ^2.

Figure 6.17: The result of an example where the template fit is performed on simulated events in which (α, r) is set to (0.8,8 GeV). The distributions correspond to selected events in the electron channel in 200 pb^{-1}.

minimal χ^2 in this example corresponds to $(\alpha, r)^{\text{fit}} = (0.78^{+0.027}_{-0.018}, 8.7^{+1.72}_{-1.09}\,\text{GeV})$, which agrees well with the input values. The contours that correspond to standard deviations of 1σ, 2σ and 3σ around the minimum are indicated in Figure 6.17(b). A correlation is observed between the scale α and the width r, indicating that their contributions to the shape of m_{T}^{W} can not be disentangled entirely.

The results of the template fit for all investigated scenarios are graphically displayed in Figure 6.18. The input values cover all combinations of $\alpha \in \{0.8, 0.9, 1.0, 1.1, 1.2\}$ and $r \in \{0, 4, 8, 12\}$ GeV. Figures 6.18(a) and 6.18(c) contain the respective values of α^{fit} and r^{fit} in the electron channel, while Figures 6.18(b) and 6.18(d) display the results in the muon channel. The results are in good agreement with the input values for most of the scenarios. The electron channel seems slightly more challenging than the muon channel, which is likely to be caused by the difference in contributions from multi-jet events. It turns out that an addition of more than 8 GeV to the original resolution is too severe to be retrieved exactly. The value of r^{fit} is generally overestimated whereas the value of α^{fit} is underestimated in these cases. This bias is caused by the fact that the fit model does not include the multi-jet contribution and by the correlation between the fit parameters. A large disagreement with the nominal values is nevertheless observed, indicating that the reconstruction algorithm and the detector performance need to be investigated. An additional resolution on $\not{E}_{\text{T}}$ of the order of the nominal resolution is however quite unlikely.

As described in Section 6.2.1, there are many possible reasons for the reconstructed $\not{E}_{\text{T}}$ to deviate from the expectation from Monte Carlo. Not all scenarios are quantitatively described by the above parametrization, although discrepancies do indicate that further investigation is required. If the nominal values are not retrieved, each of the contributions in (4.9) is to be investigated in more detail. For example, in case a discrepancy is observed in the muon channel whereas the electron channel results are in agreement with the nominal values, it makes sense to adjust the fit model as to retrieve a scale in the contribution of $\not{E}_{x,y}^{\text{MuonBoy}}$. A scenario, for instance, in which the calorimeter response is locally distorted results in nonzero values of r^{fit} and is subsequently best identified by regarding the distribution of $\varphi(\not{E}_{\text{T}})$.

Conclusion

The template fit method using m_{T}^{W} provides a way to test and understand the performance in events with large final state activity and in the electron and muon channel separately. Its results clearly indicate the compatibility of the $\not{E}_{\text{T}}$ reconstruction in the data with the expectation from Monte Carlo. The method is stable under variations of the cross sections of $W+$ jets as well as multi-jet events. As a bonus, the poorly understood contribution from multi-jet events may be extracted from data.

The proposed method is performed on a small sample of 2010 data in Chapter 8.

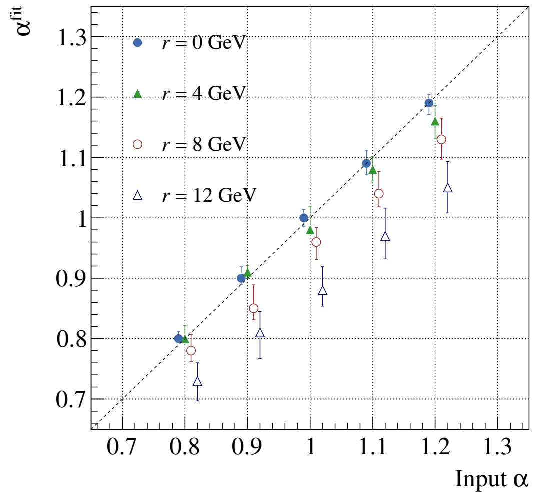

(a) The values of α^{fit} for all scenarios in the electron channel.

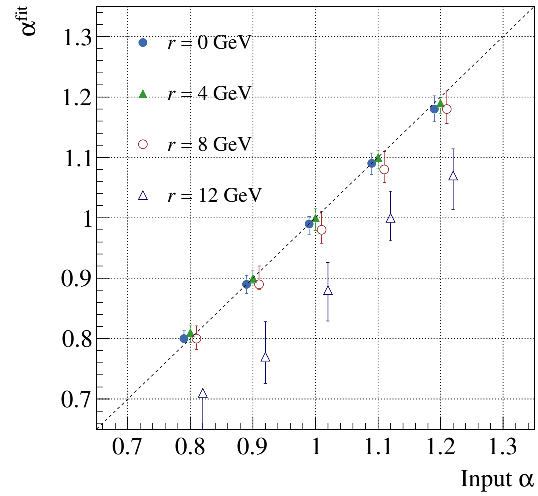

(b) The values of α^{fit} for all scenarios in the muon channel.

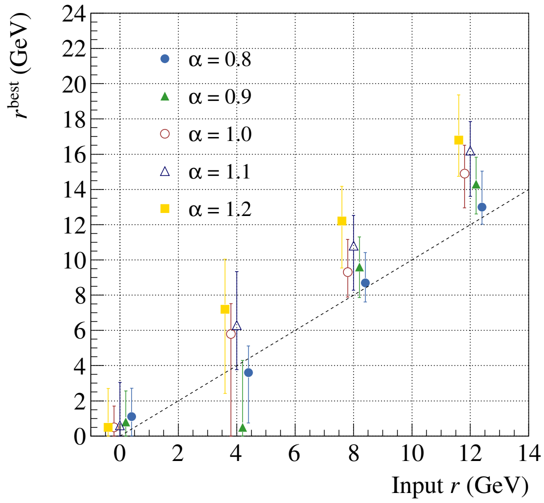

(c) The values of r^{fit} for all scenarios in the electron channel.

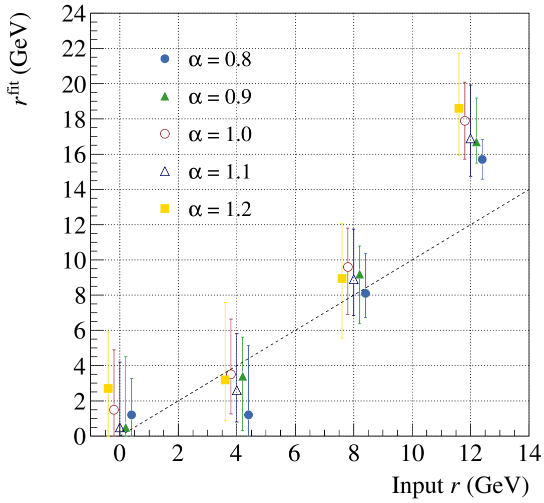

(d) The values of r^{fit} for all scenarios in the muon channel.

Figure 6.18: The results of the m_{T}^{W} template fit in all scenarios constructed with simulated events.

7

Search for $W' \rightarrow tb$

Several proposed extensions of the Standard Model introduce a heavy partner of the W boson: a W' boson. In this chapter, the discovery potential for such a W' boson is investigated in the context of Little Higgs models (cf. Section 1.3) and in particular the decay channel $W' \rightarrow tb$. The mass of the W' boson depends on the model at hand and the choice of parameters, yet results from Tevatron experiments [27] set a lower limit of 731 GeV with 95% confidence level. With that in mind, the two benchmark mass values $m_{W'} = 750$ GeV and $m_{W'} = 1$ TeV are used in the analysis here. Of particular interest is the feasibility of measuring the $W' \rightarrow tb$ signal with the ATLAS detector at an early stage. The study presented here is performed on events generated at $\sqrt{s} = 10$ TeV and is based on 1 fb^{-1} integrated luminosity.

Due to the large mass of the W' boson, its production cross section is suppressed with respect to many Standard Model processes and a sophisticated event selection is essential to isolate the $W' \rightarrow tb$ events. Along the same lines as the selection of semileptonic $t\bar{t}$ events in Chapter 5, the leptonic decay chain of the top quark is experimentally favoured over the hadronic decay as it provides good trigger and event selection possibilities. Again, the electron and the muon channel are more suitable than the tau channel. In fact, the signature of the events is quite similar to that of semileptonic $t\bar{t}$ events and they form the main background. As a consequence, however, the event selection in Section 5.2 serves as a good starting point for the pre-selection applied here. An additional number of kinematic variables is exploited to avert semileptonic $t\bar{t}$ events and reduce other background contributions, as described in Section 7.1. Subsequently, a likelihood fit is performed on the distribution of the reconstructed mass of the W' boson, which is described in Section 7.2. Finally, the results are discussed in Section 7.3.

7.1 Event Selection

The expected signature of $W' \rightarrow tb$ events in the ATLAS detector consists of a single charged isolated lepton, $\not{E}_{\mathrm{T}}$ induced by the neutrino and two jets. A sketch of the event topology is shown in Figure 7.1. The isolated charged lepton serves as the trigger object candidate. Due to the large mass of the W' boson, the accessible phase space allows for large (transverse) momenta of the final state objects, which distinguishes the signature from the Standard Model processes. The final state of the single top s-channel, $W \to tb$, is in fact exactly the same, yet the accessible phase space for the decay products is suppressed as a consequence of the Standard Model W mass being smaller than the top quark mass.

High values of the momentum fractions x_1 and x_2 are required for the W' boson to be produced in the proton collisions and little additional kinetic energy is available for the W' boson once it is produced. Figure 7.2 displays the direction φ in the transverse plane of each of the decay products of the W' boson. It shows that the t and b quarks are primarily produced back-to-back in the transverse plane. The available momentum for each quark is close to half the mass of the W' boson. Both quarks are subject to a Lorentz boost and the decay products of the top quark are expected to be produced with a small opening angle. The event selection makes use of these features. All distributions displayed in this section are scaled as to correspond to 1 fb^{-1} of integrated luminosity. The cross sections corresponding to the Littlest Higgs model are used for the signal contributions. In case of the LRTH scenario, the number of events is reduced by a factor of 3 for $m_{W'} = 750$ GeV and a factor of 5 in case of $m_{W'} = 1$ TeV (cf. Section 3.3.2).

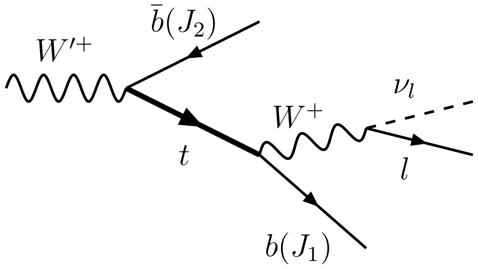

Figure 7.1: The event topology of $W' \to tb$ events.

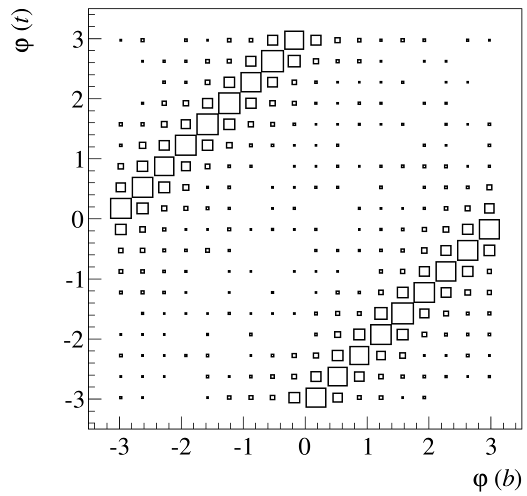

Figure 7.2: The two-dimensional distribution of the angle φ in the transverse plane of each the decay products of the W' boson. They are primarily produced back-to-back.

7.1.1 Pre-selection

First, the following pre-selection is applied to the events:

- The event passes the trigger chain `mu10` or `e20_loose`. The corresponding trigger efficiencies in $W' \to tb$ events are equivalent to those in $t\bar{t}$ events (cf. Figures 4.1(a) and 4.1(b));

- Exactly one medium electron or combined muon is reconstructed, satisfying $p_T > 20$ GeV;
- Two, three or four jets are reconstructed according to `Cone4H1TowerJets`, each of which satisfies $p_T > 20$ GeV and for each of which the opening angle with respect to the lepton satisfies $\Delta R(\text{jet}, l) > 0.3$. Figure 7.3(a) shows the number of reconstructed jets in each of the $W' \rightarrow tb$ samples, in the $t\bar{t}$ sample and in the unfiltered $W+$ jets samples. The same distribution for the remaining Standard Model background processes was displayed in Chapter 5 in Figure 5.1(c);
- $\sum E_T + \not{E}_T > 400$ GeV. The two-dimensional distribution for signal and background processes is displayed in Figure 7.3(b). For the signal, both mass reference values are displayed.

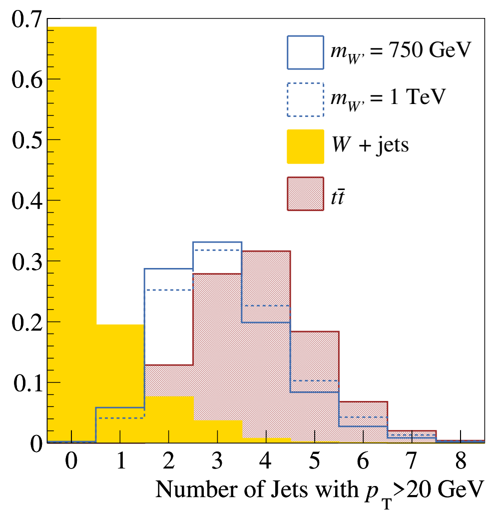

(a)

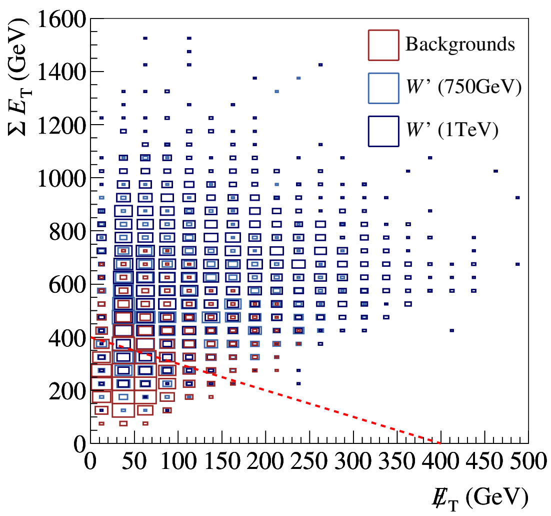

(b)

Figure 7.3: (a) The number of reconstructed jets with $p_T > 20$ GeV in each of the signal samples and in the unfiltered $W+$ jets samples. (b) Two-dimensional distribution of $\sum E_T$ versus $\not{E}_T$ in signal and cumulated background events. The sum is required to be larger than 400 GeV.

Jet Labelling

In order to be able to distinguish between their properties, the reconstructed jets are labelled for future reference. Two of the reconstructed jets are to be associated to the bottom quarks in the decay $W' \rightarrow tb \rightarrow l\nu bb$. The jet that results from the decaying top quark is likely to be in close vicinity of the reconstructed lepton that originates from the same top quark. Therefore, out of the two, three or four reconstructed jets, the one closest to the reconstructed lepton in ΔR is associated to the bottom quark from the top quark decay. This jet is labelled J_1 and will be used later on to reconstruct the intermediate top quark. Of the remaining jets, the jet with the highest transverse momentum is likely to originate directly from the W' boson decay and is labelled J_2. The efficiency of the correct assignments is investigated by matching to the respective b quarks with $\Delta R < 0.4$ and results in 72 ± 2 % for J_1 and 86 ± 2 % for J_2. The jet labels are indicated in Figure 7.1. With these jet labels in mind, the following requirements are added to the pre-selection:

- The opening angle $\Delta R(J_1, l)$ between the jet J_1 and the reconstructed charged lepton l is required to be smaller than 2.0, while $\Delta R(J_2, l)$ is required to be larger than 2.0. The normalized distributions for the signal with $m_{W'} = 750$ GeV and for the Standard Model background events are displayed in Figure 7.4(a);

- In case four jets are reconstructed, the two jets without a label are combined with J_2 and their mass is reconstructed. In $t\bar{t}$ events, this quantity is associated with the mass of the hadronically decaying top quark, which is expected to be around 175 GeV. In $W' \to tb$ events, the two additional jets originate most likely from initial or final state radiation and no excess around 175 GeV is expected. The reconstructed mass, m_t^{had}, is thus required to be larger than 200 GeV in order to suppress the contribution from $t\bar{t}$ events. The normalized distributions for $t\bar{t}$ events and $W' \to tb$ events are displayed in Figure 7.4(b);

- The p_{T} of the jet with label J_2 is required to be larger than 100 GeV. The cumulative distributions for signal and background events are shown in Figure 7.5(a) for both mass reference points. As the W' boson is produced nearly at rest, the signal distribution displays a Jacobian peak around half the W' boson mass;

- The p_{T} of the top quark is reconstructed by combining the charged lepton, the jet labelled J_1 and the missing transverse energy. The resulting $p_{\mathrm{T}}^{\mathrm{top}}$ is required to be at least 100 GeV as illustrated in Figure 7.5(b).

7.1.2 b-Tagging

Eventually, the jets with labels J_1 and J_2 are required to be b-tagged according to the b-tagging algorithm described in Section 4.3. The threshold on the combined weight is set to 5.0, i.e. a jet is b-tagged if its combined weight exceeds 5.0. The b-tagging efficiency for jets from b-quarks in $W' \to tb$ events is shown in Figure 7.6. The probability for light and c-jets in $W+$ jets events to be b-tagged is depicted in the same figure. The jets satisfy $p_{\mathrm{T}} > 20$ GeV and are matched to partons when $\Delta R < 0.3$. With this choice of threshold for the combined weight, the efficiency for b-jets in signal events to be correctly b-tagged is about 60 %. For very high transverse momenta of jets, the quality of the track reconstruction suffers from an increased density and multiplicity of tracks. Figure 7.6 shows that the b-tagging efficiency decreases accordingly. For the same choice of combined weight threshold, the efficiency of (incorrectly) b-tagged light and c-jets in the main background sample is merely a few percent and the b-tagging requirement is very successful in the suppression of these events.

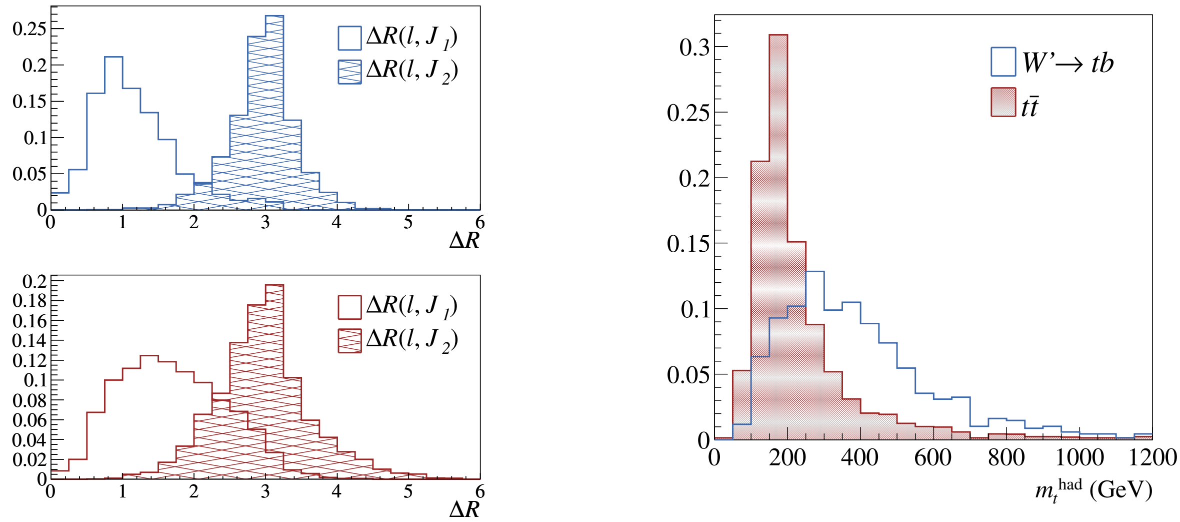

(a) (b)

Figure 7.4: (a) The opening angle ΔR between the charged lepton and each of the reconstructed jets J_1 and J_2 in $W' \to tb$ events with $m_{W'} = 750$ GeV (top) and in the Standard Model background events (bottom). (b) The reconstructed mass of the combination of the jet J_2 with the two additional jets in case four jets are reconstructed in $W' \to tb$ events and $t\bar{t}$ events.

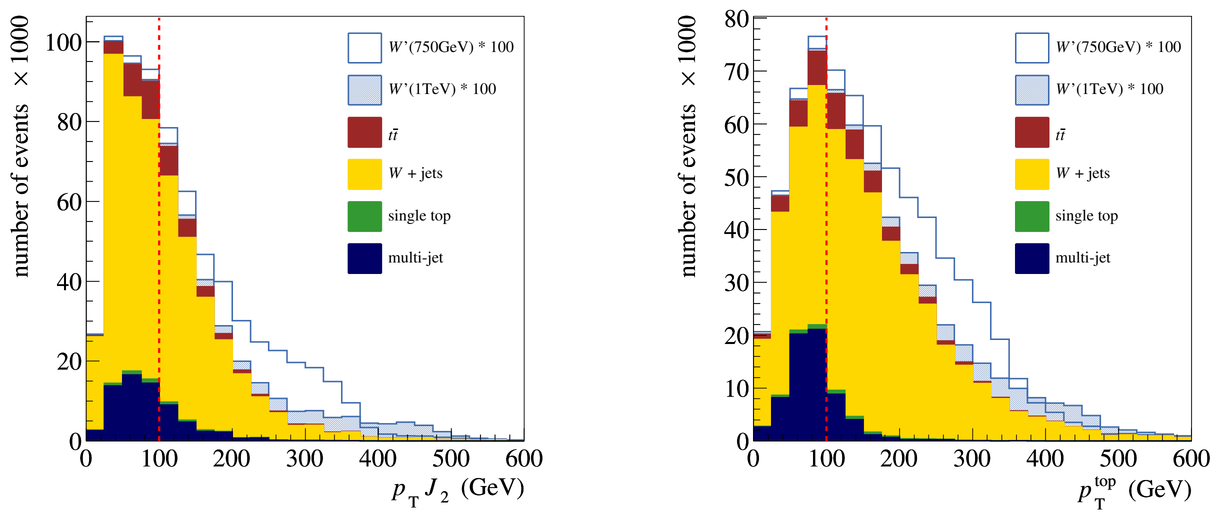

(a) The p_{T} of jet J_2. (b) The p_{T} of the reconstructed top.

Figure 7.5: Some of the kinematic variables that are part of the pre-selection criteria. The number of events corresponds to 1 fb^{-1} except for the signal, which has been multiplied by a factor of 100.

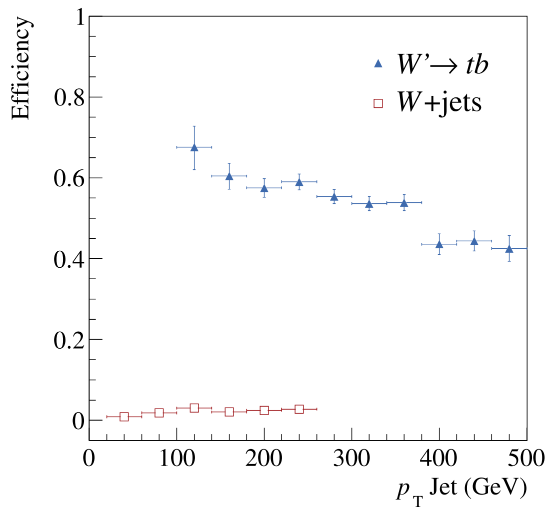

Figure 7.6: The b-tagging efficiency of b-jets in $W' \to tb$ events and that of light and c-jets in $W+$ jets events.

Figure 7.7 illustrates the impact of the b-tagging requirement on the distribution of the reconstructed mass of the W' boson. The invariant mass of the W' boson is reconstructed by combining the momenta of all reconstructed final state objects, i.e. the lepton, the neutrino, the jets J_1 and J_2 and up to two additional jets that satisfy $p_{\mathrm{T}} > 20$ GeV. The neutrino's transverse momentum is approximated by the missing transverse energy in the event as usual. Its longitudinal momentum is estimated by constraining the combination of the lepton and the neutrino to the mass of the W boson, 80.4 GeV. Setting the small mass of the charged lepton l to zero, the constraint reads

$$\begin{aligned} m_W^2 &= (P_l + P_\nu)^2 \\ &= 2E_l E_\nu - 2(\boldsymbol{p}_l \cdot \boldsymbol{p}_\nu) \\ &= 2E_l \sqrt{\not{E}_{\mathrm{T}}^2 + p_\nu^z} - 2\left(p_l^x \not{E}_x + p_l^y \not{E}_y + p_l^z p_\nu^z\right), \end{aligned} \tag{7.1}$$

where $\not{E}_x$ and $\not{E}_y$ are substituted for the neutrino's transverse momentum components. The quadratic equation generally gives two solutions for p_ν^z, the smallest of which in absolute value is used.

The distributions in Figure 7.7 correspond to 1 fb^{-1} and contain all events that remain after the pre-selection (Figure 7.7(a)) and after the additional b-tagging requirement (Figure 7.7(b)). Both mass input values are shown for the $W' \to tb$ events. Before the b-tagging requirement, the signal contribution is virtually invisible. Afterwards, however, the contribution from $W+$ jets events is effectively reduced and the contribution from multi-jet events has disappeared entirely. Since their event topology contains two b-jets as well, the remaining background is dominated by $t\bar{t}$ events. It turns out that a multivariate technique is able to reduce the Standard model background contributions further, as described in the next section. The successful suppression of background events achieved by the b-tagging requirement is saved for last.

7.1.3 Fisher Discriminant

The pre-selection and b-tagging criteria successfully suppress the contribution from $W+$ jets events and multi-jet events. However, a large number of $t\bar{t}$ events survives these selection

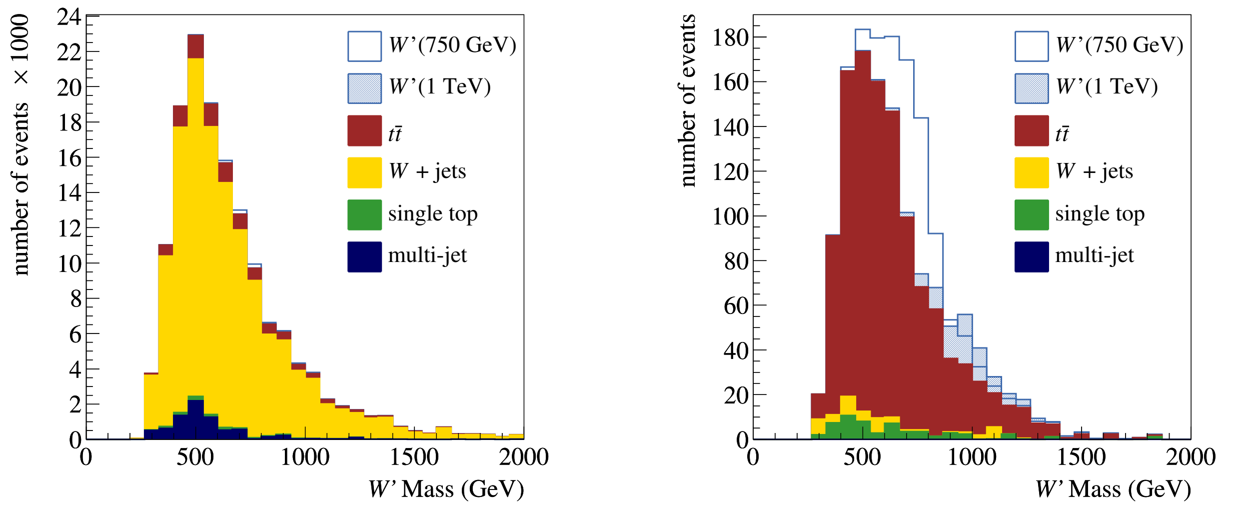

(a) After the pre-selection.

(b) After the pre-selection and the b-tagging requirement.

Figure 7.7: Reconstructed mass of the W' boson. The number of events corresponds to 1 fb^{-1} integrated luminosity.

criteria. Although Figure 7.7(b) indicates that the signal is distinguishable in case of the Littlest Higgs Model for $m_{W'} = 750$ GeV, improvement is needed in order for the scenario with $m_{W'} = 1$ TeV to give a satisfactory signal to background ratio. Moreover, the cross section for the LRTH model is even smaller (cf. Section 3.3), which enlarges the challenge.

It turns out that when exploited simultaneously, by means of a multivariate technique, the differences in the kinematic distributions for signal and background events can improve the separation. Several multivariate techniques as well as kinematic variables have been investigated. The use of the *Fisher Discriminant* is preferred here, as it is a linear selection technique[1].

The Fisher Discriminant is determined by finding the axis $\boldsymbol{w}$ in the hyperspace of N input variables onto which the projections of signal and background samples are maximally separated, while the dispersion of each of their projections is minimized. This is illustrated in Figure 7.8 for the simplified scenario with two input variables only.
The Fisher Discriminant (FD) for event i is given by

$$\mathrm{FD}(i) = F_0 + \sum_{k=1}^{N} F_k x_k(i),$$

where the coefficients F_k follow from the projection onto the axis $\boldsymbol{w}$ and depend on the number of events S and B in the input samples that describe the signal and background respectively. The offset F_0 centers the mean value of the projection of the entire input sample at zero. The calculation is performed in the `TMVA` framework [64].

[1] Similar results are achieved by *artificial neural networks* for instance, which are disfavoured here for their lack of transparency.

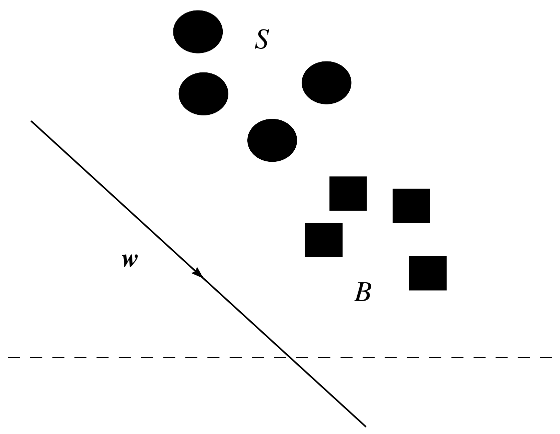

Figure 7.8: Illustration of the Fisher Discriminant procedure, which determines the axis $\boldsymbol{w}$ onto which the mean values of the projections of two classes of data are maximally separated.

As the signal cross sections are small, the electron and muon channel are summed up to increase the number of events in 1 fb^{-1}. In order to acquire a mass independent optimized Fisher Discriminant, both the sample with $m_{W'} = 750$ GeV and the sample with $m_{W'} = 1$ TeV are passed on simultaneously to the framework as signal. The b-tagging requirement is not applied just yet in order to profit from the ability of the multivariate technique to reduce the contribution from multi-jet events and $W+$ jets events based on different grounds first.

The following five input variables, in order of decreasing discriminating power, are employed:

- The p_{T} of the jet J_2;
- $p_{\mathrm{T}}^{\mathrm{top}}$, the reconstructed transverse momentum of the top quark, which is obtained by combining $\not{E}_{\mathrm{T}}$, the p_{T} of the jet J_1 and p_{T}^{l};
- The opening angle $\Delta R(J_1, l)$;
- m_{T}^{W}, the transverse W boson mass that was introduced in Chapter 6;
- The p_{T} of the jet J_1.

The normalized distributions for each of the above variables are displayed in Appendix C in Figure C.1 for signal events and background events separately. Both mass reference samples are included in the signal distributions. The resulting value of the Fisher Discriminant for each event is shown in Figure 7.9(a). The signal efficiency and background rejection that are achieved by different choices of a lower bound on the value of the Fisher Discriminant are displayed in Figure 7.9(b). Requiring this value to be positive results in a signal efficiency of 79 % with a background rejection of 84 %. This is applied in addition to the pre-selection criteria in what follows.

At this point, the b-tagging requirement described in Section 7.1.2 is applied. The resulting distribution for the reconstructed mass of the W' boson is shown in Figure 7.10 for both mass reference points in the Littlest Higgs scenario. As a consequence of the Fisher Discriminant requirement, the contribution from $t\bar{t}$ events is heavily reduced compared to Figure 7.7(b) The $W' \to tb$ signal is now clearly visible as a peak above a rather flat background distribution, which consists almost entirely of $t\bar{t}$ events.

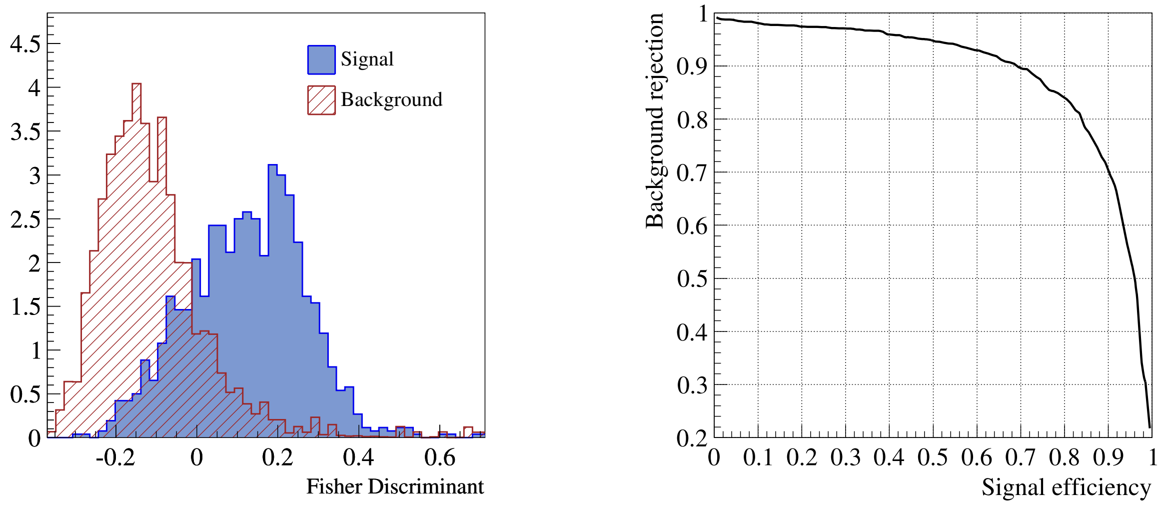

(a) The normalized output distributions of the Fisher Discriminant for the signal and background samples.

(b) Background rejection versus signal efficiency for different values of the Fisher Discriminant.

Figure 7.9: Output for the Fisher Discriminant.

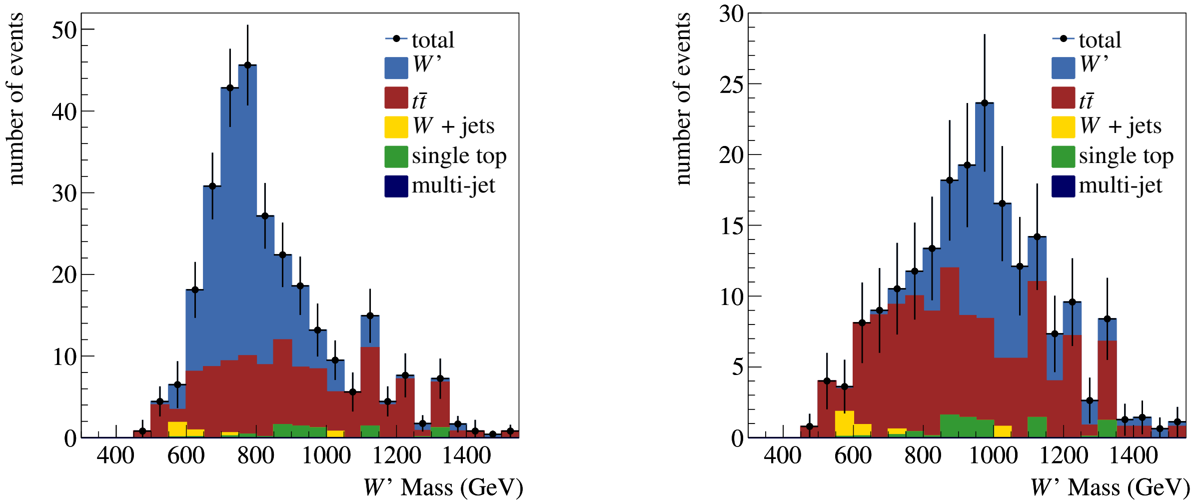

(a) $m_{W'} = 750$ GeV

(b) $m_{W'} = 1$ TeV

Figure 7.10: Reconstructed mass of the W' boson for the Littlest Higgs model after the pre-selection, the b-tagging and the Fisher Discriminant requirement. The number of events corresponds to 1 fb^{-1} integrated luminosity.

The impact of each stage of the event selection is quantified in Table 7.1 by comparing the number of signal events S to the number of background events B in the peak. It shows the statistical significance $S/\sqrt{B}$ after the pre-selection only, after including the Fisher Discriminant requirement and finally after the full selection including the b-tagging requirement. The two leftmost columns contain the numbers for the Littlest Higgs cross sections in the mass windows [700,800] and [950,1050] respectively. The two rightmost columns show $S/\sqrt{B}$ in the respective mass windows for the LRTH scenario. The numbers correspond to 1 fb^{-1} integrated luminosity. Both the b-tagging requirement and the Fisher Discriminant greatly improve the relative signal contribution.

On the right hand side, the selection efficiencies for the signal are displayed for both mass input values. The efficiency of the pre-selection and the Fisher Discriminant are highest for the larger $m_{W'}$ as the input distributions for the signal are generally more separated from the background distributions. The efficiency of the b-tagging requirement, however, is larger for the signal with $m_{W'} = 750$ GeV as the b-tagging does not suffer as much from the high-p_{T} effects.

	Littlest Higgs		**LRTH**		**Efficiency**	
$m_{W'}$	750 GeV	1 TeV	750 GeV	1 TeV	750 GeV	1 TeV
pre-selection	2.9	1.6	0.91	0.29	25 %	29 %
pre + Fisher	5.8	2.7	1.8	0.50	13 %	23 %
pre + Fisher + b-tagging	14	6.5	4.4	1.2	4 %	5 %

Table 7.1: $S/\sqrt{B}$ in a 100 GeV mass window at each stage of the event selection and the selection efficiency for the signal at each stage.

7.2 Likelihood Fit

The contribution of background and signal events to the distribution of the mass of the W' boson is estimated by means of a binned extended likelihood fit. The functional forms of both the shape of the signal contribution and the shape of the background contribution are fixed. The ratio of their contributions that best results in the total distribution is determined by the fit. In addition, the position of the signal peak is varied in order to perform a mass independent search.

7.2.1 The Shape Functions

The functional forms for the shape of the signal and the shape of the background contribution are determined empirically from the Monte Carlo distributions. The signal is described by a Gaussian that smoothly converts into a falling exponential:

$$f_S(x) = \begin{cases} \frac{p_0}{\sqrt{2\pi}} \; e^{-\frac{(x-p_1)^2}{2p_2^2}} & x < p_1 + \frac{p_2^2}{2p_3} \\ \frac{p_0'}{\sqrt{2\pi}} \; e^{-\frac{(x-p_1)}{2p_3}} & x > p_1 + \frac{p_2^2}{2p_3} \end{cases} \tag{7.2}$$

where p_0' is expressed in terms of the other parameters as

$$p_0' = p_0 \; e^{\frac{p_2^2}{8p_3^2}}.$$

The parameters p_2 and p_3 are fixed by means of a minimum χ^2 fit to the signal distribution for $m_{W'} = 750$ GeV. The normalization p_0 and the position of the peak p_1 are free parameters. The contribution from Standard Model background events is described by an asymmetric Gaussian:

$$f_B(x) = \begin{cases} \frac{q_0}{\sqrt{2\pi}} \; e^{-\frac{(x-q_1)^2}{2q_2^2}} & x < q_1 \\ \frac{q_0}{\sqrt{2\pi}} \; e^{-\frac{(x-q_1)^2}{2q_3^2}} & x > q_1 \end{cases} \tag{7.3}$$

Three out of four parameters in $f_B(x)$ are fixed by a minimum χ^2 fit to the background distribution. The normalization q_0 remains a free parameter. The normalized functions f_S and f_B are drawn in Figure 7.11 for one particular choice of p_1.

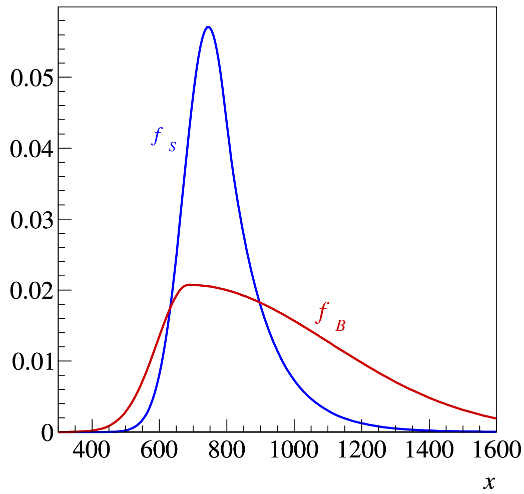

Figure 7.11: Normalized functions f_S and f_B describing the shape of the signal and background.

Background Shape Estimate

It is acknowledged that the background shape f_B is purely based on simulation, even though the high-p_T behaviour of the $t\bar{t}$ events may not be modelled perfectly well by Monte Carlo. It is actually possible to estimate the shape of the background for selected events from the data. To this end, four distributions are constructed, each corresponding to different selection criteria as schematically illustrated by Figure 7.12. On one hand, the events either pass or fail the Fisher Discriminant (FD) requirement and on the other hand, either zero or two jets are b-tagged. The events in region IV are those depicted in Figure 7.10 and the objective is to determine the share of background events in that region.

First, a sample is selected that is dominated by background events, i.e. the distribution of the reconstructed W' boson mass is made for events that contain zero b-tagged jets and for which the Fisher Discriminant (FD) takes negative values. These events correspond to region I in Figure 7.12. The contribution of signal events S_0 is negligible for these criteria, i.e. $S_0 \ll B_0$. The number of background events in the final W' mass distribution is related to B_0 through the functions β_{FD} and β_b. In order to estimate β_{FD}, the distribution for events in region II is divided by the distribution for events in region I. The obtained distribution, β_{FD}, models the impact of the requirement FD > 0 in events with zero b-tagged jets.

Assuming that the impact of this requirement is equivalent in events that do pass the b-tagging requirement, the desired background distribution for selected events is estimated as follows: the W' boson mass distribution for events in region III is multiplied by the obtained β_{FD}. Figure 7.13(b) shows that the resulting distribution agrees well with the desired background distribution.

A fit of of the function f_B to the obtained distribution results in a slightly tilted function with respect to the original background description. Therefore, in order to address the systematic effect caused by the assumption on the background shape, the likelihood fit is performed three times in the following: Once with the original f_B describing the background, once with f_B^+ and once with f_B^-. The parameters in $f_B^\pm$ are obtained by forcing the function to tilt left and right respectively with an amount corresponding to a 1σ effect on the χ^2 of the fit.

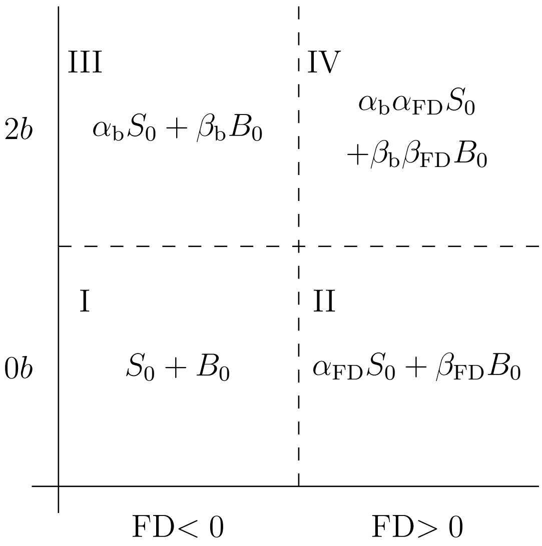

Figure 7.12: The four regions that are constructed in terms of selection criteria in the procedure to obtain an estimate of the background contribution.

7.2.2 Mass Scan

The search for an excess in the W' reconstructed mass distribution aims to be independent of the actual mass $m_{W'}$. Therefore, the likelihood L is determined for several values of $p_1 \in [550, 1150]$ GeV in search of the peak position that corresponds best to the data. For

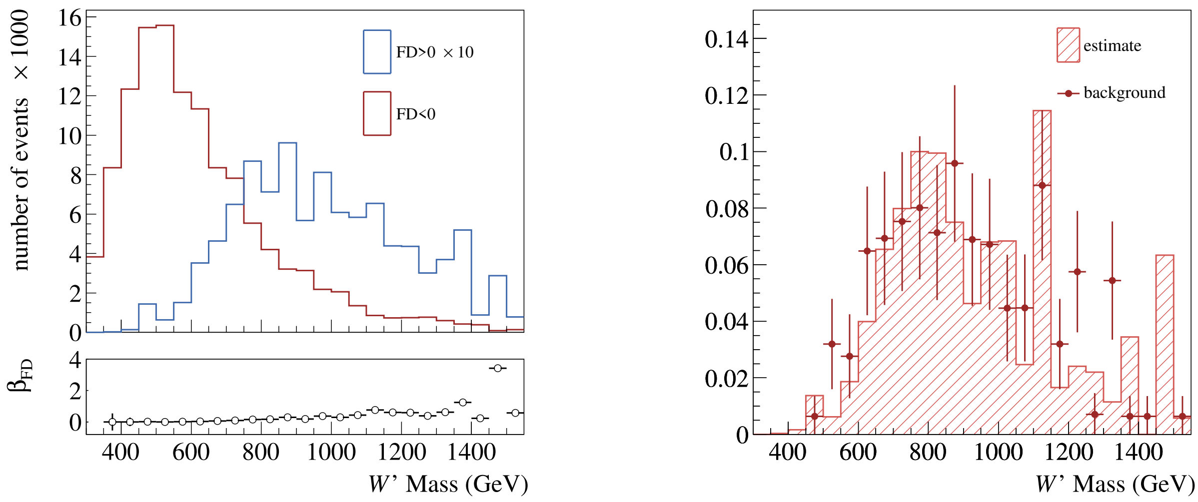

(a) (b)

Figure 7.13: (a) (top) The distributions of the reconstructed mass of the W' boson for events in regions I and II, i.e. events with zero b-tagged jets that fail and pass the Fisher Discriminant. (bottom) The ratio β_{FD} of the distributions. (b) The estimated shape of background events that pass all selection criteria and the actual background distribution.

each value of p_1, the optimal ratio of p_0 to q_0 is determined first by minimizing the negative log-likelihood. Assuming Poisson distributed histograms, the expression is

$$-\ln(L) = -\sum_i \ln\left(\frac{f_i^{k_i} e^{-f_i}}{k_i!}\right) = \sum_i (f_i - k_i \ln(f_i)) + C, \tag{7.4}$$

where k_i is the measured content of the ith histogram bin and f_i is the expected bin content according to $f_S + f_B$. The constant C is ignored as the numerical value of the likelihood is irrelevant and only ratios of likelihoods are of interest.

The outcome of the log-likelihood for each value of p_1 is depicted in Figure 7.14 for the Littlest Higgs scenario and for both input mass values. The position of the minimum of the distribution is determined by a parabolic fit as indicated in the figure. The resulting values are $p_1 = 745 \pm 11$ GeV and $p_1 = 962 \pm 21$ GeV respectively, both in good agreement with the input mass values[2]. The results obtained with the tilted background shape function f_B^+ (f_B^-) are 738 (746) GeV and 962 (948) GeV, i.e. the impact is smaller than the statistical uncertainty. Additional systematic effects, for instance due to an uncertainty on the jet energy scale estimation, are expected to be minor by the time 1 fb^{-1} of data is accumulated. At present, using 2.9 pb^{-1} of data, the uncertainty estimate is 6% for jets with $p_{\text{T}} > 100$ GeV [65].

[2] The 1σ interval for the statistical uncertainty is obtained from each negative log-likelihood distribution by finding the values of p_1 where $2\Delta\ln(L) \approx \Delta\chi^2 = 1$ with respect to the minimum.

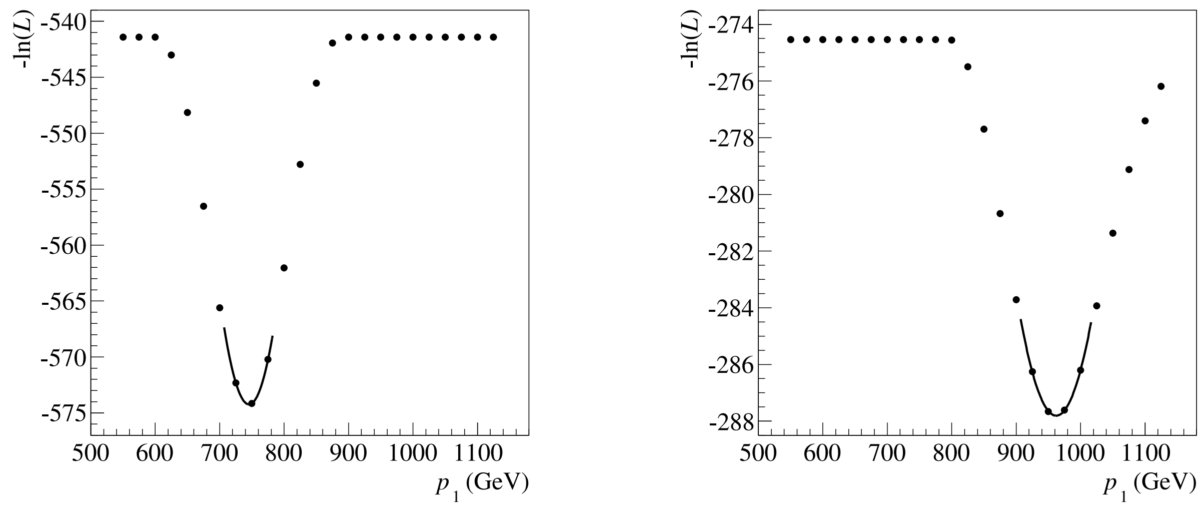

(a) For $m_{W'} = 750$ GeV.

(b) For $m_{W'} = 1$ TeV.

Figure 7.14: The results of a mass scan, i.e the value of $-\ln(L)$ according to (7.4) for each value of p_1 in (7.2).

For the first case, i.e. $m_{W'} = 750$ GeV, Figure 7.15 shows the graph of $f_S + f_B$ for $p_1 = 745$ GeV at the optimal ratio of p_0 and b_0 ("Fit result"). The curve is in good agreement with the distribution of the reconstructed mass of the W' boson ("Total"), which is indicated by the dots with error bars. Figure 7.15(a) displays in addition the signal contribution as estimated from the amplitude of f_S and the actual input signal contribution ("Signal"). The minimum of the negative log-likelihood distribution provides a good estimation of the position of the peak. Similarly, Figure 7.15(b) shows the actual background contribution and the estimation from the fit result for f_B.

7.2.3 Signal Significance

The estimated contributions of signal and background events according to the result of the likelihood fit are $N_{\text{sig}} = 157 \pm 29$ and $N_{\text{bkg}} = 128 \pm 28$ events respectively. These numbers agree with the number of events actually contained in the input distributions, which are 159 signal and 125 background events. Table 7.2 compares the fit results to the input values for all four scenarios considered. The impact of the variation of the background shape f_B described in Section 7.2.1 is indicated as well. The result of the likelihood for each of the four reference points is graphically displayed in Figure 7.17(a). It shows the 99 % confidence level contour that follows from the two-dimensional log-likelihood distribution of the fit as a function of N_{sig} and N_{bkg}.

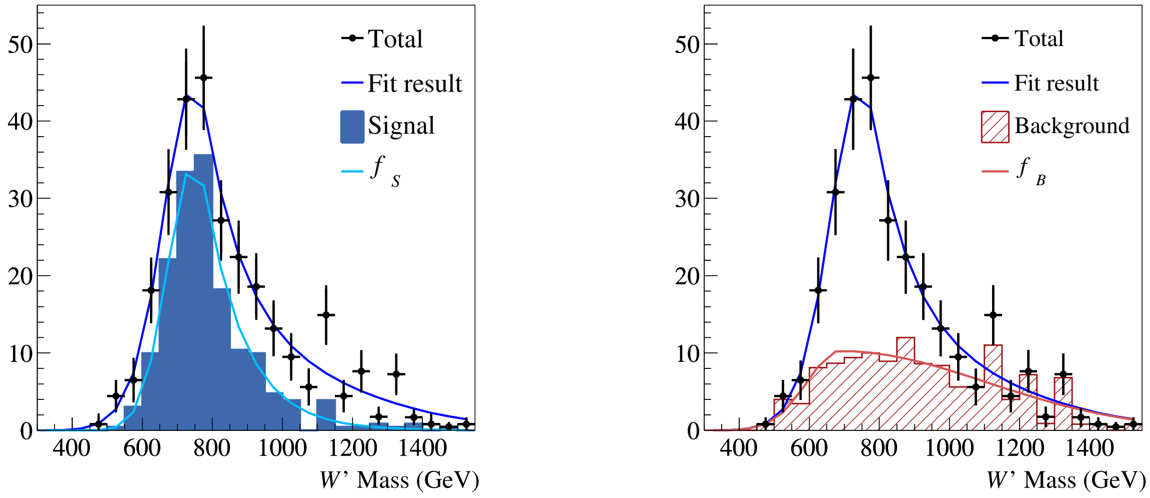

(a) Signal contribution. (b) Background contribution.

Figure 7.15: The result of the fit of $f_S + f_B$ to the reconstructed W' mass distribution at the minimum value of $-\ln L$, i.e. $p_1 = 745$ GeV.

Littlest Higgs				
	750 GeV		**1 TeV**	
	input	result	input	result
N_{sig}	159	$157 \pm 29\ ^{+19}$	72	$68 \pm 20\ ^{+3}_{-8}$
N_{bkg}	125	$128 \pm 28\ _{-20}$	125	$128 \pm 23\ ^{+9}_{-3}$

LRTH				
	input	result	input	result
N_{sig}	50	$48 \pm 22\ ^{+17}$	13	$17 \pm 11\ ^{+4}_{-7}$
N_{bkg}	125	$128 \pm 25\ _{-19}$	125	$121 \pm 15\ ^{+7}_{-4}$

Table 7.2: The number of events in the signal distribution, N_{sig}, and in the background distribution, N_{bkg}, according to the fit result compared to the input values in 1 fb^{-1}.

Toy Experiments

In order to claim an observation or discovery of a W' boson mass resonance, the level of compatibility of the data to the description with $N_{\text{sig}} > 0$ needs to be quantified. To this end, it is compared to the level of agreement of the data to the *null hypothesis*, which corresponds to the background-only description f_B.

A million *toy experiments* are generated to describe the expected distribution of Standard Model background events according to the shape in (7.3). The number of generated events per toy experiment is sampled from a Poisson distribution with mean value $N_{\mathrm{bkg}} = 125$. For each toy experiment, the complete model $f_S + f_B$ is fitted to the obtained distribution. The probability for the Standard Model to fluctuate such that a signal is observed is now obtained by simply counting the number of toy experiments for which the fit result N_{sig} is larger than the numbers listed in Table 7.2. The results of the toy experiments for the respective signal descriptions with $p_1 = 745$ GeV and $p_1 = 962$ GeV are displayed in Figure 7.16. Assuming normally distributed results, the probabilities are converted into significance values. Although the number of toy experiments is not sufficient to determine the significance in for the Littlest Higgs scenario, a lower limit can be deduced from the fact that the threshold is exceeded zero times. The results are given in Table 7.3.

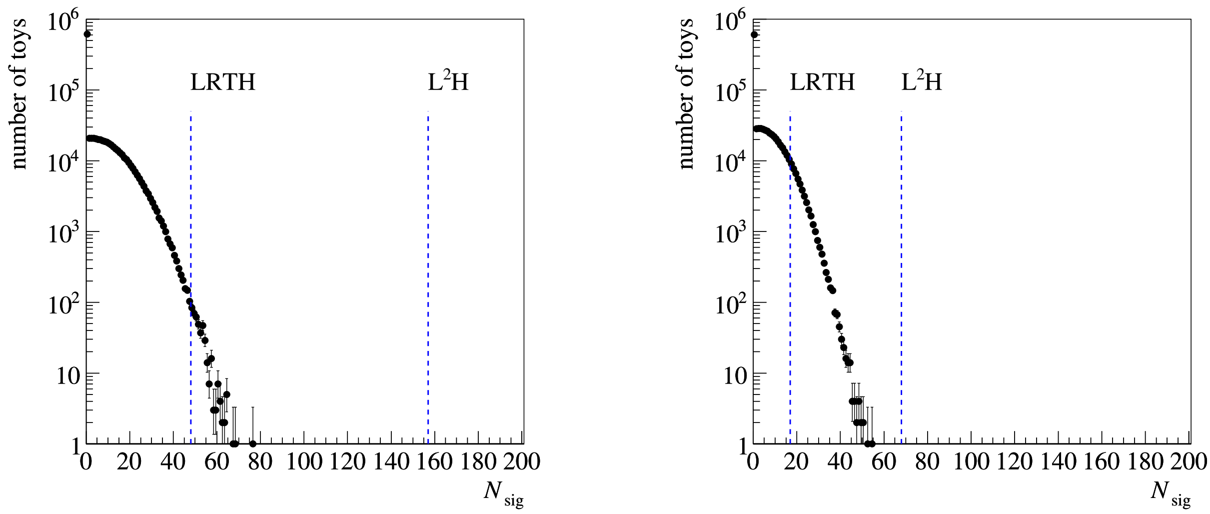

(a) For $p_1 = 745$ GeV.

(b) For $p_1 = 962$ GeV.

Figure 7.16: The outcome N_{sig} for each of the 1M toy experiments. The dotted lines indicate the values of N_{sig} as given in Table 7.2, i.e. when the signal is included.

Profile Likelihood Ratio

The *profile likelihood ratio* provides an analytical approach to determine the signal significance. It is constructed as

$$\lambda(\boldsymbol{X}; N_{\mathrm{sig}}) = -\ln\left(\frac{L(\boldsymbol{X}; N_{\mathrm{sig}}, N^*_{\mathrm{bkg}})}{L(\boldsymbol{X}; \hat{N}_{\mathrm{sig}}, \hat{N}_{\mathrm{bkg}})}\right). \tag{7.5}$$

The likelihood in the denominator of $\lambda(\boldsymbol{X}; N_{\mathrm{sig}})$ is evaluated at the parameters $\hat{N}_{\mathrm{sig}}$ and $\hat{N}_{\mathrm{bkg}}$, which maximize the likelihood of the signal-plus-background hypothesis given the data $\boldsymbol{X}$. The likelihood in the nominator is evaluated at N^*_{bkg}, which maximizes the likelihood for fixed values of N_{sig}.

Figure 7.17(b) displays the distribution of the profile likelihood ratio as a function of $N_{\rm sig}$. The compatibility of the data to H_{S+B} is now compared to the compatibility to H_B by evaluating the profile likelihood ratio at $N_{\rm sig} = 0$. According to *Wilk's Theorem*, $\lambda(N_{\rm sig})$ is assymptotically distributed as a χ^2, which implies that the significance is obtained as $\sqrt{2\lambda(0)}$. It follows from the figure that for $m_{W'} = 750$ GeV the significance of $N_{\rm sig} > 0$ is as large as $\sqrt{2 \cdot 33}\ \sigma \approx 8.1\sigma$. In case $m_{W'} = 1$ TeV, the significance of the signal is clearly smaller due to the decreased production cross section, but it still exceeds the 99 % confidence level with a result of 5.1σ.

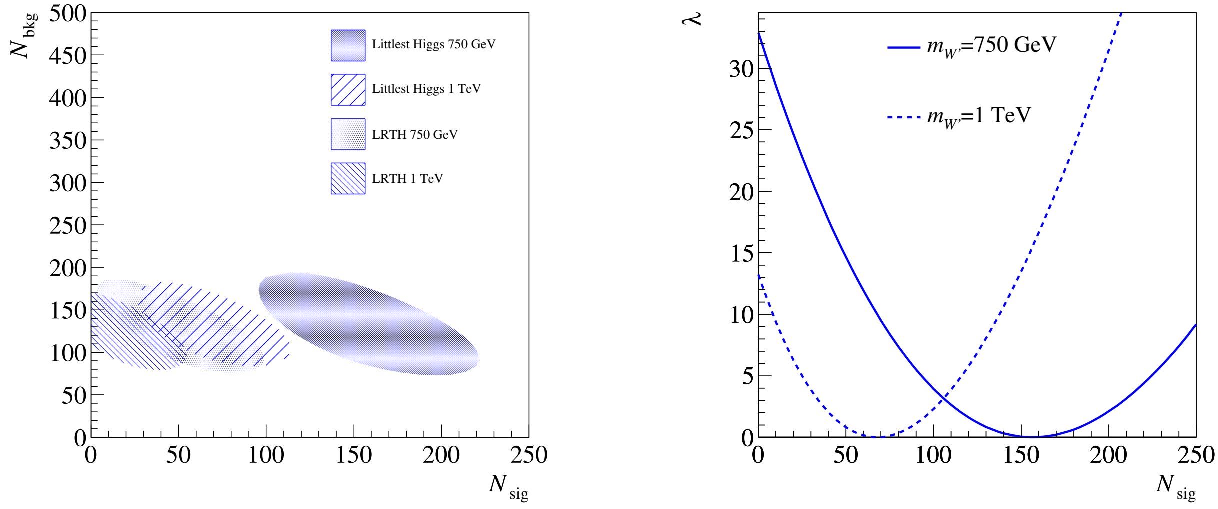

(a)

(b)

Figure 7.17: (a) The 99 % confidence level contours with 1 fb^{-1} for each of the four reference points. (b) The profile likelihood distribution of $N_{\rm sig}$ for both mass input values in the Littlest Higgs Model for 1 fb^{-1}.

The obtained values for the signal significance are compared to the values previously obtained with the toy experiments in Table 7.3. All results are in agreement and the lower limits for the Littlest Higgs model are replaced by the more precise values from the profile likelihood method.

	$m_{W'}$	$P(N_{\rm sig}\|H_B > N_{\rm sig}\|H_{S+B})$	Toy significance	PL significance
Littlest Higgs	750 GeV	0/1M	$> 4.8\sigma$	8.1σ
	1 TeV	0/1M	$> 4.8\sigma$	5.1σ
LRTH	750 GeV	360/1M	3.4σ	3.2σ
	1 TeV	43206/1M	1.7σ	1.6σ

Table 7.3: Comparison between the significance values obtained from the toy experiments and the values from the profile likelihood method in 1 fb^{-1}.

7.3 Results

This section investigates how the discovery potential of a $W' \to tb$ signal with ATLAS depends on the signal cross section and how it depends on the available amount of integrated luminosity. In addition, the impact of an uncertainty on the b-tagging efficiency is addressed.

Cross Section and Luminosity Reach

In the previous section, the significance of the $W' \to tb$ signal with 1 fb^{-1} for $m_{W'} =$ 750 GeV was investigated in two scenarios: the Littlest Higgs model and the LRTH model. In alternative models the $W' \to tb$ signal may be introduced with a different cross section. The question arises what the lower bound on the cross section is for ATLAS to reach a 5σ discovery with 1 fb^{-1} of data. This is investigated by varying the signal cross section and performing the likelihood fit for each distribution of the reconstructed mass of the W' boson. The result is displayed in Figure 7.18(a) and indicates a lower bound of 2.5 pb on the signal cross section for a 5σ significance with 1 fb^{-1}.

The figure also displays the belt corresponding to the uncertainty on the b-tagging efficiency. In the presented study, the efficiency is estimated from simulation (cf. Figure 7.6), although ultimately it is to be determined from the data. The precision will be limited and improve as the availability of jets with large transverse momenta will start to become sufficient for these performance studies[3]. Therefore, a conservative variation is considered here to investigate the impact on the expected discovery potential with 1 fb^{-1}. The probability for the jets J_1 and J_2 to be b-tagged is varied simultaneously for signal and background events. By matching each jet to a quark with $\Delta R < 0.3$, the efficiency is varied by ± 10 % for b-jets, ± 20 % for c-jets and by ± 50 % for light jets. This results in significance values of 8.3σ and 7.3σ respectively for $m_{W'} = 750$ GeV in the Littlest Higgs model. The impact is modest due to the fact that the majority of the events in both the signal and the background contribution contain two actual b quarks and thus scale proportionally.

Similarly, the lower bound on the integrated luminosity that suffices for a 5σ signal significance is investigated. For each of the four reference models, Figure 7.18(b) displays the signal significance versus the integrated luminosity. The 3σ and 5σ thresholds are indicated as well. It shows that with 400 pb^{-1} of data some conclusions may already be drawn regarding the Littlest Higgs model. In the most challenging scenario considered, however, the required amount of data for a 5σ signal significance is clearly larger than 5 fb^{-1}. For this LRTH scenario with $m_{W'} = 1$ TeV, extrapolation of the best fit of the function $a\sqrt{L}$ beyond the boundary of the figure indicates that 10 fb^{-1} is required for a signal significance that exceeds the 5σ threshold.

7.4 Discussion

The discovery potential of the decay $W' \to tb$ with the ATLAS detector was investigated for $m_{W'} \gtrsim 750$ GeV and $\sqrt{s} = 10$ TeV. By maximally exploiting the kinematic properties using

[3] In fact, the efficiency may be extracted from semileptonic $t\bar{t}$ events using m_t and m_W constraints to identify the b-jets.

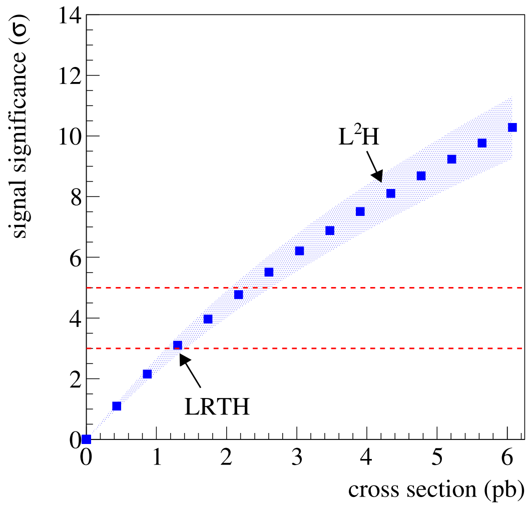

(a)

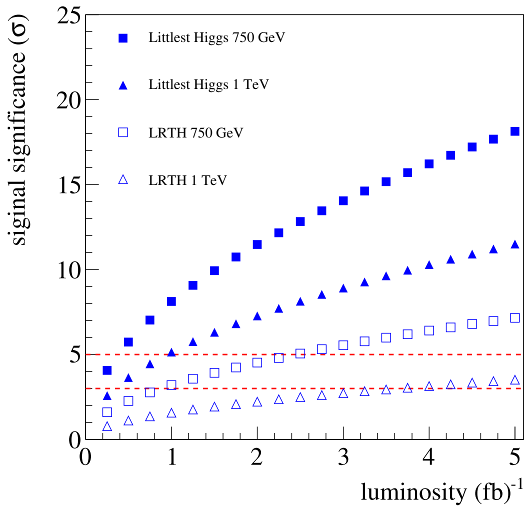

(b)

Figure 7.18: (a) A cross section scan of the expected signal significance for $m_{W'}$ = 750 GeV and for 1 fb^{-1} of data. (b) A luminosity scan of the expected signal significance for all four reference scenarios.

the Fisher Discriminant, the signal was successfully separated from the background. As soon as 400 pb^{-1} of data is recorded by ATLAS, the mass of the W' boson can be constrained for models in which the cross section is as large as that in the Littlest Higgs model. Even though for smaller cross sections the required amount of data is naturally larger, a resonance could well be observed within the first 10 fb^{-1} of data. The production cross section decreases with increasing values of the mass $m_{W'}$, but so does the contribution from Standard Model background events and the proposed method is expected to be successful for larger mass values than those studied here as well.

The discovery potential at the LHC design center of mass energy, $\sqrt{s}$ = 14 TeV, has been investigated previously [66]. The cross section for the signal increases more strongly with increasing collision energy than the cross sections of the Standard Model background processes and the situation improves when the LHC starts delivering proton collisions at the design value of $\sqrt{s}$ = 14 TeV.

In case a model similar to the Littlest Higgs describes the physics beyond the Standard Model, the discovery of a W' boson is likely accomplished in its leptonic decay channel, as the branching ratio is large and Standard Model background contributions are small. A straightforward event selection with large $\not{E}_{\mathrm{T}}$ and lepton p_{T} requirements will strongly reduce the contribution from Standard Model $W \to l\nu$ decays and a maximum on the allowed number of reconstructed jets will suppress the contribution of multi-jet events in which a charged lepton is falsely reconstructed. The transverse mass of the W' boson is reconstructed by combing the $\not{E}_{\mathrm{T}}$ with the transverse momentum of the lepton along the same lines as described in Chapter 6. A Jacobian peak will reveal the W' boson.

As soon as such a discovery is made, more information about the actual model to which this W' boson belongs is determined from the remaining decay channels and the $W' \rightarrow tb$ decay becomes important. In case of the LRTH model, however, the leptonic decay channel is absent (cf. Section 1.3) and the $W' \rightarrow tb$ decay may be the first evidence for its existence.

Either way, the discovery or the exclusion of a $W' \rightarrow tb$ signal provides insight in the possible descriptions of physics beyond the Standard Model and is well within reach for the ATLAS experiment.

8

A First Look at Data

In the course of 2010, the LHC delivered proton collisions at $\sqrt{s} = 7$ TeV with increasing luminosity. This chapter is a preview of $t\bar{t}$ candidate events in the first 3 pb^{-1} recorded by ATLAS. Some of the reconstruction algorithms changed with respect to those described in Chapter 4, either as a result of an improved understanding or deliberately simplified in favour of robustness. The differences are minor and the comparison is beyond the scope of this study[1]. Instead, the main focus is on the very first acquaintance with collision data. The aim is to select semileptonic $t\bar{t}$ events by making use of the selection criteria presented in Chapter 5 and performing the template fit described in Chapter 6. However, as the accumulated amount of data is still very limited and the $t\bar{t}$ production cross section is significantly smaller than at $\sqrt{s} = 10$ TeV, the selection criteria need to be relaxed in order to acquire a data sample of reasonable size. The event selection and the acquired sample are described in Section 8.1. Subsequently, the kinematic distributions for selected data are compared to the distributions from Monte Carlo samples in Section 8.2. The missing transverse energy reconstruction is investigated in Section 8.3 and the template fit on the m_{T}^{W} distribution is performed in Section 8.4.

8.1 Data Selection

The 2010 ATLAS data periods A through F are investigated, during which approximately 3.5 pb^{-1} of data was recorded (cf. Figure 2.2). The data used in this chapter is required to have been taken with all subdetectors fully operational and performing well[2]. Table 8.1 lists the integrated luminosity taken under these circumstances in each of the data periods, which add up to approximately 3 pb^{-1}. The uncertainty on the luminosity is 11% [32].

The data in the muon and electron trigger streams are considered for event selection. Firstly, the number of tracks associated to the reconstructed primary vertex is required to be at least 4 in order to select actual collision events and thus reject cosmic muon data. Subsequently, the following requirements are applied, along the same lines as the event selection described in Section 5.2:

[1] Details on the reconstruction algorithms can be found in [67].
[2] The quality is defined by experts in terms of a so called *Good Run List*.

Period		Luminosity
A	March 30 - April 19	0.37 nb^{-1}
B	April 23 - May 16	8.06 nb^{-1}
C	May 18 - June 5	8.44 nb^{-1}
D	June 24 - July 19	278 nb^{-1}
E	July 29 - August 18	1002 nb^{-1}
F	August 19 - August 30	1589 nb^{-1}
		2.886 pb^{-1}

Table 8.1: The 2010 data periods that are used in this chapter.

- **The trigger requirement:** The events are required to pass a specific single electron or a specific single muon trigger chain, the exact choice of which is data period dependent[3]. The available trigger chains become more advanced with increasing instantaneous luminosity, yet they are all defined such that efficiency is at the plateau for leptons with $p_{\mathrm{T}} > 20$ GeV;

- **The lepton requirement:** Exactly one medium electron and zero combined muons are reconstructed in the electron stream data and exactly one combined muon and zero medium electrons are reconstructed in the muon stream data. The additional quality criteria described in Section 5.2.2 are applied;

- **The missing transverse energy requirement:** $\not{E}_{\mathrm{T}} > 20$ GeV;

- **The jets requirement:** Three or more jets satisfying $p_{\mathrm{T}} > 20$ GeV are reconstructed.

When applying the stricter jets requirement described in Section 5.2, 52 events survive in the electron channel and 36 events in the muon channel. The event display of one of the so obtained semileptonic $t\bar{t}$ candidate events in the electron channel is shown in Figure 8.3. The acquired sample is however too small for the template fit from Section 6.2.2 to be performed. Therefore, the jets requirement is relaxed as described above.

The number of events that pass the selection criteria are presented in Table 8.2. The electron stream contains more events than the muon stream as the electron triggers are more likely to falsely trigger on jets than the muon triggers, which are situated further away from the interaction point. The difference between the channels becomes smaller when the lepton requirement is applied, although it is still more likely to falsely reconstructed a jet as a medium electron than as a combined muon. Consequently, the number of events in the electron stream remains largest. The distributions of the reconstructed $\not{E}_{\mathrm{T}}$ are displayed in Figure 8.1(a) for the electron and muon stream separately. After the requirement $\not{E}_{\mathrm{T}} >$ 20 GeV the difference between the number of events in each of the streams is reduced further. However, the difference in shape between the distributions suggests that the selected sample is still more diluted with multi-jet events in the electron channel.

[3] For instance, the electron trigger chain for period F is `e10_medium`.

Figure 8.1(b) displays the number of reconstructed jets with $p_{\mathrm{T}} > 20$ GeV in the electron and muon stream after the lepton and $\not\!\!E_{\mathrm{T}}$ requirements are applied. Ultimately, the sample containing 316 events from the muon stream and 524 events from the electron stream is investigated in the remainder of this chapter.

	Muon stream	**Electron stream**
A priori	10 206 456	38 212 624
Primary vertex	8 526 922	38 167 428
Trigger requirement	2 996 835	20 418 984
Lepton requirement	23 494	46 075
$\not\!\!E_{\mathrm{T}}$ requirement	15 025	15 274
Jets requirement	**316**	**524**

Table 8.2: The number of events that pass the event selection in the data periods A through F.

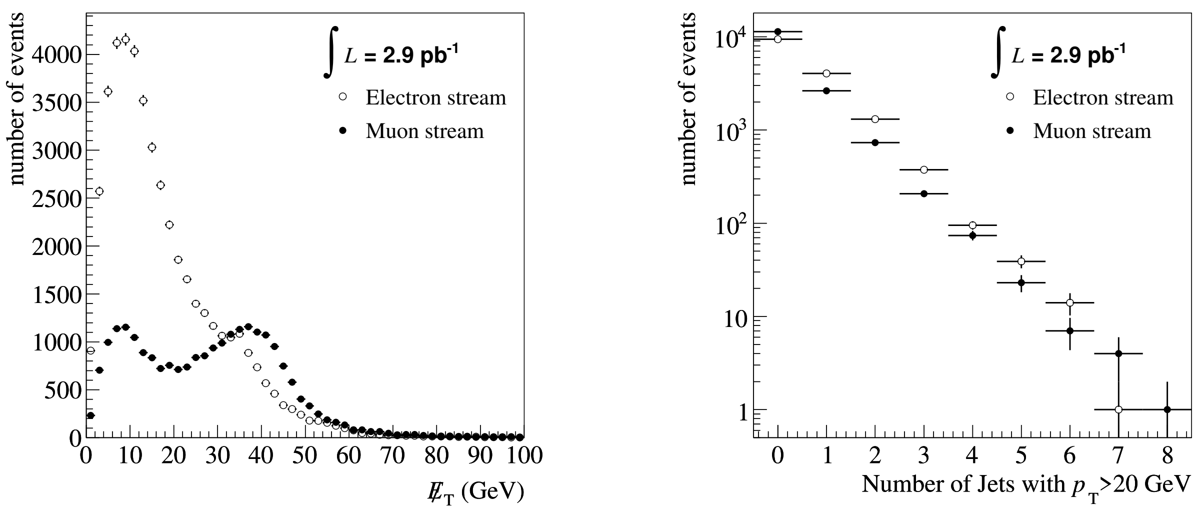

(a) (b)

Figure 8.1: (a) The reconstructed $\not\!\!E_{\mathrm{T}}$ in events that pass the trigger and lepton requirements in the 2010 data. (b) The number of reconstructed jets with $p_{\mathrm{T}} > 20$ GeV in events that pass the trigger, lepton and $\not\!\!E_{\mathrm{T}}$ requirements.

The next section compares the kinematic distributions of the selected data to simulated events. First, as an intermezzo, the reconstructed transverse W boson mass, m_{T}^{W}, is considered. Figure 8.2(a) displays the distributions before the jets requirement. The sample thus selected is large and expected to be dominated by $W \to e\nu$ and $W \to \mu\nu$ events. The distributions in Figure 8.2(a) display a clear Jacobian peak around $m_W = 80.4$ GeV, which assures that the selected sample is dominated by events that contain actual W bosons. The ATLAS detector and the reconstruction software are evidently capable of delivering the expected Standard Model physics distributions already at this early stage. We are however interested in events that contain additional jets, in which the reconstruction of the missing transverse energy is more challenging. Therefore, the sample of events that obey the aforementioned jets requirement is used in the following, albeit smaller and relatively more diluted with multi-jet events. The selected events are expected to show a closer resemblance to $t\bar{t}$ events as well as to the expected signatures from many new physics models, which is why these type of events need to be understood. The m_{T}^{W} distributions for these events are displayed in Figure 8.2(b) and will be further investigated in Section 8.4.

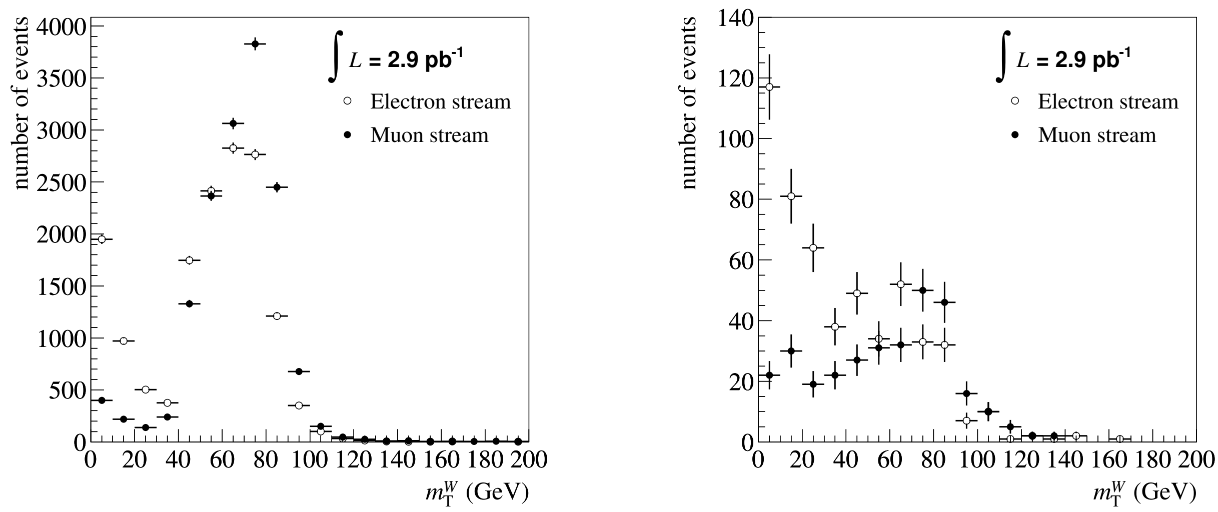

(a) (b)

Figure 8.2: The distributions of the transverse W boson mass in the 2010 data before (a) and after (b) the jets requirement is applied.

8.2 Comparison to Simulated Events

To compare the data to simulated events, an updated set of Monte Carlo samples is used, which are generated at $\sqrt{s} = 7$ TeV. The corresponding cross sections are listed in Table 8.3. The $t\bar{t}$ sample contains both semileptonic and dileptonic $t\bar{t}$ events. The filters applied to the multi-jet samples are the same as those described in Section 3.3.1, although they are only applied to a subset of the samples. The $W+$ jets samples are not subject to any filter.

Firstly, the number of reconstructed jets with $p_{\mathrm{T}} > 20$ GeV in selected events is shown in Figure 8.4. Both in the muon and the electron channel, the number of events in which three jets are reconstructed displays a disagreement between the data and the prediction from Monte Carlo simulation. For the electron channel, this could well be explained by the fact that part of the simulated multi-jet events are subject to the `top_jet` filter described

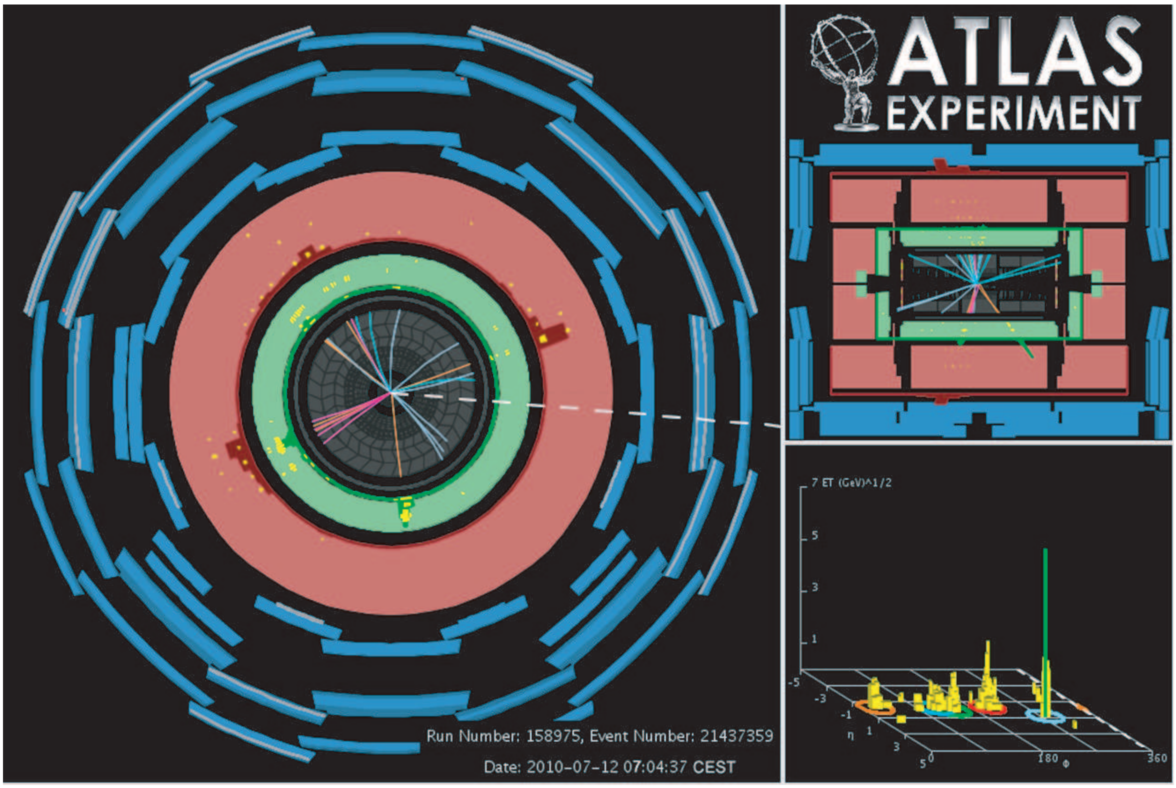

Figure 8.3: Event display of a $t\bar{t}$ electron channel event candidate recorded in July 2010. The left figure represents the transverse projection of the ATLAS detector. The dotted line indicates the direction of the reconstructed missing transverse energy and the inner detector track pointing downwards, which is matched to the electromagnetic cluster, belongs to the reconstructed electron. The top right figure is a longitudinal cross section and the bottom right figure shows an (η, φ) lego-plot of the calorimeter tower energies.

Event properties	
Electron p_{T}	41.4 GeV
Jet p_{T}	76.5 GeV
Jet p_{T}	53.9 GeV
Jet p_{T}	40.3 GeV
Jet p_{T}	33.7 GeV
$\not{E}_{\mathrm{T}}$	90.9 GeV
m_{T}^{W}	67.4 GeV
$\lvert\Delta\varphi(\not{E}_{\mathrm{T}}, \mathrm{jet})\rvert$	0.66
$\sum E_{\mathrm{T}}$	327 GeV

Sample	Filter	σ(7 TeV)
$t\bar{t}$ (non-hadronic)	none	88.2 pb
$W+$ jets	none	31.9 nb
single top		
leptonic s-channel	none	1.41 pb
leptonic t-channel	none	21.5 pb
inclusive Wt	none	14.6 pb
multi-jet (e)	partly `top_jet`	$\mathcal{O}(\mu b)$
multi-jet (μ)	partly `top_mu`	$\mathcal{O}(\mu b)$

Table 8.3: The cross sections for $\sqrt{s}$ =7 TeV including the efficiencies of the applied filters.

in Section 3.3.1, which is more rigorous than the actual jets requirement.

Due to the relaxed jets requirement and the decreased center-of-mass energy, the relative contribution from $t\bar{t}$ events is smaller than in Chapter 5. Instead, the sample of selected events is dominated by $W+$ jets events in the muon channel. In the electron channel, however, the multi-jet events are more prominent. The contribution from single top events turns out to be negligible.

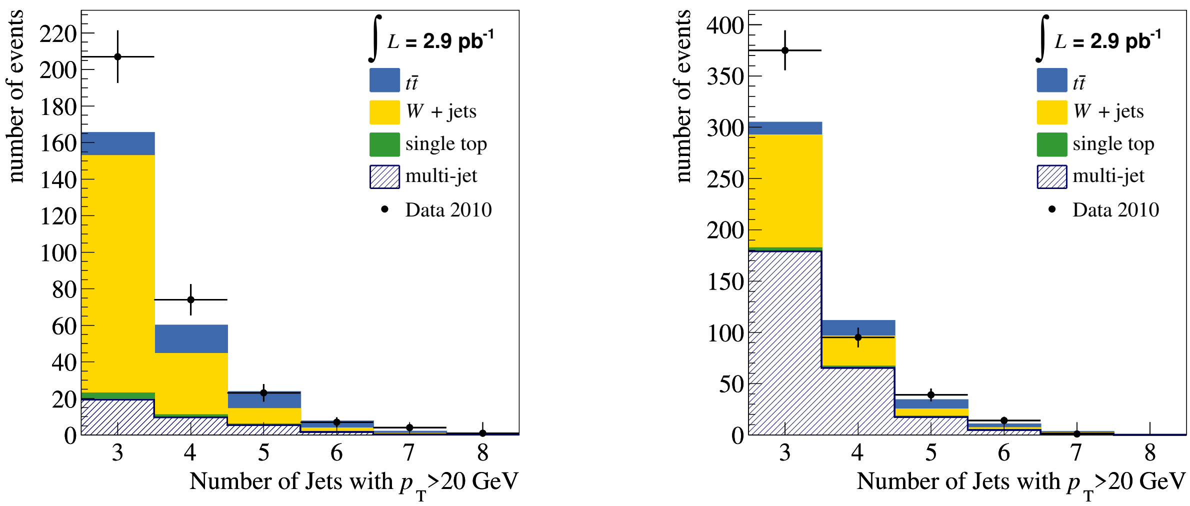

(a) The muon channel.

(b) The electron channel.

Figure 8.4: The number of reconstructed jets with $p_{\mathrm{T}} > 20$ GeV in selected events in 2.9 pb^{-1}.

Figure 8.5 shows the reconstructed transverse momenta of the electron and the muon for selected events in the respective channels. For values $p_{\mathrm{T}} \lesssim 30$ GeV, the number of events is underestimated by the simulation in both channels.

Figure 8.6 shows the reconstructed $\not{E}_{\mathrm{T}}$ in selected events for the muon and electron channel respectively. The agreement between data and Monte Carlo is good in events with large $\not\!\!E_{\mathrm{T}}$. The comparison is performed in more detail in the following two sections.

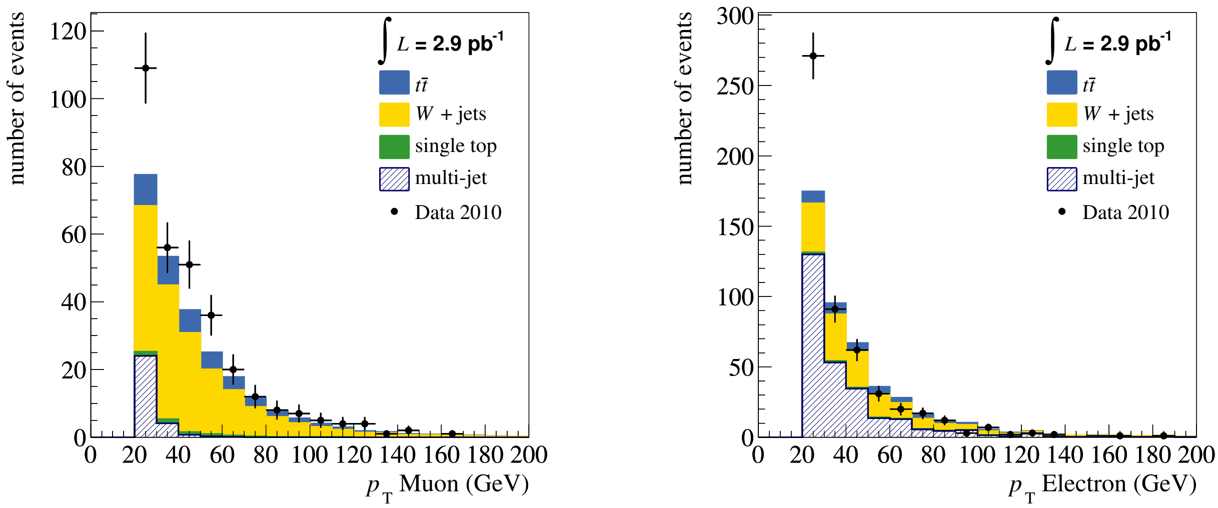

(a) The muon channel.

(b) The electron channel.

Figure 8.5: The reconstructed transverse momentum of the charged lepton in selected events in 2.9 pb^{-1}.

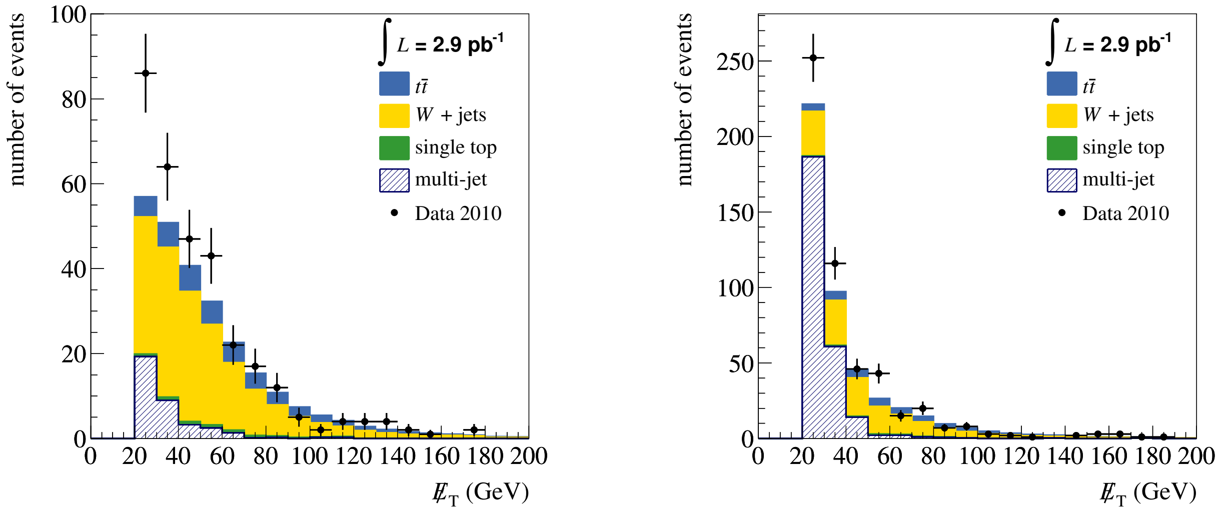

(a) The muon channel.

(b) The electron channel.

Figure 8.6: The reconstructed missing transverse energy in selected events in 2.9 pb^{-1}.

Although the validation and calibration of the reconstruction algorithms with the accumulated data is still ongoing[4], a certain level of agreement is observed between the reconstructed objects in data and Monte Carlo. Discrepancies are observed in the low-p_{T} regime for both channels. This is most likely due to an underestimation of the contribution from multi-jet events in simulation, which is known not to be a reliable prediction in general. In the electron channel all the more since the applied jets requirement is looser than the `top_jet` filter applied to part of the sample. In Section 8.4, we will attempt to estimate the multi-jet contributions from the data by means of the template fit based on the transverse W boson mass distribution as proposed in Chapter 6.

8.3 Missing Transverse Energy

In this section, the reconstructed missing transverse energy in data is investigated in some detail. All types of reconstructed objects contribute to the calculation according to (4.9). As shown in Figure 6.2, the largest fractional contributions to $\sum E_{\mathrm{T}}$ are expected to come from the jets (RefJet), from the charged lepton (RefEle or MuonBoy) and from calorimeter cells that are not assigned to any reconstructed object (CellOut). The distributions of the total $\sum E_{\mathrm{T}}$ and the three largest contributions in selected events in the data are displayed in Figure 8.7 for the electron and muon channel separately. Overall, as expected, the reconstructed $\sum E_{\mathrm{T}}$ is smaller than for the simulated events with $\sqrt{s} = 10$ TeV shown in Chapter 6. When comparing Figure 8.7(b) to Figure 8.7(a), the contribution from the charged lepton seems lower in the electron channel, while contributions of comparable size are expected. Closer examination reveals that in 12% of the selected events, the contribution of electrons to the reconstructed $\sum E_{\mathrm{T}}$ is zero, even though an electron is reconstructed satisfying $p_{\mathrm{T}} > 20$ GeV. This is likely due to the more robust definition applied to the reconstructed electron at this stage, which is not adapted in the calculation of $\not\!\!E_{\mathrm{T}}$. As a consequence, the assignment of calorimeter cells to objects may disagree with the actual reconstructed objects and corresponding event selection. This is expected to be solved in the future as soon as the more advanced electron reconstruction is applied.

The x- and y-components of the reconstructed missing energy are expected to be symmetric distributions around zero. The comparison between data and Monte Carlo for selected events is shown for the x-component, $\not\!\!E_x$, in Figure 8.8. The requirement $\not\!\!E_{\mathrm{T}} > 20$ GeV is clearly reflected by the diminished contribution at low values of $\not\!\!E_x$. The agreement between the data and the simulated events is quite good for both the muon and the electron channel. The distribution of the azimuthal angle of the reconstructed missing energy is more sensitive to asymmetries or non-uniformities of the detectors (cf. Section 6.1). Figure 8.9 shows what the distributions look like for selected events in the electron channel and muon channel respectively. Although the number of events is still rather limited, the $\varphi(\not\!\!E_{\mathrm{T}})$ distributions are observed not to be perfectly flat.

[4] Thus far, the validation and calibration is performed on test beam and cosmic data only.

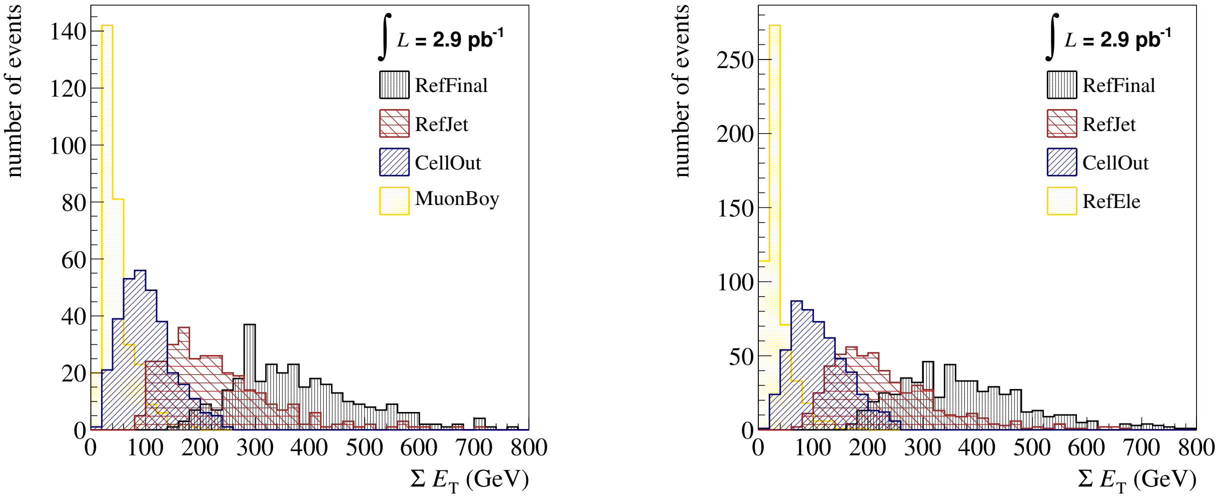

(a) The muon channel. (b) The electron channel.

Figure 8.7: The reconstructed $\sum E_T$ in selected events in 2.9 pb^{-1} and the three largest contributions.

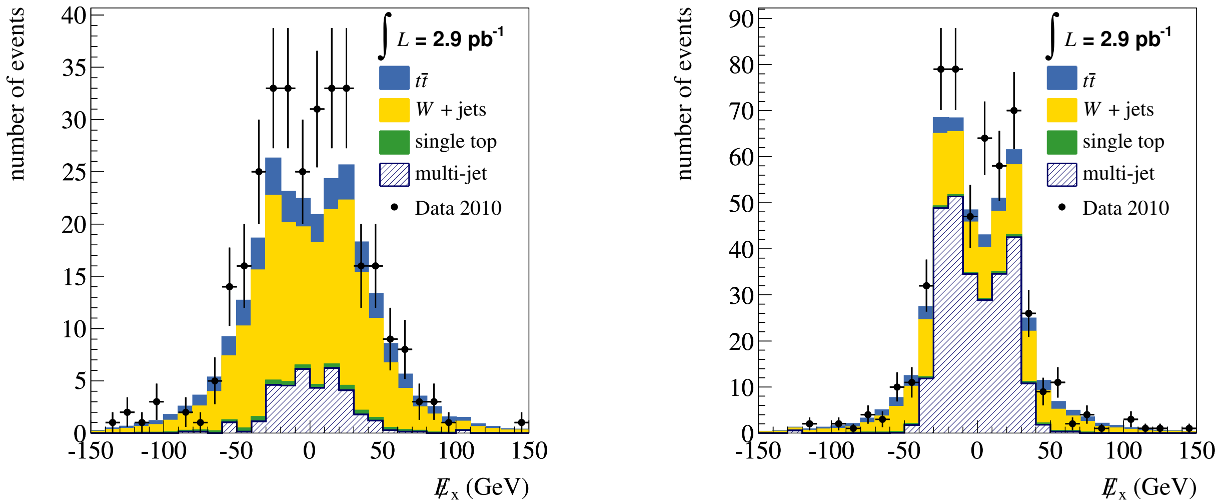

(a) The muon channel. (b) The electron channel.

Figure 8.8: The x-component of the reconstructed missing transverse energy in selected events in 2.9 pb^{-1}.

8.4 Transverse W Boson Mass

Although the accumulated amount of events is still limited, we perform the template fit introduced in Chapter 6 in order to assess the quality of the $\not{E}_T$ reconstruction. Note that

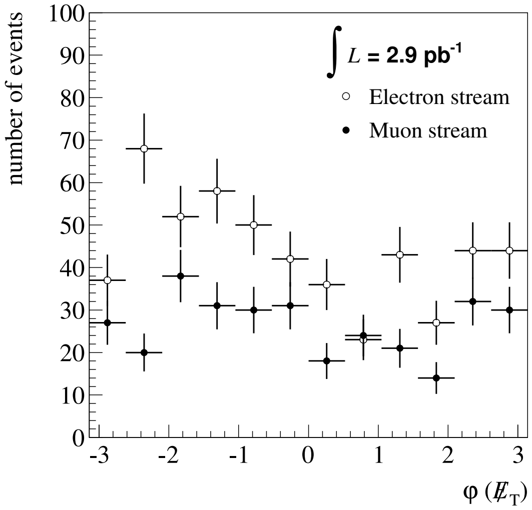

Figure 8.9: The azimuthal angle of the reconstructed missing energy, $\varphi(\not{E}_{\mathrm{T}})$, in selected events in 2.9 pb^{-1}.

this is a very preliminary study and the validation and calibration of e.g. jet, electron and muon reconstruction algorithms would preferably be performed first. Moreover, the starting point for the validation of the reconstruction of missing transverse energy are events without actual missing energy from neutrinos, such as di-jet events or $Z \to ll$ events, which is still ongoing at this point. Out of curiosity, the procedure is nevertheless pursued.

The template distributions from Monte Carlo are fitted to the data in the range $m_{\mathrm{T}}^{W} \in [50, 120]$ GeV. Multi-jet events are not included in the templates as the prediction is not considered to be reliable. In order to suppress the contribution from multi-jet events in the fit range, the opening angle between the reconstructed $\not{E}_{\mathrm{T}}$ and the nearest jet is required to be larger than 0.3:

- $|\Delta\varphi(\not{E}_{\mathrm{T}}, \mathrm{jet})| > 0.3$,

as argued in Section 6.2. Figure 8.10 displays the distributions for selected events that satisfy $m_{\mathrm{T}}^{W} > 50$ GeV. Both the data and the prediction from Monte Carlo in 2.9 pb^{-1} are shown. The agreement of the distributions is good for events that satisfy $\Delta\varphi(\not{E}_{\mathrm{T}}, \mathrm{jet}) > 0.3$ and the requirement indeed suppresses the contribution from multi-jet events.

The transverse mass of the W bosons, m_{T}^{W}, is now reconstructed for selected events that pass $\Delta\varphi(\not{E}_{\mathrm{T}}, \mathrm{jet}) > 0.3$ for both the muon and the electron channel. The obtained distributions for the data are displayed in Figure 8.11 together with the nominal Monte Carlo templates.

Despite the additional requirement on $\Delta\varphi(\not{E}_{\mathrm{T}}, \mathrm{jet})$, the contribution from multi-jet events in the electron channel remains enormous and a number of events enters the fit range according to Figure 8.10(b). These events could cause the result of the template fit not to reflect the performance of the $\not{E}_{\mathrm{T}}$ reconstruction as intended. Therefore, an additional requirement is imposed on the electron channel only:

- $\not{E}_{\mathrm{T}} > 30$ GeV in the electron channel.

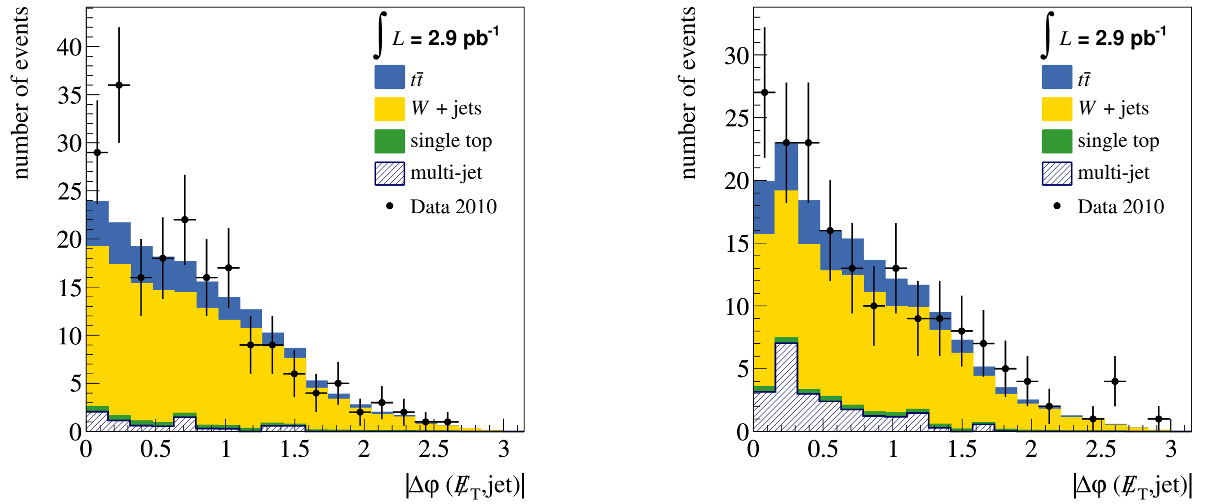

(a) The muon channel.

(b) The electron channel.

Figure 8.10: The opening angle $\Delta\varphi(\not{E}_{\mathrm{T}}, \mathrm{jet})$ in selected events that satisfy $m_{\mathrm{T}}^{W} > 50$ GeV.

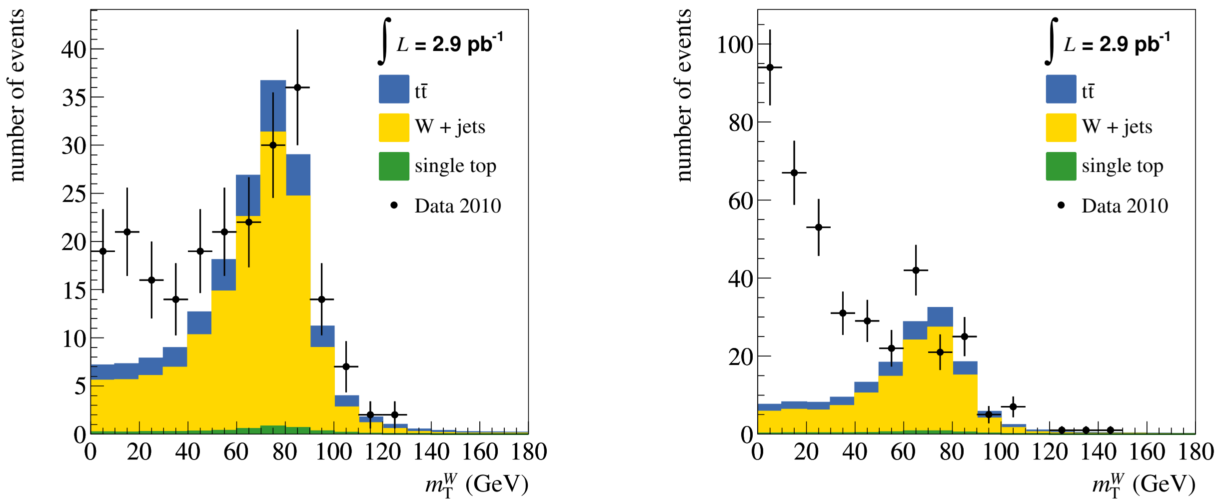

(a) The muon channel.

(b) The electron channel.

Figure 8.11: The m_{T}^{W} distributions in selected events in 2.9 pb^{-1}. The multi-jet events are not included in the templates.

According to the Monte Carlo sample for multi-jet events, this reduces the number of multi-jet events in the fit range by 50%. As soon as more data is accumulated, the more severe jets requirement as suggested in Chapter 5 is preferred, in both channels, to enhance the purity of the sample. For now, the template fit in the electron channel is performed for events that satisfy $\not{E}_{\mathrm{T}} > 30$ GeV. The obtained m_{T}^{W} distribution is displayed in Figure 8.12.

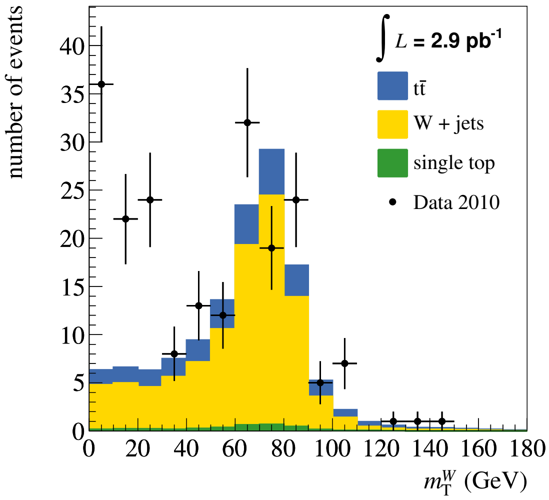

Figure 8.12: The m_T^W distribution in the electron channel for events that satisfy $\not{E}_T > 30$ GeV. Multi-jet events are not included in the templates.

8.4.1 Fit Results

Templates are constructed for all combinations of the scale $\alpha \in [0.7, 1.3]$ and the Gaussian width $r \in [0, 30]$ GeV. The χ^2 is calculated for each template according to (6.6), thus indicating possible deviations from the Monte Carlo simulation. Subsequently, the m_T^W distribution for multi-jet events is extracted from the result by subtracting the best template from the data distribution.

Muon Channel

The χ^2 distribution as a function of the template parameters α and r takes its minimal value at $(\alpha, r)^{\text{fit}} = (1.08^{+0.13}_{-0.07}, 0.0^{+10.2}$ GeV$)$ for the muon channel. The contours that correspond to 1σ and 2σ around the minimum are indicated in Figure 8.13(a). The template distribution corresponding to the best fit is compared to the distribution in data and to the nominal template in Figure 8.13(b). Although the fit result is consistent with the nominal values within the statistical uncertainty, the result $\alpha > 1.0$ is consistent with what one would expect when inspecting Figure 8.11(a).

Electron Channel

In the electron channel, the minimum χ^2 is found at $(\alpha, r)^{\text{fit}} = (1.08^{+0.05}_{-0.22}, 0.0^{+13.9}$ GeV$)$. The contours that correspond to 1σ and 2σ around the minimum are indicated in Figure 8.14(a). The uncertainties are large due to the small number of events and because the shape of the m_T^W distribution in data differs more from the expected shape than in the muon channel. Figure 8.14(b) compares the best m_T^W template to the data and to the nominal template distribution. At this point, the data sample is still too small to come to a conclusion about the performance of the reconstruction.

8.4.2 Multi-jet Estimation

The contribution from multi-jet events is estimated by subtracting the m_T^W template corresponding to the minimum χ^2 from the data distribution. The contribution in the

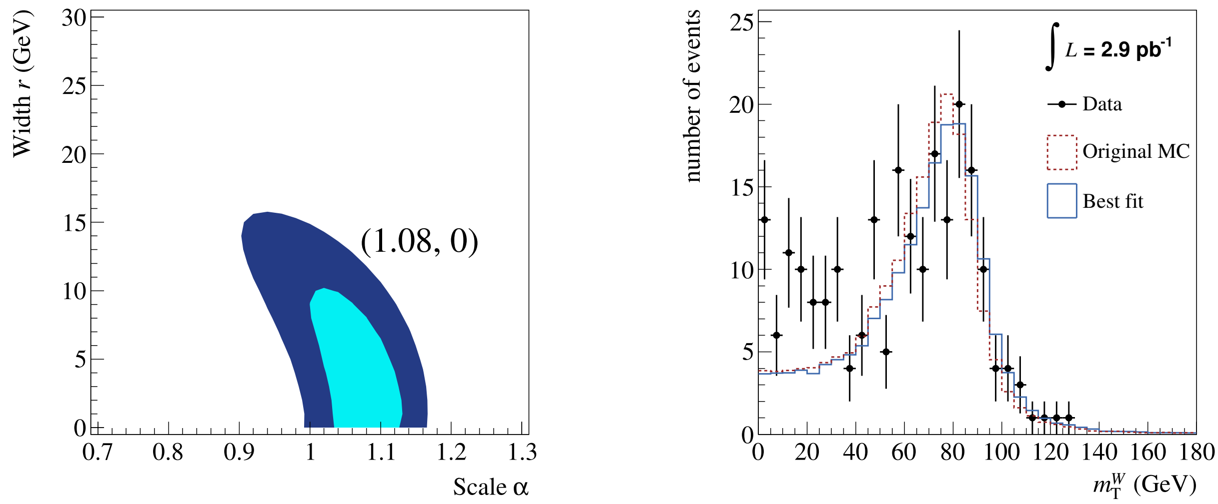

(a) (b)

Figure 8.13: The result of the template fit in muon channel events in 2.9 pb^{-1}: (a) The 1σ and 2σ contours that follow from the χ^2 distribution. The minimum is found at $\alpha = 1.08$ and $r = 0.0$ GeV. (b) The template that corresponds to the minimum χ^2, the m_{T}^W distribution for data and the nominal template distribution.

electron channel is expected to differ from the contribution in the muon channel and the estimation is performed separately. The result is shown in Figure 8.15 for both channels. The distribution as predicted by simulation is overlaid. The estimated number of multi-jet events that pass the event selection in 2.9 pb^{-1} is compared to the prediction from simulation in Table 8.4.

For both channels, the number of multi-jet events in data is larger than predicted by simulation, although the numbers agree within the statistical uncertainties. The relative difference between the estimation and the prediction from Monte Carlo is largest in the muon channel. Despite the additional requirement $\not{E}_{\mathrm{T}} > 30$ GeV in the electron channel, the number of multi-jet events is larger than in the muon channel.

	Muon channel	**Electron channel**
Simulation	26 ± 5	56 ± 8
Estimation	38 ± 15	67 ± 14
Ratio	1.46 ± 0.64	1.20 ± 0.30

Table 8.4: The number of multi-jet events that pass the event selection in 2.9 pb^{-1} according to simulation and according to the estimate that follows from the template fit.

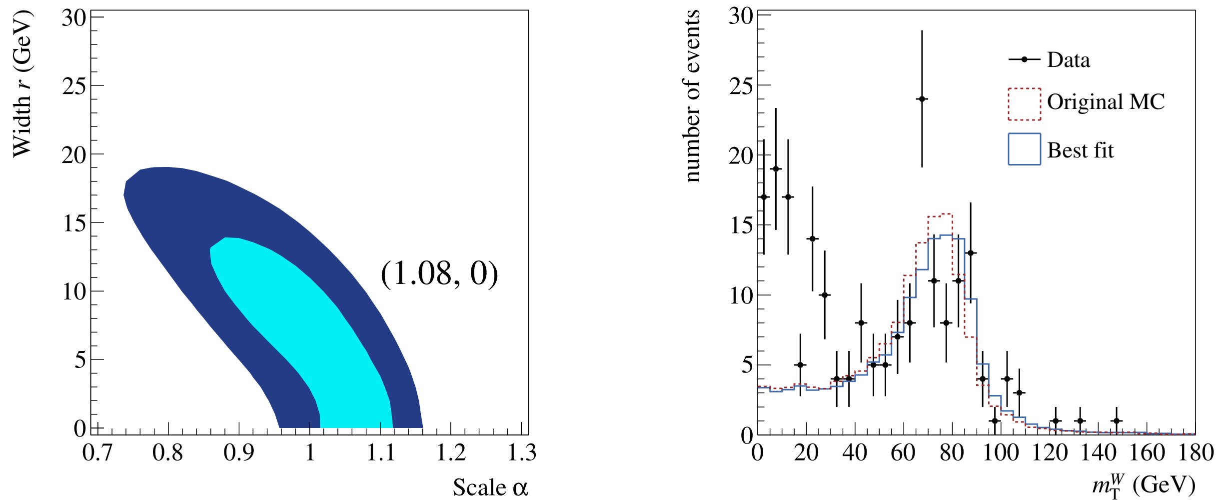

(a) (b)

Figure 8.14: The result of the template fit in electron channel events in 2.9 pb^{-1}: (a) The 1σ and 2σ contours that follow from the χ^2 distribution. The minimum is found at $\alpha = 1.08$ and $r = 0.0$ GeV. (b) The template that corresponds to the minimum χ^2, the m_T^W distribution for data and the nominal template distribution.

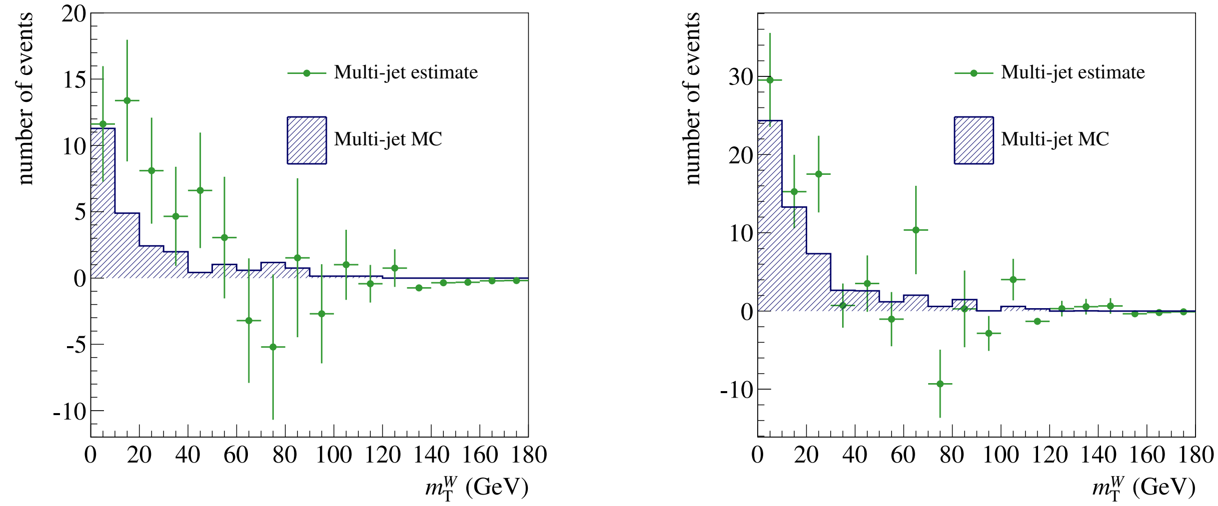

(a) The muon channel. (b) The electron channel.

Figure 8.15: The result of the multi-jet estimate from the template fit in 2.9 pb^{-1}.

8.5 Summary

In this chapter, a preliminary study on the first 2.9 pb^{-1} of ATLAS data at $\sqrt{s} = 7$ TeV has been performed. Events were selected using criteria similar to those for the semileptonic $t\bar{t}$ selection described in Chapter 5, apart from the loosened jets requirement in both channels and the more severe $\not{E}_{\mathrm{T}}$ requirement in the electron channel. As a result of this modification, a sample of reasonable size was acquired, which was dominated by $W+$ jets events.

Already at this early stage, the distributions of the kinematic variables that play a part in the event selection are in agreement with the distributions from Monte Carlo over a large range. Deviations are observed in the low-p_{T} regime in both channels. For the electron channel, the observation that the contribution $\not{\boldsymbol{E}}_{\mathrm{T}}{}^{\mathrm{RefEle}}$ is zero in events that do pass the electron selection criteria is worrisome and calls for further investigation.

The distribution of the transverse W boson mass was studied in order to quantify the performance of the $\not{\boldsymbol{E}}_{\mathrm{T}}$ reconstruction as proposed in Chapter 6. The results are $(\alpha, r)^{\mathrm{fit}} = (1.08^{+0.13}_{-0.07}, 0.0^{+10.2}\ \mathrm{GeV})$ for the muon channel and $(\alpha, r)^{\mathrm{fit}} = (1.08^{+0.05}_{-0.22}, 0.0^{+13.9}\ \mathrm{GeV})$ for the electron channel. Although the uncertainties are still very large, the fact that the two channels give the same result is promising.

Subsequently, the contribution of multi-jet events to the m_{T}^{W} distribution was estimated from the data distribution. For both channels, the estimated number of events is larger than the prediction from Monte Carlo. For the electron channel this is no surprise, given that the Monte Carlo sample is subject to a filter that is stronger than the selection criteria. The observation that the multi-jet contribution is underestimated in the Monte Carlo samples does explain the discrepancies in the low-p_{T} regime in all kinematic distributions displayed in Section 8.2, which is where the multi-jet events are expected to contribute. In general, the shape of the kinematic variables in the multi-jet samples does seem to agree with the data, save for the normalization.

The results of this very first investigation of the 2010 data are too preliminary to be completely conclusive and more detailed systematic studies, preferably on a larger data sample, are required. Nevertheless, the presented distributions and observations may serve as a starting point. The fit method is in place and awaits more data.

Summary

In this thesis, two types of events have been studied: The 'top' (semileptonic $t\bar{t}$ events) and 'beyond' ($W' \to tb$ events).

The topology of semileptonic $t\bar{t}$ events contains a large variety of final state objects: a charged lepton, missing energy and at least four jets, two of which originate from b quarks. The complex final state is expected to resemble signatures of physics beyond the Standard Model. The kinematics are however well understood, which makes it a good place to study and understand reconstruction algorithms before setting out to search for signals of new physics. The procedure to select semileptonic $t\bar{t}$ events was outlined in Chapter 5.

Of all final state objects, the missing transverse energy is the most challenging to reconstruct as it is built up of all other reconstructed objects in the event. In Chapter 6, the expected reconstruction performance was studied in simulated $t\bar{t}$ events. A method was introduced to estimate the performance of the reconstruction in data. It makes use of the distribution of the transverse W boson mass; a Jacobian peak which is sensitive both to the magnitude and the angle of the reconstructed missing energy in the transverse plane. By comparing this m_{T}^{W} distribution to templates from simulated events, the method aims to reveal any deviations from the expected resolution and scale of the missing transverse energy. Apart from semileptonic $t\bar{t}$ events, the sample of selected events contained a large contribution from $W+$ jets events. It was demonstrated that these events can be regarded as part of the signal when studying the m_{T}^{W} distribution. In order to test the template fit method, several possible scenarios were considered by distorting the missing transverse energy by hand. It followed that both an overal scale and an additional resolution up to 8 GeV on the missing energy can indeed be retrieved by means of a template fit of the m_{T}^{W} distribution. In addition, an estimate of the poorly predicted contribution from QCD multi-jet events to the selected sample of events was demonstrated to follow from the method.

In chapter 8, the proposed template fit was ultimately carried out on the very first data recorded by ATLAS up to September 2010, corresponding to an integrated luminosity of 2.9 pb^{-1}. The event selection was relaxed with respect to Chapter 5 in order to increase the size of the sample, albeit thereby dominated by $W+$ jets events. The template fit resulted in the following values of the scale α and the additional resolution r:

$$\begin{aligned}
\text{muon channel:} \quad & (\alpha, r)^{\mathrm{fit}} &= (1.08^{+0.13}_{-0.07}, 0.0^{+10.2}\ \mathrm{GeV}) \\
\text{electron channel:} \quad & (\alpha, r)^{\mathrm{fit}} &= (1.08^{+0.05}_{-0.22}, 0.0^{+13.9}\ \mathrm{GeV})
\end{aligned}$$

The statistical uncertainties were large due to the limited size of the data sample and will decrease rapidly in the near future.

The W' boson is introduced in several proposed extensions of the Standard Model. One particular class, the Little Higgs models, were briefly discussed in Chapter 1. In these models, a handful of heavy new particles follow from a symmetry breaking mechanism, which is inspired by the desire to solve the little hierarchy problem. The W' boson thus introduced accomplishes the cancellation of the divergent contribution to the Higgs mass from the Standard Model W boson loop. The discovery potential of its decay channel $W' \to tb$ with ATLAS was investigated in Chapter 7. The main background is formed by semileptonic $t\bar{t}$ events, which underlines the importance of a thorough understanding of 'top' events.

Two particular realizations of Little Higgs models were considered as benchmarks to illustrate the procedure. Two different possible values of $m_{W'}$ were used for each model, motivated by the lower limit set by previous experiments. It was demonstrated that by means of a multivariate selection technique the signal can be isolated from the Standard Model backgrounds. The mass of the W' boson was reconstructed by summing up the four-momenta of all final state objects and the number of events in the signal peak was estimated by means of a likelihood fit. It was shown that a signal significance of 5σ can be achieved as soon as 400 pb^{-1} of data[5] is accumulated in case of the Littlest Higgs model and when $m_{W'} = 750$ GeV. In the scenario of the left-right Twin Higgs model, the signal cross section is smaller and in particular for $m_{W'} = 1$ TeV the amount of data needed for discovery turned out to be 10 fb^{-1}. The discovery or exclusion of a peak in the W' mass spectrum lies within reach for ATLAS and will contribute to our understanding of what physics lies beyond the Standard Model.

[5]The study was performed on simulated collisions at $\sqrt{s} = 10$ TeV.

A

Triggers

A.1 Trigger Menu for Initial Luminosity

Table A.1 lists the trigger menu for $L = 10^{31}$ cm^{-1}s^{-1}. Out of the available trigger chains, e20_loose and mu10 are most suitable for analyses involving top quarks and they are used throughout this thesis.

Data Stream	Trigger Chains		
egamma	2e5_medium	e20_loose	em105_passHLT
	g20_loose		
muon	mu10	2mu4	mu20_MSonly
jet/tau/EtMiss	tau50_loose	2tau20i_loose	2tau29_loose
	j10	j50	j80
	j115	j140	j180
	j265	j350	3j25
	3j60	3j180	4j45
	4j80	4j95	3j35
	xe30	xe35_tight	te360
minimum bias	mbSpTrk	mbMbts_2	

Table A.1: The primary triggers per physics data stream for initial luminosity. The naming convention is discussed in Section 2.2.5.

A.2 Trigger Efficiency for e20_loose

The trigger efficiency for e20_loose is obtained from a $t\bar{t}$ sample in which the reconstruction is performed with a newer version of Athena because of a problem in the algorithm used in the original sample. The problem and the implementation of the correction are described here.

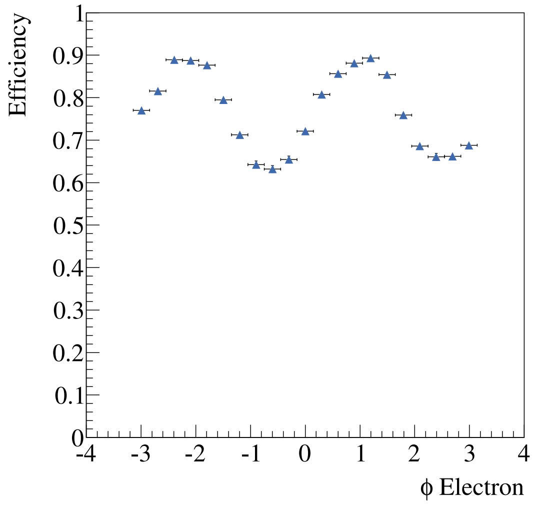

(a) The efficiency of `e20_loose` versus the φ of the electron in the original sample.

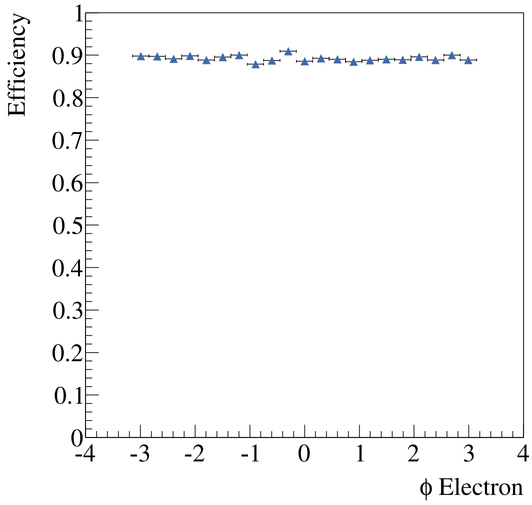

(b) The efficiency of `e20_loose` versus the φ of the electron in the reprocessed sample.

Figure A.1: The efficiency of `e20_loose` versus the φ of the electron from the leptonically decaying top quark, which satisfies $|\eta|$ <2.5 and $p_{\mathrm{T}} > 20$ GeV.

In the sample that is used to describe the semileptonic and dileptonic $t\bar{t}$ events in this thesis, the event reconstruction is performed with `Athena` release 14.2.20.3. It turns out that the algorithm used for the Level-2 electron trigger is not implemented correctly in this release, which results in inefficient tracking in some regions. This is reflected by a modulation in the trigger efficiency as a function of the azimuthal angle φ of the electron, which is expected to be an approximately flat distribution based on the symmetry of the detector. Figure A.1(a) displays the observed modulation in semileptonic $t\bar{t}(e)$ events. Obviously, this faulty simulation of `e20_loose` should not be used.

In the presented analyses, the effect of `e20_loose` is obtained from an alternative sample, in which the electron trigger is simulated correctly with `Athena` release 15.3.1.6. Indeed, Figure A.1(b) shows that the efficiency of `e20_loose` is practically constant over the entire range of the azimuthal angle of the MC electron in this sample. In fact, it turns out that the `e20_loose` requirement has very little impact on the distributions for selected events. This is explained by the event selection. A medium electron is required to be reconstructed with $p_{\mathrm{T}} > 20$ GeV and $|\eta| \notin [1.35, 1.57]$, which is a stronger requirement than `e20_loose`. Figure A.2 shows how the trigger requirement hardly affects the distributions of reconstructed medium electrons. The ratio of distributions before and after the `e20_loose` requirement for the reconstructed electrons is nearly 100% and well-nigh flat in φ as well as η. The only impact is due to the finite resolution of the reconstructed transverse momentum, which is reflected by the *turn-on* behaviour in the region $p_{\mathrm{T}} \in [20, 30]$ GeV (cf. Figure A.3).

Since the applied selection requirements always include both the trigger requirement

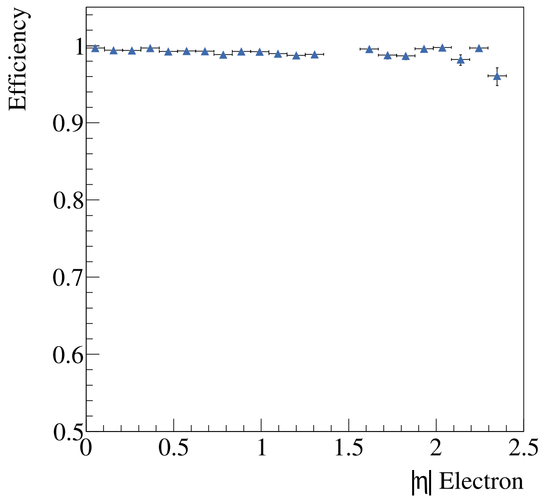

(a) The impact of e20_loose on the η of the reconstructed medium electron in the reprocessed sample.

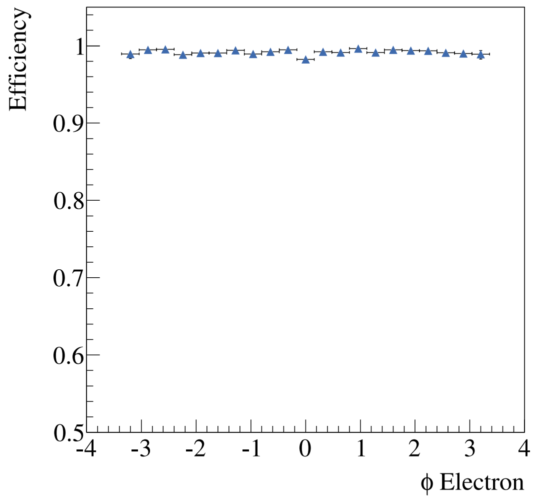

(b) The impact of e20_loose on the φ of the reconstructed medium electron in the reprocessed sample.

Figure A.2: The efficiency of e20_loose with respect to the reconstructed medium electron in the reprocessed sample.

and the medium electron requirement, an effective way to account for e20_loose is to parameterize the impact on the reconstructed medium electron. In the original sample, each event in which one medium electron is reconstructed acquires a weight according to this parametrization,which depends on the p_{T} of the reconstructed electron. This weight ensures that the efficiency distribution follows the correct behaviour. The parametrization is described by the function

$$f_{\text{eff}}(p_{\mathrm{T}}) = \begin{cases} f_{\text{turn-on}}(p_{\mathrm{T}}) = \left(\frac{a}{p_{\mathrm{T}}^2} + b\right) \mathrm{Erf}(cp_{\mathrm{T}} - d) & \text{for } p_{\mathrm{T}} < 30 \text{ GeV} \\ f_{\text{const}} = f_{\text{turn-on}}(p_{\mathrm{T}}) \,|_{p_{\mathrm{T}}=30 \text{ GeV}} & \text{for } p_{\mathrm{T}} > 30 \text{ GeV} \end{cases}$$

The curve in Figure A.3 corresponds to the best fit in the interval $p_{\mathrm{T}} \in [20, 30]$ and the obtained parameters are

$$\begin{aligned} a &= -46.5 \\ b &= 1.05 \\ c &= 1.71 \\ d &= -33.8 \end{aligned} \tag{A.1}$$

The achieved behaviour with the correction applied to the original sample turns out to be in good agreement with the desired behaviour. The parameterized efficiency of e20_loose is applied to all results concerning $t\bar{t}$ events presented in this thesis, unless specified otherwise.

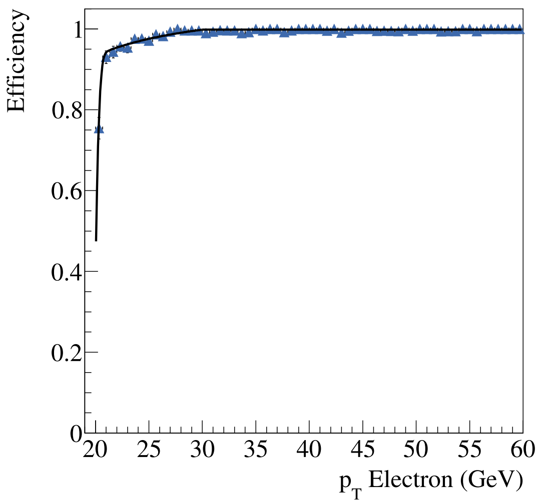

Figure A.3: Impact of `e20_loose` on the reconstructed medium electron in $t\bar{t}(e)$ events in the reprocessed sample.

B

Monte Carlo Parameter Settings

B.1 Pythia Event Generation

The two Monte Carlo samples that are used in Chapter 7 to describe $W' \to tb$ events are obtained by running `Pythia` with the parameter settings listed in Table B.1. The couplings of the W' boson to the fermions are taken equal to those of the Standard Model W boson.

Parameter	**Value**	**Meaning**
`pysubs msub`	142	subprocess: $q + \bar{q} \to W'$
`pydat2 pmas 34`	750, 1000	W' mass (GeV)
`pyinit win`	10000	beam energy (GeV)
`pydat3 mdme 321`	1	W' decay mode: $\bar{b} + t$
`pydat3 mdme 206`	1	W decay mode: $e + \nu_e$
`pydat3 mdme 207`	1	W decay mode: $\mu + \nu_\mu$
`pydat3 mdme 208`	1	W decay mode: $\tau + \nu_\tau$

Table B.1: The parameter settings used during the event generation with `Pythia`.

The cross section that follows from the event generation with `Pythia` is 4.34 pb for $m_{W'} = 750$ GeV and 1.39 pb for $m_{W'} = 1$ TeV. These numbers include the appropriate branching fraction corresponding to the leptonic decay of the W boson.

Subsequently, the generated events are propagated through the `ATLFAST II` detector simulation with geometry description version ATLAS-GEO-02-01-00.

B.2 Calchep Cross Section Calculation

The cross sections for the left-right Twin Higgs Model are obtained from the package `Calchep` [51] by implementing the Lagrangian as described in [26]. The mass dependent model parameters are given in Table B.2. The mixing parameter M is set to 150 GeV, as suggested in [26] [1]. All other parameter values follow from their relation to $m_{W'}$.

Parameter	Value (GeV)	
f_1	383.3	466.7
f_2	1581	2115
m_H	171.5	172.1
$m_{Z'}$	893.6	1192
$m_{W'}$	750.0	1000
m_T	402.2	484.7
$m_{\hat{h}_1}$	239.0	298.0
$m_{\hat{h}_2}$	239.0	298.0
m_{φ^0}	101.6	121.1
$m_{\varphi^\pm}$	131.8	157.4

Table B.2: The parameter settings used when determining the cross sections for the Twin Higgs Model for each of the two reference mass points.

The PDFs describing the parton density in each proton are set to CTEQ6L and the momentum of each proton is set to 5000 GeV. The cross section provided by `Calchep` per initial state pair of partons is indicated in Table B.3. A factor of two comes in because of the pp initial state symmetry and the resulting cross sections for $W' \to tb$ are 4.04 pb and 0.78 pb for the reference mass values 750 GeV and 1 TeV respectively.

Process	$m_{W'} = 750$ GeV	$m_{W'} = 1$ TeV
$\bar{u}d \to \bar{t}b$	0.566 pb	0.104 pb
$\bar{u}s \to \bar{t}b$	0.005 pb	0.001 pb
$\bar{c}d \to \bar{t}b$	0.015 pb	0.002 pb
$\bar{c}d \to \bar{t}b$	0.035 pb	0.005 pb
$\bar{d}u \to t\bar{b}$	1.313 pb	0.267 pb
$\bar{d}c \to t\bar{b}$	0.003 pb	0.008 pb
$\bar{s}u \to t\bar{b}$	0.045 pb	0.000 pb
$\bar{s}c \to t\bar{b}$	0.035 pb	0.005 pb
Total cross section	2.018 pb	0.392 pb

Table B.3: The $W' \to tb$ cross sections for the Twin Higgs Model for each initial state pair of partons for both reference mass values.

[1] In case of zero mixing between the Standard Model top quark and its heavy partner t', the decay channel of interest would not exist as the right-handed W' boson would not couple to the Standard Model top quark.

C

Fisher Discriminant Input Variables

Figure C.1 displays the normalized distributions of the input variables that are used in the calculation of the Fisher Discriminant in the final stage of the event selection in Chapter 7:

- The p_{T} of the jet J_2, which is the jet with the highest p_{T};
- $p_{\mathrm{T}}^{\mathrm{top}}$, the reconstructed transverse momentum of the top quark, which is obtained by combining $\not{E}_{\mathrm{T}}$, the p_{T} of the jet J_1 and p_{T}^{l};
- The opening angle $\Delta R(J_1, l)$;
- m_{T}^{W}, the transverse W boson mass that was introduced in Chapter 6;
- The p_{T} of the jet J_1.

The discriminating power of the transverse momentum of the jet J_2 is by far the largest.

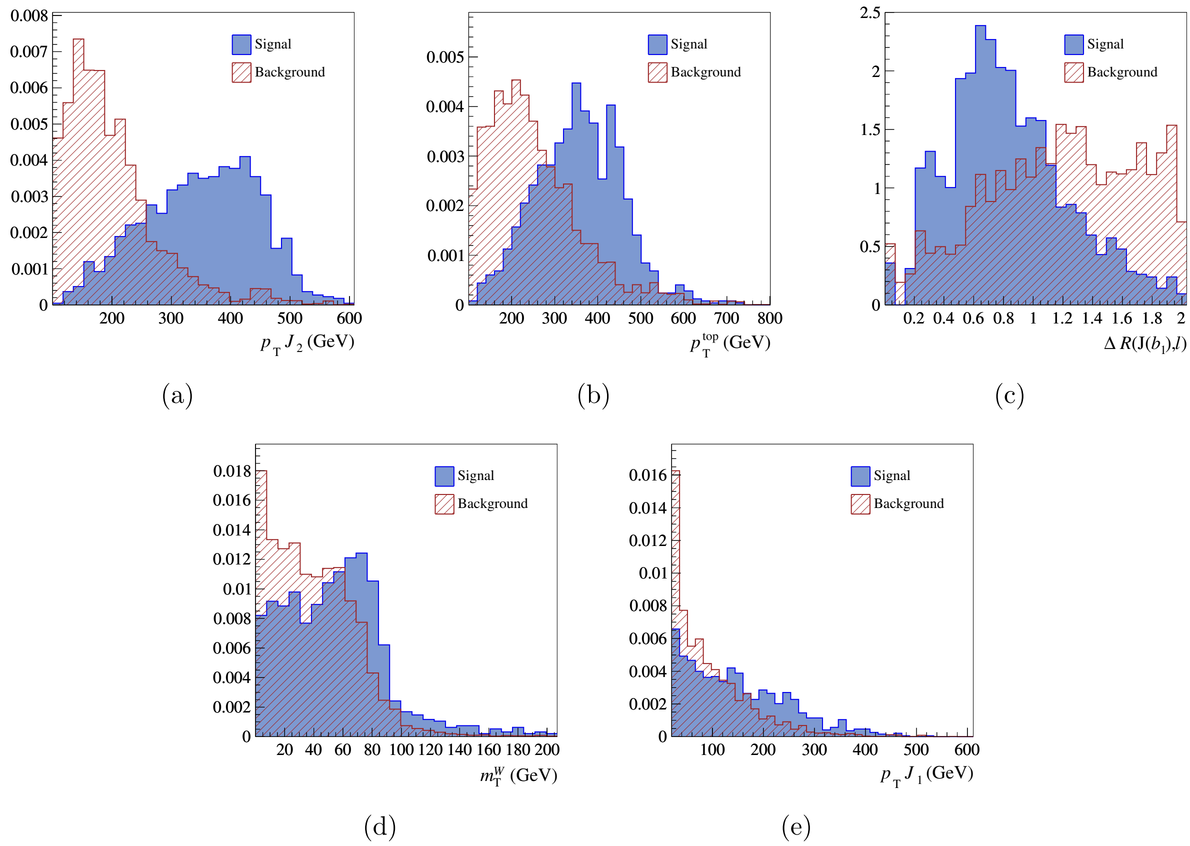

Figure C.1: The normalized distributions of the input variables for the Fisher Discriminant for signal events and background events seperately.

References

[1] Sheldon L. Glashow. Partial-symmetries of weak interactions. *Nuclear Physics*, 22(4):579 – 588, 1961.

[2] Gerard 't Hooft and M. J. G. Veltman. REGULARIZATION AND RENORMALIZATION OF GAUGE FIELDS. *Nucl. Phys.*, B44:189–213, 1972.

[3] Steven Weinberg. A Model of Leptons. *Phys. Rev. Lett.*, 19(21):1264–1266, Nov 1967.

[4] Makoto Kobayashi and Toshihide Maskawa. CP-Violation in the Renormalizable Theory of Weak Interaction. *Progress of Theoretical Physics*, 49(2):652–657, 1973.

[5] Peter W. Higgs. Broken Symmetries and the Masses of Gauge Bosons. *Phys. Rev. Lett.*, 13(16):508–509, Oct 1964.

[6] F. Englert and R. Brout. Broken Symmetry and the Mass of Gauge Vector Mesons. *Phys. Rev. Lett.*, 13(9):321–323, Aug 1964.

[7] G. S. Guralnik, C. R. Hagen, and T. W. B. Kibble. Global Conservation Laws and Massless Particles. *Phys. Rev. Lett.*, 13(20):585–587, Nov 1964.

[8] CDF collaboration. Observation of Top Quark Production in Pbar-P Collisions. *Physical Review Letters*, 74:2626, 1995.

[9] DØ Collaboration. Observation of the Top Quark. *Physical Review Letters*, 74:2632, 1995.

[10] C. Amsler et al. Review of Particle Physics. *Phys. Lett. B*, 667:1, 2008.

[11] W.-M. Yao et al. Review of Particle Physics. *Journal of Physics*, G 33:1, 2006.

[12] S. Eidelman et al. Review of Particle Physics. *Phys. Lett. B*, 592:1, 2004.

[13] The LEP Experiments. A Combination of preliminary electroweak measurements and constraints on the standard model. 2004.

[14] Y. Fukuda et al. Evidence for Oscillation of Atmospheric Neutrinos. *Phys. Rev. Lett.*, 81(8):1562–1567, Aug 1998.

[15] NASA. WMAP Cosmological Parameters Model: lcdm+sz+lens Data: wmap5. `http://lambda.gsfc.nasa.gov/product/map/dr3/params/lcdm_sz_lens_wmap5.cfm`.

[16] G. Abbiendi et al. Search for the Standard Model Higgs boson at LEP. *Phys. Lett. B*, 565:61, 2003. arXiv:hep-ex/0306033v1.

[17] CDF and DØ collaborations. Combined CDF and D0 Upper Limits on Standard Model Higgs- Boson Production with up to 6.7 fb^{-1} of Data. 2010. arXiv:hep-ex/1007.4587.

[18] M. J. G. Veltman. The Infrared - Ultraviolet Connection. *Acta Phys. Polon.*, B12:437, 1981.

[19] Nima Arkani-Hamed, Andrew G. Cohen, and Howard Georgi. Electroweak symmetry breaking from dimensional deconstruction. *Phys. Lett.*, B513:232–240, 2001.

[20] Martin Schmaltz and David Tucker-Smith. Little Higgs Review. *Ann. Rev. Nucl. Part. Sci.*, 55:229–270, 2005.

[21] Maxim Perelstein. Little Higgs Models and Their Phenomenology. 2005.

[22] N. Arkani-Hamed, A. G. Cohen, E. Katz, and A. E. Nelson. The Littlest Higgs. *JHEP*, 07:034, 2002.

[23] Tao Han, Heather E. Logan, Bob McElrath, and Lian-Tao Wang. Phenomenology of the little Higgs model. *Phys. Rev.*, D67:095004, 2003.

[24] Csaba Csaki, Jay Hubisz, Graham D. Kribs, Patrick Meade, and John Terning. Big corrections from a little Higgs. *Phys. Rev.*, D67:115002, 2003.

[25] Z. Chacko, Hock-Seng Goh, and Roni Harnik. A twin Higgs model from left-right symmetry. *JHEP*, 01:108, 2006.

[26] Hock-Seng Goh and Shufang Su. Phenomenology of The Left-Right Twin Higgs Model. *Phys. Rev.*, D75:075010, 2007.

[27] DØ Collaboration. Search for W' Boson Resonances Decaying to a Top Quark and a Bottom Quark. *Phys. Rev. Lett.*, 100(21):211803, May 2008.

[28] K. Aamodt et al. The ALICE experiment at the CERN LHC. *JINST*, 0803:S08002, 2008.

[29] R. Adolphi et al. The CMS experiment at the CERN LHC. *JINST*, 0803:S08004, 2008.

[30] A. Alves et al. The LHCb Detector at the LHC. *JINST*, 3:S08005, 2008.

[31] Lyndon Evans and Philip Bryant. LHC Machine. *JINST*, 3:S08001, 2008.

[32] B Heinemann, A Hoecker, and E Torrence. Online Luminosity plots by Week. Sep. ATL-COM-PHYS-2010-720.

[33] G. Aad et al. The ATLAS Experiment at the CERN Large Hadron Collider. *JINST*, 3:S08003, 2008.

[34] A. Airapetian et al. ATLAS calorimeter performance. CERN-LHCC-96-40.

[35] F. Bergsma. Calibration of Hall sensors in three dimensions. Proceedings of 13th International Magnetic Measurement Workshop, Stanford, California, 19-22 May 2003.

[36] S. Lloyd et al. The ATLAS Athena Framework. `https://twiki.cern.ch/twiki/bin/view/Atlas/AthenaFramework`.

[37] Richard P. Feynman. Very high-energy collisions of hadrons. *Phys. Rev. Lett.*, 23(24):1415–1417, Dec 1969.

[38] John C. Collins, Davison E. Soper, and George Sterman. Factorization of Hard Processes in QCD. *Adv. Ser. Direct. High Energy Phys.*, 5:1–91, 1988.

[39] H Abramowicz and A. Caldwell. HERA collider physics. *Rev. Mod. Phys.*, 71:1275–1410, 1999.

[40] J. Pumplin et al. New generation of parton distributions with uncertainties from global QCD analysis. *JHEP*, 07:012, 2002.

[41] Torbjorn Sjostrand, Stephen Mrenna, and Peter Skands. PYTHIA 6.4 Physics and Manual. *JHEP*, 05:026, 2006.

[42] Bo Andersson, G. Gustafson, G. Ingelman, and T. Sjostrand. Parton Fragmentation and String Dynamics. *Phys. Rept.*, 97:31–145, 1983.

[43] G. Corcella, I.G. Knowles, G. Marchesini, S. Moretti, K. Odagiri, P. Richardson, M.H. Seymour, and B.R. Webber. HERWIG 6.5: an event generator for Hadron Emission Reactions With Interfering Gluons (including supersymmetric processes). *JHEP*, 0101:010, 2001. arXiv:hep-ph/0011363v3; arXiv:hep-ph/0210213v2.

[44] S. Frixione, P. Nason, and B. R. Webber. Matching nlo qcd and parton showers in heavy flavour production. *JHEP*, 0308:007, 2003.

[45] Michelangelo L. Mangano, Mauro Moretti, Fulvio Piccinini, Roberto Pittau, and Antonio D. Polosa. ALPGEN, a generator for hard multiparton processes in hadronic collisions. *JHEP*, 07:001, 2003.

[46] B.P. Kersevan and E. Richter-W as. The Monte Carlo Event Generator AcerMC version 3.5 with interfaces to PYTHIA 6.3, HERWIG 6.5 and ARIADNE 4.1. arXiv:hep-ph/0405247v1.

[47] A. Shibata, M. Bosman, R. Hawkings, U. Husemann, S. Allwood-Spiers, L. Mijovic, B. Kersevan, G. Khoriauli, N. F. Castro, A. Lucotte, J. Donini, C. Feng, W. Verkerke, L. Fiorini, S. Grinstein, A. Gaponenko, D. Whiteson, B. Cooper, A. Messina, M. Gosselink, N. Vlasov, and M. Cristinziani. Understanding Monte Carlo Generators for Top Physics. Jun 2009. ATL-COM-PHYS-2009-334.

[48] Martijn Gosselink. *Radiating top quarks.* PhD thesis, Amsterdam, 2010. ISBN-9789461080899.

[49] M.L. Mangano. Matching matrix elements and shower evolution in hadronic collisions. `https://mlm.web.cern.ch/mlm/talks/lund-alpgen.pdf`.

[50] J. A. M. Vermaseren. Axodraw. *Comput. Phys. Commun.*, 83:45–58, 1994.

[51] A. Pukhov. Calchep 2.3: MSSM, structure functions, event generation, 1, and generation of matrix elements for other packages. 2004.

[52] S. Agostinelli et al. G4–a simulation toolkit. *Nuclear Instruments and Methods in Physics Research Section A: Accelerators, Spectrometers, Detectors and Associated Equipment*, 506(3):250 – 303, 2003.

[53] ATLAS Collaboration. Atlfast II. `https://twiki.cern.ch/twiki/bin/view/Atlas/AtlfastII`.

[54] The ATLAS Collaboration. The simulation principle and performance of the ATLAS fast calorimeter simulation FastCaloSim. Oct 2010. ATL-PHYS-PUB-2010-013.

[55] The ATLAS Collaboration. The ATLAS Simulation Infrastructure. 2010. arXiv:1005.4568v1.

[56] G. Aad et al. Expected Performance of the ATLAS Experiment - Detector, Trigger and Physics. 2009.

[57] C. Roda and I. Vivarelli. Cell Based Jet Calibration. 2005. ATL-PHYS-PUB-2005-019. ATL-COM-PHYS-2005-017. CERN-ATL-PHYS-PUB-2005-019.

[58] O. Fedin. Reconstruction and identification of photons and electrons with the ATLAS detector. *Nuclear Instruments and Methods in Physics Research Section A: Accelerators, Spectrometers, Detectors and Associated Equipment*, 623(1):306 – 308, 2010. 1st International Conference on Technology and Instrumentation in Particle Physics.

[59] W. Lampl, S. Laplace, D. Lelas, P. Loch, H. Ma, S. Menke, S. Rajagopalan, D. Rousseau, S. Snyder, and G. Unal. Calorimeter Clustering Algorithms: Description and Performance. (ATL-LARG-PUB-2008-002. ATL-COM-LARG-2008-003), Apr 2008.

[60] M Aharrouche, C Anastopoulos, V Dao, F Derue, F Dudziak, O Fedin, D Fournier, D Froidevaux, J Hartert, L Iconomidou-Fayard, K Kerschen, S Koenig, T Koffas, V Maleev, E Paganis, G Psztor, J Poveda, A Robichaud-Vronneau, A Schaffer, T Sarangi, E Sedykh, V Solovyev, K Tackmann, T Theveneaux-Pelzer, P Urquijo, M Wielers, and S L Wu. Electron performance in the ATLAS experiment. Apr. ATL-COM-PHYS-2010-208.

[61] S. Hassani, L. Chevalier, E. Lanon, J.-F. Laporte, R. Nicolaidou, and A. Ouraou. A muon identification and combined reconstruction procedure for the ATLAS detector at the LHC using the (MUONBOY, STACO, MuTag) reconstruction packages. *Nuclear Instruments and Methods in Physics Research Section A: Accelerators, Spectrometers, Detectors and Associated Equipment*, 572(1):77 – 79, 2007.

[62] J. Abdallah et al. Measurement of missing tranverse energy. ATL-PHYS-PUB-2009-016.

[63] A. Doxiadis and M. Kayl. Estimating the isolated lepton rate in multi-jet events. ATL-PHYS-INT-2008-022.

[64] A. Hoecker et al. TMVA - Toolkit for Multivariate Data Analysis. *POSACAT*, 040, 2007.

[65] The ATLAS Collaboration. Jet Selection for Top Physics. ATL-COM-PHYS-2010-835.

[66] S. Ferrag, L. Gonzalez de la Hoz, L. March, E. Ros, M. Rijpstra, M. Vos, and M. Vreeswijk. Looking for signatures of the left-right twin higgs model with the ATLAS detector at the LHC. 2008. ATL-PHYS-PUB-2008-004.

[67] The ATLAS Collaboration. Observation of top quark pair production in ATLAS at $\sqrt{s} = 7$ TeV. ATLAS-CONF-2010-044.

Samenvatting

Onlangs is een langverwacht en baanbrekend tijdperk aangebroken voor het vakgebied van de deeltjesfysica: de LHC (*Large Hadron Collider*) is van start gegaan. Deze deeltjesversneller bevindt zich in een cirkelvormige tunnel onder de grond, nabij Genève en bestaat uit supergeleidende magneten die ertoe dienen om protonen te versnellen tot nagenoeg de lichtsnelheid. Twee bundels van protonen bewegen zich in tegenovergestelde richting door de tunnel en worden op vier locaties op elkaar gericht. Bij de hoogenergetische botsingen die op deze punten plaatsvinden worden elementaire deeltjes geproduceerd, zoals elektronen en quarks, in verschillende samenstellingen en met variërende waarschijnlijkheid. De geproduceerde deeltjes vervallen doorgaans onmiddellijk in nog meer deeltjes die vervolgens uiterst nauwkeurig gemeten worden door speciaal daarvoor ontworpen detectoren met afmetingen van tientallen meters in diameter. Eén van die detectoren heet ATLAS en vormt de context van dit proefschrift.

De ATLAS-detector bestaat uit verschillende lagen van specifieke subdetectoren die ieder geoptimaliseerd zijn voor het meten van een bepaald type deeltjes. Er is echter één type deeltjes dat geen enkele interactie aangaat met materiaal en ongemoeid door de ATLAS-detector vliegt: neutrino's. Desondanks kan er, door behoud van impuls toe te passen, een schatting worden gemaakt van de neutrino's die bij een botsing geproduceerd zijn. In het vlak loodrecht op de protonbundels wordt de som van impulsvectoren van alle deeltjes uit de botsing die wél gedetecteerd zijn in evenwicht gebracht met een vector, $\not{\mathbf{E}}_{\mathrm{T}}$. Deze vector wordt de ontbrekende transversale energie genoemd en wordt geassocieerd met de neutrinos die geproduceerd zijn.

Alle waarnemingen die tot nu toe bij soortgelijke experimenten gedaan zijn, worden perfect beschreven door het zogenaamde Standaard Model: een verzameling van formules die voorspelt welke wisselwerkingen er spelen tussen elementaire deeltjes—de bouwstenen van alle materie op aarde. Er zijn echter sterke aanwijzingen dat het Standaard Model niet voldoet bij de enorm hoge energie waarbij de oerknal plaatsvond en evenmin bij de energie die momenteel gecreëerd wordt bij de botsingen van de LHC. Verschillende suggesties voor een uitbreiding van het Standaard Model zijn op papier gezet, welke nu stuk voor stuk in de praktijk worden getest worden bij de LHC.

De voorspelde samenstelling van geproduceerde deeltjes bij de botsingen volgens de mogelijke nieuwe modellen bevat vaak hoogenergetische neutrino's of nieuwe deeltjes die niet gemeten kunnen worden en evengoed ontbrekende energie veroorzaken. Het is belangrijk om de nauwkeurigheid van de associatie van de ontbrekende energie met deze deeltjes goed te bestuderen voordat kan worden geconcludeerd met welk van de hypothetische modellen de waarnemingen corresponderen. Daartoe is in dit proefschrift een studie gedaan naar de nauwkeurigheid van de reconstructie van de ontbrekende energie in botsingen die door het Standaard Model worden beschreven. In het bijzonder zijn daarvoor botsingen gebruikt waarin twee 'top'-quarks worden geproduceerd.

In een aantal geopperde modellen worden zwaardere varianten van de elementaire deeltjes geïntroduceerd, zoals het W'-boson. In dit proefschrift is de mogelijke ontdekking van dit deeltje met de ATLAS-detector onderzocht door gesimuleerde botsingen te bestuderen. Doordat het hypothetische W'-boson zo zwaar is, kan het vervallen in een 'top'- en een 'bottom'-quark—de twee zwaarste quarks in het Standaard Model. De 'top'-quark vervalt vervolgens in nog een 'bottom'-quark, een elektron en een neutrino. In de detector worden dus metingen verwacht die corresponderen met de twee 'bottom'-quarks en een elektron, waarbij bovendien ontbrekende energie wordt gereconstrueerd wegens het neutrino. Het is een uitdaging om het signaal te selecteren uit het totale aantal gemeten botsingen, waarvan er miljoenen per seconde plaatsvinden. De waarschijnlijkheid dat er bij een botsing de reeds bekende deeltjes worden geproduceerd is namelijk vele malen groter. Door gebruik te maken van een geavanceerde selectieprocedure bleek het mogelijk het signaal te onderscheiden van de overige botsingen. De massa van het W'-boson kan worden gereconstrueerd door alle vervalproducten te combineren. Een piek in het massaspectrum van geselecteerde botsingen zou het bestaan kunnen aantonen van het W'-boson. Het onderzoek in dit proefschrift heeft uitgewezen dat, onder aanname van één van de mogelijke modellen, een hoeveelheid gemeten botsingen die correspondeert met een jaar voldoende moet zijn om een piek van een W'- boson waar te nemen. Binnenkort zijn we dus in staat om ofwel het model te ontdekken dat de complete deeltjesfysica beschrijft ofwel een aantal van de opties uit te sluiten.